ABSTRACT

Title of Dissertation: Searches on Weakly Interacting Massive Particles and sub-MeV Fermionic Dark Matter in PandaX-II and PandaX-4T

Dan Zhang
Doctor of Philosophy, 2022

Dissertation Directed by: Professor Xiangdong Ji
Department of Physics

The nature of dark matter is a crucial problem for both cosmology and particle physics. The weakly interactive massive particle (WIMP) is one of the top dark matter candidates searched for decades because of the so-called 'WIMP-miracle'. Dual phase liquid xenon time projection chambers (LXeTPCs) have led the most sensitive searches on the GeV-scale spin-independent WIMP-nucleus scattering cross section for years because of the strong background suppression and scalability. With 3.7 tonne liquid xenon in the sensitive region of the LXeTPC, the Particle AND Astrophysical Xenon (PandaX) collaboration is now running PandaX-4T experiment at the B2 Hall of China Jinping Underground Laboratory after the PandaX-II experiment. The strongest limit back to the release time was published with the 0.63 tonne·year exposure on the standard thermal WIMP search with a lowest excluded cross section (90% C.L.) of 3.8×10^{-47} cm^2 at a dark matter mass of 40 GeV/c^2.

In this thesis, I discuss research and developments correlated to PandaX experiments. I

present the whole procedure of ^{83}Rb/^{83m}Kr calibration in the PandaX-II detector from sources production with 3.4/20 MeV protons bombardment on natural krypton to the data analysis after injection into the PandaX-II detector, which becomes crucial for the increasingly larger detectors. With the ^{83m}Kr events, I present the developments on the horizontal position construction algorithms in PandaX-II, which is important to fully take advantage of the self-shielding ability of xenon, determining the fiducial volume directly related to the exposure. Moreover, I discuss the procedure of the profile likelihood ratio analysis to set the limits and sensitivities, where probability distribution functions are prepared with reweighting Monte Carlo to handle the systematic uncertainties in the detector response modeling more robustly. The methodology is applied on the spin-independent WIMP search to prove consistency with the template morphing method. Then, I conduct a search on electronic absorption of sub-MeV fermionic dark matter which shares similarities with sterile neutrino dark matter. Such dark matter with a 60 keV/c^2 mass can explain the low-energy ER excess reported by XENON1T collaboration, but is only marginally allowed by our constraints.

SEARCHES ON WEAKLY INTERACTING MASSIVE PARTICLES AND SUB-MEV FERMIONIC DARK MATTER IN PANDAX-II AND PANDAX-4T DETECTORS

by

Dan Zhang

Dissertation submitted to the Faculty of the Graduate School of the
University of Maryland, College Park in partial fulfillment
of the requirements for the degree of
Doctor of Philosophy
2022

Advisory Committee:
Professor Xiangdon Ji, Chair/Advisor
Professor Carter Hall
Professor Anson Hook
Professor Kara Hoffman
Professor Da-lin Zhang

Acknowledgments

I want to express deep gratitude to all the people who have helped me in the past five years and made this thesis possible.

First and foremost I'd like to thank my advisor, Professor Xiangdong Ji, for giving me the opportunity to continue working with PandaX collaboration after a two-year experience as an undergraduate student. I have received extensive guidance from Xiangdong for research and life in many aspects. I appreciate a lot to get opportunities to work with many fantastic people in PandaX. And I still clearly remember going through one writing week straight with Xiangdong years ago, getting daily immediate feedbacks, and an almost one-year weekly online journal/book club together with him and his previous graduate student, Andi Tan, after the Covid pandemic started. Xiangdong's enthusiasm in physics and optimism encourage me to pursue an academic career in the next stage.

My special thanks go to Andi Tan for the help since my undergraduate internship in PandaX. His cautious attitude sets atandards to me at the early stage of my research career, including small things like welding a wire in a neat way, keeping the lab organized and bearing in mind the matches of different screws and drivers. Furthermore, I thank for extra supports including precious suggestions and helps received even after his graduation. I admire him for his intelligence, generosity and integrity.

I would also like to thank the talented PIs I have worked with, especially Jianglai Liu, Ning

Zhou and Xun Chen. Jianglai creates such a good environment that I feel free to ask any questions until I really understand everything I want to know, and on the other hand, helps to prioritize the to-do list while I am overwhelmed. Especially after the PandaX-4T commissioning data were published and all of us started to work in smaller groups, the one-to-one meetings with Jianglai are really important to keep me on track. I appreciate the days working with Ning's group with special thanks to Jingkai Xia and Zhou Huang on the hardware while I felt very supportive to test my ideas and plans even if some of them led nowhere. Xun provided important supports with his professional computational skills especially after I started to work remotely. It was enjoyable to discuss with the members in the computational group including Qiuhong Wang, Abdusalam Abdukerim, Chen Cheng and Nasir Shaheed. I appreciate many cross-group discussions that extend my knowledge with Pengwei Xie, Xiaopeng Zhou and Wenbo Ma. I acknowledge other insightful and experienced coworkers in the PandaX collaboration without whom the detectors won't be built smoothly.

My special thanks also go to Qing Lin and Shao-Feng Ge who are the two PIs I have closely collaborated with but I haven't got a chance to meet in person yet. The discussions were so organized, efficient and insightful that I felt on track. I express my gratitude to Yunshan Cheng and Xuyang Ning who worked together with Qing as well on the PandaX-4T analysis, and Jie Sheng and Xiao-dong Ma in Shao-Feng Ge's group who helped a lot on the theories of another project.

I am indebted to all the members of PandaX collaboration that contribute to the construction and commissioning of PandaX-4T detector.

I would like to thank Cater Hall, Alberto Belloni, and again Jianglai and Xiangdong for writing a recommendation letter for my postdoctoral applications. I also thank Mengjiao Xiao

and again Andi Tan for precious suggestions and discussions together during the application.

I acknowledge my dissertation committee for their precious time to improve this thesis.

I also owe my deepest thanks to my family's unconditional love and support. My parents have provided freedom for me to make almost all the important decisions in my life. My cousin sister, Qi Zhang, texted me a very detailed list of essential food and medicines at the beginning of the Covid-19 lockdown, and my cousin brother, Hongyu Zhang, sent me an oversea package while it was hard to buy masks.

I would like to thank my best friend and also my boyfriend, Chaobo Shen, for being supportive for the past four years. Even if we only physically stayed together for about a year, what we have been through together makes you my go-to person to share everything in my life.

I appreciate company from my friends in College Park. My friendship with Yukari Yamauchi has some destiny as we came to Maryland in the same year, and will go to the same university as postdoctoral researchers in the soon future. I also thank for Yingyue Zhu who joined us later, and we spent great time together for barbeques, workouts and excursions. I also thank Dinh Duy Vu, Yixu Wang, Saurabh Vasant Kadam, Emily Jiang, Beini Gao, Yanda Geng, Hyunwoo Oh, Edward Broadberry, Jack Holligan for enjoying time together in the PSC 3rd-floor lunch break and off-from-work parties, which makes my graduate student life much happier and easier.

I thank my girl friends who I've known for about/over ten years, including Tianji Cai, Qianxia Zhao and Yuwen Zhu for being listeners to each other no matter where we are.

I am lucky to have great housemates in the past five years. My special thanks go to Xinxin Sun and Chuchu Zhang who babysat me after my first surgery when I almost slept 24/7 for one week.

I would like to acknowledge financial support from the University of Maryland.

Table of Contents

Acknowledgements ii

Table of Contents v

List of Tables viii

List of Figures x

List of Abbreviations xx

Chapter 1: Introduction 1
- 1.1 Astronomical and Cosmological evidence of dark matter . . . 3
  - 1.1.1 Rotational curves . . . 3
  - 1.1.2 Bullet cluster . . . 5
  - 1.1.3 Cosmic microwave background . . . 6
- 1.2 Dark matter candidates . . . 8
  - 1.2.1 Particle-like . . . 8
  - 1.2.2 Wave-like . . . 12
  - 1.2.3 Massive Compact Halo Objects . . . 16
- 1.3 WIMP search . . . 17
  - 1.3.1 Direct detection . . . 18
  - 1.3.2 Indirect detection . . . 21
  - 1.3.3 Particle collision . . . 23
- 1.4 Dual-phase liquid-xenon time projection chamber . . . 24
  - 1.4.1 Principle . . . 25
  - 1.4.2 Advantages . . . 27
  - 1.4.3 Double beta decay searches with Xe . . . 30
- 1.5 Summary . . . 30

Chapter 2: Overview of PandaX-II experiment 32
- 2.1 China Jinping Underground Laboratory . . . 33
- 2.2 PandaX-II final analysis . . . 34
  - 2.2.1 Detector assembly and data taking history . . . 34
  - 2.2.2 Data analysis with the complete PandaX-II exposure . . . 38
- 2.3 R&Ds in the PandaX-II finale . . . 54
  - 2.3.1 End-of-run calibration campaign . . . 54
  - 2.3.2 Different drifting electric fields in a large TPC . . . 58

2.3.3 Low gain in PMTs for ER signals in MeV . . . 60
2.3.4 CH_3T calibration . . . 61
2.3.5 ^{222}Rn without active circulation . . . 63

Chapter 3: ^{83}Rb/^{83m}Kr calibration for PandaX detectors 65
3.1 Production of ^{83}Rb/^{83m}Kr with 3.4 MeV protons . . . 68
3.1.1 Theoretical consideration . . . 68
3.1.2 Design of the target cells . . . 70
3.1.3 Preparation and measurement of the ^{83}Rb/^{83m}Kr sources . . . 71
3.2 Production of ^{83}Rb/^{83m}Kr with 20 MeV protons . . . 75
3.2.1 Upgrading consideration . . . 75
3.2.2 Production . . . 80
3.3 Contamination tests before injection . . . 81
3.3.1 Radioactivity contamination test . . . 83
3.3.2 Electronegative impurity test . . . 87
3.4 Brief data analysis of ^{83m}Kr events in PandaX-II . . . 88
3.4.1 ^{83m}Kr injection process . . . 89
3.4.2 ^{83m}Kr event analysis . . . 89
3.4.3 Contamination analysis . . . 94

Chapter 4: Horizontal position reconstruction algorithms in PandaX-II 97
4.1 Reconstruction procedure with PAF . . . 100
4.2 Refined analytical PAF . . . 101
4.2.1 Extended single-variable PAF . . . 102
4.2.2 Model training with ^{83m}Kr in PandaX-II . . . 104
4.3 Simulation-based PAF . . . 109
4.4 Comparison . . . 114
4.4.1 Simulation event . . . 114
4.4.2 ^{83m}Kr event . . . 116
4.4.3 Gate event . . . 119
4.4.4 Surface event . . . 122
4.5 Summary . . . 129

Chapter 5: Overview of PandaX-4T experiment 132
5.1 Subsystems . . . 132
5.1.1 TPC and electrodes . . . 132
5.1.2 PMT, readout electronics and DAQ system . . . 137
5.1.3 Cryogenics, circulation system and distillation tower . . . 141
5.1.4 Background control . . . 144
5.1.5 Calibration . . . 147
5.1.6 Slow control . . . 149
5.1.7 Data processing and reconstruction . . . 150
5.1.8 Detector simulation . . . 151
5.2 Run 1 for WIMP search . . . 152
5.2.1 P4-chain . . . 153

5.2.2 Main backgrounds and fiducialization . . . 160
5.2.3 Signal modeling and limit setting . . . 163

Chapter 6: Signal model with reweighting Monte Carlo in limit setting 168
6.1 Probability distribution functions with reweighting Monte Carlo . . . 170
6.1.1 Principle . . . 171
6.1.2 Example . . . 172
6.1.3 Uncertainties . . . 176
6.1.4 Brief summary . . . 177
6.2 Fast detector simulation . . . 177
6.3 Reweighted probability distribution functions . . . 192
6.3.1 Major detector parameters . . . 193
6.3.2 Other detector parameters . . . 196
6.4 Application on WIMP search in PandaX-4T . . . 200
6.4.1 Profile likelihood ratio analysis . . . 203
6.4.2 Subtleties in the PLR analysis . . . 208
6.4.3 Comparison with template morphing . . . 212

Chapter 7: A Search for Light Fermionic Dark Matter Absorption on Electrons 217
7.1 Overview on keV sterile neutrino . . . 219
7.1.1 νMSM model . . . 219
7.1.2 Free streaming scale . . . 220
7.1.3 Controversial 3.55 keV excess . . . 221
7.2 A light fermionic dark matter search in direct detection . . . 223
7.2.1 Atomic form factor smearing . . . 225
7.2.2 Detector response smearing . . . 226
7.3 Astronomical and cosmological limits . . . 232
7.4 Limit and sensitivity setting with PandaX-4T Run 1 data . . . 235

Chapter 8: Summary and outlook 241

Bibliography 243

List of Tables

2.1 The 7 inhibited 3-inch PMTs in the complete data set out of 110 with a position map in Fig. 4.2 for both top and bottom arrays. . . . 39
2.2 Uniformity calibration events used in the three runs. . . . 43
2.3 Summary of PDE, EEE and SEG in PandaX-II. . . . 45
2.4 Backgrounds in the dark matter search runs inside the FV (1 mDRU = 1×10^{-3} evt/keV$_{ee}$/day/kg) in 0-25 keV$_{ee}$. The total flat ER backgrounds of Run 9 and 10 are sums of the independent estimations, and that of Run 11 is estimated with data in the region of 20-25 keV$_{ee}$. . . . 50
2.5 Number of events in Runs 9, 10, and 11 after successive selection cuts. . . . 51
2.6 The best fit total and below-NR-median background events in Run 9, Run 10 and Run 11 in the FV with the signal model $m_\chi = 400$ GeV/c^2. The BNM backgrounds are estimated with the PDFs. . . . 54
2.7 Decay data of ^{220}Rn and its progenies. . . . 57
2.8 Overview of the ^{220}Rn calibration sources. . . . 58

3.1 The radioactivity of the three zeolite samples on the date when they were measured. 73
3.2 Decay channels of the ^{83m}Kr isotope [1]. . . . 90

4.1 Values of RSD with $c = 1$ and different w_e and d. . . . 108
4.2 Tuned group parameters. . . . 108
4.3 The χ^2 dependence on the reflectivity r with $z = 6$ mm at (X_7, Y_7). . . . 112
4.4 The position of selected gaps in the gate events and standard deviations. . . . 120
4.5 The results of fitting Eq. 4.17 with the y_{fRec} of the gate events reconstructed with the two algorithms. . . . 122

5.1 Basic information of Run 1 data of PandaX-4T experiment. . . . 152
5.2 A single hit defined. One sample in a waveform corresponds to 4 ns. . . . 155
5.3 The main backgrounds for the WIMP-nucleus scattering search [2]. . . . 161
5.4 A summary of the basic detector parameters for PandaX-4T Run 1. . . . 166

6.1 Brief summation of the simulation steps in the fast detector simulation. The step with a star mark ($\star$) means a different parameterization is used compared to NEST2. 179
6.2 The detector simulation parameters for the 5 sets in PandaX-4T Run 1. The main uncertainties of the parameters are shown in the round brackets. The rows with only one value have the 5 sets sharing the same parameter. . . . 180

7.1 Summary of nominal values, uncertainties (fractional), and best fits for the detector response parameters p_* (upper), and signal and individual background components (lower). p_* include PDE, $G2_b$, SEG$_b$ and ionization recombination parameters p_0 and p_f (see text for details). Similar to Ref. [2], the common DM signal and tritium background for each set are left float in the fit. The best fit values of the number of events have been corrected for their efficiencies. 231
7.2 The leading visible decay of χ. 234

List of Figures

1.1 The rotational curves along the south-west (SW) and the north-east (NE) major axis in M31 [3] . . . 4
1.2 The standard hale model speed distribution in the lab-frame on the earth [4]. . . . 5
1.3 Bullet cluster [5]. . . . 6
1.4 The temperature angular power spectrum released by $planck$ 2018 data [6] 7
1.5 The axion search with the decay channel of $a \rightarrow \gamma\gamma$ limits on the effective coupling constant $g_{a\gamma\gamma}$ [7]. . . . 13
1.6 Zoom-in AMDX's 90% C.L. upper limits on $g_{a\gamma\gamma}$ [8]. . . . 15
1.7 The projections of the DMRadio family searching for f_a on the GUT scale. . . . 17
1.8 Existing limits on the DM fraction vs PBH mass (blue for more conservative assumptions and gray for less) and selected projections for future expectations (gold) [9]. . . . 18
1.9 The status of the spin-independent WIMP-nucleon cross section unitl April 2021 (PandaX-4T commissioning data and the first result of LZ are not included on this plot) [10]. . . . 18
1.10 Limits of the (a) SD WIMP-neutron and (b) WIMP-proton scattering cross section as a function of WIMP mass published by the PandaX-II 56 tonne·day exposure overlain with some other works by April 2019 [11]. . . . 20
1.11 (a) AMS-02 positron (different channels labeled), Fermi-LAT ($b\bar{b}$ channel) and WMAP (cyan) limits on annihilation cross-section versus mass [12]. (b) AMS-02 antiproton-to-proton ratio (different channels labeled) limits. The grey lines correspond to the thermal relic cross section [13]. . . . 21
1.12 The projected sensitivities on antideuteron fluxes as a function of the kinetic energy per nucleon of AMS-02 after 5 years of operation and GAPS after three 35-day flights overlain with the limit from BESS and the predicted signals of the benchmark WIMP models [14]. . . . 22
1.13 ATLAS 90% C.L. limits on the SI (left) and SD (right) DM-nucleon scattering compared to other direct detection experiments [15]. . . . 24
1.14 A schematic view of a LXeTPC [16]. . . . 26

2.1 Location of China Jinping Underground Laboratory with the site of PandaX-4T marked at the upper-right corner. . . . 33
2.2 A view of the PandaX-II workspace. . . . 35
2.3 Sketch of the PandaX-II passive shielding 36
2.4 Schematics of cryogenics and circulation system in PandaX-II (also in Fig. 3.11). 37

2.5 The accumulation of DM exposure (black line) and the evolution of the electron lifetime (blue curve, right axis) in PandaX-II. 38
2.6 An example of gain correction to low gain PMTs. (a) The $S1$ charge distribution of α events in the low gain Ch.10707 (yellow line) and the other reference PMTs located at the same radius (green lines). (b) The evolution of gain of Ch.10707. The yellow open circles represent gains obtained in the LED calibration and the green dots are the corrected gains. The tendency in green dots is reasonable w.r.t. the supply voltages of Ch.10707. 40
2.7 $S2$ TBA before (top) and after (bottom) fixing with qS2_ibad. The qS2T and qS2B are the sum top and bottom $S2$ charges, respectively. 42
2.8 $S2$ TBA as a function of $r = \sqrt{x^2 + y^2}$ before (left) and after (right) fixing with qS2_ibad. The red lines on the right plot cut the outliers. 43
2.9 Fractional difference between the reconstructed energy $E_{\rm ee}$ and expected energy $E_{\rm expect}$ for characteristic gamma peaks in Run 9 (blue circles), Run 10 (magenta squares), and Run 11 (green diamonds). Closed symbols represent points used in the fits, and open symbols are those test peaks. 45
2.10 (a) Charge yield of NR and (b) light yield of ER from PandaX-II calibration data compared with results from the worldwide data (ER: Refs. [17, 18, 19, 20], NR: Refs. [21, 22, 23, 24, 25, 26]). 47
2.11 The comparison of model simulation and calibration data in the projection of deposited energy, $S1$ and $S2$, in Run 9 and Runs 10/11. 48
2.12 Comparison of the distribution of events away from the median of ER band with $S1 \in (45, 200)$ PE between the ^{220}Rn calibration data (magenta dots) and Run 11 DM search data (green dots). The fitted Gaussian functions are overlaid. 49
2.13 (a) The full waveform of event 167193 in run 20922. The second small $S2$ was split into a few $S1$s in our clustering algorithm, so that it was incorrectly recognized as a single scattering events; (b) The partial waveform of event 112727 in run 22940. Two of the three hits in the reconstructed $S1$ are due to the coherent noise pickup in channel 10506 and 10507. 52
2.14 The spatial and signal distributions of events within $S1$ and $S2$ range cuts for (a) Run 9, (b) Run 10 and (c) Run 11 with events outside the FV. Only the final candidates in the DM search data are shown on the signal distributions for (d) Run 9, (e) Run 10 and (f) Run 11. The ten most likely DM candidates are labeled. References of the ER band median (blue solid line) and NR band median (pink solid line) are shown in the signal distributions. The magenta lines are the boundaries of the acceptance window. The solid and dotted magenta lines are the 99.99% NR and 99.9% ER acceptance cuts, respectively. The dashed magenta line is the $S2 = 100$ PE boundary. The dashed grey curves represent the equal-energy curves in nuclear recoil energy (keV$_{\rm nr}$). 53
2.15 The normalized likelihoods of the most likely DM events for $m_\chi = 400$ GeV/c^2. . 55
2.16 The schedule of the R&Ds and calibration data taking in the last running year of PandaX-II. 56
2.17 The wide energy spectrum of ^{220}Rn calibration data (red) compared to the data for the dark matter runs (black) [27]. 57

2.18 Light yields measured by PandaX-II detector under different drifting electric fields and different energy depositions compared with other works [28]. 59
2.19 The ^{83m}Kr event distribution under different drifting electric fields ($Z_T = 0$ corresponds to the liquid-gas interface) [28]. The magenta dashed lines mark the fiducial volume for the dark matter search in PandaX-II. For clarification, the R^2 refers to the horizontal position at the anode. 59
2.20 Examples of saturated and normal waveforms of PMTs. Yellow line: an asymmetric waveform due to PMT saturation. Black line: an asymmetric waveform with digitizer truncation. The others are norm waveforms [29]. 60
2.21 The schematics of the circulation of the CH_3T calibration R&D. 62
2.22 The time evolution of methane (blue, monitored by RGA) and tritium (green, monitored by the low energy event rate). The thoron calibration refers to ^{228}Th/^{220}Rn sources injected into the detector. 63
2.23 The time evolution of tritium after turning the circulation with hot purifiers on again. 63
2.24 The time evolution of ^{222}Rn tracked with ^{214}Bi-^{214}Po and the evolution of electron lifetime after stopping the active circulation in PandaX-II. 64

3.1 This measurement compared to the theoretical extensions on the yields of proton beams bombarding on 1 bar $^{\mathrm{nat}}$Kr according to former works [30, 31, 32] for ^{83}Rb. The lines are fitted with the function $y = a \cdot (E - E_{th})^b$, where y is the yield, E_{th} is the threshold of the proton energy with a unit of MeV, and a and b are fitting parameters. 69
3.2 (a) The whole view of the first $^{\mathrm{nat}}$Kr chamber. (b) The whole view of the second $^{\mathrm{nat}}$Kr chamber. (c) The Al window. (d) The positions where we used PTFE gaskets to electrically insulate the $^{\mathrm{nat}}$Kr chamber (the middle flange is the Al window) (e) The inner Al dump with Kapton tape wrapped to avoid possible activation of stainless steel. (f) The wrapped bolt and the paper gasket to insulate the $^{\mathrm{nat}}$Kr chamber. 69
3.3 The storage of the baked zeolite. 72
3.4 The comparison between the simulation and the measurement for different zeolite beads samples. Sample 1, sample 2, sample 3 absorbs rubidium from the Al window, the Al dump and the CF35-straight tube respectively. 73
3.5 The thick target yield integrated for ^{83}Rb. The black point marks our measurement with 3 MeV effective proton energy bombarding on 1 bar $^{\mathrm{nat}}$Kr. The interpretation as the thin target yield can be found in Fig. 3.1 74
3.6 The thin target yields of rubidium isotopes with protons bombardments on $^{\mathrm{nat}}$Kr [30, 31, 32]. Plots from left to right are for ^{83}Rb, ^{84}Rb, ^{86}Rb, respectively. 75
3.7 The stopping power in Al as a function of the proton energy [33]. 77
3.8 (a) The design (marked size in millimeter) and zoom-in cross sections for (b) the Al window CF35 and (c) the CF35 connected to the Al dump. 79
3.9 The assembled target cell for the 20 MeV proton bombardment. 80
3.10 Comparison of the (a) $^{\mathrm{nat}}$Kr(p, xn)^{83}Rb, (b) $^{\mathrm{nat}}$Kr(p, xn)^{84}Rb and (c) $^{\mathrm{nat}}$Kr(p, xn)^{86}Rb cross sections at 20 MeV between this work and previous measurements [30, 31, 32]. 81

3.11 The schematic of the purification system for PandaX-II. The orange arrows indicate the purification LOOP1 for daily purification. The blue arrows show the LOOP2 which induces ^{83m}Kr into detector. The red arrows form a self-circulating route in LOOP2, reducing electro-negative gases released by the source before injection with the help of Getter 2. The black dash line marks the calibration module. . . . 82
3.12 The simulated energy spectrum before reclustering of ^{83}Rb, ^{84}Rb and ^{86}Rb in the PandaX-II fiducial volume after normalization. The isotopes are assumed to be uniformly distributed in the LXe. . . . 84
3.13 The blue line is the energy spectrum of the ^{228}Th zeolite source. The red and green lines are the spectra of the cloth and the background respectively. . . . 86
3.14 (a) The N_2 flushing test arrangement for radioactivity leakage concern. (b) The 0.2 μm filter with a custom holder to stop zeolite powder to enter the detector. . . 86
3.15 (a) The vacuuming test arrangement which is also used for zeolite residue test. (b) The filter to stop zeolite powder for pumping. . . . 87
3.16 The spectrum of the residues with different pumping time. The background is measured with V1 closed in Fig. 3.15. . . . 88
3.17 A typical $S2$ waveform for ^{83m}Kr decays. The red line indicates the $S2$ time window according to the standard data processing. The blue line is the summed waveforms of the bottom PMT array, and the magenta line is of the top PMT array. 90
3.18 (a) The waveform with the two $S1$ separated for ^{83m}Kr decays. (b) The waveform with the two $S1$ mixed. The red lines indicate the $S1$ time window according to the standard data processing. The blue lines are the summed waveforms of the bottom PMT array, and the magenta lines are of the top PMT array. . . . 91
3.19 Typical ^{83m}Kr events with the data processing algorithm for WIMP search. . . . 91
3.20 (a) The rate of ^{83m}Kr during injection including 532 kg LXe. In the fitting, $p0$ is the rate of ^{83m}Kr with backgrounds subtracted. (b) The decay of ^{83m}Kr after injection. The fitting function is $r_{^{83m}\mathrm{Kr}} = p0 \cdot \exp(\frac{-\ln 2 \cdot t}{p1}) + p2$, where $p0$ and $p2$ have unit of Bq, and $p1$ has unit of hour. . . . 92
3.21 The fit of the halflife ($p1$) for the first excited state of ^{83m}Kr. . . . 93
3.22 The energy spectrum of ^{83m}Kr with backgrounds subtracted. The fitting function is $N = \frac{p0}{\sqrt{2\pi}p2} \cdot \exp[-\frac{(E-p1)^2}{2 \cdot p2^2}]$ . . . 94
3.23 (a) The electron lifetime before ^{83m}Kr injection checked by $\log S2_b$ of ^{222}Rn. $\tau_e = 1/p1$ is the electron lifetime . (b) The electron lifetime during ^{83m}Kr injection checked by $\log S2$ of ^{83m}Kr, $\tau e = 1/p1$ was the electron lifetime. In both (a) and (b), t_z is the drifting time of the electrons. The dark blue dots with error bars show the profiled average of the vertical axis, $\log S2_b$ for (a) and $\log S2$ for (b). The red lines are the fittings of the first order polynomial ($\log(S2_b)$ or $\log(S2) = p0 + p1 \cdot (-t_z)$), where $p1$ has the unit of μs^{-1}. . . . 96

4.1 Sketch of a dual-phase nobel gas TPC. The two arrays of light sensors collect both prompt $S1s$ and delayed $S2s$. E_{drift} and $E_{\text{extraction}}$ with their directions indicated by the magenta arrows are established with the electric potential differences among the anode, cathode and gate electrode. More complicated designs for a real TPC are not included in this sketch. The Cartesian coordinate marked on the upper-left corner is used throughout this work where z is for vertical vertexes and (x, y) for horizontal ones. 100
4.2 The arrangement of the top PMTs in the PandaX-II detector. The distance between two closest PMTs is 81.5 mm. The average diameter of the detector is 658 mm. The ones marked as banned are not included in the position reconstruction, those with semi-transparent color are image PMTs to account for the reflections on the PTFE field cage wall surfaces. 103
4.3 An example of the extended PAF in PMT_7 in Fig. 4.2. The blue line is the $\eta_{7,\text{data}}$ along the line from the origin to the center of PMT_7, $(X_7, Y_7) = (204, 71)$ mm, and the red line is the fitted $\eta^0_{7,\text{ana}}$. 106
4.4 R^2_{fRec} distribution of ^{83m}Kr along R^2_{fRec} using the analytical (blue) and simulation-based (red) algorithms. The dashed black line is $0.2P|_{R^2_{\text{rec}}=0}$ used in the analytical algorithm. The peaks along R^2_{fRec} in the analytical algorithm corresponding to the PMT centers (see Fig. 4.10(a)). 109
4.5 An example of simulation-based PAF in the PandaX-II detector with half-million events. The maximum of $\eta_{7,\text{simu}}$ is at the center of PMT_7 in Fig. 4.2. 110
4.6 An example of the data and simulation η_j comparison at the center of PMT_7, $(X_7, Y_7) = (204, 71)$ mm. The simulation templates are generated with different z heights for the light emission.. 112
4.7 The optimized surface of $z(x, y)$ (the effective vertical position of $S2$ emissions) for the PandaX-II detector with 2D linear interpolation applied. The red circles are $\{(x_k, y_k)\}$ which used to optimize $z(x, y)$ at the edge. 114
4.8 The deviation between ML reconstructed (Eq. 4.2) and true positions using simulated data (mean $S2$ at 10000 PE with a 5000 PE sigma) with corresponding simulated PAF, (a) Total deviation, $|\Delta R|$, vs R^2 (b) Radial deviation, ΔR_r, vs R^2. The red line represents the mean deviation, and therefore serve as an estimate of the intrinsic uncertainty of the ML fit. 116
4.9 The total deviation between the reconstructed positions obtained by the two algorithms for the ^{83m}Kr events. (a) Total deviation, $|\Delta R_{\text{fRec}}|$, vs $R^2_{\text{fRec,ana}}$. (b) The radial deviation, $\Delta R_{r,\text{fRec}}$, $R_{\text{fRec,simu}} - R_{\text{fRec,ana}}$, vs $R^2_{\text{fRec,ana}}$. In both figures, the x-axis, $R^2_{\text{fRec,ana}}$, is calculated with the analytical algorithm. The red line again represents the mean deviation. 117
4.10 $x_{\text{fRec}} - y_{\text{fRec}}$ ^{83m}Kr event distribution using the (a) analytical and (b) simulation-based algorithms. The four red circles mark the inhibited PMTs. 118
4.11 The sketch of the gate electrode geometry. 119
4.12 The positions of gate events reconstructed with the analytical (left) and simulation-based (right). 120
4.13 The gate events y_{fRec} distribution projected along the grid wires with the analytical (blue) and simulation-based (magenta) algorithms. The solid lines are the corresponding fittings to the y_{fRec} distribution by six Gaussian functions with the same width. . . 123

4.14 The toy gate events smeared with a 3 mm 2D Gaussian. 123
4.15 The $\log_{10}(S2/S1)$ vs $S1$ for the surface events in PandaX-II. 124
4.16 The stretched soft walls and 1σ inward fluctuation bands with analytical and simulation-based PAF algorithms. The vertical range is bounded from $z = 0$ (the bottom of the TPC) to $z = 60$ cm (the liquid surface). 126
4.17 The soft walls and equivalent radial cuts with different position reconstruction algorithms. The radius of the solid boundary (329.7 mm) and the old FV cut used in Run 10 [34] are drawn for reference. 127
4.18 Run 10 surface-background distribution with different $S2$ ranges and different position reconstruction algorithms with all cuts applied in Ref. [34] except the $S1$-$S2$ and FV cut. Small $S2$ is for 200 to 250 PE, and large $S2$ for 900 to 1100 PE. The inner flat event distribution has been subtracted. 128
4.19 The change of σ_{surf} as a function of $S2$ in a wide range. 129
4.20 The Δt_z distribution of the Run 10 surface events after applying the WIMP-search cuts excluding the radial cut. Other dimensions are integrated. The drifting time from 20 to 350 μs corresponds to z from 56.7 to 1.7 cm 130
4.21 The projections of $P_{b,\text{wall}}$ onto different axes. The top / bottom panel is for the analytical / simulation-based PAF algorithm respectively. The left panels integrate the other two dimensions ($S1$ and z), and the right panels only integrate events in the corresponding FV. 130

5.1 Overview of the PandaX-4T experiment 133
5.2 The arrangement of the ports for the IV and OV of PandaX-4T. 134
5.3 (a) A cross-sectional view of the PandaX-4T detector. (b) The layout of the four main electrodes in PandaX-4T. 135
5.4 (a) The gate electrode in PandaX-4T (b) The cathode in PandaX-4T. 136
5.5 The front view of the PandaX-4T TPC. 136
5.6 (a) The blue LED covered with a PTFE diffuser. (b) The short level meter. (c) The overflow port at the liquid-gas interface. (d) The overflow chamber at the bottom of the IV. 138
5.7 The quantum efficiency of R8520 (left) and R11410 (right) PMTs used in PandaX-II and PandaX-4T as a function of scintillation wavelength 138
5.8 The PMT readout in PandaX-4T with a new readout at DY8 for MeV-scale analysis [35]. 139
5.9 The overivew of PandaX-4T readout electronics and DAQ system [36]. 140
5.10 The decoupling circuit and amplifying circuit [36]. 141
5.11 The cooling bus of PandaX-4T [37]. 142
5.12 The flow rate of xenon filling with the cooling bus for PandaX-4T [37]. 142
5.13 A sketch of the two circulation loops with hot purifiers [37]. 143
5.14 The PandaX-4T distillation tower [38]. 144
5.15 (a) A photo of the water purification system. (b) A side view of the water tank. . . 145
5.16 The radon removal system for the clean rooms. 146
5.17 The calibration system connected to the PandaX-4T circulation system. 148
5.18 The three PVC calibration tubes attached to the OV (left) and the handling port (right) to load the calibration sources in the workspace. 148
5.19 The sketch of the tunnel welded to the OV for DD fusion neutrons for NR calibration. 149

5.20 The schematics of the slow control system of PandaX-4T [39]. 150
5.21 Flow chart of P4-chain. Not all the actions in the chain are listed. 154
5.22 An example of the LED calibration of one PMT with the integrated area of the waveform before correction in unit of ADC (left) and after correction in unit of PE (right). The 4 ns refers to the sampling width of the waveforms 155
5.23 Estimation of the double photon emission probability with AmBe neutron (left) and ^{83m}Kr (right) events. 156
5.24 (a) $S1$ uniformity map (Z vs. X) calibrated with ^{83m}Kr where the color bar means the light yield $S1/E_{\rm ee}$. (b) $S2_b$ uniformity map (Y vs. X) calibrated with ^{83m}Kr where the color bar means the charge yield $S2_b/E_{\rm ee}$. (c) The electron lifetime for z correction in $S2_b$ traced with ^{131m}Xe (164 keV$_{\rm ee}$) and α events ranges in $5.5-6$ MeV. 'A' marks for the HV training of the electrodes, especially the cathode, and 'B' for a circulation pump replacement. 158
5.25 The optimization of fiducial volume of PandaX-4T Run 1 data with simulation events. The amount of uniform ER are scaled with summation of tritium, flat ER and ^{127}Xe. The spatial distributions of neutron and material ER contribution are generated by BambooMC, and the event numbers are scaled with independent estimations, respectively. 161
5.26 Dark matter candidates survived the quality cuts and showing up in the region of interest. The region below NR median and above the NR acceptance can be taken as a golden signal search window for an intuitive cut-and-count analysis. Compared to the 'below NR median' background estimation in Tab. 5.3, Run 1 data present a downward fluctuation. 162
5.27 An event energy spectrum example of SI WIMP-nucleon scattering in xenon detector with $m_\chi = 100$ GeV/c^2 and $\sigma_n^{SI} = 1\times10^{-31}$ cm^2. 164
5.28 Single electron gain in $S2$ with the small $S2$s under $V_{\rm gate} = -5$ kV (if $S2_b$ is used, the $S2/S2_b$ can be used to find SEG$_b$ as shown in Fig. 5.29). The total fitting function (red line) is the summation of the Gaussians as a function of $S2$ for single and double electrons convoluted with a Fermi-Dirac function for efficiency (blue dashed line). 165
5.29 $S2/S2_b$ of AmBe neutron events with $V_{\rm gate} = -5$ kV. 166
5.30 A prediction of WIMP PDF ($m_\chi = 100$ GeV/c^2) for Run 1 set 4 or 5 with the calibrated fast detector simulation. 167
5.31 The 90% C.L. exclusion limit and 1σ sensitivity band of spin-independent WIMP-nucleus scattering reported with PandaX-4T Run 1 data. 167

6.1 The step function example of P_1 in Eq. 6.5 with different Θ_1 as in Eq. 6.7 and Eq. 6.8. 173
6.2 The reweighting example of one-dimensional Gaussian distributions for a target $G(x,\mu=1,\sigma=1)$. The red line is generated with conventional MC. (a) Reweighting with a qualified pool $G(x,\mu=0,\sigma=3)$, (b) Reweighting with an unqualified pool $G(x,\mu=0,\sigma=1)$. 174

6.3 Reweighting example for one-dimension binomial distribution target $B(n, N = 10, p = 0.05)$ with a pool (black line) prepared by truncating a Gaussian $G(x, \mu = 1, \sigma = 0.9)$ with $x > -0.5$ and rounding x to integers n. The red line is generated with conventional MC. . . . 176
6.4 The schematics of the fast detector simulation with NEST. . . . 178
6.5 The Fano factor dependence on the total quanta number N_q for ER under different electric fields. . . . 181
6.6 The probability of n_q to be an electron-ion pair instead of an exciton, $p_{n_{\rm ion}}$ for NR under different drifting electric fields. . . . 182
6.7 Covariance matrix of $\mathbf{p}_{\rm extra}$ for ER (a) and NR (b). . . . 184
6.8 (a) ER recombination ratio mean. (b) ER recombination ratio standard deviation. (c) NR recombination ratio mean. (d) NR recombination ratio standard deviation. The deviation of the $\mu_r(E)$ and $\sigma_r(E)$ calibrated with data taken under $E_{\rm drift} = 92.8$ V/cm for ER (^{220}Rn) and NR (DD and AmBe sources) respectively. The extensions to 127.4 V/cm are also plotted. The transparent red band is the 1σ band of the . . . 185
6.9 The dependence of photon detection efficiency $G1$ on z calibrated by the 164 keV$_{\rm ee}$ peak of ^{131m}Xe. The $z = 0$ accords to the liquid-gas interface. The black lines mark the vertical fiducial cuts to avoid excessive cathode events and gate events. . . 186
6.10 The data calibration nonlinear charge losses in the reconstruction: (a) BLS of $S1_{\rm ori}$ and (b) charge loss of $S2_{b,{\rm ori}}$. The color bar represents the distribution of the probability but with non-normalized scale. . . . 187
6.11 The elifetron lifetime τ_e for the five subsets in the PandaX-4T commissioning run. 188
6.12 Calibration data taken under 92.8 V/cm . . . 190
6.13 Quality-cut efficiencies on $S1$ and $S2_b$ except diffusion band cut (95%) according to data in Fig. 6.12 before calibrating the detector simulation. The interpretation in the region of $S1 < 2$ PE and $S2_b < 20$ PE is not valid as no calibration data cover this region. NEST at the threshold already ensures a 0 efficiency at 0 PE, the quality-cut efficiencies on $S1$ and $S2$ are added onto NEST which is fine if it's not 0 at 0 PE in the parameterization. . . . 191
6.14 Efficiencies of ER and NR due to pre-calibrated quality cuts and detector simulation integrated cuts. For reference, the total efficiencies reach 50% at 1.95 keV$_{ee}$ for ER and 7.65 keV$_{\rm nr}$ for NR. . . . 191
6.15 Charge yield vs. light yield in PE/keV and the linear fit with uniformly distributed ER peaks, ^{131m}Xe (164 keV$_{\rm ee}$), ^{129m}Xe (236 keV$_{\rm ee}$), ^{127}Xe (408 keV$_{\rm ee}$), and ^{83m}Kr (41.5 keV$_{\rm ee}$), which are used in the detector parameter fit of $G1$ and $G2_b = {\rm EEE} \times {\rm SEG}_b$ listed in Tab. 6.2. . . . 192
6.16 The comparison of the original NEST2 and the calibrated version with observable $(S1, S2_b)$. A flat energy spectrum is used for ER, and 10 TeV WIMP for NR. The contour lines correspond to 10% of the largest probability. . . . 193
6.17 The tuned NEST model compared to calibration data with projections on $S1$ and $S2_b$ for DD neutron (NR), AmBe neutron (NR) and ^{220}Rn progenies in the low-energy window (ER). . . . 194

6.18 The recombination ratio $r_{\rm rec}$ prepared in a pool (a) reweighted with new parameters $(p_0^{'}, p_f)$ and for set 1 (b) with $E_{\rm drift} = 127.4$ V/cm and set 4, 5 (c) with $E_{\rm drift} = 92.8$ V/cm in Run 1. 197
6.19 Energy spectrum reweighting example with a 'flatER' pool and a tritium target. . 198
6.20 Distributions of $\log_{10} n_{\rm hit1,ori}$ vs. $\log_{10} n_{\rm pho}$ in the pool (a) prepared by a roundoff and truncated Gaussian and (b) the reweighted target for the nominal $\bar{G}_1$ in Tab. 6.2. 198
6.21 Distributions of $\log_{10} n_{\rm eGas}$ vs. $\log_{10} n_{\rm ele}$ in the pool (a) prepared by a roundoff and truncated Gaussian and the reweighted target for (b) set 1 and (c) set 4 with different electron lifetimes (Fig. 6.11) and the nominal EEE for different data sets in Tab. 6.2. 200
6.22 Distributions of $\log_{10} n_{\rm hit2}$ vs. $\log_{10} n_{\rm eGas}$ in the pool (a) prepared by a roundoff and truncated Gaussian and the reweighted target for (b) set 1 and (c) set 4, 5 with different nominal SEGs in Tab. 6.2. 201
6.23 The 2D Gaussian penalty of $(p_f, p_0^{'})$ with the color bar showing the probability constraints (not-normalized). The red points indicate the templates prepared for the publication in Ref. [2]. The black circle marks the one for the best fit of $(p_f, p_0^{'})$ by the template morphing methode with Run 1 data. 203
6.24 An example of $q_{\mu,\rm obs}$ vs. cross sections $\mu_{40\ \rm GeV/c^2}$ for $m_\chi = 40$ GeV/c^2 in PandaX-4T Run 1. 204
6.25 Accidental background PDF in PandaX-4T Run 1 prepared with equal bin size along $S1$ (left) and $\log_{10}(S1\ [\rm PE])$ (right). 210
6.26 The 90% limits with three different trials of the same PDF generators with 1×10^6 (left) and 1×10^8 (right) simulation events. The limits are not the same as the publication in Ref. [40] because more conservative ER band widths are finally used. And these problems are found and fixed during the procedure of analysis . . 211
6.27 Performance of different extrema finding algorithms provided by 'scipy' [41]. $N_{\rm call}$ is the number of iteration (first-order and second-order derivatives of the function may need to be updated in one iteration). $N_{\rm par}$ is the number of fitting parameters. 212
6.28 Run 1 set 4 (or set 5) examples of the binned background PDFs. Accidental background is not in this plot, and ER backgrounds are plotted with the calibrated NEST p_*. 213
6.29 The best fit of (p_f, p_0, p_1, p_2) with Run 1 data using the reweighting MC. 215
6.30 The $f(q_\mu)$ with the template tritium and 'flatER' PDFs (2^{28} events) and the reweighting ones (2^{24} events) generated with the signal hypothesis μ_s for a $40\ GeV/c^2$ WIMP with a 2.6×10^{-47} cm^2 SI cross section with nucleus. 216
6.31 The comparison in the 90% C.L. limit and sensitivity band of SI WIMP-nucleus scattering cross section vs. the WIMP mass between the template morphing and the reweighting before applying power constraint. 216

7.1 The 3.55 keV line excess reported in Ref. [42] with Perseus cluster as an example. 222
7.2 The Feynman diagram of the leading visible decay channel of keV sterile neutrino. 222
7.3 The 95% C.L. limit of the mixing angle vs. mass of keV sterile neutrino with X-ray telescopes [43] 223

7.4 The projected sensitivity of the mixing angle vs. mass of keV sterile neutrino in XENON1T [44]. 'NC' stands for neutral current , and 'LRT' for low reheating temperature. 224
7.5 Total efficiencies (black line with gray shaded region representing the uncertainties) for ER signals, and event spectra of the fermionic DM absorption via a vector mediator on electron targets for $m_\chi = 50$ keV (dashed red line) and $m_\chi = 130$ keV (solid red line) with $\Lambda = 1$ TeV for $\mathcal{O}^V_{e\nu\chi}$. The left axis is for the total efficiencies and the right axis is for the event spectra. 227
7.6 Efficiencies as a function of m_χ. 227
7.7 Predicted probability distribution functions of signals ($\chi e \to e\nu$) for $m_\chi = 50$ keV/c^2 (left) and $m_\chi = 130$ keV/c^2 (right). 229
7.8 DM candidates (black dots with center markded as the red line, 10% and 90% quantiles marked as blue lins) for set 4 and 5 taking under the drifting electric field 93 V/cm compared with the calibrated NEST model (green bands represent the 1σ variation of the detector parameters summarized in Tab. 7.1) for the 90% quantiles, center and 10% quantiles from up to bottom. The dashed gray lines are the equal-energy lines for set 4 and 5. 230
7.9 (a) The map between the m_χ and the recoiling energy E_R :with a free electron in $\chi e \to e\nu$. (b) Energy resolution estimated with FWHM vs. E_R according to different effects (atomic smear and detector response). 230
7.10 Related Feynman diagrams of the leading order decays of χ [45]. 233
7.11 Upper: The recoiling energy spectrum E_R of data (black dots with uncertainty bars) campared to the best fit (solid magenta histogram) of the absorption fermionic dark matter signal model with $m_\chi = 130$ keV/c^2 (red histogram) and backgrounds as listed in Tab. 7.1. The dash solid lines mark the 1σ uncertainty band according the the best fitted detector parameters p_* taken as systematic uncertainties. Lower: the relative deviation of the data (black dots with uncertainty bars) compared to the total uncertainties (green band as $\pm 1\sigma$ and yellow band as $\pm 2\sigma$) in each energy bin (1 keV wide) where the statistic uncertainties are dominant. 237
7.12 The 90% C.L. exclusion limits (red lines) and ± 1 and 2σ sensitivity (green and yellow band) on σ_e of fermionic DM absorption on electrons with the PandaX-4T commissioning data for the axial-vector (upper) and vector (lower) operators. Upper limits from the leading visible decays from X-ray satellites (blue), cosmological constraints from leading invisible decays (magenta) and DM overproduction (orange) [45] are overlaid. The 2σ contour according to the XENON1T's ER excess (black line) is overlain. 239

List of Abbreviations

$0\nu\beta\beta$	Neutrino-less double beta decay
$2\nu\beta\beta$	Two-neutrino double beta decay
2D	Two Dimensional
3D	Three Dimensional
ADC	Analog Digital Converter
ADMX	Axion Dark Matter eXperiment
ALP	Axion Like Particle
AMS	Alpha Magnetic Spectrometer
ATLAS	A Toroidal LHC ApparatuS
BBN	Big Bang Nucleosynthesis
BDT	Boosted Decision Tree
BESS	Balloon-borne Experiment with Superconducting Spectrometer
BNM	Below-NR-Median
C.L.	Confidence Level
CCD	Charge-Coupled Device
CDEX	China Dark Matter Experiment
CDM	Cold Dark Matter
CEνNS	Coherent Elastic neutrino-Nucleus Scattering
CJPL	China Jinping Underground Laboratory
CMS	Compact Muon Solenoid
COM	Center Of Mass
COG	Center of Gravity
CP	Charge Parity
CY	Charge Yield
DAMIC	DArk Matter In CCDs
DAQ	Data Acquisition
DARWIN	DARk matter WImp search with liquid xenoN
DD	Deuteron-Deutron
DFSZ	Dine-Fischler-Srednicki-Zhitnitsk
DM	Dark Matter
DPE	”Double Photon Emission ”
DR	Dark Radiation
EDELWEISS	Expérience pour DEtecter Les WIMPs En Site Souterrain
EEE	Electron Extraction Efficiency

EoS	Equation of State
ER	Electron Recoil
Fermi-LAT	Fermi Large Area Telescope
FS	Free Streaming
FV	Fiducial volume
FWHM	Full Width Half Maximum
GAPS	General AntiParticle Spectrometer
GC	Galactic Center
GEANT	GEometry ANd Tracking
GUT	Grand Unified Theory
HAYSTAC	Haloscope At Yale Sensitive To Axion Cold dark matter
HE	Heat Exchanger
HPGe	High Purity Germanium detector
HV	High Voltage
ICP-MS	Inductively Coupled Plasma Mass Spectrometry
IV	Inner Vessel
JNE	Jinping Neutrino Experiment
JP-I	JinPing high purity germanium detector I
JP-II	JinPing high purity germanium detector II
JPA	Josephson parametruc Amplifiers
JUNA	Jinping Underground Nuclear Astrophysics experiment
KDE	Kernel Density Estimator
KSVZ	Kim-Shifman-Vainshtein-Zakharov
LED	Light Emitting Diode
LEE	Look Elsewhere Effect
LHC	Large Hadron Collider
LHF	LikeliHood Function
LKP or LKK	Lightest Kaluza-Klein Particle
LN2	Liquid Nitrogen
LNGS	Laboratori Nazionali del Gran Sasso
LSP	Lightest Supersymmetric Particle
LSS	Large-Scale Structure
LUX	Large Underground Xenon
LXe	Liquid Xenon
LXeTPC	Liquid Xenon Time Projection Chamber
LY	Light Yield
LZ	LUX-ZEPLIN
MACHO	Massive Astrophysical Compact Halo Object
MC	Monte Carlo
MCMC	Markov Chain Monte Carlo

ML	Maximum Likelihood
MSSM	Minimal Supersymmetric Standard Model
MW	Milky Way
NAA	Neutron Activation Analysis
NEST	Noble Element Simulation Technique
NR	Nuclear Recoil
OV	Outer Vessel
PAF	Photon Acceptance Function
PandaX	Particle and astrophysical Xenon
PBH	Primordial Black Hole
PDE	Photo Detection Efficiency
PDF	Probability Density Function
PE	PhotoElectron
PICO	PICASSO (Project In CAnada to Search for Supersymmetric Objects) and COUPP (Chicagoland Observatory for Underground Particle Physics)
PLR	Profile Likelihood Ratio
PMT	PhotoMultiplier Tube
PSD	Pulse Shape Discrimination
PSTAR	Stopping-power And Range Tables for Protons
PTFE	PolyTetraFluoroEthylene
PTR	Pulse Tube Refrigerator
PVC	PolyVinyl Chloride
QCD	Quantum Chromodynamics
RGA	Residue Gases Analyser
RSD	Relative Standard Deviation
SCS	Slow Control system
SD	Spin Denpendent
SDSS	Sloan Digital Sky Survey
SEG	Single Electron Gain
SENSEI	Sub-Electron-Noise Skipper CCD Experimental Instrument
SHM	Standard Halo Model
SI	Spin Indenpendent
SLPM	Standard Liter Per Minute
SM	Standard Model
SNO	Sudbury Neutrino Observatory
SPE	Single Photon Electron
SS	Stainless Steel
SuperCDMS	Super Cryogenic Dark Matter Search
SN	SuperNova
SURF	Sanford Underground Research Facility

SUSY	Supersymmetry
TBA	Top-Bottom Asymmetry
TES	Transition-Edge Sensor
TPC	Time Projection Chamber
WDM	Warm Dark Matter
WIMP	Weakly Interacting Massive Particle
WMAP	Wilkinson Microwave Anisotropy Probe
w.r.t.	With Respect To
ZEPLIN	ZonEd Proportional scintillation in LIquid Noble gases
ΛCDM	Lambda-Cold Dark Matter

Chapter 1: Introduction

Lambda cold dark matter (ΛCDM) model has been widely accepted as the standard model of Big Bang cosmology. With the comic microwave anisotropies and baryon acoustic oscillation measurements, the mass-energy densities of baryon matter, non-baryon cold DM and dark energy are pinpointed more and more accurately [6]. However, the success of ΛCDM leads to a series of problems unsolved including the missing baryon problem, the baryon asymmetry, and the nature of DM and dark energy, etc.

The standard model (SM) of particle physics was established as a theory of electromagnetic, weak and strong interactions, which has achieved great successes in predicting fundamental particles like charm quarks [46, 47], W and Z [48] and Higgs [49], but still has imperfectness such as not including non-zero neutrino mass [50, 51], a lack of unified description of the three fundamental interactions and the exclusion of gravity. The nature of DM is a crucial problem for both cosmology and particle physics. The weakly interacting massive particles (WIMP) is one of the most promising DM candidates because of the WIMP-miracle. A GeV-scale WIMP with a self-annihilating rate on the electro-weak scale can produce the DM relic density observe at the current epoch, and some theories beyond SM like supersymmetry (SUSY) [52] already provide such DM candidate.

Dual-phase liquid xenon time projection chambers (LXeTPCs) are used in the Particle and

astrophysical Xenon (PandaX) projects to directly search DM scattering with nuclei or electrons, running at the China Jinping Underground Laboratory [53, 54]. The capability of reconstructing vertexes in TPCs suppresses backgrounds with volume fiducialization. Collecting scintillation and ionization signals for the events helps to reduce the electron recoiling backgrounds further for nuclear recoiling signals. The LXeTPCs including LUX [55], XENON [56], PandaX [34] collaborations have led the sensitivities of the GeV-scale WIMP search for the last decade with the strong background suppression and coherence amplification. In the near future, the scientific data from LUX-ZEPLIN (LZ) [57], XENONnT [58], PandaX-4T [2] will further search the unexplored parameter space for the GeV-scale WIMP with LXeTPCs.

As no solid evidence has been found, DM search is a growingly complex community. Besides direct searches, they can be searched with missing transverse momentum if created with standard model particles in colliders, or with annihilation into traceable signals in the telescopes. Generalizing the possible mass range of WIMP, sub-GeV DM searches become popular with frontier techniques in semiconductors [59], cryogenic crystals [60] as well as colliders [15]. sub-MeV DM models serve as one main motivation for the pioneering R&Ds to measure the energy deposition smaller than 0.1 eV with Dirac materials [61], superconductors [62] and doped semiconductors [63], etc.

Another top DM candidate extending to the smaller mass range is wave-like QCD axions [64] which is proposed to explain the extraordinarily small neutron electric dipole moment. Generalizing from the golden mass range 10^{-6} to 10^{-4} eV, the possible mass range can be as small as 10^{-21} eV [65]. Other dark matter models are also searched actively including keV sterile neutrino dark matter [66], WIMPZilla [67], primordial black holes (PBH) [9], etc.

In this chapter, the astronomical and cosmological evidences in the history to support the

existence of DM are reviewed first. Then, the WIMP and QCD axions as the top DM candidates are discussed in details, and short summaries are provided for some other DM models. Finally, I briefly introduce the principle and advantages of LXeTPCs.

1.1 Astronomical and Cosmological evidence of dark matter

The existence of dark matter is well-accepted in the community nowadays because of extensive complementary astronomical and cosmological observations. The concept was proposed around a century ago by Fritz Zwicky [68] and Jan Oort [69] with different works. Zwicky estimated the mass of galaxies and clusters with the virial theorem according to the radial velocity, and Jan Oort found the stars having higher velocities than expected in the Milky Way (MW) Galaxy with the Doppler shifts in the spectra. I review a couple of observations without the attempt to be complete.

1.1.1 Rotational curves

Dark matter started to be widely accepted in 1970s because of the measurements of the rotational curves in different galaxies by Vera Rubin and other astronomers. It is suggested by Newtonian dynamics that the circular velocity of a star at a distance r without any dark matter should be:

$$v\left(r\right)=\sqrt{\frac{GM\left(r\right)}{r}}, \tag{1.1}$$

where $M\left(r\right)$ is the total mass in the sphere with radius r, which should have been approximately equal to a constant when r is large enough to reach outside of the optical disk because stars are distributed so sparse that the average density among the dark space is negligible. The circular

velocity should have decreased with greater r. However, as typical rotational curves in Fig. 1.1 [3] show, the velocities appear to be flat when r increases. Therefore, introducing dark matter in the space is a promising way to explain the discrepancy, and it is usually referred as the dark matter halo in the literature.

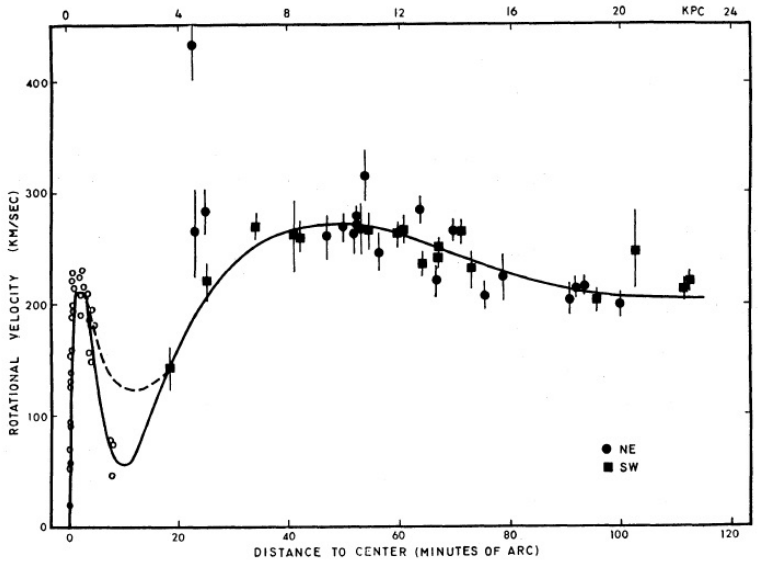

Figure 1.1: The rotational curves along the south-west (SW) and the north-east (NE) major axis in M31 [3]

.

The velocities in the MW nowadays reach a much better resolution to provide the speed distribution of the DM flux going through the earth. The speed distribution in the lab-frame on the earth in the standard halo model (SHM) is presented in the Fig. 1.2 where the uncertainty band accounts for different parameters including the annual variation, the local standard velocity v_0 (=238 km/s) the galactic escape velocity $v_{\rm esc}$ and the sun's peculiar velocity $v_{\rm pec}$. It should be noted that recent studies released by the Gaia mission and the Sloan Digital Sky Survey (SDSS) [70] have put the SHM into question, which suggest that DM streams with specific directions are preferred. These work may be used to re-interpret the direct detection data with the SHM. But generally, it is more suggested to stay with the SHM to make the results of different collaborations

comparable.

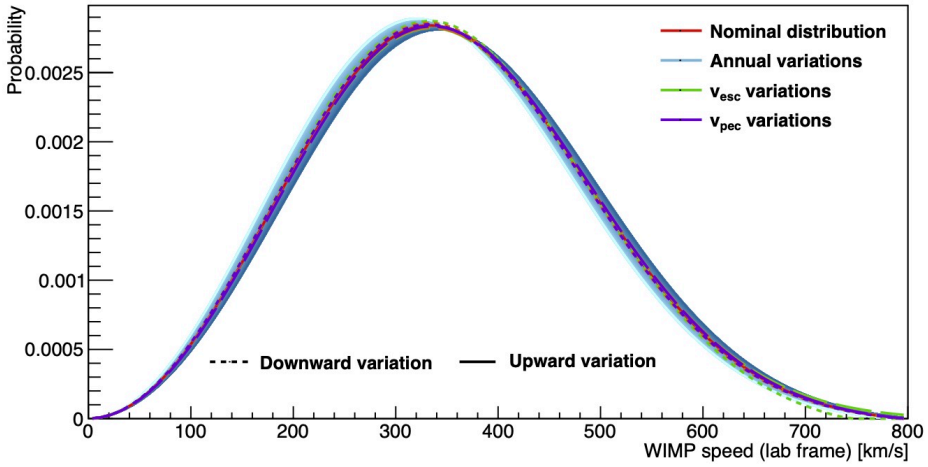

Figure 1.2: The standard hale model speed distribution in the lab-frame on the earth [4].

1.1.2 Bullet cluster

Figure 1.3 is a composite image of the galaxy cluster 1E 065756 a.k.a. 'Bullet Cluster' which provides another evidence of the dark matter with the two large galaxies cluster passing through each other [5]. The pink profiles are the X-rays observed by Chandra which follow the hot gas that contains most of the baryonic matter in the two clusters. The one with a bullet shape indicates an active movement toward right. The blue profiles follow the mass distribution of the two clusters after gravitational lensing correction which don't follow the visible baryon matter. The separation between the blue and the red reflects the major massive component in the two clusters is non-baryonic matter. Moreover, the elliptical shape in the blue clumps indicates that the non-baryon matter passes through each other with a much weaker interaction compared to the baryonic matter.

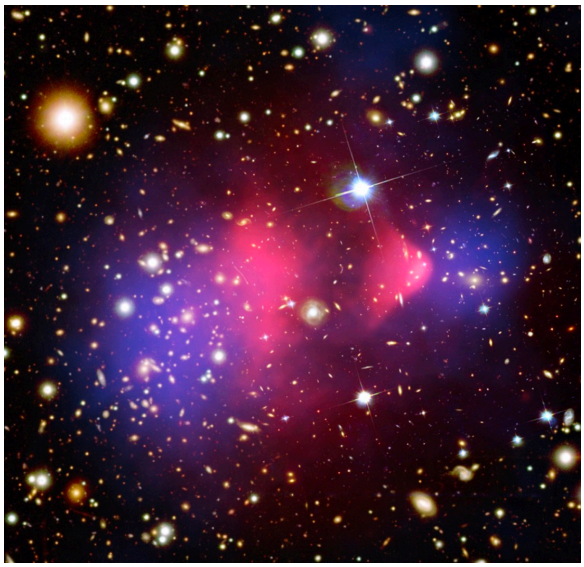

Figure 1.3: Bullet cluster [5].

.

1.1.3 Cosmic microwave background

Together with the mass power spectrum, the temperature anisotropies in the cosmic microwave background (CMB) strongly supports the ΛCDM. The latest result released by $planck$ [6] updates the relic densities of baryon matter and DM in the base ΛCDM to

$$\begin{aligned} \Omega_b h^2 &= 0.0224 \pm 0.0001 \\ \Omega_c h^2 &= 0.1204 \pm 0.001 \end{aligned} , \tag{1.2}$$

where the Ω_b and Ω_c are defined as the ratio of the baryon density and DM density to the critical density for a flat universe, respectively, and $h(= 0.674 \pm 0.005)$ is the Hubble constant with a unit of 100 km/s/Mpc.

The seven visible peaks in the temperature angular power spectrum shown in the Fig. 1.4 can pin down a number of important parameters in the thermal history of the universe. The

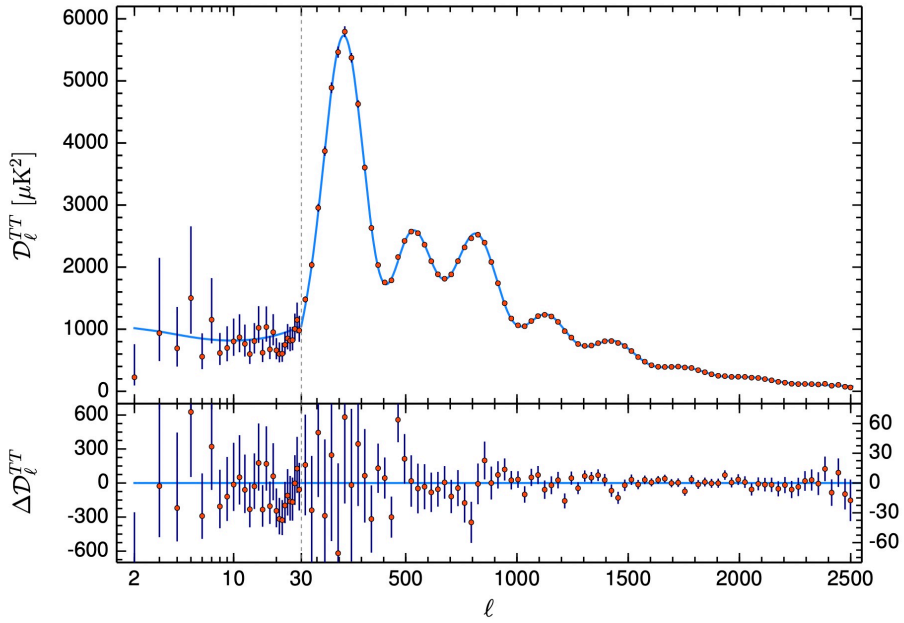

Figure 1.4: The temperature angular power spectrum released by $planck$ 2018 data [6]

.

position of the first peak is sensitive to the curvature of the universe which evaluates the optical horizontal after the recombination era at around 380,000 years after the Big Bang. The amplitude of the first peak is strongly correlated to the baryon density. The disappearance of peaks at the l larger than 2000 is due to the silk damping, which corresponds to a higher red shift z while the photon energy density is larger than the matter. If the the photons diffuse away, the amplitude of the fluctuation will be severely reduced because a noticeable fraction of the baryon and photon densities fluctuating together via adiabatic fluctuations. Even though there are some cosmological inconsistencies like the lithium abundance, the great agreement in general between the CMB and Big Bang Nucleosynthesis (BBN) [71] are used to confine the allowed parameter space of DM models.

1.2 Dark matter candidates

As mentioned above, the two top cold DM candidates are the standard thermal relic WIMPs and QCD axions for being able to solve some other big mysteries in the same time. With WIMPs representing the particle-like candidates, a wider mass range is allowed more than the GeV-scale. Similarly, wave-like candidates with QCD axions as the representative also cover a wide possible mass range. Dark photons cover a very wide range all the way from wave-like mass range to particle-like mass range, which is not further discussed in this thesis but should be noted as a viable candidate. Another interpretation of the DM without any new particle is the Massive Compact Halo Objects (MACHOs).

1.2.1 Particle-like

The top particle-like DM candidate is the thermal relic WIMPs on the GeV scale. The extension to lower masses larger than $\mathcal{O}(1)$ MeV/c^2 could be fairly good freezing-out light DM candidates which won't affect the BBN observations. For further extensions onto sub-MeV DM models, the freezing-in mechanism has been taken as a standard thermal production [72]. If we explore a smaller mass range, keV sterile neutrino is another well-motivated DM candidate that has been proposed to solve several important mysteries together.

1.2.1.1 Weakly interacting massive particles

The standard thermal relic WIMPs refer to a hypothetical particle with a mass from 1 GeV to 100 TeV, interacting with the standard model particles via gravitation and a possible weak-scale interaction. The so-called 'WIMP miracle' refers to the coincidence that the thermal relic of DM

density Ω_c in Eq. 1.2 can be explained by a new particle with a mass $\mathcal{O}(100)$ GeV/c^2 and the self-annihilating cross section on the weak interaction scale, and well-motivated theories call for such a new particle as well. The promising WIMP candidates include the lightest supersymmetric particle (LSP) in the minimal supersymmetric SM (MSSM) [52], inert Higgs doublet [73], the lightest Kaluza-Klein particle (LKP) [74] arising from universal extra dimension (UED).

Conventionally, there are three ways to detect the non-gravitational interaction between the hypothetical WIMP and the visible sector [75]. Direct detection experiments measuring the recoiling energy of the nuclei or electrons search for WIMPs in an nearly model-independent way for the spin-independent case. Indirect detection experiments [76] is complementary to the direct detection which search for annihilation or decay signals through visible photons, neutrinos and charged cosmic rays. Colliders are able to search for DM through the transverse missing momentum with the possible generation of DM on the final states. Both indirect detection and creation often require more concrete models to interpret the results. Section 1.3 provides more details about the experiments on the WIMP search.

1.2.1.2 Light dark matter particles

With the GeV-scale WIMP search window likely to be closed up in the following one decade or two, other particle-like DM candidates are attracting more and more attentions in case no WIMP is found.

Sub-GeV DM

The sub-GeV DM often refer to a DM particle with a mass in the range from 1 MeV/c^2 to 1 GeV/c^2. For a freeze-out DM particle, BBN [71] puts constraints for DM mass less than

$\mathcal{O}(1)$ MeV/c^2. CMB [77] and large-scale structures (LSS) [78] put a limit on DM-nucleon cross section of $\sim 10^{-29}$ cm^2. The supernova SN1987A cooling [79] excludes some parameter space at a much smaller cross section region between 10^{-47} and 10^{-40} cm^2.

Even though the DM-nucleon recoiling energy falls below the energy threshold of the ton-scale noble detectors, Xe and Ar detectors are likely to still be competitive for the sub-GeV DM search with the DM-electron scattering, Migdal and bremsstrahlung effects [80, 81], cosmic-ray boosted stream [82] and absorption of DM on nuclear targets [83].

Besides the ton-scale Xe and Ar detectors, semiconductor detectors with energy thresholds around $\mathcal{O}(10)$ eV detecting electronic excitations in Si and Ge are likely to be the most sensitive sub-GeV direct detection experiments including SENSEI [59], DAMIC [84], SuperCDMS [60], CDEX [85], Edelweiss [86]. Skipper CCD [87] is developed in recent years used in SENSEI and will also be used in the future DAMIC and Oscura [88], which helps to reach a single electron resolution with only the readout method changed compared to a normal CCD, with a 120 to 140 K running temperature for the electronics reachable cryogenic requirement in a large volume. CDMS is using superconductors (Si and Ge) under a temperature lower than 100 mK with the photon readout by the temperature edge sensors (TES). In the future, we can expect that a germanium detector with an exposure of 50 kg·year and a CCD silicon detector with an exposure of 1 kg·year and a dark current rate of $\mathcal{O}(10^{-7})$ counts/pixel/day to reach 10^{-41} cm^2 sensitivities on the DM-electron scattering (for a heavy mediator).

Sub-MeV and keV DM

KeV sterile neutrino DM is a well-motivated DM candidate locating in this mass range which can also be made to connect to the neutrino mass origin and baryogenesis[66, 89, 90, 91]. Particular interests arose from the ~3.5 keV unidentified excess in X-ray spectrum from

satellites [42, 92, 93]. However, later analyses have challenged the sterile neutrino interpretation because no such excess is observed in some other X-ray data sets [94], and in tension with the DM profiles at the center of galaxies [95]. To date the standard Dodelson-Widrow sterile neutrino DM [96] as the major specie is strongly excluded by the structure formation constraints and X-ray limits [97, 98, 99]. However, a general sub-MeV DM is still a well-defined DM candidate with the possibilities to be warm or cold, depending on the initial conditions in the thermal history.

To detect DM in this mass range, a direct detection will require a $\mathcal{O}(1)$ meV energy threshold. The promising experiments in the next generation experiments including 3D Dirac materials [61], graphene trapping [100] and fine semiconductor doping [63]. Of course, the similar extensions for the noble-gas detectors to sub-GeV sensitivities apply for the Si and Ge semiconductors to gain sensitivities in this sub-MeV region. DM absorption generally opens up the sensitivities for the detectors with $\mathcal{O}(1)$ keV energy threshold [101].

In chapter 7 of this thesis, I discuss a search on the absorption signal of a sub-MeV fermionic DM on electron targets with the PandaX-4T data which shares the similar signal in the direct detection experiments as the keV sterile neutrino DM. Conventionally, the keV sterile neutrino DM has been strongly constraint with astrophysical X-ray telescopes on the decay channel $\chi \rightarrow \gamma\nu$ [102]. But this search is on a new kind of interaction instead of the weak interaction where in some parameter space, PandaX-4T data become competitive.

1.2.1.3 Heavy dark matter particles

A super heavy DM particle ($m_\chi > 10^{10}$ GeV/c^2) can be a sufficiently good DM candidate. DM candidates with mass close to the grand unified theory (GUT) energy level particles are

not conventional DM candidates because the standard interactions have heavy particles decaying away at the early universe, but some special mechanisms can make the super-heavy particle stable or hold a lifetime much longer than the age of the universe. The standard thermal freeze-out of a super-heavy DM particle cannot give a right thermal relic. However, some other thermal histories can open up a wide parameter space. For instance, WIMPZilla [67] is a super-heavy DM candidate which is expected to super weakly interacting to the SM particles, and undergoes a non-equilibrium freeze-out (the interaction rate is much smaller than the expansion of the universe). Another example is the super-heavy gravitino in the supersymmetric theories which is supposed to interact strongly with regular matter, creating a multi-scattering track in the DM direct detectors but may evade the detector with a very low density. The multiplicity makes it searchable with the current particle radiation detectors [103].

1.2.2 Wave-like

Taking a DM local density ρ_χ as 0.3 GeV/cm^3 and a DM flux around 250 km/s, the de Broglie wavelength of a very light DM is

$$\lambda_{\rm dB} = \frac{2\pi}{m_\chi v} = 0.48\ {\rm kpc} \times \frac{10^{-22}\ {\rm eV}}{m_\chi} \times \frac{250\ {\rm km/s}}{v} = 1.49\ {\rm km} \times \frac{10^{-6}\ {\rm eV}}{m_\chi} \times \frac{250\ {\rm km/s}}{v}. \quad (1.3)$$

The number density estimated with $\lambda_{\rm dB}$ is

$$n_\rho = \frac{\rho_\chi}{m_\chi} = \frac{3 \times 10^5\ {\rm eV/cm^3}}{m_\chi}, \quad (1.4)$$

which leads to the number of DM particles in the volume $\lambda_{\rm dB}^3$ to be

$$N_{\rm dB} = n_\rho \cdot \lambda_{\rm dB}^3 = (\frac{10\ {\rm eV}}{m_\chi})^4 \times (\frac{250\ {\rm km/s}}{v})^3. \tag{1.5}$$

If $m_\chi \ll 10$ eV, the DM is better described by classical waves similar to photons described by the electromagnetic fields. Because of the Pauli exclusion principle, such a light DM candidate must be bosonic. The well-motivated DM candidates in this wide range are QCD axions [64] in $1 \sim 100$ μeV and fuzzy CDM [104] in $10^{-22} \sim 10^{-20}$ eV. A wave-like DM between these two ends is also a sufficiently good DM candidate, and often called axion-like particles (ALP) [105]. The existing QCD axion searches and ALP searches are summarized in the Fig. 1.5 [7].

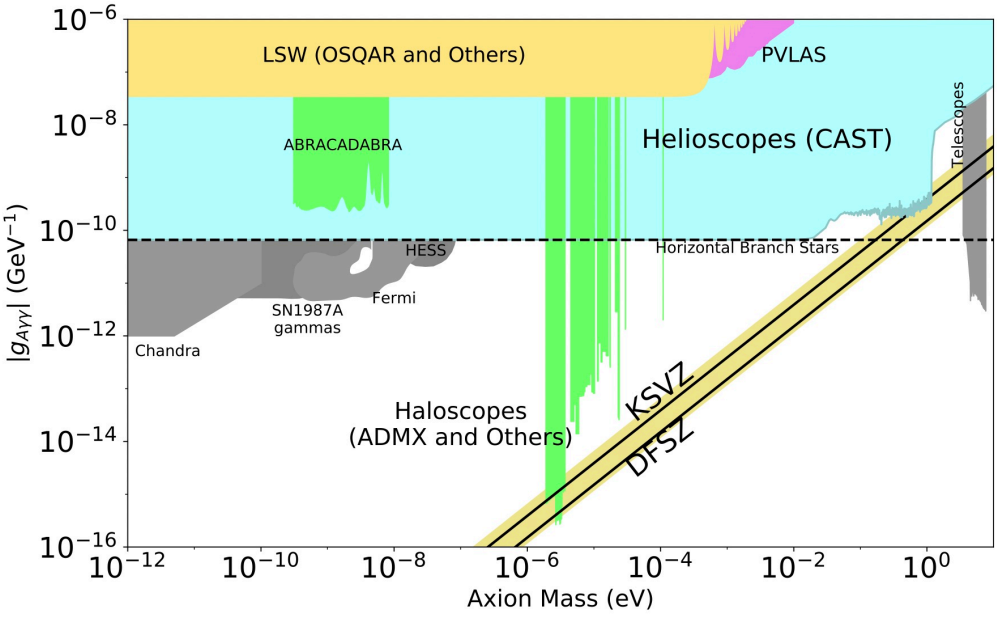

Figure 1.5: The axion search with the decay channel of $a \to \gamma\gamma$ limits on the effective coupling constant $g_{a\gamma\gamma}$ [7].

1.2.2.1 QCD axion

QCD axion is regarded as one top DM candidate for solving two important problems together: the nature of DM and the strong CP problem [64, 106]. The strong CP problem arises from the fact that no experiment present to violate the CP symmetry in the the quantum chromodynamics (QCD). After the CP violation was confirmed in 1960s [107, 108, 109], it became intuitive to predict a CP violation phase θ in the SU(3) strong interaction. The θ should be a number randomly selected from $-\pi$ to π and very unlikely to be extremely close to 0, but is constraint by the neutron electric dipole moment as $\theta < 10^{-10}$. A new spontaneously broken global symmetry U$(1)_{\rm PQ}$ was proposed by Helen Quinn and Roberto Peccei [64] in the late 1970s to solve the problem. Briefly, while the universe cools below the symmetry-breaking scale f_a, a new vacuum expectation value leads to a new $\theta_{\rm eff} = 0$. This pseudo-Nambu Goldstone boson of U$(1)_{\rm PQ}$ is QCD axion. QCD axion can explain the whole DM relic with two benchmark models: the Kim-Shifman-Vainshtein-Zakharov (KSVZ) and the Dine-Fischler-Srednicki-Zhitnitsky (DFSZ). The latter is more compelling for being easily included into the minimum supersymmetric GUT based on SU(5).

QCD axion often refers to the mass range from 1 to 100 μeV. If the PQ symmetry breaks before the inflation, the relic axion abundance is only related to the mass of the axion field and the initial θ which is the same throughout the whole universe. The Ω_c in the ΛCDM can naturally be explained by an axion mass around $\mathcal{O}(1)$ μeV. In the post-inflationary scenario, different part of the universe will have different values of the initial θ randomly selected between $-\pi$ and π. Most theoretical calculations predict that the axion mass in the $\mathcal{O}(1\text{–}100)$ μeV range.

Axion Dark Matter eXperiment (ADMX) [8] is the first experiment reaching the sensitivity

to the DFSZ model with the decay channel of QCD axion into two photons. A haloscope is built on the ground with a resonant cavity immersed in a 7.5 T superconducting magnetic field under a temperature below 100 mK. Josephson Parametric Amplifiers (JPAs) are used to achieve ultra-low noises close to the quantum limit. Because of the resonance only applied for a narrow photon frequency, different axion masses are searched step-by-step with the cavity resonant frequency tuned with a dielectric rod by a 10 Hz step, which results in the spikes in the limit Fig. 1.6. Quite a large golden mass range of QCD axion from 1 to 50 μeV can be searched with the haloscope which is about a matter of time.

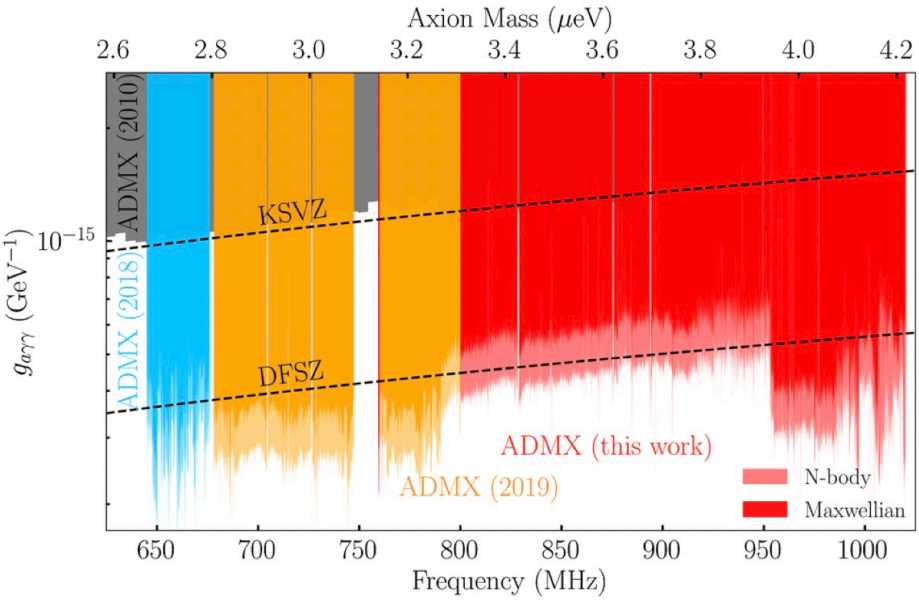

Figure 1.6: Zoom-in AMDX's 90% C.L. upper limits on $g_{a\gamma\gamma}$ [8].

For the high mass end which corresponds to higher resonant frequencies and smaller resonance wavelength, it is more difficult to reach the similar level of sensitivities because a smaller cavity means a smaller energy in the haloscope. A brute-force solution might be a stronger magnetic field which is still quite limited. Some quantum techniques like quantum squeezing technology, backaction evasion and entangled cavities are promising to lower down the noises and increase

the signal-to-noise ratio in the resonance. HAYSTAC [110] appears to be one pioneer in applying the novel quantum technologies in the fundamental particle physics experiment.

1.2.2.2 Ultra-light dark matter

Fuzzy DM, very light bosons or ALPs in the mass range 10^{-22} to 10^{-20} eV, can explain the small scale observations ($<$ 10 kpc) which is problematic for CDM. The $\mathcal{O}(1)$ kpc $\lambda_{\rm dB}$ prevents the density to increase sharply within the small scale ($<$ 1 kpc). Moreover, the DM relic density can be naturally explained by a fuzzy DM with a decay length f close to but below the Planck scale. Earth-based experiments are not sensitive to search for this ultra-light DM, but astrophysical observations are actively setting limits on the smallest allowed mass including the DM density profile in the dwarf satellites [111], the abundance of the dwarf galaxies [112], the matter power spectrum viewed by the Lyman-α forest [113]. In general, the mass region over 1×10^{-21} eV is not excluded.

In this wide mass range between 10^{-20} to 10^{-6} eV, the ALP with 1 to 10 neV is actively searched by ABRACADABRA-10cm [114] on the $g_{a\gamma\gamma}$ with the RLC resonance. The preference comes from the f_a scale on the GUT scale around 10^{15} to 10^{16} GeV. Figure 1.7 shows the projection of the future family expriments of the upgraded ABRACADABRA-10cm including DMRadio-50L, DMRadio-50L-m^3 and DMRadio-GUT [115].

1.2.3 Massive Compact Halo Objects

MACHOs [116] may explain the DM relic without introducing any new interaction beyond SM, including PBHs [9], brown and white dwarfs and neutron stars. Baryonic DM candidates

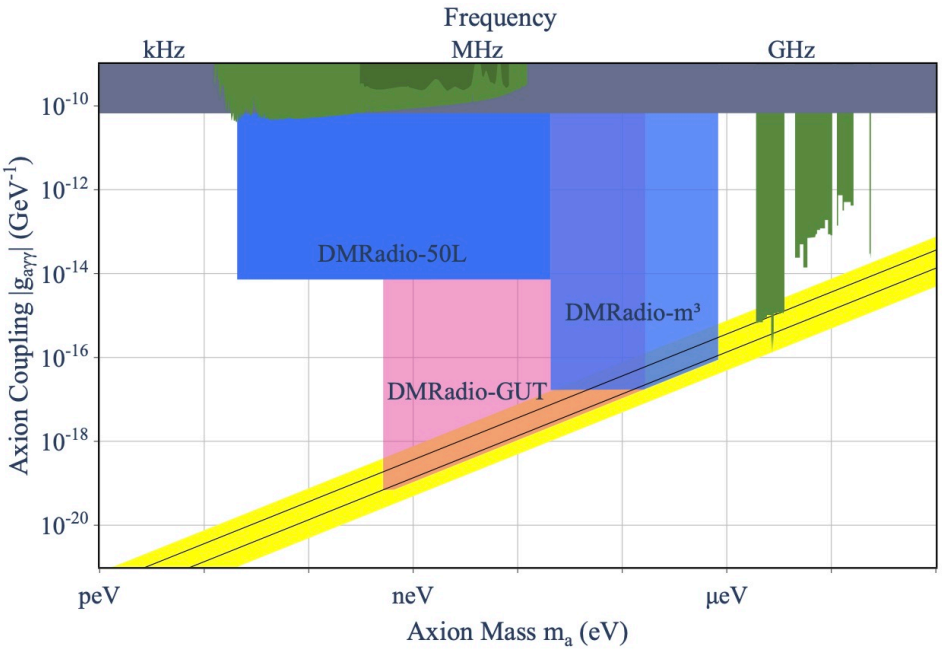

Figure 1.7: The projections of the DMRadio family searching for f_a on the GUT scale.

like MACHOs were challenged to make up the major DM density, but recent works alleviate constraints on the limits of PBHs, making it a vaible candidate to comprise all of the DM. PBHs could form through the gravitational collapse of density perturbations during inflation while the whole universe was dense. These astronomical objects can be searched observationally by gravitational microlensing, gravitational wave detection, and pulsar timing and γ-rays of BH evaporation. Figure 1.8 presents the current limit of PBH on the DM fraction and future projections.

1.3 WIMP search

As this thesis is mainly related to PandaX detectors for the GeV-scale WIMP search, I would like to introduce the experiments that are promising to hunt WIMPs with different channels.

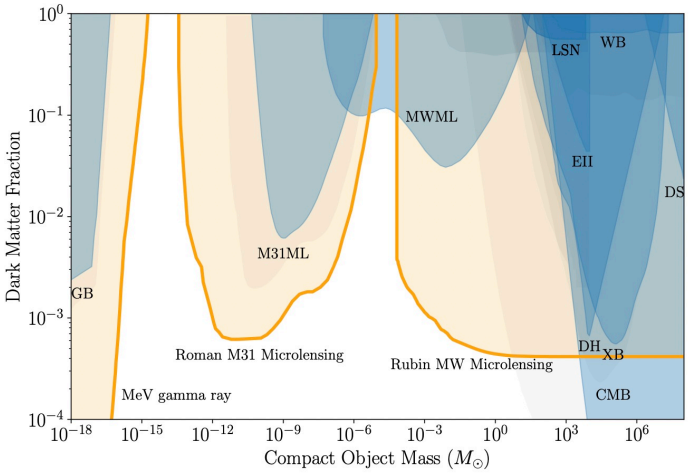

Figure 1.8: Existing limits on the DM fraction vs PBH mass (blue for more conservative assumptions and gray for less) and selected projections for future expectations (gold) [9].

1.3.1 Direct detection

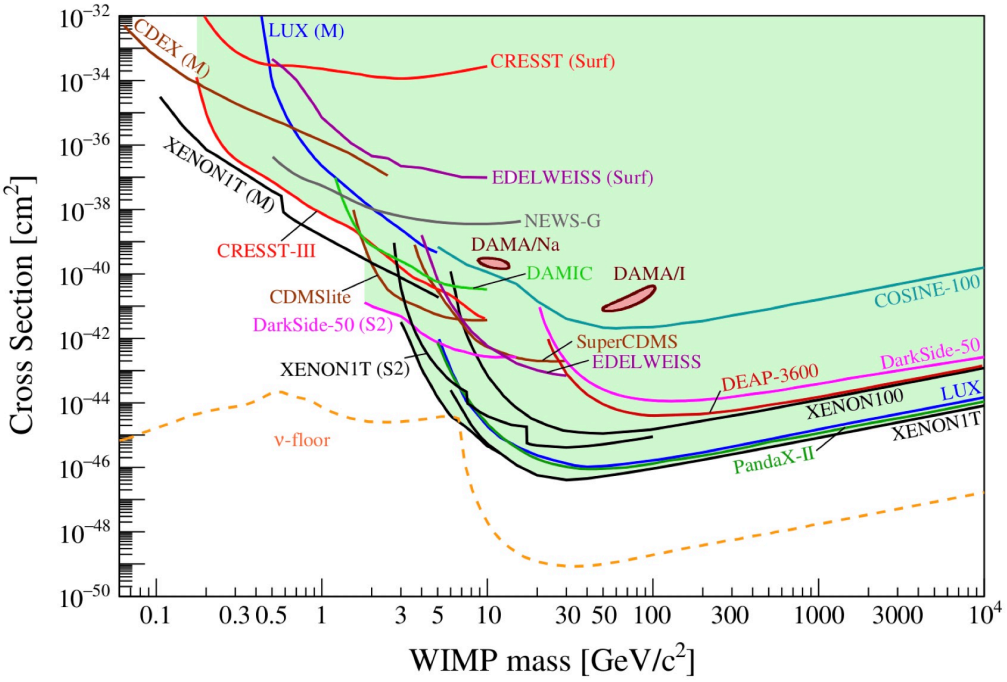

Figure 1.9: The status of the spin-independent WIMP-nucleon cross section unitl April 2021 (PandaX-4T commissioning data and the first result of LZ are not included on this plot) [10].

Direct detection dark matter experiments refer to the measurement of the recoiling between the dark matter particle and a SM particle or the absorption of a dark matter particle. Figure 1.9 is a summary of the status of the spin-independent (SI) WIMP-nucleus cross section by April 2021, after which the commissioning data of PandaX-4T with a 0.63 tonne·year exposure have put the strongest constraint on the GeV-scale SI WIMP-nucleus cross section as discussed later in chapter 2 by the time the author is writing this thesis[1]. The mass range of WIMP around 100 GeV/c^2 is strongly constrained by the LXeTPCs including XENON100 [117], XENON1T [56], LUX [55], PandaX-II [34], PandaX-4T [2] in the past decade, because of the coherence factor A^2 (A is the atomic mass) in the xenon isotopes, the scalability of a monolithic piece and the feasibility to keep lowering down the backgrounds. In a higher mass region over 1 TeV, liquid argon detectors like Darkside-20t are expected to be competitive for the smaller loss of the coherence with a larger momentum transfer q compared to xenon which is often factorized in a finite form factor related to q. In a lower mass region lower than 10 GeV, calorimeters with a lower energy threshold is preferred. Experiments working on germanium (Ge), silicon (Si) or other crystals like $CaWO_4$ are expected to reach a better sensitivity including CRESST [118], SuperCDMS [60] and DAMIC [84]. Some novel techniques in the noble-gas detectors including ionization only ($S2$-only) analysis [119], Migdal effect [80] and bremsstrahlung [81] help to reach a lower energy threshold. Even with a higher background level than the conventional analysis and non-ideal efficiencies, because of the ton-scale target, noble-gas detectors can still be very competitive in this low-mass range.

A non-reducible physics background in the direct detection is the coherent elastic neutrino-

[1]Right before this thesis is submitted, LZ released the first science run result which put the strongest limit on searches for the standard thermal relic WIMPs

nucleus scattering (CEνNS) [120], which is often called as 'neutrino floor' and marked as the orange dashed line on Fig. 1.9. But this line is not hard and solid. The most important composition in the plot is the solar neutrino flux. By adding other astrophysical origins of the neutrino flux, the neutrino signal might be larger than the line in Fig. 1.9. Plus, the uncertainties in the theoretical calculation are pointed out to span for an order of magnitude. It has been suggested to name it as 'neutrino fog' instead [121].

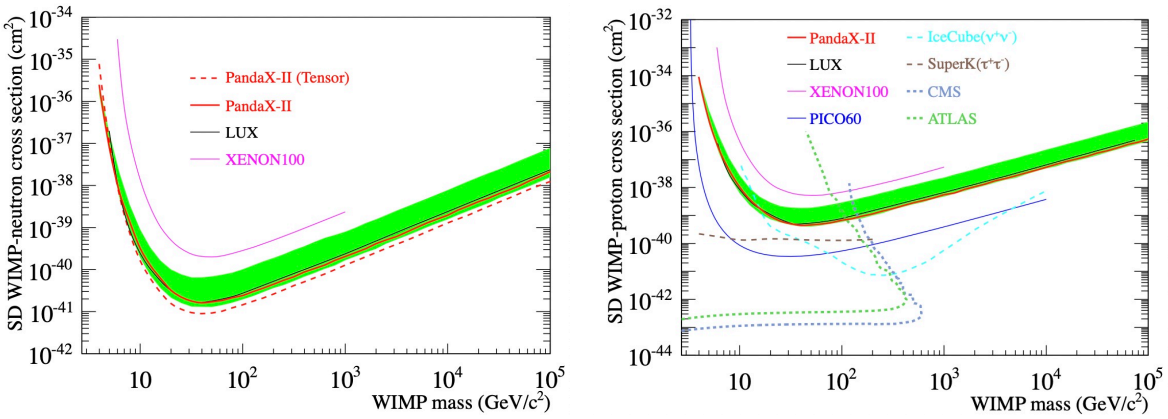

Figure 1.10: Limits of the (a) SD WIMP-neutron and (b) WIMP-proton scattering cross section as a function of WIMP mass published by the PandaX-II 56 tonne·day exposure overlain with some other works by April 2019 [11].

The spin-dependent (SD) WIMP-nucleus scattering refers to the coupling between the WIMP and the unpaired nuclear spin where the large A coherence doesn't apply anymore. The nucleus targets with an odd proton number or an odd neutron number effectively search for SD WIMP-neutron or WIMP-proton interactions (Fig. 1.10) [11]. As the calculation is related to nuclear models, more theoretical uncertainties are carried in compared to the SI case. The strongest direct detection limits on the WIMP-proton interaction is from PICO-60 [122] which builds a bubble chamber with target as C_3F_8, and their complete data set has put 2.5×10^{-41} cm^2 for a 25 GeV WIMP (overlain on the Fig. 1.13).

1.3.2 Indirect detection

If WIMPs decay or annihilate into lighter SM particles, the traces will live in the universe. So far the competitive channels include γ-rays, neutrinos or charged comic particles on the final states. The standard WIMP mass range is correlated to the γ-ray detection ranging from 100 MeV to 100 TeV. Probing γ-rays from the galactic center (GC) should provide the strongest DM signal but with large uncertainties in the DM profile in the region close to the GC. Complementary to the GC γ-rays, dwarf galaxies provide a robust DM density determination and negligible astrophysical background. Both are very important for the γ-ray detection in the DM indirect experiments. The DM searches of AMS-02 [12, 13] on different channels are compared to those of Fermi-LAT [123] and WMAP [124] in the Fig. 1.11.

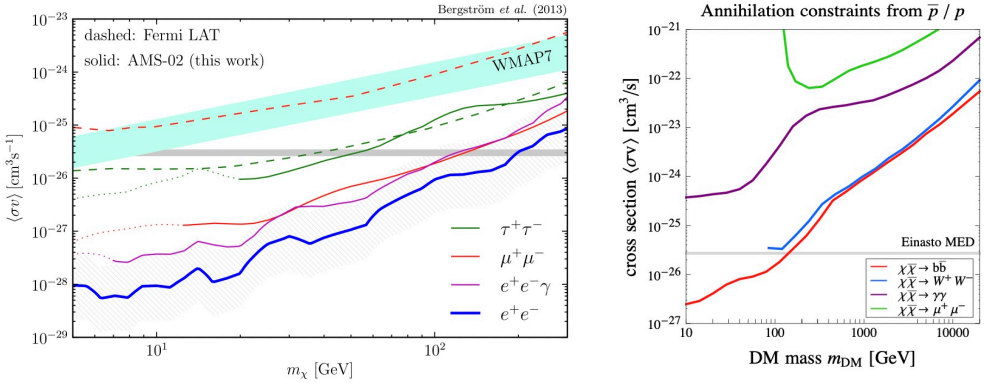

(a) (b)

Figure 1.11: (a) AMS-02 positron (different channels labeled), Fermi-LAT ($b\bar{b}$ channel) and WMAP (cyan) limits on annihilation cross-section versus mass [12]. (b) AMS-02 antiproton-to-proton ratio (different channels labeled) limits. The grey lines correspond to the thermal relic cross section [13].

High energy neutrino telescopes including IceCube [125]and SuperK [126] can be very competitive for the SD WIMP-proton search with the DM annihilation in the sun. The results of IceCube and SuperK are overlain on Fig. 1.10(b). Their best sensitivities are reached via the

$\tau^+\tau^-$ in the DM decay that can create high energy neutrino flux in a nearly background-free region. SuperK presents a better sensitivity compared to IceCube on the low-mass WIMP with a lower neutrino energy threshold.

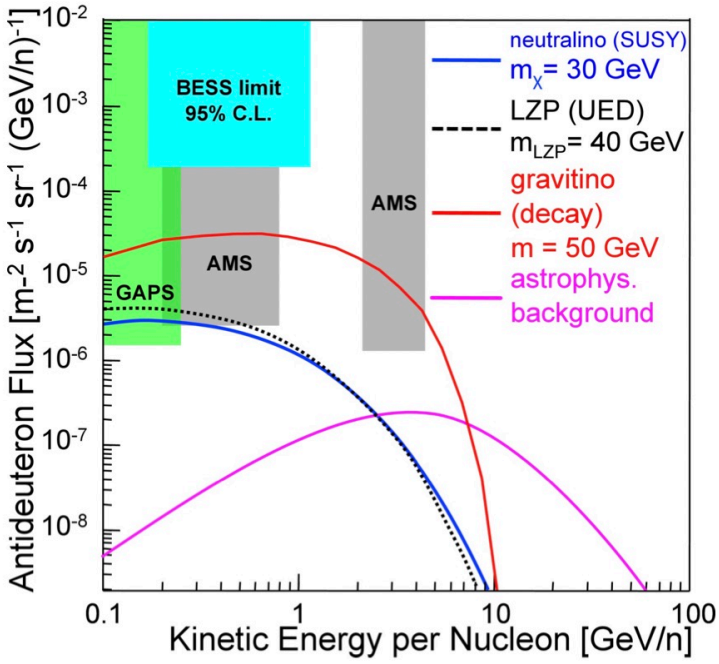

Figure 1.12: The projected sensitivities on antideuteron fluxes as a function of the kinetic energy per nucleon of AMS-02 after 5 years of operation and GAPS after three 35-day flights overlain with the limit from BESS and the predicted signals of the benchmark WIMP models [14].

Charged antimatter is also a sensitive indirect detection channel for the local DM. AMS-02 with a broad spectrum on different cosmic rays has reported sensitive searches on different annihilation channels (e^+e^-, $e^+e^-\gamma$, $\mu^+\mu^-$ and etc.) with the position flux and antiproton-to-proton ratio as shown in Fig. 1.11, which is better than the Fermi-LAT dwarf galaxies searches. While comparing the observations of different DM halos, σv is often used instead of σ. GAPS [14] can be complementary with more sensitive searches on the antimatter using an exotic atom technique that can identify the antiprotons and antideuterons with fingerprint-like features. As

shown in Fig. 1.12, the projected sensitivity of GAPS is in a different energy window, and the DM annihilation signals are often a continuous spectrum with respect to the kinetic energy per nucleon.

1.3.3 Particle collision

The Large Hardon Collider (LHC) can reach a 13 TeV center-of-mass (COM) energy using proton-proton collisions, which is high enough to search quite a large region of WIMPs with the missing transverse momentum. Because of the high energy, the mediator in the interaction might not be able to parameterized into an effective coupling constant. The complexity make the WIMP search at the LHC to be a multi-dimensional parameter space at least including the coupling constant to the quark g_q of the mediator, the mediator type and mass, the coupling constant to the $\chi\bar{\chi}$ generation g_χ and the DM mass m_χ. On one hand, the higher energy brings the potential to view more details in the interaction. On the other hand, compared to DM direct detection experiments, the data are often interpreted with some pre-assumptions of the models and parameters. In the Fig. 1.13, the ATLAS result with 139 fb^{-1} luminosity presents the strongest SI WIMP-nucleon scattering for the 1 GeV/c^2 WIMP searching on the production of one Z boson with an invisible intermediate mediator decaying into a pair of $\chi\bar{\chi}$ on the final state [15]. For the SD WIMP-nucleon scattering on the right plot of the Fig. 1.13, the ATLAS limit is the strongest for a wide range of the m_χ all the way up to the energy limited by the collision energy. But the interpretation is conditional and requires slicing down the high-dimensional parameter space. Very similar limits are released by the CMS detector (137 fb^{-1}) searching on the leptonically decaying Z boson with $\chi\bar{\chi}$ on the final states, which is also constraint with the

missing transverse momentum.

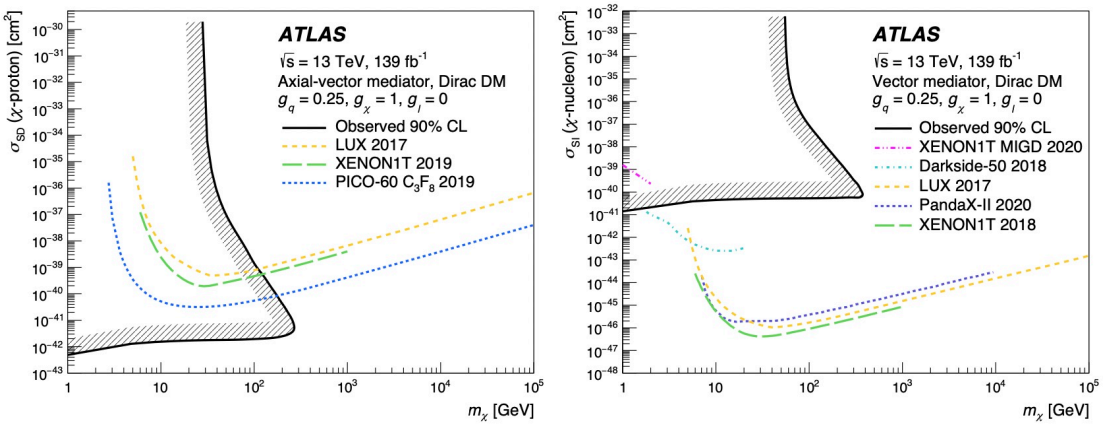

Figure 1.13: ATLAS 90% C.L. limits on the SI (left) and SD (right) DM-nucleon scattering compared to other direct detection experiments [15].

1.4 Dual-phase liquid-xenon time projection chamber

TPCs are particle detectors able to extract the vertex information with the help of electric and magnetic fields. The history can be traced back to 1970s when a gaseous TPC was developed to view the out-going particles from the electron-positron collisions. In the past decades, LArTPCs and LXeTPCs have been developed for low energy neutrino interaction measurements [127] and particle-physics rare-event searches, along with other applications such as Compton telescopes in astrophysics [128] and the positron emission tomography in medical physics [128]. This section mainly focuses on the discussion of the LXeTPCs developed for DM direct detection including the principle and the major advantages followed by a brief introduction to use LXeTPCs to search for two-neutrino and neutrino-less double beta decays, not tightly relevant to this thesis but too important to be overlooked.

To date, there are three ton-scale LXeTPCs actively search for the standard WIMP throughout

the world including PandaX-4T at CJPL-II, XENON-nT at LNGS and LZ at SURF, which makes it possible to cross check the potential discoveries among one another without any waiting period.

1.4.1 Principle

Figure 4.1 is a sketch of the LXeTPC. The energy transferred from the in-coming particle to the xenon nuclei or the electrons. The former is NR, and the latter is ER. The standard WIMP with a GeV-scale mass can scatter off xenon nucleus with more effective momentum transfer for kinematics, which generates a NR signal. Generally, NR events within the SM scope include neutrons, α particles and nuclei with a large atomic number like ^{206}Pb in the ^{210}Pb decay. ER events generally include β particles, X-rays and γ-rays, whose responses share similarities if it is single-site. The decay of ^{83m}Kr which includes an intermediate state with a half-life $T_{1/2} = 156$ ns appears to have very different ER responses which cannot be fully understood so far. If the same amount of single-site events mentioned above appear in the LXeTPC, neutron events will be the most important and dreadful backgrounds. But as discussed in more details in chapter 2, so far, ER backgrounds from the ^{222}Rn decay chain is the most important background limiting the sensitivity for PandaX-4T.

A TPC is able to collect a prompt scintillation $S1$ and a delayed ionization $S2$ of the recoiling, and the property of $S2/S1$ presents a strong power to separate the major ERs from NRs as is shown in the right plot of the Fig. 4.1. $S1$ is from the decay of the excited dimers Xe_2^* back to the ground state. For LXe, the wavelength of the scintillation photons is centered at 178 nm, which is detected by the photomultiplier tubes (PMT) specially developed by Hamamatsu Photonics Co. in 1990s. In principle, the de-excitations of singlet ($T_{1/2} = 4$ ns) and triplet states ($T_{1/2} =$

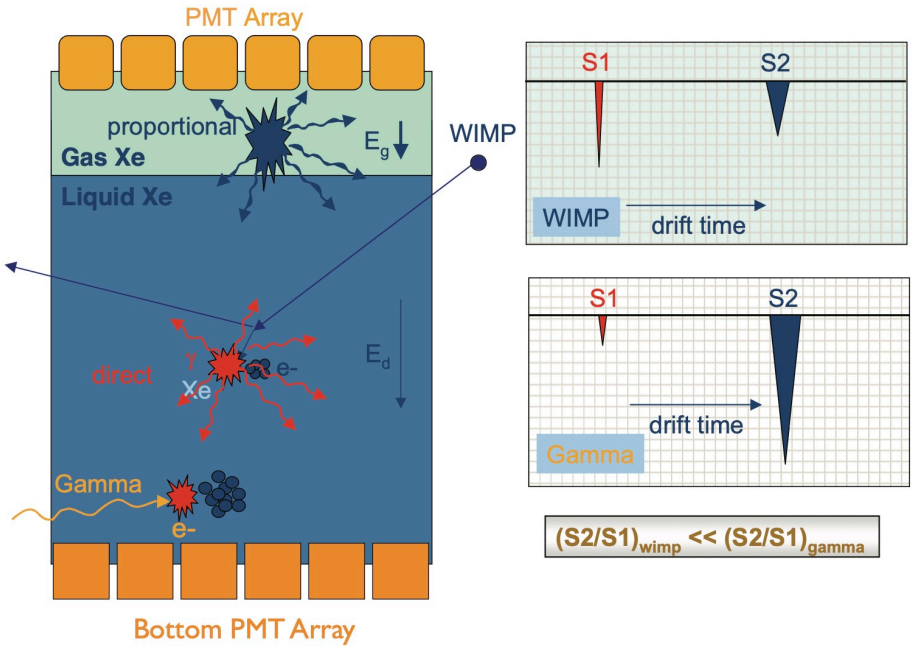

Figure 1.14: A schematic view of a LXeTPC [16].

$21-27$ ns) have different half-lives can also be utilized to distinguish different recoiling types by different ratios of the excited singlet and triplet states via the $S1$-only pulse shape discrimination (PSD) [128]. However, the smaller difference in the half-lives makes PSD much less effective in comparison to the $S2/S1$ ratio.

The ionization signal $S2$ doesn't count the part recombined back into scintillation right after the recoiling which is effectively counted in $S1$ instead. The ionized free-electrons are drifted upward in the electric field applied which should be ideally higher than 500 V/cm but ton-scale detectors have verified that a drifting electric field as low as 100 V/cm is sufficient [28]. Since the electrons moving upward may be absorbed by electron-negative gases, the electron lifetime τ_e (usually has a unit of μs) which describes the amount of electrons survive to the gas phase is a crucial quantity to monitor the data quality. At the liquid-gas interface, the electrons are extracted out with a electric field to generate the proportional scintillation which typically higher

than 1 kV/cm and lower than the avalanche field (1 MV/cm). This delayed scintillation is the so-called $S2$.

The recoiling energy is reconstructed with $S1$ and $S2$ which sums up the part of scintillation and ionization yields after efficiency corrections. ERs have most energy deposited in these two channels, but for NRs, taking a 50 keV_{nr} recoiling as an example, 80% of the recoiling energy is converted into heat and not detected by the LXeTPC. For clarification, the equivalent electron recoiling energy is used with a unit keV_{ee} and the NR energy with keV_{nr} .

As the scintillation photons are viewed by the PMTs, which convert photons into electrons with the photoelectric effect. The number of initial electrons entering the first dynode of the PMT is recalculated with a unit defined as photoelectrons (PEs). With the PMTs typically holding $30-35\%$ quantum efficiencies, the energy threshold is around $\mathcal{O}(1)$ keV_{ee} by accounting for the work function of LXe about 13.7 eV and the detectability of $\mathcal{O}(1)$ PE in $S1$ and $\mathcal{O}(1)$ electrons converted from $S2$. The details of the energy reconstruction based on the noble element simulation techniques (NEST) is presented in chapter 6.

1.4.2 Advantages

Besides the $S2/S1$ discrimination power, the best sensitivities reached by LXeTPCs in the past decade to search for the standard WIMPs also come from the the following features at least.

1.4.2.1 A large atomic mass in Xe

The average atomic mass of natural Xe is $A = 131.3$, which is larger than many other materials used in particle detectors including silicon, germanium and iodine. For the SI WIMP-

nucleus scattering, the cross section is

$$\sigma_A^{SI} = A^2 \frac{\mu_\chi^2}{\mu_n^2} \sigma_n^{SI}, \tag{1.6}$$

where σ_n^{SI} is the SI WIMP-nucleon (proton/neutron) cross section, μ_χ is the reduced mass of the WIMP-nucleus system and μ_n is the reduced mass of the WIMP-nucleon system.

A larger atomic mass also means a stronger stopping power of the penetrable radioactivities including gammas and neutrons as well as the unavoidable radioactivities from the detector materials. Together with the vertex information, a clean data set can be selected.

1.4.2.2 Effective volume fiducialization

A reliable position reconstruction of the events makes the self-shielding of LXe effective. The delayed time of $S2$ is used to reconstructed the vertical position with the known drifting electron velocity. The $S2$ distribution in the top array of PMTs has the best resolution to the horizontal position with a large angular coverage by assuming that the center of the electron clouds staying the same during drifting. Even if the drifting electric field is so low that the electron clouds shift inward while reach the gas phase, with a reliable map of the static electric field in LXe, the origin vertex can be inferred. Compared to the sensitive region viewed by spherically distributed light sensors [129], the risk of wrongly reconstructing the events at a very large radius to the center is lower. Even though non-negligible statistical uncertainties in the horizontal position reconstruction especially for small $S2$ is still limiting the advantage of the strong stopping power of LXe, the data with a much smaller backgrounds (more than 90% come from the border region) at the center of the detector can be selected easily by the effective and

robust volume fiducialization. More details about the horizontal position reconstruction can be found in chapter 4.

1.4.2.3 Viable $in\ situ$ purification

The impurities mixed in the Xe can be divided into two categories. The electron-negative impurities that are composited of non noble-gas elements, and the noble-gas impurities. The electron-negative elements whose absorption spectra overlapped with the scintillation spectrum of xenon (peaked at 178 nm) will affect the τ_e. Because of different chemical properties between these electron-negative impurities and xenon, the techniques to reduces these impurities have been well-developed. In PandaX, hot zirconium getters in the xenon circulation system are sufficient to preserve a large enough electron lifetime.

But getters are not enough to fully remove all the non noble-gas impurities like the tritiated methane (CH_3T). In the PandaX-II stage, after using CH_3T as a ER calibration source, they stayed in the Xe with a non-negligible level. But because of a large mass different between CH_3T and Xe, it can be reduced via distillation.

The long-lived noble-gas radioactivities compared to the detector operation can be notorious, including ^{85}Kr and ^{222}Rn. Distillation can separate different components with the differences in the boiling points, and has been used to effectively reduce the ^{85}Kr level in PandaX experiments as well as XENON. The activated charcoal has been used to reduce the ^{85}Kr level as well as ^{222}Rn in LUX and LZ.

In brief, because LXe can be purified $in\ situ$ with the circulation system, any novel technology developed to reduce the radioactivities can be applied right away, which brings the

potential to reach a background level dominated by the irreducible physics backgrounds from solar neutrinos and double decays of ^{136}Xe.

1.4.3 Double beta decay searches with Xe

Two-neutrino double beta decay ($2\nu\beta\beta$) process is predicted in the SM as a second-order weak-interaction process with a half-life orders of magnitude longer than the age of the universe. EXO-200 [130] has successfully measured the first $2\nu\beta\beta$ ever seen with 80% enriched ^{136}Xe. Also, the double-decay of ^{124}Xe reported by XENON1T [131] is the longest lifetime measured directly. The $2\nu\beta\beta$ of ^{134}Xe can also be searched with ton-scale LXeTPCs [132]. The measurements of $2\nu\beta\beta$ half-lives are important for understanding nuclear structure models better.

The success of $2\nu\beta\beta$ measurements also pave the way to search for neutrinoless double beta decay ($0\nu\beta\beta$), which is another important rare-event search for new physics. After the neutrino oscillation is measured, the neutrino mass becomes the first verification of new physics beyond SM. Then, the $0\nu\beta\beta$ search which once shew up in the last century before the establishment of SM becomes interesting again, which is now tightly related to three important problems including the existence of Majorana particles, the hierarchy of the three neutrinos and the absolute mass of the neutrinos. LXeTPCs can be competitive in searching for $0\nu\beta\beta$ with enriched ^{136}Xe as proposed by nEXO [133] with all the technologies available at hand.

1.5 Summary

The whole thesis is organized as eight Chapters. After this introduction chapter, Chapter 2 summarizes the final analysis with the complete PandaX-II exposure and the R&Ds in the season

finale of PandaX-II. Chapter 3 presents the details about the ^{83m}Kr calibration including the generation with the proton bombardment on natural krypton, and the injection into the PandaX-II experiment. Chapter 4 describe the development on the horizontal position reconstruction algorithms with the help of ^{83m}Kr. Chapter 5 overview the subsystems of PandaX-4T and its comissioning data (Run 1). Chapter 6 presents the details in the fast detector simulation used in the PandaX-4T, and the application of the reweighting technique in the profile likelihood ratio analysis to test dark matter models. Chapter 7 presents details of a search on an alternative sub-MeV fermionic DM model with the PandaX-4T commissioning data which share similarities to keV sterile neutrino DM search in the direct detection experiments. Chapter 8 provides a brief summary of the thesis and the outlook for the future.

Chapter 2: Overview of PandaX-II experiment

This chapter mainly introduces the China Jinping Underground Laboratory (CJPL), the PandaX-II final data analysis and the hardware R&Ds during the end-of-run period of PandaX-II. Chapter 5 provides a more systematic summary on the hardware subsystems and data analysis procedure of PandaX-4T experiment to search for WIMPs.

All the PandaX detectors take scientific data at CJPL with a 6800 m.w.e shielding [53, 54]. PandaX collaboration was established back to 2009. PandaX-I, the pathfinder, took more than 5 years before taking data, with details presented in the dissertations [134, 135, 136, 137, 138, 139, 140, 141, 142]. PandaX-II built a new dual-phase liquid xenon time projection chamber (LXeTPC) with 1.1 tonne xenon in the pressure container, whose details can be found in the dissertations [138, 141, 143, 144, 145, 146, 147]. Some important developments for controlling backgrounds for PandaX experiments deserve acknowledgements including the two distillation towers [145, 148, 149] and high purified germanium detectors (HPGes) [150]. PandaX-4T has published the commissioning data result on GeV-scale WIMP search in 2021. Designs of PandaX-I and PandaX-II mainly focus on the energy window below 100 keV$_{ee}$[1]. PandaX-4T upgrades include designs for search on neutrinoless double beta decay ($0\nu\beta\beta$) with $\mathcal{O}(1)$ MeV energy deposition. PandaX-III focuses on searching for $0\nu\beta\beta$ with enriched ^{136}Xe which is still

[1]The subscript 'ee' is for equivalent ER energy deposition.

under preparation and beyond the discussion of this thesis.

In this chapter, section 2.1 introduces the CJPL. Then, section 2.2 discusses the final analysis of PandaX-II. Section 2.3 presents the R&Ds studied with PandaX-II detector in the last running year.

2.1 China Jinping Underground Laboratory

To reduce the amount of the penetrable radioactivities including neutrons and gammas, direct dark matter search experiments resort to underground laboratories for lower secondary particles generated by cosmic rays. CJPL is at the middle of the tunnel going through Jinping mountain in Sichuan province of China (Fig. 2.1). The 2400 m rock shielding, equivalent to 6800 m of water, makes it the deepest underground lab in the world to-date.

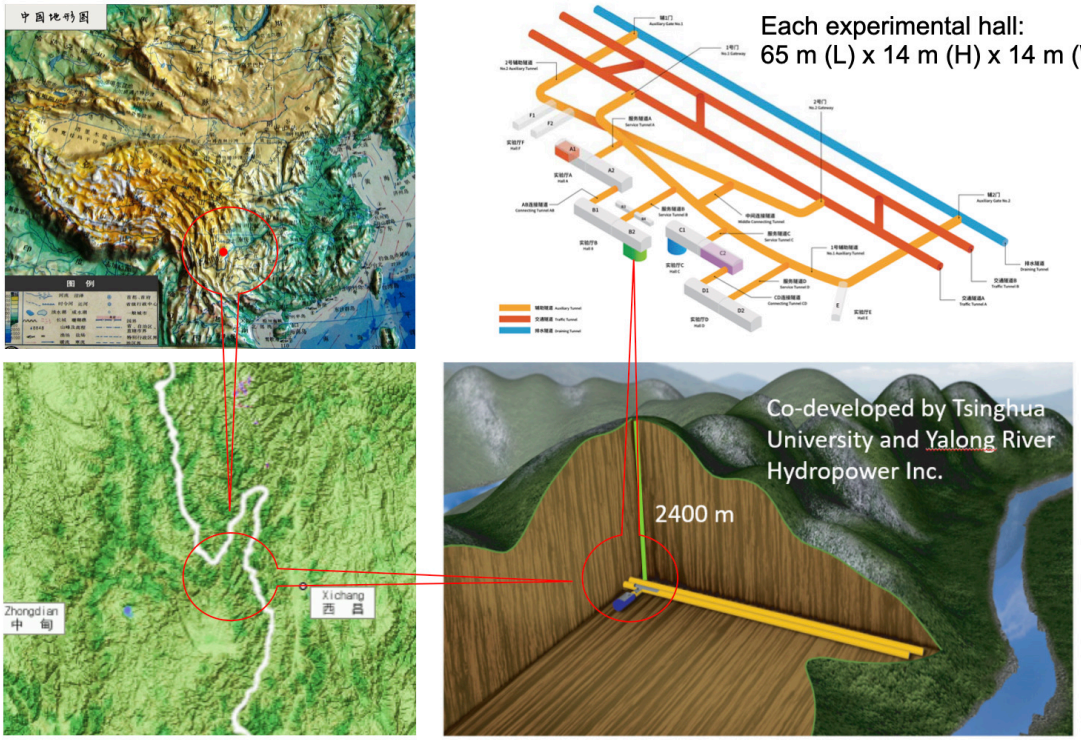

Figure 2.1: Location of China Jinping Underground Laboratory with the site of PandaX-4T marked at the upper-right corner.

CJPL phase I and II occupies 4000 m^3 and 330, 000 m^3, respectively. CJPL-II is divided in to four halls (A, B, C, D) as indicated in Fig. 2.1, accommodating PandaX, CDEX and JUNA already. PandaX-I and PandaX-II was built in CJPL-I, and PandaX-4T in the B2 hall of CJPL-II.

The cosmic muon flux at CJPL-I measured by JNE Collaboration is $(3.61 \pm 0.19_{\rm stat} \pm 0.10_{\rm syst}) \times 10^{-10}\ {\rm cm}^{-2}{\rm s}^{-1}$ [151], which is the second smallest, being slightly higher than Sudbury Neutrino Observatory (SNO) $(3.31 \pm 0.01_{\rm stat} \pm 0.09_{\rm syst}) \times 10^{-10}\ {\rm cm}^{-2}{\rm s}^{-1}$ [152] w.r.t. existing measurements. The estimated muon flux with Monte Carlo (MC) simulation of CJPL-II is $(2.3 - 4.0) \times 10^{-10}\ {\rm cm}^{-2}{\rm s}^{-1}$, which means two muons per meter square are expected to reach the lab every week.

2.2 PandaX-II final analysis

In this section, the hardware of the PandaX-II detector is first reviewed and then the data taking history. The final analysis is more complicated because the deterioration of photomultiplier tubes (PMTs), calibration for the long run data and increasing importance of backgrounds accumulated over time which were negligible before.

2.2.1 Detector assembly and data taking history

Figure 2.2 shows the workspace of PandaX-II. The four dewar vessels to retrieve 1.1 tonne xenon can be seen besides the stairs, the cooling bus is on the second floor, the shielding can be barely seen which is behind the stair, and the data acquisition (DAQ) system is invisible in this picture and close to the white wall.

The multi-layer passive shielding to stop the ambient radioactivities is shown in Fig. 2.3

Figure 2.2: A view of the PandaX-II workspace.

with the materials used in different layers marked. Polythene is used to stop neutrons with collisions on hydrogen which is preferred because of a mass similar to neutron. Lead is used to attenuate γ-rays with its high density and atomic number. The inner copper stops the radioactivities from the other shielding materials.

The cryogenic system which can be found in Fig. 2.4 includes a cooling bus and a circulation purifier. The cooling bus working at 178.5 K (1.2 barG) consists of a heat exchanger, a pulse tube refrigerator (PTR), an emergency cooling component and sensors. If problems like PTR failure happen or the xenon gas pressure is higher than 1.5 barG, the emergency cooling will be triggered with the liquid nitrogen cooling.

Two circulation loops are connected to the cryogenic system with a total mass flow rate of approximately 560 kg/day through hot getters to remove non-noble gaseous impurities which can also be found in Fig. 2.4. And two kinds of circulation pumps, Q-Drive and KNF, are used in the

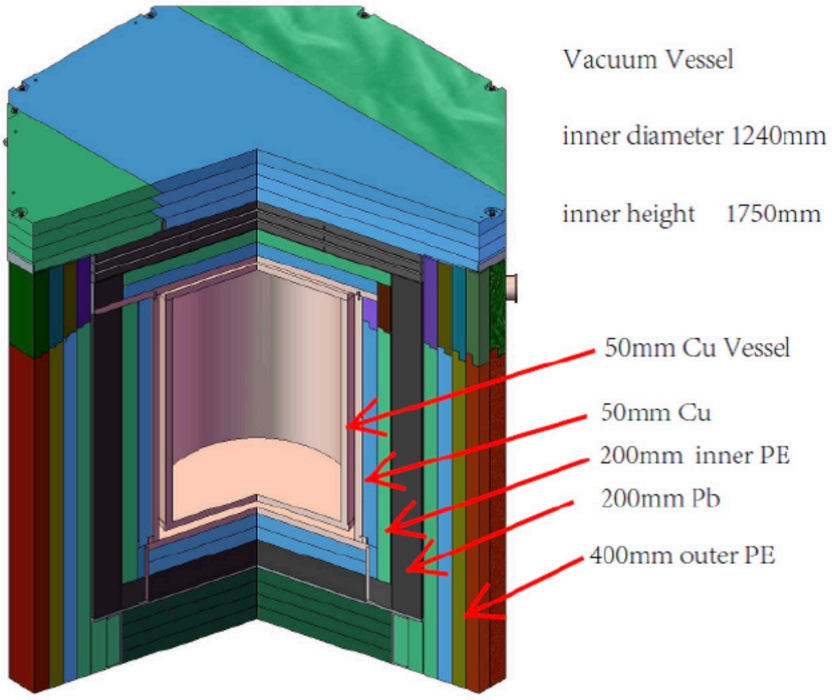

Figure 2.3: Sketch of the PandaX-II passive shielding

loops.

The sketch of the TPC can also be seen in Fig. 2.4. The PandaX-II TPC is a dodecagonal chamber with a 646 mm diameter and a height of 719.9 mm out of which the maximum drifting distance is 600 mm defined by the distance from the bottom cathode mesh to the top gate grid. A total of 580 kg of liquid xenon is contained in the sensitive volume. Two arrays of Hamamatsu R11410 photomultiplier tubes (PMTs) located at the top (55) and bottom (55) of the TPC, respectively. Recoiling events produce the prompt scintillation photons ($S1$) and delayed electroluminescence photons ($S2$).

Immediately after 79.6 days of data collection in Run 9, an ER calibration with tritiated methane and a subsequent distillation campaign were performed, after which Run 10 collected DM search data for 77.1 days. Run 10 ended with a power failure, and Run 11 started right after

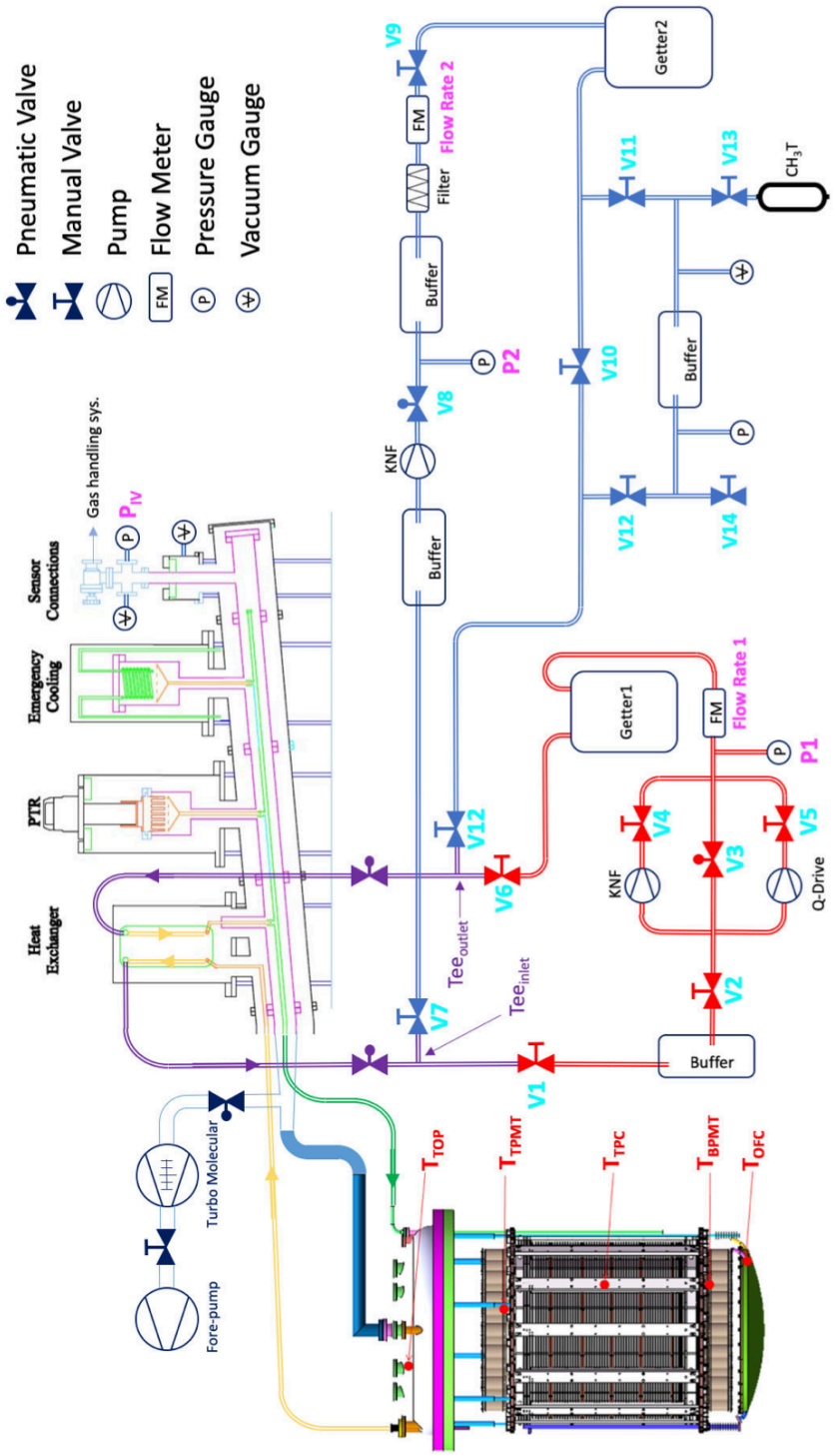

Figure 2.4: Schematics of cryogenics and circulation system in PandaX-II (also in Fig. 3.11).

the recovery, collecting a total of 244.2 days of data from July 17, 2017 to Aug. 16, 2018. The evolution of the electron lifetime can also be found in Fig. 2.5.

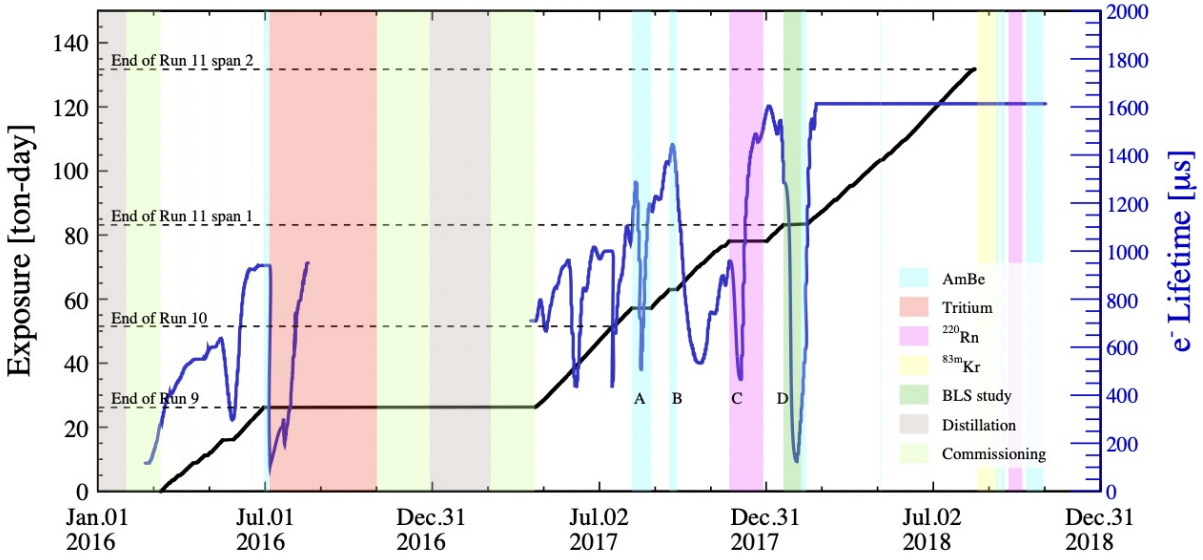

Figure 2.5: The accumulation of DM exposure (black line) and the evolution of the electron lifetime (blue curve, right axis) in PandaX-II.

2.2.2 Data analysis with the complete PandaX-II exposure

As more systematically discussed in section 5.2, the main data analysis for the GeV-scale WIMP search has three main parts including waveform processing to interpret the data scientifically, background estimation and signal modeling before search for any suspicious exotic features over the backgrounds. In this section, only specific handling for the long run data and important parameters/results are presented, mainly following the publication [40]. It's suggested to read chapter 5 first for readers who are unfamiliar with LXeTPCs.

2.2.2.1 Data processing and quality cuts

The data processing chain is very similar to PandaX-4T in section . The dissertation [141] presents more information of the PandaX-II data processing chain. Specific handling is required for the final analysis due to decrease of PMT gains, increase of PMT noises and unavoidable inhibition of some PMTs. Seven 3-inch PMTs are fully inhibited in this analysis for all data sets, whose history can be found in Tab. 2.1[2].

Index	Timing	Position	Reason
1	Run 9	Bottom 52	Afterpulsing
2	Run 10	Bottom 46	Failure in PMT base
3	Run 10	Top 26	Failure in PMT base
4	Run 11	Top 16	High discharge rate
5,6,7	Software after Run 11	Top 1, 28, 46	High noises

Table 2.1: The 7 inhibited 3-inch PMTs in the complete data set out of 110 with a position map in Fig. 4.2 for both top and bottom arrays.

Low-gain PMTs

PMT gains were calibrated twice a week with blue light-emitting diodes (LEDs) inside the detector by fitting the single photoelectron (SPE) peak in the spectrum (see example in PandaX-4T in Fig. 5.22). After a vacuum failure between Run 9 and 10, degradation in some high-voltage feedthroughs limited a number of PMTs to run at lower voltages and reduced gains. The average gain changed from 1.41×10^6 in Run 9 to 0.96×10^6 in Run 11. The LED calibration became problematic for low-gain PMTs with SPE peaks close to baseline noises, leading to failed fits and jumps.

If more than two other PMTs work properly with the same distance to the TPC center

[2]Top 1 was not turned off while the horizontal algorithm was studied as presented in chapter 4 but prohibited in the PandaX-II final analysis.

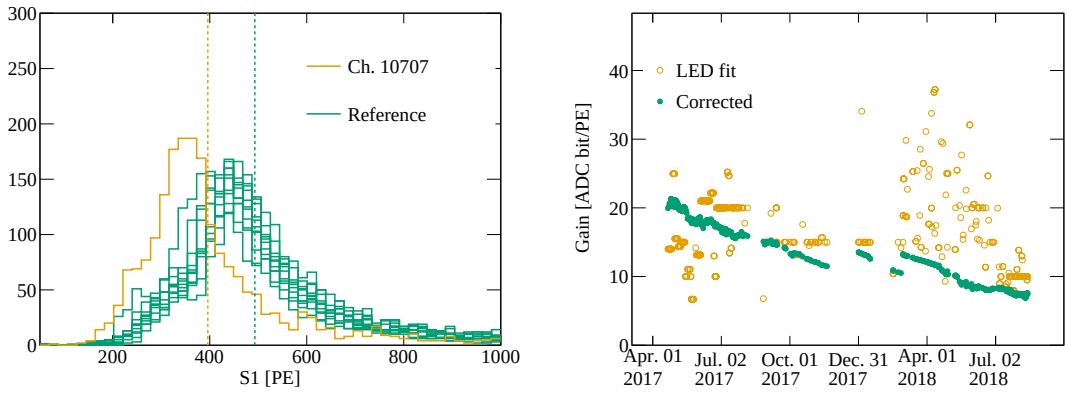

(a) (b)

Figure 2.6: An example of gain correction to low gain PMTs. (a) The $S1$ charge distribution of α events in the low gain Ch.10707 (yellow line) and the other reference PMTs located at the same radius (green lines). (b) The evolution of gain of Ch.10707. The yellow open circles represent gains obtained in the LED calibration and the green dots are the corrected gains. The tendency in green dots is reasonable w.r.t. the supply voltages of Ch.10707.

(within the same group as shown in Fig. 4.2), we can monitor and correct the gains with horizontally uniformly distributed events. We use the $S1$ of alpha events for the gain correction. An example is shown in Fig. 2.6.

Quality cuts

The cuts developed in Ref. [153] are preserved with some updates according to the PMT conditions. The $S2$ top-bottom asymmetric (TBA) cut need modification more than slight changes in the values of the outlier cuts, and two addition cuts are further developed:

1. The previous $S2$ TBA outlier cuts become problematic for the events with horizontal positions close to inhibited top PMTs as shown at the top of Fig. 2.7 and left of Fig. 2.8. The made-up qS2_ibad is calculated as

$$\mathrm{qS2\_ibad} = \mathrm{qS2T}_{\max} \frac{\eta_{i_{\mathrm{bad}}}(x,y)}{\eta_{i_{\max}}(x,y)}, \tag{2.1}$$

with the knowledge of reconstructed horizontal position (x, y) and photon acceptance function (PAF), $\eta_i(x, y)$, where i is the index of the PMT (chapter 4 has more details). $\mathrm{qS2T_{max}}$ is the maximum hit in $S2$ collected by the $i_{\max}$ PMT. If an inhibited channel, i_{bad}, is next to the $i_{\max}$, then qS2_ibad is calculated and used to fix the $S2$ TBA outlier cuts as shown in Fig. 2.8 (red lines).

2. Because a top PMT close to the TPC center is off (46 in Fig. 4.2), some events in the gas xenon happen right under Top 46 are not removed by old quality cuts (these events can have physical $S2$s with electrons in the gas drifted towards the anode). They have a typical drifting time about 40 μs in PandaX-II detector. Due to longer tracks and weak drift fields, these $S2$s have larger width in comparison with the normal events. A cut on the $S2$ widths is developed and applied.

3. We observed that occasional mini-discharges occurred in the detector, resulting in waveforms containing 'trains' of small pulses. An extra cut for waveform cleanliness is developed to remove such events.

By analyzing the NR and ER calibration data, the inefficiency of the two new cuts for single-scattering events is estimated to be less than 5%.

2.2.2.2 Detector response calibration

The main calibration includes detector uniformity, baseline suppression (BLS) and energy reconstruction.

Uniformity calibration

Detector uniformity is calibrated with uniformly distributed mono-energetic peaks in the

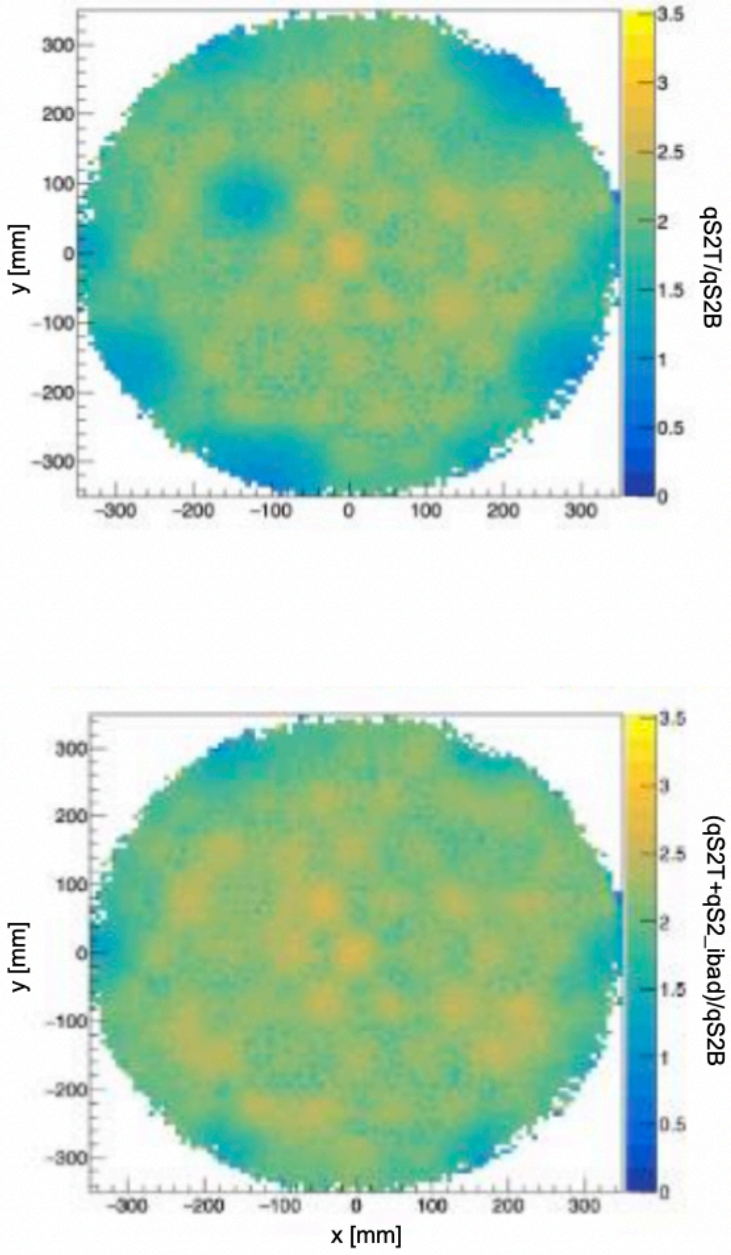

Figure 2.7: $S2$ TBA before (top) and after (bottom) fixing with qS2_ibad. The qS2T and qS2B are the sum top and bottom $S2$ charges, respectively.

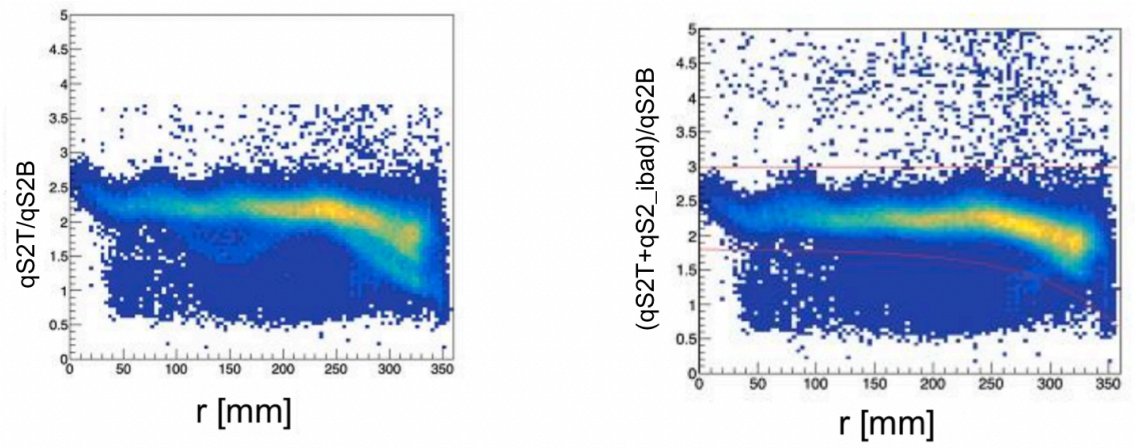

Figure 2.8: $S2$ TBA as a function of $r = \sqrt{x^2 + y^2}$ before (left) and after (right) fixing with qS2_ibad. The red lines on the right plot cut the outliers.

detector. PandaX-II has used ^{131m}Xe, tritium, ^{83m}Kr and α events as summarized in Tab. 2.2. A more detailed example can be found in section 5.2.1.3 for PandaX-4T Run 1, and the PandaX-II uniformity calibration can be found in the publications [34, 40, 153].

Item	Run 9	Run 10	Run 11
$S1$ three-dimensional	^{131m}Xe	^{83m}Kr	^{83m}Kr
$S2$ electron lifetime (vertical)	^{131m}Xe	^{131m}Xe	internal α
$S2$ horizontal	^{131m}Xe and tritium	^{131m}Xe	^{83m}Kr

Table 2.2: Uniformity calibration events used in the three runs.

BLS nonlinearity

The BLS threshold for each digitizer channel was set at an amplitude of 2.75 mV above the baseline. For comparison, the SPE for a gain of 10^6 corresponds to a mean amplitude of 4.4 mV in the digitizer. The channel-wise BLS inefficiency is negligible for Run 9, since all PMTs were operating under the normal gain, but becomes more significant during Run 10 and 11 due to the low-gain PMTs as discussed before. Consequently, the detected $S1$ and $S2$ are suppressed from the original $S1_o$ and $S2_o$. As long as $S1$ and $S2$ fall into selection windows, BLS does not cause an event loss but rather a nonlinearity in $S1$ and $S2$, which is more visible for small signals and

approaching unity for large ones.

In Run 10, we adopted the single-channel BLS efficiency from the LED calibration as in Ref. [34]. In Run 11, we performed direct measurement using neutron calibration data with the BLS firmware disabled. All thresholdless waveforms were saved as $S1_o$ and $S2_o$, and the software threshold for pulse identification is very low with negligible inefficiency.. We then applied the BLS algorithm on the data as that in the firmware and obtained $S1$ and $S2$, from which the BLS nonlinearities $f_1 = \frac{S1}{S1_o}$ and $f_2 = \frac{S2}{S2_o}$ were determined in an event-by-event manner. The distributions of f_1 and f_2 are modeled into smooth probability density functions (PDFs) and fed into our fast detector simulation [40]. An example of BLS in PandaX-4T Run 1 can be found in Fig. 6.10(a) and Fig. 6.10(b).

Energy reconstruction with mono-energetic peaks

As discussed later in section 5.2.3, ER mono-energertic peaks are used to calibrate universal detector parameters in the ER equivalent energy reconstruction $E_{\rm ee}$(Eq. 5.3) including $G1$ and $G2$. Together with the small $S2$s in the detector, photo detection efficiency (PDE), electron extraction efficiency (EEE) and single electron gain (SEG) are determined. In PandaX-II Run 9, we select the prompt de-excitation gamma rays from the neutron calibration, 39.6 keV$_{\rm ee}$ from ^{129}Xe, and 80.2 keV$_{\rm ee}$ from ^{131}Xe, both corrected for the small shifts caused by the mixture of NR energy. ER peaks due to the same neutron illumination, 164 keV$_{\rm ee}$ ($^{131\rm m}$Xe) and 236 keV$_{\rm ee}$ ($^{129\rm m}$Xe), are also selected. For higher energy gamma peaks, we only select the 662 keV$_{\rm ee}$ peak from ^{137}Cs to avoid potential bias in energy due to the saturation of $S2$. In Run 10, to avoid BLS nonlinearities at lower energies, higher energy peaks are selected, including 164 keV$_{\rm ee}$, 236 keV$_{\rm ee}$ and 662 keV$_{\rm ee}$, together with gammas of 1173 keV$_{\rm ee}$ and 1332 keV$_{\rm ee}$ from ^{60}Co. The calibrated parameters in different run sets are summarized in Tab. 2.3. For Run 11, since the field

configurations stays the same as in Run 10, the PDE and EEE are obtained by scaling the Run 10 values according to the average $S1$ and $S2$ from the 164 keV$_{\rm ee}$ peak in the detector. The deviation of the $E_{\rm ee}$ for different events from the expectation can be found in Fig. 2.9.

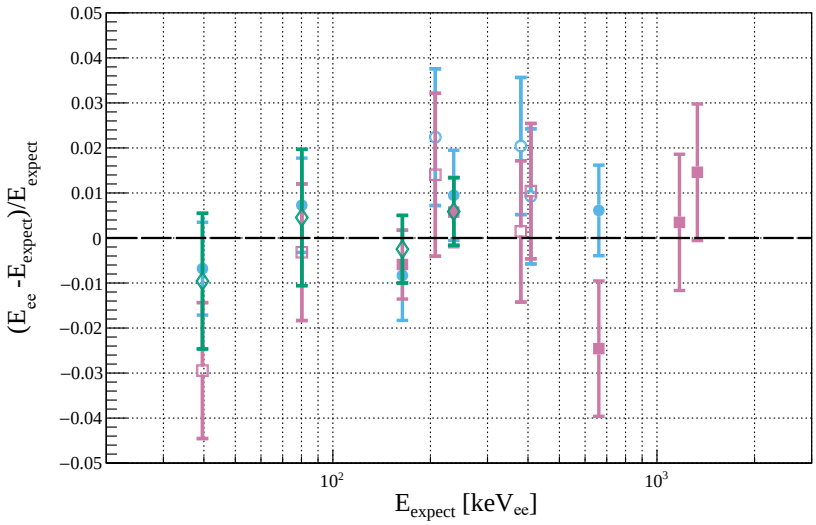

Figure 2.9: Fractional difference between the reconstructed energy $E_{\rm ee}$ and expected energy $E_{\rm expect}$ for characteristic gamma peaks in Run 9 (blue circles), Run 10 (magenta squares), and Run 11 (green diamonds). Closed symbols represent points used in the fits, and open symbols are those test peaks.

Run	PDE (%)	EEE (%)	SEG (PE/e^-)
9	11.5 ± 0.2	46.3 ± 1.4	24.4 ± 0.4
10	12.1 ± 0.5	50.8 ± 2.1	23.7 ± 0.8
11	12.0 ± 0.5	47.5 ± 2.0	23.5 ± 0.8

Table 2.3: Summary of PDE, EEE and SEG in PandaX-II.

The low-energy ER and NR energy responses are calibrated based on NEST2 in the PandaX-II final analysis, which integrates all the aforementioned calibrated information into the fast simulation. An iterative fitting of the charge yield (CY) and light yield (LY) is carried out according to the centroids of our data in PandaX-II final analysis with the definitions as

$$\mathrm{CY} = \frac{S2}{\mathrm{EEE} \times \mathrm{SEG}} / E_{\rm ee}\,, \quad \mathrm{LY} = \frac{S1}{\mathrm{PDE}} / E_{\rm ee}\,. \tag{2.2}$$

But in PandaX-4T Run 1 (see chapter 6 for details), the degrees of freedom are merged with those on the recombination ratio of the initial ionization yield. The comparison of CY and LY of our calibration data and the other experiments can be found in Fig. 2.10. The agreement between the tuned NEST2 and our calibration data can be found in Fig. 2.11.

With the detector responses calibrated, we could predict the signal distributions in the observable space ($S1$, $S2$, vertexes and etc.) with the theoretical energy spectrum as an input (see an example in section 5.2.3). It's worthwhile to mention the Run 11 data was blinded while the selection cuts for final candidates are set. The signal window to search for DM candidates and the fiducial radius are optimized by requiring the best DM sensitivity at the mass of 40 GeV/c^2 optimized with a below-NR-median (BNM) signal acceptance within which the background is evaluated with a cut-and-count approach. For $S1$, we inherit the range of $[3, 45]$ PE as in the previous analysis, as the sensitivity flattens for upper cuts from 45 to 70 PE. As was done previously, $S2$ is selected between 100 (raw) and 10000 PE, together with the 99.99% NR acceptance line and an additional 99.9% ER acceptance cut to eliminate a few events with unphysically large sizes of $S2$. All runs share the same selection cuts on the fiducial radius, i.e., $R^2 < 720\ \mathrm{cm}^2$. The range of the drift time is determined to be $(18, 310)$ μs in Run 9, and $(50, 350)$ μs in Runs 10 and 11, based on the vertical distribution of events with $S1$ between 50 and 70 PE. The xenon mass within the FV is estimated to be 328.9 ± 9.9 kg in Run 9 and 328.6 ± 9.9 kg in Runs 10 and 11, where the uncertainties are estimated using a 5-mm resolution in the position reconstruction.

We also compare the aforementioned ER model with the ER event distributions in Runs 10 and 11, by selecting the events within $S1 \in (45, 200)$ PE (outside DM search window). Although the band centroid agree well, the observed width in the data is larger than that from the calibration

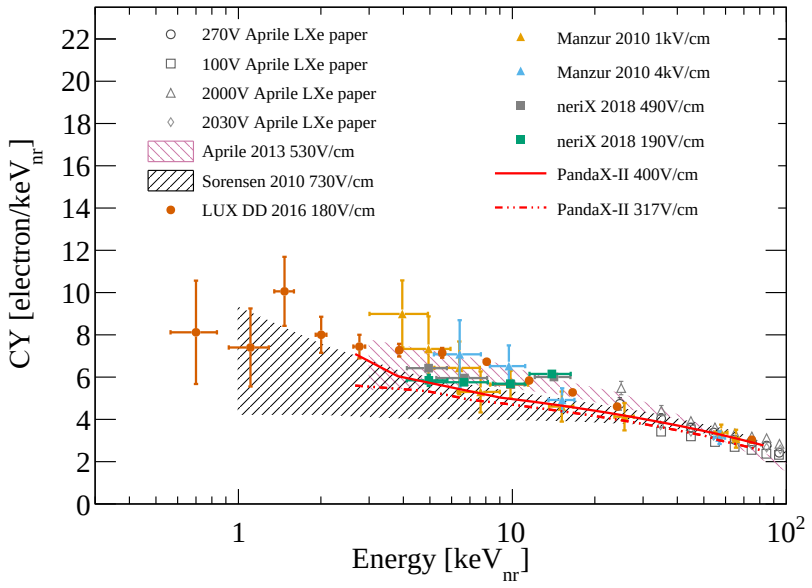

(a)

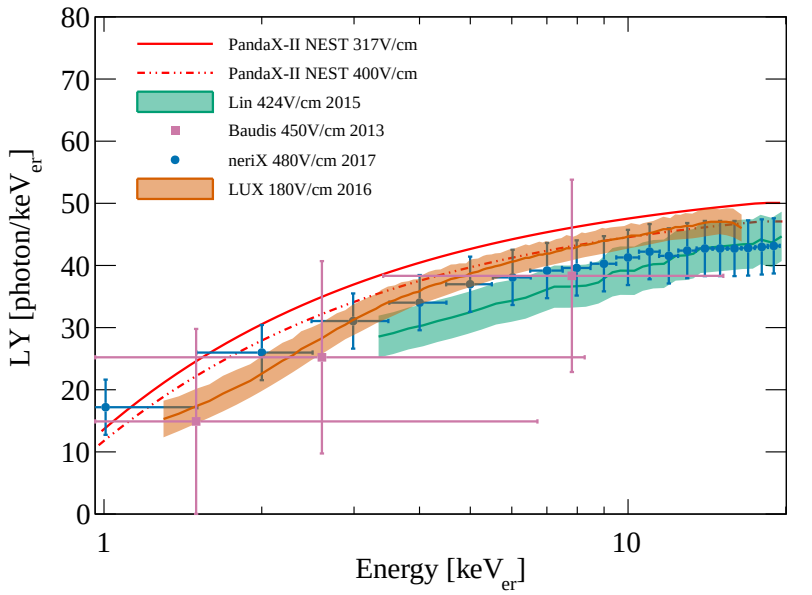

(b)

Figure 2.10: (a) Charge yield of NR and (b) light yield of ER from PandaX-II calibration data compared with results from the worldwide data (ER: Refs. [17, 18, 19, 20], NR: Refs. [21, 22, 23, 24, 25, 26]).

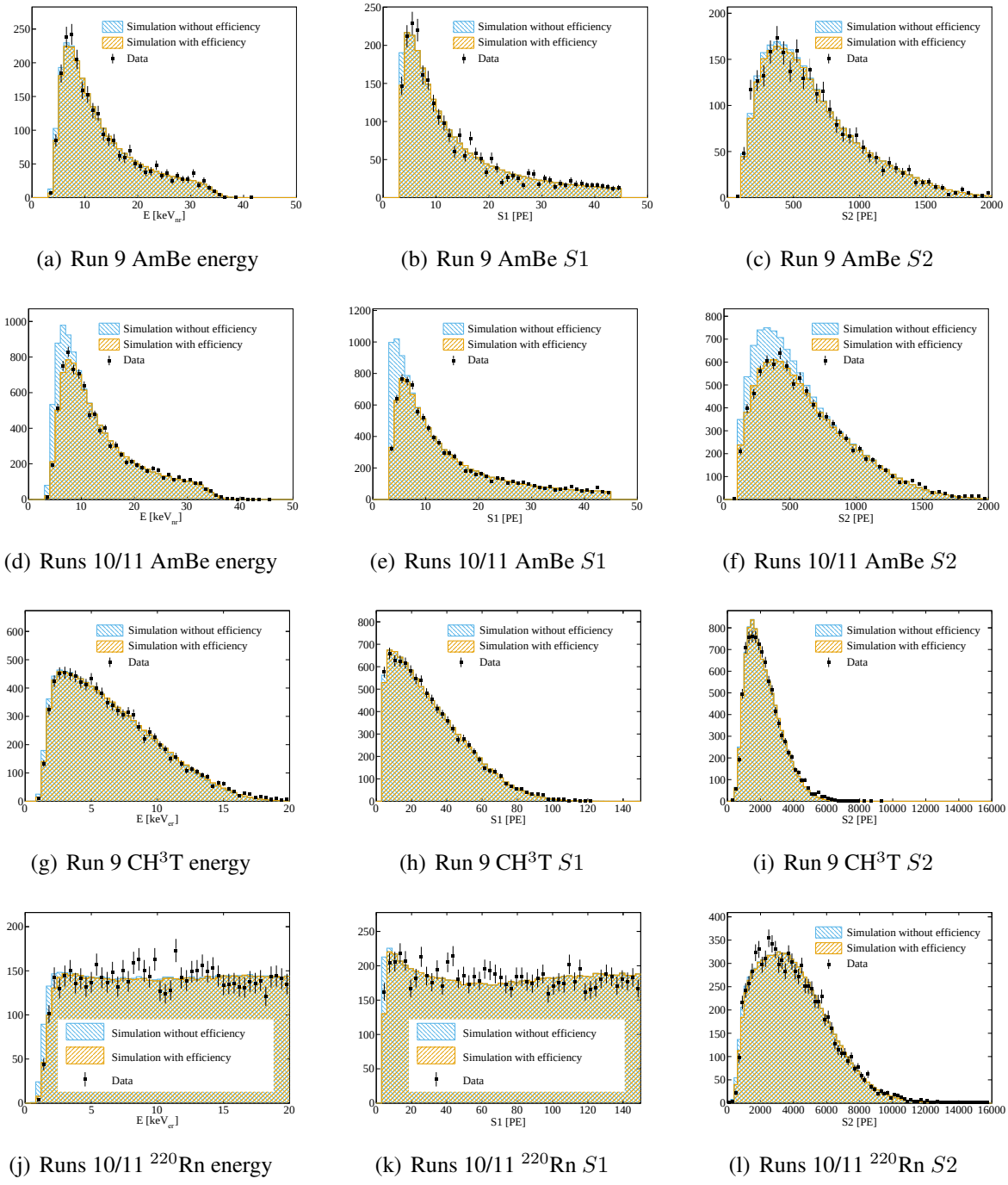

(a) Run 9 AmBe energy (b) Run 9 AmBe $S1$ (c) Run 9 AmBe $S2$

(d) Runs 10/11 AmBe energy (e) Runs 10/11 AmBe $S1$ (f) Runs 10/11 AmBe $S2$

(g) Run 9 CH^3T energy (h) Run 9 CH^3T $S1$ (i) Run 9 CH^3T $S2$

(j) Runs 10/11 ^{220}Rn energy (k) Runs 10/11 ^{220}Rn $S1$ (l) Runs 10/11 ^{220}Rn $S2$

Figure 2.11: The comparison of model simulation and calibration data in the projection of deposited energy, $S1$ and $S2$, in Run 9 and Runs 10/11.

(Fig. 2.12), presumably due to the accumulated fluctuations over time. For conservativeness, we increase the fluctuations in the ER model for Runs 10 and 11 accordingly, leading to larger

leakage ratios to the region below NR median. This problem showing up becomes one motivation for the author to study how to add the uncertainties in the detector responses into the later excess searching in the profile likelihood ratio (PLR) analysis (see chapter 6).

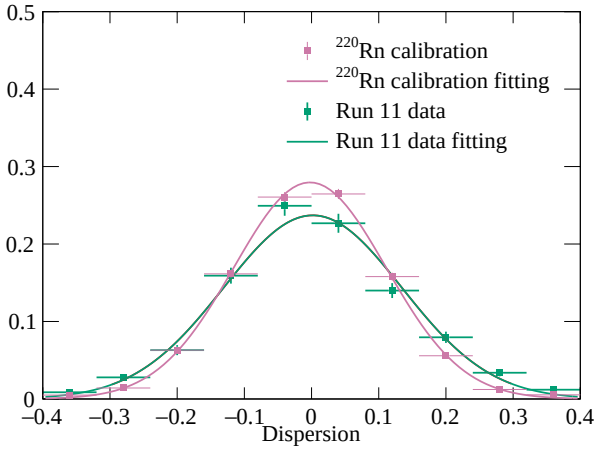

Figure 2.12: Comparison of the distribution of events away from the median of ER band with $S1 \in (45, 200)$ PE between the ^{220}Rn calibration data (magenta dots) and Run 11 DM search data (green dots). The fitted Gaussian functions are overlaid.

2.2.2.3 Background

The four main backgrounds including ER, neutron, accidental and surface events are summarized in Tab. 2.4.

The radioactivity input of ^{3}H takes the best fit in Ref. [154]. Others are estimated independently similar to the previous work [34] except ^{222}Rn and ^{220}Rn which incorporates the development in section 2.3.1 [27].

The neutron background from detector materials is evaluated based on a new method with smaller uncertainties discussed in Ref. [155], using the high-energy gammas to constrain the low-energy single-scattering neutrons.

Accidental backgrounds are produced by the random coincidence of isolated $S1$ and $S2$ [156].

The rates of isolated $S1$s and $S2$s are estimated first in the time window nothing should appear but noises. Then, the contamination for DM search is estimated with simulation of randomly paired isolated $S1$s and $S2$s which survive the same data quality cuts. A boosted decision tree (BDT) cut is developed using the AmBe and accidental samples as the training data for the signal and background, respectively.

Surface backgrounds are estimated in the search window of S1 within 3-45 PE and S2 within 100(raw)-10000 PE . The β-decay of daughter ^{210}Pb ($T_{1/2}$=22.2 y) on the PTFE surface is observed, presumably due to the radon plate-out. A data-driven surface background model is developed to estimate the surface background in the present analysis (see section 4.4.4 for details).

Item		Run 9	Run 10	Run 11, span 1	Run 11, span 2
Flat ER components (mDRU)	^{85}Kr	1.19 ± 0.2	0.18 ± 0.05	0.20 ± 0.06	0.40 ± 0.07
	^{222}Rn	0.19 ± 0.10	0.17 ± 0.02	0.19 ± 0.02	0.19 ± 0.02
	^{220}Rn	0.01 ± 0.01	0.01 ± 0.01	0.01 ± 0.01	0.01 ± 0.01
	ER (material)	0.20 ± 0.10	0.20 ± 0.10	0.20 ± 0.10	0.20 ± 0.10
	Solar ν	0.01	0.01	0.01	0.01
	^{136}Xe	0.0022	0.0022	0.0022	0.0022
Total flat ER (mDRU)		1.61 ± 0.24	0.57 ± 0.11	0.73 ± 0.08	1.03 ± 0.08
^{127}Xe (mDRU)		0.14 ± 0.03	0.0069 ± 0.0017	< 0.0001	
^{3}H (mDRU)		0	0.11		
Neutron (mDRU)		0.0022 ± 0.0011			
Accidental (event/day)		0.014 ± 0.004			
Surface (event/day)		0.041 ± 0.008		0.063 ± 0.0013	

Table 2.4: Backgrounds in the dark matter search runs inside the FV (1 mDRU = 1×10^{-3} evt/keV$_{ee}$/day/kg) in 0-25 keV$_{ee}$. The total flat ER backgrounds of Run 9 and 10 are sums of the independent estimations, and that of Run 11 is estimated with data in the region of 20-25 keV$_{ee}$.

2.2.2.4 Limit and sensitivity

After settling the data processing and the signal response model, the data candidates are selected as summarized in Tab. 2.5. A post-unblinding event-by-event waveform check removes two spurious events (Fig. 2.13) in Run 11. The final number of candidates is 1220.

Cut	Run 9	Run 10	Run 11
All triggers	24502402	18369083	49885025
Single S2 cut	9806452	6731811	20896629
Quality cut	331996	543393	2708838
DM search window	76036	74829	257111
FV cut	392	145	710
BDT cut	384	143	695
Post-unblinding cuts	384	143	693

Table 2.5: Number of events in Runs 9, 10, and 11 after successive selection cuts.

Without any excess found for SI WIMP-nucleus scattering search, limits and sensitivities are set with PLR analysis, which is introduced in detail in section 6.4.1. Instead of simply dividing the data into three runs, we separated the data into 14, 4, and 6 sets in Runs 9, 10, and 11 (so n runs up to 24), respectively, according to different operating conditions, such as the drift/extraction fields and electron lifetime, which affect the expected signal distributions. The PDFs for signals and backgrounds are extended to four dimensions ($S1$, $S2$, r, z). Except for the surface background, the signal distributions of DM and other backgrounds are treated to be independent from their spatial distributions. The distribution of the candidates can be found in Fig. 2.14.

The best fit of the candidates for a 400 GeV/c^2 WIMP is provided in Tab. 2.6. The result of PandaX-II complete data set can be found in Fig. 5.31. A more intuitive view of how much the candidates look like backgrounds and DM is shown in Fig. 2.15.

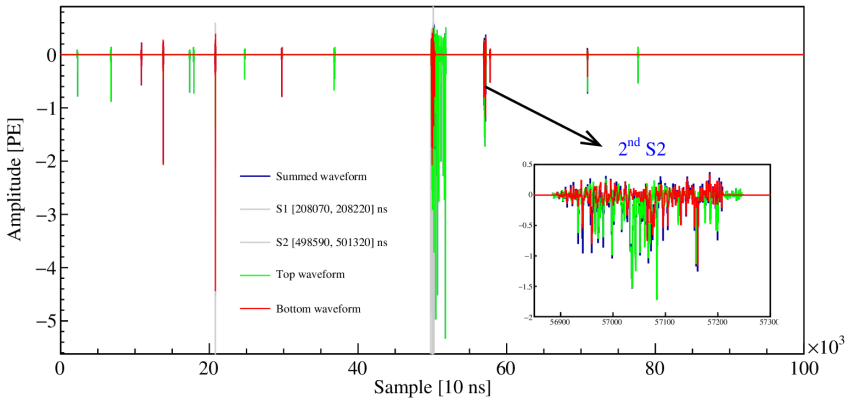

(a)

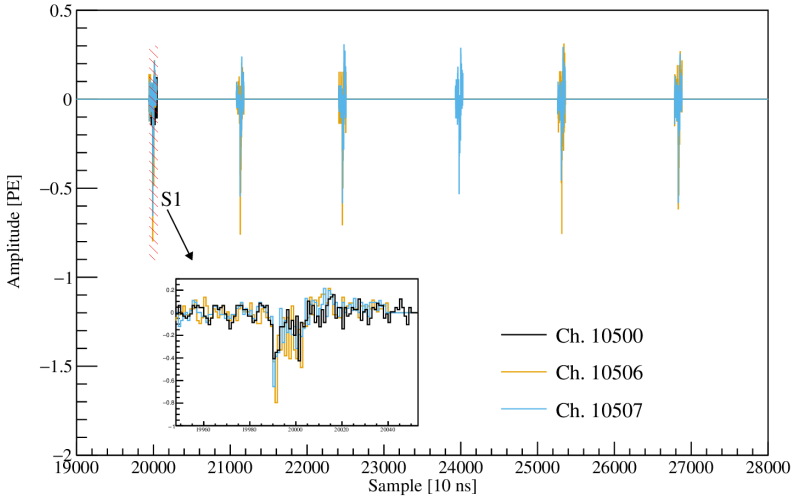

(b)

Figure 2.13: (a) The full waveform of event 167193 in run 20922. The second small $S2$ was split into a few $S1$s in our clustering algorithm, so that it was incorrectly recognized as a single scattering events; (b) The partial waveform of event 112727 in run 22940. Two of the three hits in the reconstructed $S1$ are due to the coherent noise pickup in channel 10506 and 10507.

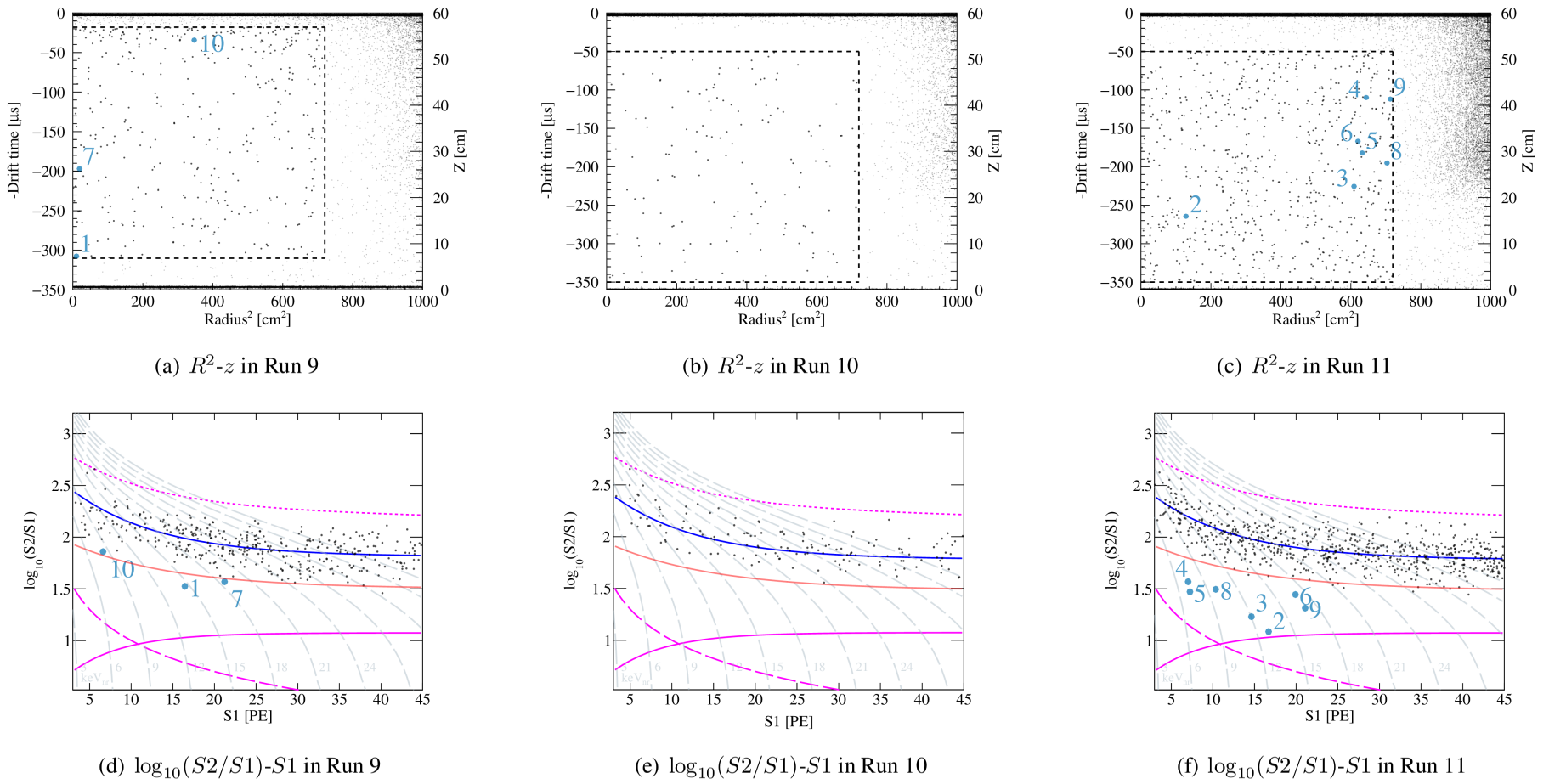

(a) R^2-z in Run 9

(b) R^2-z in Run 10

(c) R^2-z in Run 11

(d) $\log_{10}(S2/S1)$-$S1$ in Run 9

(e) $\log_{10}(S2/S1)$-$S1$ in Run 10

(f) $\log_{10}(S2/S1)$-$S1$ in Run 11

Figure 2.14: The spatial and signal distributions of events within $S1$ and $S2$ range cuts for (a) Run 9, (b) Run 10 and (c) Run 11 with events outside the FV. Only the final candidates in the DM search data are shown on the signal distributions for (d) Run 9, (e) Run 10 and (f) Run 11. The ten most likely DM candidates are labeled. References of the ER band median (blue solid line) and NR band median (pink solid line) are shown in the signal distributions. The magenta lines are the boundaries of the acceptance window. The solid and dotted magenta lines are the 99.99% NR and 99.9% ER acceptance cuts, respectively. The dashed magenta line is the $S2 = 100$ PE boundary. The dashed grey curves represent the equal-energy curves in nuclear recoil energy (keV_{nr}).

	ER	Accidental	Neutron	Surface	Total fitted	Total observed
Run 9	381.5	2.20	0.77	2.13	387 ± 23	384
Below NR median	2.7	0.46	0.37	2.12	5.6 ± 0.5	4
Run 10	141.7	1.08	0.48	2.66	145.9 ± 16	143
Below NR median	1.7	0.24	0.22	2.65	4.8 ± 0.6	0
Run 11, span 1	216.5	1.04	0.60	6.24	224 ± 22	224
Below NR median	4.2	0.32	0.32	6.22	11.1 ± 1.1	13
Run 11, span 2	448.2	1.60	0.92	9.58	460 ± 35	469
Below NR median	8.26	0.50	0.50	9.54	18.8 ± 1.7	21
Total	1187.9	5.9	2.77	20.6	1217 ± 60	1220
Below NR median	16.8	1.52	1.42	20.5	40.3 ± 3.1	38

Table 2.6: The best fit total and below-NR-median background events in Run 9, Run 10 and Run 11 in the FV with the signal model $m_\chi = 400$ GeV/c^2. The BNM backgrounds are estimated with the PDFs.

2.3 R&Ds in the PandaX-II finale

The schedule at the end of PandaX-II phase is presented in Fig. 2.16. Some of the hardware R&Ds results have been published, including developments of injected calibration sources (^{83m}Kr [157] and ^{220}Rn [27]) and a study on detector responses under different drifting electric fields [28]. The unpublished work includes runs with low-gain PMTs for a better energy resolution in MeV scale, the removal of CH_3T after injection and a study of ^{222}Rn emanation of the circulation system in PandaX-II. During this period, some other hardware preparations for PandaX-4T upgrade are not discussed in this thesis but listed in Fig. 2.16 such as new circulation pumps, a new trigger board and a study on the cross talks among the PMTs.

2.3.1 End-of-run calibration campaign

Internal calibration sources are important to calibrate the uniformity of detector responses, especially for ton-scale LXeTPCs.

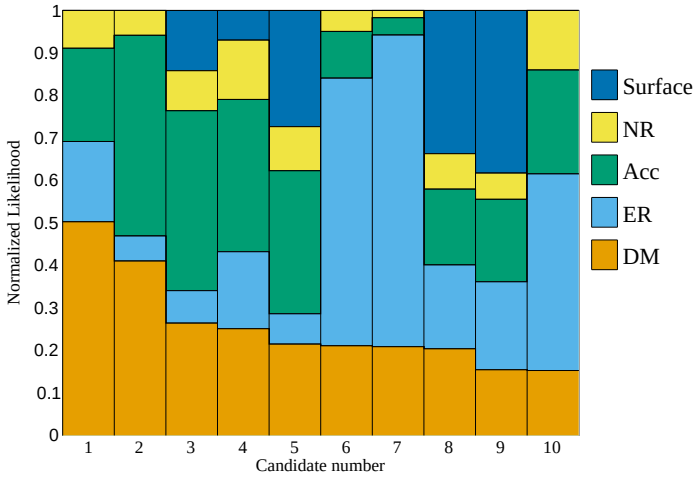

Figure 2.15: The normalized likelihoods of the most likely DM events for $m_\chi = 400$ GeV/c^2.

2.3.1.1 ^{83m}Kr calibration

^{83m}Kr was developed at the beginning of this century as a synthetic calibration source, and has been widely used in different experiments nowadays for calibration in the keV-scale energy window. But while we started to prepare for ^{83m}Kr sources for PandaX, there was no easy access in China. We followed the previous work [158] to generate and store the ^{83}Rb/^{83m}Kr sources first with 3.5 MeV proton beams and then 20 MeV. As there was no available yield data of 3.5 MeV protons bombarding on natural Kr ($^{\mathrm{nat}}$Kr) for ^{83}Rb generation, we published the work as a procedure to prepare very safe and soft-radioactive ^{83}Rb/^{83m}Kr sources with the yield measured, which agrees with a phenomenological extension from higher proton energy data. More details are presented in chapter 3.

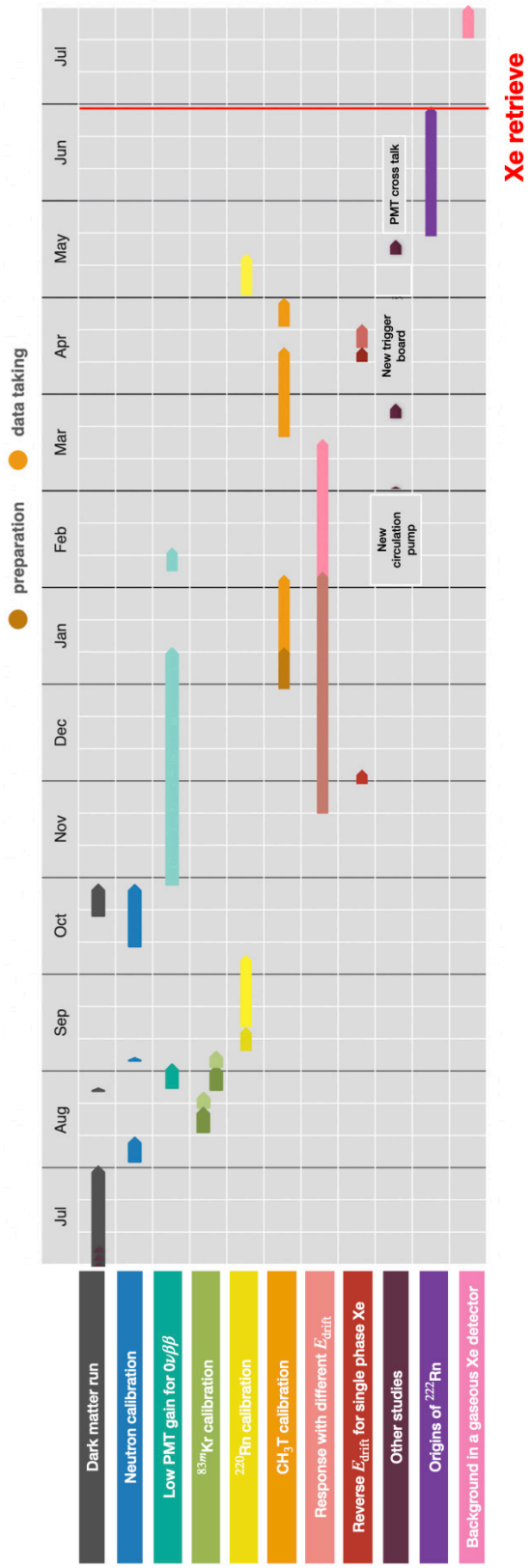

Figure 2.16: The schedule of the R&Ds and calibration data taking in the last running year of PandaX-II.

2.3.1.2 ^{220}Rn calibration

^{220}Rn provides electron recoiling (ER) calibration for LXeTPCs spreading very large energy range, serving for detector calibration from keV to MeV scale as shown in Tab. 2.7 [27]. In the energy threshold of LXeTPC (below 20 keV$_{ee}$), the continuous β-decay mainly from ^{212}Pb in the chain can be fairly taken as a uniform distribution as shown in Fig. 2.17. Moreover, the MeV-scale signals are important to validate the dark matter search detector for the $0\nu\beta\beta$ search.

Isotope	^{220}Rn	^{216}Po	^{212}Pb	^{212}Bi	^{212}Po
Half-life	55 s	0.14 s	10.6 h	61 m	299 ns
Decay mode	α	α	β	β (64.1%)	α
E (α) or Q-value [MeV]	6.288	6.778	0.574	2.254	8.784

Table 2.7: Decay data of ^{220}Rn and its progenies.

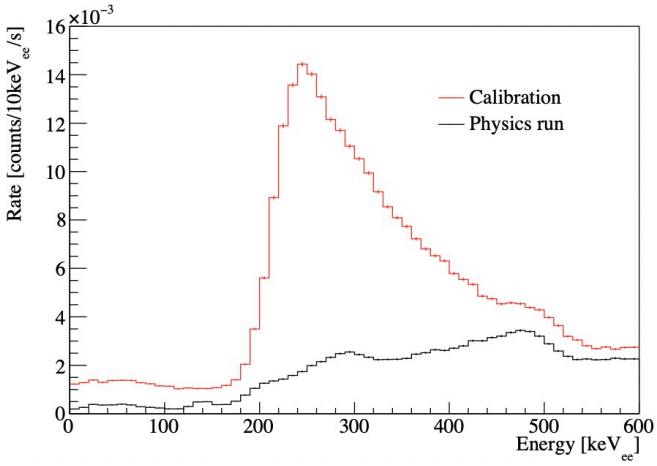

Figure 2.17: The wide energy spectrum of ^{220}Rn calibration data (red) compared to the data for the dark matter runs (black) [27].

An ideal ^{220}Rn source is expected to introduce a significant amount of ^{220}Rn with durable amount of ^{222}Rn ($T_{1/2} = 3.8$ day) contamination. Three different ^{228}Th-based sources are tested with the PandaX-II detector (Tab. 2.8), among which the tungsten electrodes and lantern mantles

both satisfy the ^{222}Rn contamination requirement, and can be commercially prepared easily. The filtration has been verified to avoid thorium particulate contamination with a 0.4 μm-rated gasket-type filter and a 3 nm-rated filter mounted at the downstream of the source chamber, and a 0.4 μm-rated filter at the upstream.

Campaigns	2017	2018	2019
Thoriated Source	Tungsten electrodes	Lantern mantles	Coated resin
Duration [days]	35	20	2.1
Live Time [days]	18.9	11.9	1.3
Injected ^{220}Rn [Bq]	2.521 ± 0.001	31.7 ± 0.3	45.5 ± 0.2
Injected ^{222}Rn [Bq]	$(1.60 \pm 0.02) \times 10^{-2}$	0.28 ± 0.04	6.1 ± 0.1
^{220}Rn from thorium particulate [μBq/kg]	0.20±0.03	-0.01±0.06	

Table 2.8: Overview of the ^{220}Rn calibration sources.

2.3.2 Different drifting electric fields in a large TPC

A high drifting electric field ($>$ 1 kV/cm) is preferred to avoid the marginal effect at the boundary of the TPC for a large fiducial volume. However, the growing size of TPC makes it harder to reach such a high drifting electric field with the cathode high voltage (HV) often limited up to -50 kV. The three drifting electric fields tested besides zero cover 317 V/cm (PandaX-II), 81 V/cm (XENON1T) and 180 V/cm (LUX) in Ref. [28]. The data taken to study the detector responses include 9.4 keV$_{\rm ee}$ (^{83m}Kr), 32.1 keV$_{\rm ee}$ (^{83m}Kr), 41.5 keV$_{\rm ee}$ (^{83m}Kr), 164 keV$_{\rm ee}$ (^{131m}Xe) and 236 keV$_{\rm ee}$ (^{129m}Xe and ^{127}Xe). Their light yields under different drifting electric fields in the unit of photons/keV$_{\rm ee}$ are compared to NESTv2.1.0 and other works in Fig. 2.18. The uncertainties in Fig. 2.18 are mainly related to PDE which converts the observable $S1$ to photon numbers. The spatial non-uniformity in the detector response can be traced by the ^{83m}Kr injection

data as shown in Fig. 2.19 where the marginal effect starts to be non-negligible below 100 V/cm.

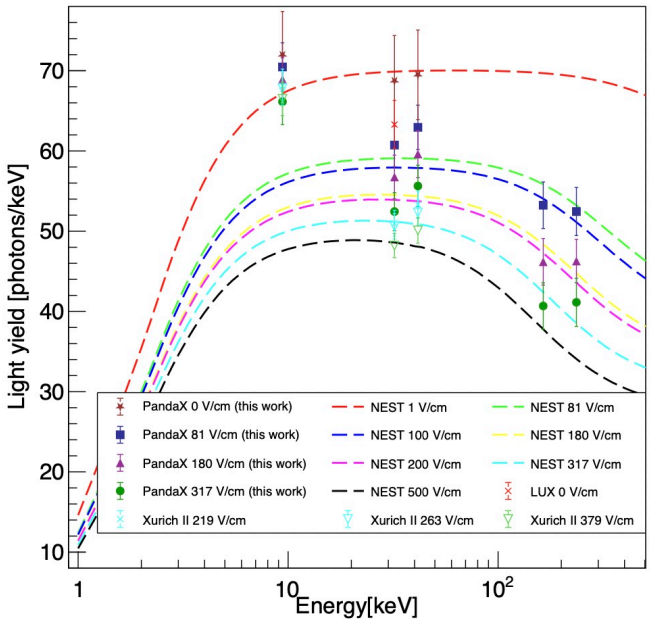

Figure 2.18: Light yields measured by PandaX-II detector under different drifting electric fields and different energy depositions compared with other works [28].

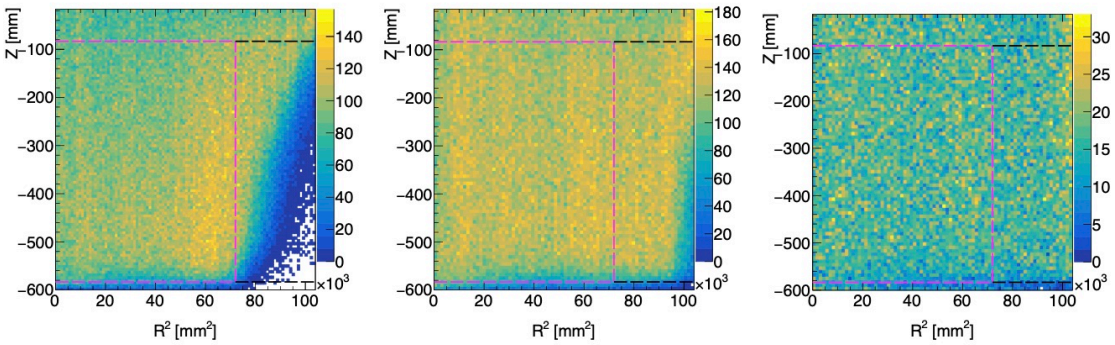

(a) 81 V/cm (b) 180 V/cm (c) 317 V/cm

Figure 2.19: The ^{83m}Kr event distribution under different drifting electric fields ($Z_T = 0$ corresponds to the liquid-gas interface) [28]. The magenta dashed lines mark the fiducial volume for the dark matter search in PandaX-II. For clarification, the R^2 refers to the horizontal position at the anode.

2.3.3 Low gain in PMTs for ER signals in MeV

Hamamatsu R11410 3-inch PMTs are specifically designed for LXeTPCs to collect 178 nm scintillation photons, and the materials have been screened for a low radioactivity. The normal voltages over PMTs are optimized for responses in keV scale, and will have saturation effects for energy depositions over about 200 keV_{ee} where the waveforms are distorted (yellow line in Fig. 2.20). For even higher energy depositions, digitizer saturation also appears with a truncation (black line in Fig. 2.20).

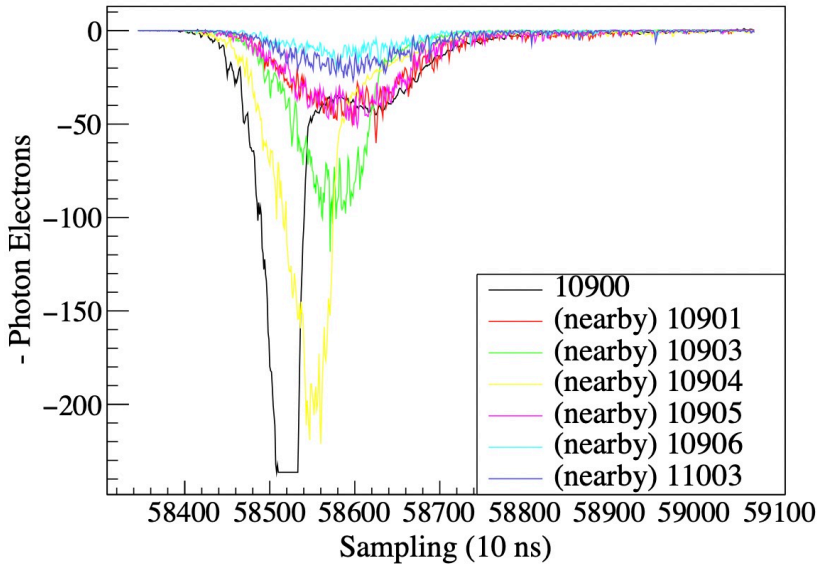

Figure 2.20: Examples of saturated and normal waveforms of PMTs. Yellow line: an asymmetric waveform due to PMT saturation. Black line: an asymmetric waveform with digitizer truncation. The others are norm waveforms [29].

Lowering down the voltages applied on PMTs leads to lower gains that are beneficial for signals in MeV range like the $0\nu\beta\beta$ search. In PandaX-II data taking, the threshold of the single photoelectron (SPE) is set at 20 ADC, which corresponds to 0.4 SPE in Run 9 and 0.6 SPE in Run 10 for the voltages of PMTs tuning down gradually over time to avoid discharges [34]. In

Run 11, 20 ADC is still preserved as the threshold but corresponding to various SPE for different PMTs.

The lowest averaged gain reached for the PMTs in this R&D is 7 ADC/PE, which only presents a slightly better energy resolution if no extensive efforts are put in. The energy resolution of ^{208}Tl at 2615 keV reduces from 6.95% to 6.45%. Later studies reveal that a better energy resolution can be reached after optimizing the lower-level data processing including the clustering algorithm and desaturation of the waveforms with rising edge of the $S2$.

The $0\nu\beta\beta$ search with PandaX-II data was published without lowering gains in PMTs [29] which puts a lower limit (90% C.L.) on the $0\nu\beta\beta$ decay half-life of ^{136}Xe as 2.4×10^{23} yr, corresponding to an upper limit an effective Majorana neutrino mass $m_{\beta\beta} < (1.3 - 3.5)$ eV/c^2.

2.3.4 CH_3T calibration

CH_3T was first injected into PandaX-II detector at the end of Run 9, which became one major ER background afterwards. The Getter (hot purifier) with a hydrogen removal unit at the downstream was expected to remove CH_3T to negligible level but failed to. In PandaX-II, a tritium removal compaign was done with the distillation of xenon and a nitrogen flushing of the detector heated up to 80°C. The total ER backgrounds below 10 keV$_{ee}$ were reduced by half.

The goal of this R&D is to keep the contamination of CH_3T calibration lower than 0.1 μBq/kg in the PandaX-II detector by loading methane (CH_4) before injecting CH_3T and extracting liquid xenon for more efficient purification. Figure 2.21 sketches the circulation for methane and tritiated methane. As shown in Fig. 2.22, methane was first injected into detector to coat the surface of the tubes and vessels. The amount of CH_4 was monitored with xenon samples extracted

out which measured by residue gas analyzer (RGA). However, the first group of tritium injected was not fully reduced to the required level by directly monitoring the total event rate in the low energy window. Also the two later methane injections clearly brought more tritium into the detector, especially the second jump in May, 2019 (Fig. 2.22).

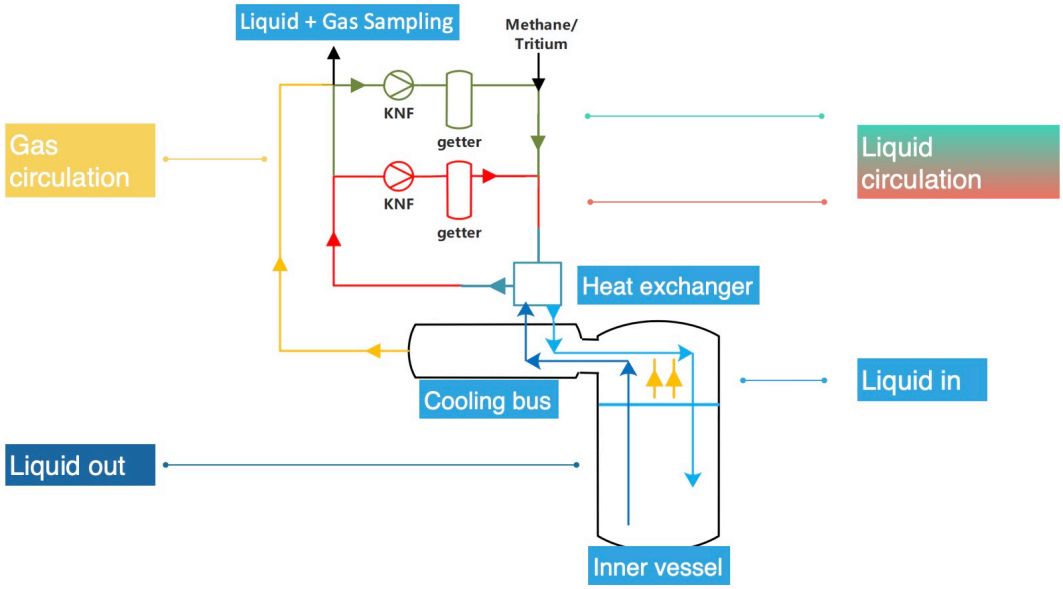

Figure 2.21: The schematics of the circulation of the CH_3T calibration R&D.

At least we learned that methane cannot protect the surface from absorbing CH_3T, and liquid circulation doesn't dramatically enhance the tritium removal ability. Several scenarios may explain the residue tritium after calibration which are not tested, including the possible dead corners with trapping tritium or the purification of tritium with the Getter reaching equilibrium. We observed that tritium dropped by itself while no circulation was on after mid-May, 2019 (Fig. 2.22), which means tritium started to separate in the liquid and gas spontaneously. After turning circulation back on, a more-than-one-order drop of the low-energy event rate was observed (Fig. 2.23), which means Getters are effective in reducing tritium but not enough.

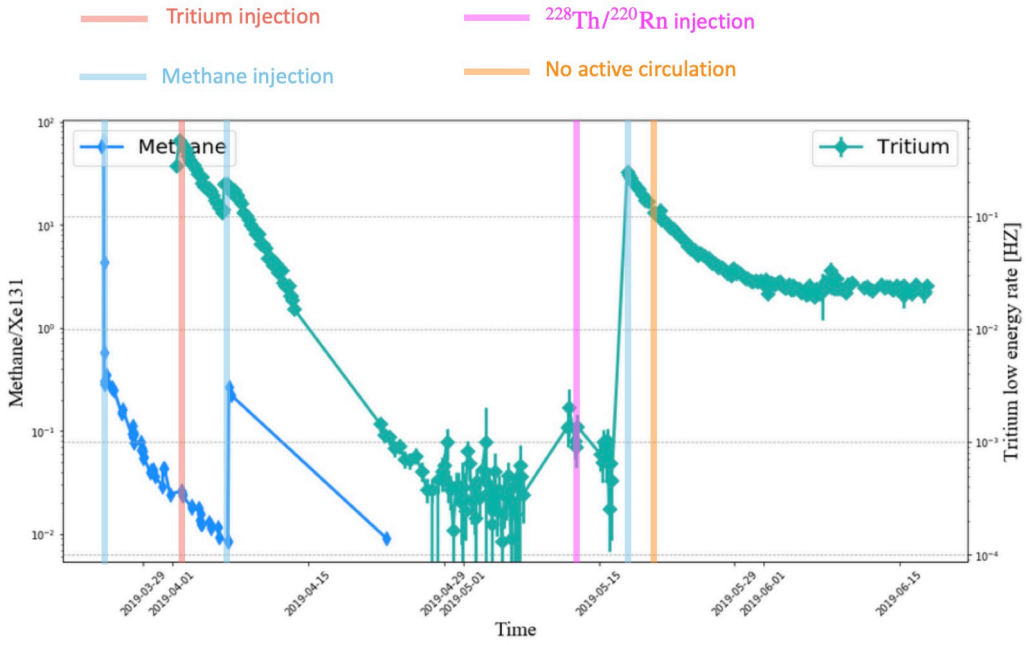

Figure 2.22: The time evolution of methane (blue, monitored by RGA) and tritium (green, monitored by the low energy event rate). The thoron calibration refers to ^{228}Th/^{220}Rn sources injected into the detector.

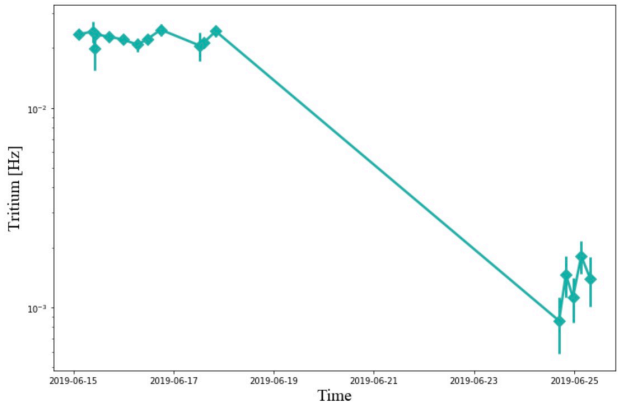

Figure 2.23: The time evolution of tritium after turning the circulation with hot purifiers on again.

2.3.5 ^{222}Rn without active circulation

The daughters of ^{222}Rn are expected to be the major ER backgrounds in PandaX-4T. Recent studies reveal that radon out-gassing highly depends on the temperature, which is naturally suppressed under a low temperature [159]. Figure 2.24 tracks the change of ^{222}Rn with ^{214}Bi-

^{214}Po (β-α) coincidence, where the the extremely high starting radioactivity was from the injected ^{228}Th/^{220}Rn source (magenta line marked in Fig. 2.22). Cooling bus was still working with an estimated flow rate 10 SPLM. The stable radioactivity of ^{222}Rn tracked by ^{214}Bi-^{214}Po was only about one-third of the average Run 11 level, which verified the argument that components under room temperature were the major ^{222}Rn sources. Last but not least, the electron lifetime was amazingly kept over 1 ms during the one-month silent run.

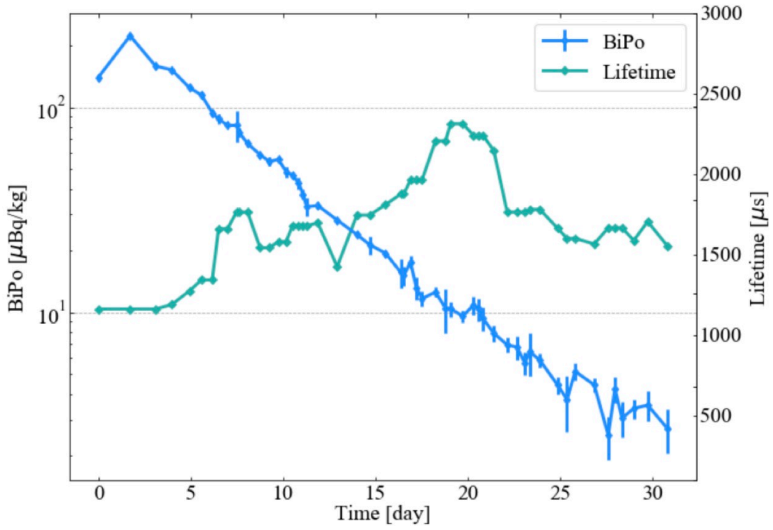

Figure 2.24: The time evolution of ^{222}Rn tracked with ^{214}Bi-^{214}Po and the evolution of electron lifetime after stopping the active circulation in PandaX-II.

Chapter 3: ^{83}Rb/^{83m}Kr calibration for PandaX detectors

Since the recoil energy of the xenon atoms in the interaction with 100 GeV/c^2 WIMPs is mostly below 10 keV$_{ee}$, it is very important to calibrate the detector response in this low-energy range. In the PandaX-I project [160], ^{60}Co and ^{252}Cf sources outside the detector were used to calibrate the low-energy electron recoils (ERs) and nuclear recoils (NRs). While the detectors become larger and larger, the non-uniformity of the spatial response should be considered seriously. Gaseous calibration sources which generate spatially uniform distribution in the detector are preferred. Tritium ($T_{1/2} = 12.3$ y) carried by tritiated methane was used to calibrate the ERs in PandaX-II [161], but there were problems in removing it completely. Gammas of activated xenon are also used to calibrate the detector uniformity. However, these gammas have energies over 100 keV$_{ee}$, and the gammas in the neutron calibration runs are mixed with NR events. We need to find better sources to do the spatial calibration for future detectors.

^{83m}Kr ($T_{1/2} = 1.83$ h) is an ideal source to calibrate the spatial response in liquid xenon (LXe). It has a long enough half-life such that we can inject it into xenon uniformly. On the other hand, the half-life of ^{83m}Kr is short compared with the detector operation time, so the source only has a short-term effect on the detector. Moreover, the isotope has energy peaks less than 100 keV$_{ee}$, which is close to the energy range we are interested in.

^{83m}Kr has been used as a calibration source for different experiments in recent years, such

as tritium β decay experiments [162], electron-positron colliders [163] and a heavy-ion detector, ALICE, at CERN [164]. An experiment at Yale University reported the first use of ^{83m}Kr in the in liquid noble element detectors for spatial and energy calibration [165, 166].

Since ^{83m}Kr is short-lived, one has to use the mother isotope, ^{83}Rb ($T_{1/2} = 86.2$ day), to make sources, which decays into the excited energy levels of ^{83}Kr through pure electron capture. ^{83}Rb can be synthesized by protons bombarding on krypton or α-particles on bromine. $^{\mathrm{nat}}$Kr(p, xn)^{83}Rb is preferred because it yields fewer unwanted radioactive isotopes.

According to the safety requirement and the accessibility of proton beams, we tried to produce ^{83}Rb with a 3.4 MeV proton beam at the threshold of $^{\mathrm{nat}}$Kr(p,xn)^{83}Rb, even though the experimental data on the reaction below 5 MeV did not seem to exist. The radioactivity level of ^{83m}Kr in PandaX-II detector is the best at several tens Bq during calibration. This intensity can provide several hundred thousand events within one day, which is statically enough for the correction of the spatial response. Meanwhile, the activity is low enough to sustain a high trigger efficiency of the data acquisition system. Because the half-life of ^{83m}Kr is long enough compared with the time in the pipes before entering the detector, we expect that a significant amount of ^{83m}Kr decays inside the detector. Moreover, 74% of the ^{83}Rb decays produces ^{83m}Kr, and therefore, a ^{83}Rb source on the level of several hundred Becquerel should be sufficient.

^{83}Rb is a synthetic radioisotope that can be produced by proton beams bombarding natural krypton with peak production rate at around 20 MeV proton energy. Due to limited access to such a high energy proton facility in China, a lower energy proton beam was used first. We successfully produced ^{83}Rb/^{83m}Kr with the 3.4 MeV proton beam at the China Institute of Atomic Energy, and reported the first measurement of the yield of the $^{\mathrm{nat}}\mathrm{Kr}(\mathrm{p},\mathrm{xn})^{83}$Rb reaction for proton energy below 5 MeV. Another production performed with a recently available 20 MeV proton beam at

the Institute of Modern Physics, Chinese Academy of Sciences is discussed in this chapter as well.

The injection test of ^{83}Rb/^{83m}Kr in the PandaX-II detector was carried out in the R&D stage at the end of PandaX-II. A calibration module is constructed to induce the radioactive gas into PandaX-II detector. The rubidium carried zeolite source is put in a chamber mounted with filters, which is implemented in the circulation loop of the PandaX-II detector.

It is important to make sure that the injection of ^{83m}Kr does not contaminate the detector. Rubidium isotopes, including ^{83}Rb, ^{84}Rb and ^{86}Rb, will cause low energy ERs for months if they enter the detector. Moreover the zeolite carries electronegative gases that may affect the electron lifetime in xenon for days as reported by [167]. Our calibration module succeeds in inducing ^{83m}Kr into the sensitive volume during calibration, and no significant contaminations were noticed. The upper limit of the ^{83}Rb leakage is 5 μBq/h at the 90% confidence level (C.L.). No significant drop of the electron lifetime has been observed.

This chapter is largely follows the publications [157] where the author is one major contributor. The bombarding chamber design and experiment setup to produce ^{83}Rb/^{83m}Kr with 3.4 MeV and 20 MeV proton beams are demonstrated in section 3.1 and 3.2, respectively. The contamination tests before the first injection are described in section 3.3. Some short analyses with the ^{83m}Kr events are presented in section 3.4 including the energy spectrum and half-life as well as the contamination evaluation.

3.1 Production of ^{83}Rb/^{83m}Kr with 3.4 MeV protons

In this section, we describe the generation of ^{83}Rb/^{83m}Kr by the 3.4 MeV proton beam at the China Institute of Atomic Energy, although no data with proton energy lower than 5 MeV for $^{\mathrm{nat}}$Kr(p, xn)^{83}Rb is found in the literature. We first present our theoretical expectation on the yield. Then we describe the design of the target cells in details. Following this, we report the storage and measurement. Finally, we compare the measured yield of $^{\mathrm{nat}}$Kr(p, xn)^{83}Rb with our theoretical analysis.

3.1.1 Theoretical consideration

$^{\mathrm{nat}}$Kr(p, xn)^{83}Rb data reported before have proton energy higher than 5 MeV. As the theoretical energy threshold for the reaction ^{83}Kr(p,n)^{83}Rb is 1.7 MeV, it is possible to produce useful ^{83}Rb/^{83m}Kr sources with the 3.4 MeV proton beam.

According to the textbook [168], the cross section near the reaction threshold is proportional to the velocity of the proton. But the data don't fit the simple theory, so we relax the power of the proton velocity as a new fitting parameter to extend the former work to the range under consideration. The fitting of the $^{\mathrm{nat}}$Kr(p, xn)^{83}Rb yield is based on the data in [30, 31, 32] using the function $y = a \cdot (E - E_{th})^b$, where y is the yield, E_{th} is the threshold of the proton energy, and a and b are fitting parameters. This work is also overlain on Fig. 3.1 which will be discussed later. According to the analysis, 1 μA protons bombarding on 1 bar natural krypton for several hours can generate several hundred Becquerel ^{83}Rb.

Besides ^{83}Rb, the appearance of ^{86}Rb ($T_{1/2} = 18.6$ d) is also expected because the threshold of the proton energy for ^{86}Kr(p,n)^{86}Rb is 1.3 MeV. Based on the data in [30, 31], we expect the

thick target yield of ^{nat}Kr(p, xn)^{86}Rb with 3 MeV protons is in the range [0.17, 1.6] MBq/C.

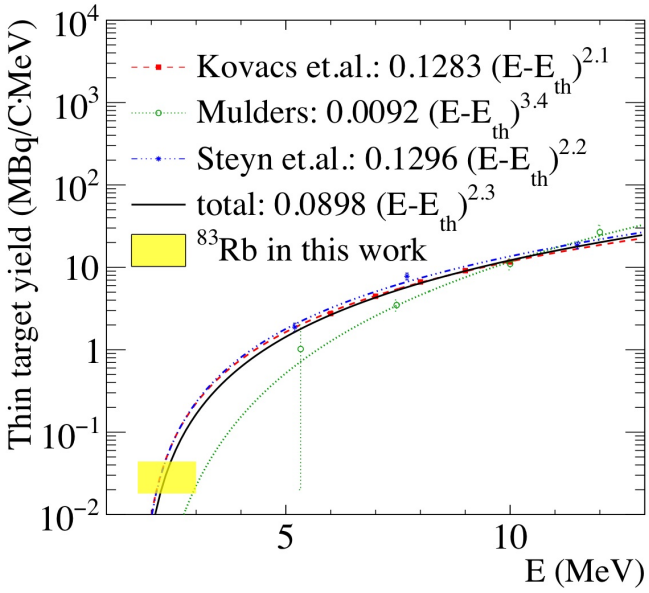

Figure 3.1: This measurement compared to the theoretical extensions on the yields of proton beams bombarding on 1 bar ^{nat}Kr according to former works [30, 31, 32] for ^{83}Rb. The lines are fitted with the function $y = a \cdot (E - E_{th})^b$, where y is the yield, E_{th} is the threshold of the proton energy with a unit of MeV, and a and b are fitting parameters.

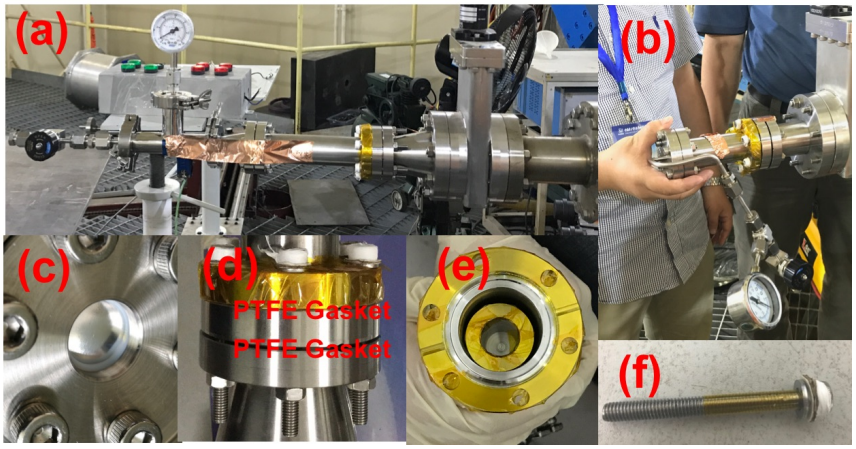

Figure 3.2: (a) The whole view of the first ^{nat}Kr chamber. (b) The whole view of the second ^{nat}Kr chamber. (c) The Al window. (d) The positions where we used PTFE gaskets to electrically insulate the ^{nat}Kr chamber (the middle flange is the Al window) (e) The inner Al dump with Kapton tape wrapped to avoid possible activation of stainless steel. (f) The wrapped bolt and the paper gasket to insulate the ^{nat}Kr chamber.

3.1.2 Design of the target cells

In this work, two target cells are prepared for the proton beam bombardment (Fig. 3.2). The first one is studied in detail in the next subsection and the other serves as the calibration source to be used in section 3.3. The details of the target cell design are presented here.

(I) We use a 20 μm aluminum (Al) foil as the window to separate the gas and vacuum based on the work in [158]. The diameter of the window is chosen to be 10 mm, which prevents the foil from breaking due to the force on the edge. This design is able to hold at least 1.5 bar pressure drop.

(II) In order to monitor whether the beam hits on the Al foil, the current of the $^{\mathrm{nat}}$Kr chamber to the ground during the bombardment is measured, which requires the $^{\mathrm{nat}}$Kr chamber to be insulated to the upstream part. We used polytetrafluoroethylene (PTFE) gaskets to seal the CF35 flanges instead of copper gaskets. Moreover, the bolts and the flange are wrapped by Kapton tape (Fig. 3.2(e)). We use paper gaskets to insulate the stainless steel (SS) bolts and the flange, as shown in Fig. 3.2(f).

(III) The Al foil may be potentially melted due to the energy deposition of the proton beam. The heat effect was estimated to check whether water cooling is needed . According to the stopping power of proton in Al provided by PSTAR [33], 3.4 MeV proton beam deposits 0.4 MeV in 20 μm Al. A conservative heat estimation is done by considering the conduction of the heat. Assuming a 10 μA proton beam with a 2 mm diameter and 300 K room temperature boundary condition, the equilibrium temperature at the center of the Al foil is 360 K, which is far below the working temperature limits of both PTFE and Al. Hence a simple target cell without water cooling is enough.

(IV) To determine the length of the target cell, we calculate the effective penetration length of the proton beam in $^{\mathrm{nat}}$Kr, with the stopping power $\frac{dE}{dx}$ from PSTAR [33]. The effective reaction length is calculated by taking the numerical integral

$$L_{\mathrm{eff}} = \int_{1.7\ \mathrm{MeV}}^{3\ \mathrm{MeV}} \frac{dx}{dE} dE = 5.2\ \mathrm{cm}. \tag{3.1}$$

Hence the target cells with 10 cm are long enough.

(V) An Al dump is put in the target cell (Fig. 3.2(e)) to avoid activation of the stainless steel. The smaller the atomic mass of the dump element is, the fewer the products are generated during the bombardment. Also Al has a higher thermal conductivity compared to SS. The side close to the window for the Al dump is insulated by Kapton tape.

The beam bombardment was taken place on Jun 20, 2018 from 9:50 am to 10:29 am for the first chamber and from 12:05 pm to 15:00 pm for the second one . Both had 1 bar krypton gas inside. The average proton current was 1.5 μA for the first cell, and 1.6 μA for the second. The operation was stable.

3.1.3 Preparation and measurement of the ^{83}Rb/^{83m}Kr sources

After the bombardment, the target cells were exposed to air before further processing to ensure the rubidium was fully oxidized. The first cell has three parts: the Al window (include the foil and the flange), the Al dump, and the CF35-straight tube. Different parts of the first target cell were washed by 60 ml to 150 ml deionized water separately, to study the distribution of the ^{83}Rb produced. Zeolite beads (Merck 2 mm diameter, 0.5 nm molecular sieve) were used to absorb rubidium in each solution. The solutions were gently heated in water bath at 70$\sim$80°C

until dried. Then the zeolite was baked at 300°C under pumping for further degassing. It was finally stored in a sealed plastic bag (Fig. 3.3).

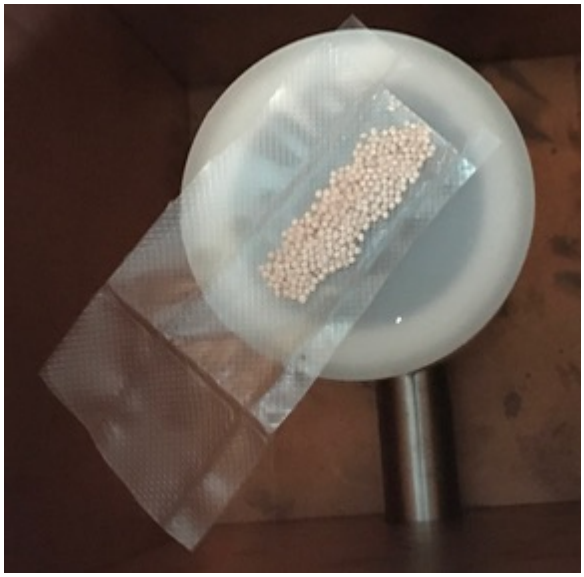

Figure 3.3: The storage of the baked zeolite.

After being degassed, the zeolite samples were measured by a germanium detector at Shanghai Jiao Tong University which moved to CJPL later (JP-II). The spectra of the samples are shown in Fig. 3.4, and compared with the MC simulation done by the GEANT4 package [169]. The radioactivity estimated from each sample is listed in Tab. 3.1. The uncertainty of our measurement is dominated by the detector efficiency of the detector, which is highly geometry-dependent. Compared with the systematics, the statistical uncertainties are minor (generally 5%).

By measuring the gamma peaks of each part before and after washing, we determine the transfering efficiency is (66±2)% for the Al window, (83±6)% for the Al dump, and (92±1)% for the CF35-straight tube.

The rubidium distribution in Al window, Al dump and CF35-straight tube when generated was separately $100:13:20$ for ^{83}Rb, $100:23:19$ for ^{84}Rb, $100:12:18$ for ^{86}Rb (the decay

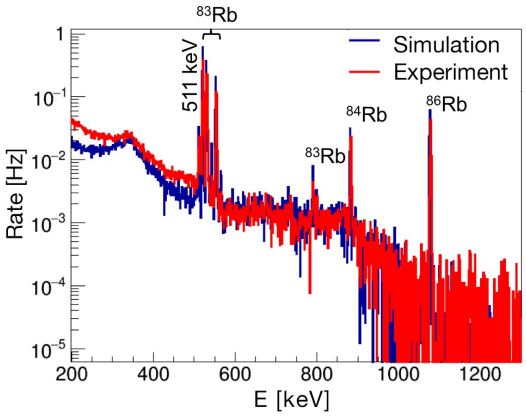

(a) Sample 1 spectrum

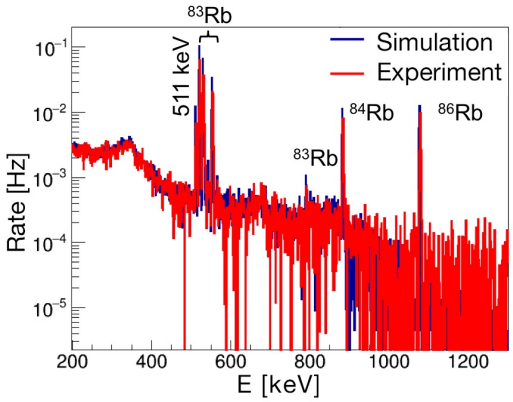

(b) Sample 2 spectrum

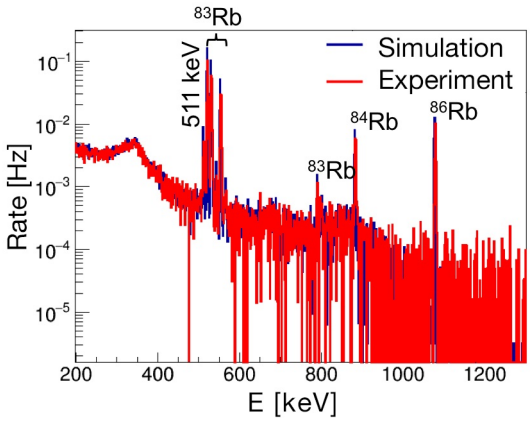

(c) Sample 3 spectrum

Figure 3.4: The comparison between the simulation and the measurement for different zeolite beads samples. Sample 1, sample 2, sample 3 absorbs rubidium from the Al window, the Al dump and the CF35-straight tube respectively.

Table 3.1: The radioactivity of the three zeolite samples on the date when they were measured.

Isotope	Al window (Bq) (Jul 30 12 PM)	Al dump (Bq) (Jul 18 12 PM)	CF35-straight tube (Bq) (Jul 31 12 PM)
^{83}Rb	53.4 $\pm$ 2.7	9.5 $\pm$ 0.4	14.7$\pm$ 0.6
^{84}Rb	3.68 $\pm$ 0.14	1.35 $\pm$ 0.06	0.95 $\pm$ 0.05
^{86}Rb	62.6 $\pm$ 1.7	15.2 $\pm$ 0.6	15.3 $\pm$ 0.6

of the isotopes has been considered). According to the data, the rubidium was mainly produced near the Al window.

To calculate the yield for the rubidium isotopes, the radioactivity of each zeolite sample in

Tab. 3.1 is summed and corrected for the half-lifes of the decays and the transferring efficiencies. The total radioactivity generated in the first target cell is 149.2 Bq for ^{83}Rb, 18.3 Bq for ^{84}Rb, and 545.6 Bq for ^{86}Rb, respectively. The charge of the protons used is 3.5×10^{-3} C. Therefore, the thick target yield at 3 MeV (effective energy) proton bombardment is 0.041 MBq/C for ^{83}Rb, 0.005 MBq/C for ^{84}Rb and 0.16 MBq/C for ^{86}Rb.

The comparison between our theoretical analysis and the measurement of the thick target yield for ^{83}Rb is shown in Fig. 3.5. The thick target yield of ^{86}Rb is slightly smaller than the prediction range. We observed ^{84}Rb in the bombardment even though the theoretical threshold of the reaction ^{84}Kr(p,n)^{84}Rb is 3.46 MeV [30, 170]. The protons are accelerated with a tandem pelletron (1.7 MV, Model 5SDH, National Electrostatics Corp.) [171], which has the highest energy of incoming protons as 3.4 MeV with an uncertainty of 1 keV, which is below the theoretical threshold 3.46 MeV. Theoretically, the ^{84}Kr(p,n)^{84}Rb reaction is unlikely to happen in this bombardment.

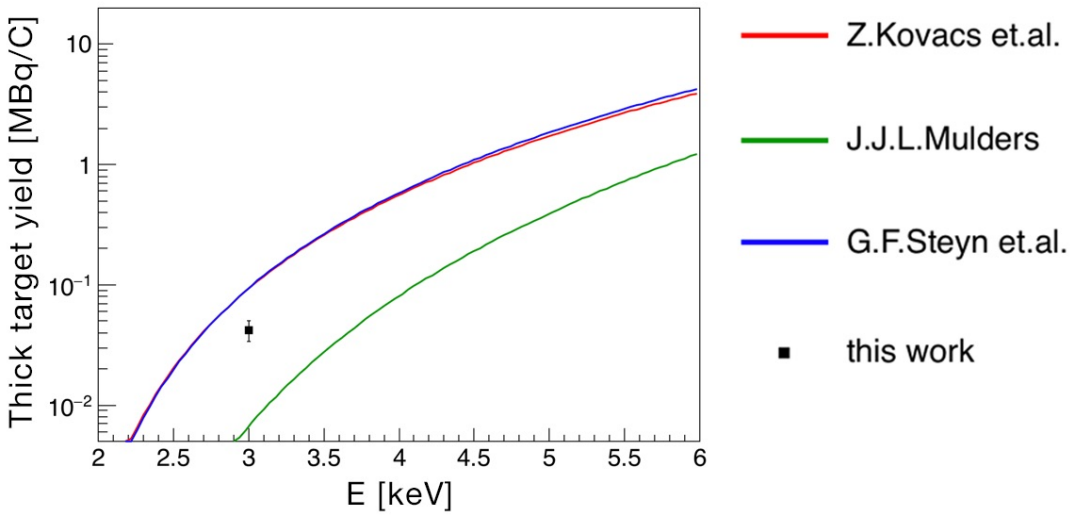

Figure 3.5: The thick target yield integrated for ^{83}Rb. The black point marks our measurement with 3 MeV effective proton energy bombarding on 1 bar $^{\text{nat}}$Kr. The interpretation as the thin target yield can be found in Fig. 3.1

3.2 Production of ^{83}Rb/^{83m}Kr with 20 MeV protons

Sustainable ^{83}Rb/^{83m}Kr sources for three years requires a MBq level radioactivities for the 86 day half-life of ^{83}Rb. Moreover, to minimize the yields of other by-products is preferred. According to the yields of rubidium isotopes for protons bombarding on $^{\mathrm{nat}}$Kr in Fig. 3.6, a proton energy at 20 MeV is the optimized energy to produce ^{83}Rb/^{83m}Kr sources. After the success with 3.4 MeV protons, we were able to convince Chinese ADS Front End demo linac (CAFE) at the Institute of Modern Physics, Chinese Academy of Sciences with proton energy up to 25 MeV to cooperate in the ^{83}Rb/^{83m}Kr sources production.

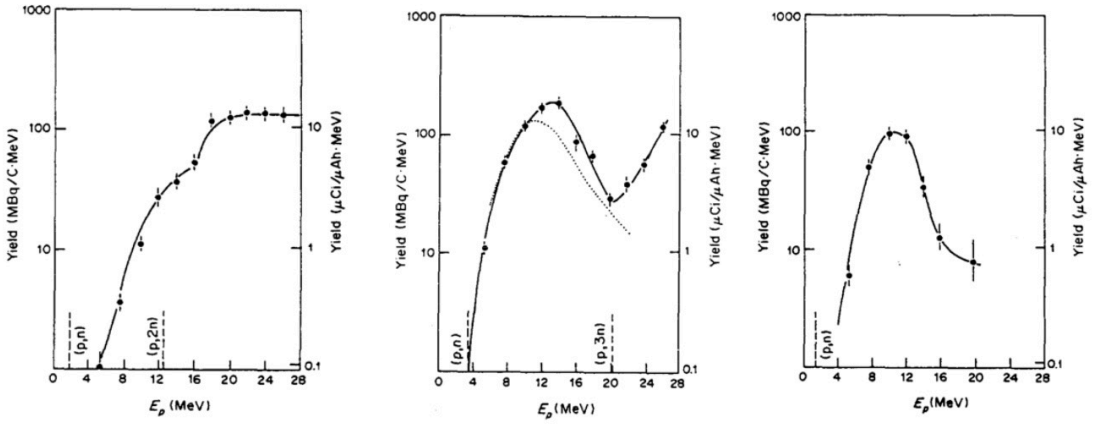

Figure 3.6: The thin target yields of rubidium isotopes with protons bombardments on $^{\mathrm{nat}}$Kr [30, 31, 32]. Plots from left to right are for ^{83}Rb, ^{84}Rb, ^{86}Rb, respectively.

3.2.1 Upgrading consideration

A higher proton energy needs a longer dumper, and more importantly, a more powerful cooling system is potentially needed, which is the main consideration before starting the experiment at CAFE. Following the track of the protons, the Al window, the $^{\mathrm{nat}}$Kr and the Al dumper all need taking care of.

3.2.1.1 Al dump

By putting in the stopping power of the Al, the energy deposited by one proton on the Al foil is

$$\begin{aligned}\Delta E_{\mathrm{Al}} &= \left(\frac{dE}{dx}\right)_{\mathrm{Al}}\Bigg|_{E=20\ \mathrm{MeV}} \cdot \Delta x \\ &= 19.7\ \mathrm{MeV}\cdot\mathrm{cm}^2/\mathrm{g} \times 2.7\ \mathrm{g/cm}^3 \times 20\ \mu\mathrm{m} \\ &= 0.11\ \mathrm{MeV}.\end{aligned} \tag{3.2}$$

Similarly, for a 20 MeV proton, the energy loss going through a 30 cm $^{\mathrm{nat}}$Kr cell under 1 bar is

$$\begin{aligned}\Delta E_{\mathrm{Kr}} &= \left(\frac{dE}{dx}\right)_{\mathrm{Kr}}\Bigg|_{E=20\ \mathrm{MeV}} \cdot \Delta x \\ &= 14.9\ \mathrm{MeV}\cdot\mathrm{cm}^2/\mathrm{g} \times 0.0034\ \mathrm{g/cm}^3 \times 30\ \mathrm{cm} \\ &= 1.5\ \mathrm{MeV}.\end{aligned} \tag{3.3}$$

The energy of the proton stays around 20 MeV after passing through the gas, so it is necessary to put a dumper at the end of the target cell to avoid activation on the SS as discussed above For the Al dump, the minimum length is

$$L_{\mathrm{Al}} = \int_0^{20\ \mathrm{MeV}} \left(\frac{dx}{dE}\right)_{\mathrm{Al}} dE = 0.21\ \mathrm{cm}, \tag{3.4}$$

by using the stopping power from PSTAR as shown in Fig. 3.7.

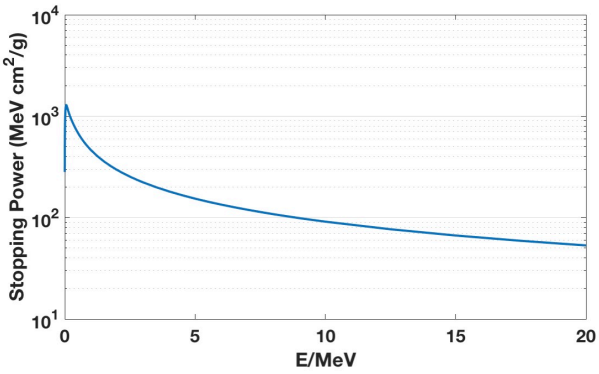

Figure 3.7: The stopping power in Al as a function of the proton energy [33].

3.2.1.2 Heat load

The heat load is estimated with the maximum load of a $f = 50$ Hz proton pulse with $100\ \mu$A and $1000\ \mu$s width of each pulse. The energy deposition on the Al foil for one pulse is

$$\Delta E_0 = 0.11\ \text{MeV} \times 100\ \mu\text{A} \times 1000\ \mu\text{s} = 1.1 \times 10^{-2}\ \text{J}. \tag{3.5}$$

Then the power is $P = f \cdot \Delta E_0 = 5.5$ W. The width of the proton beam σ_r is 1 to 2.5 mm and the thickness of the foil is $d = 20\ \mu$m. The volume carrying the initial head load is $V = \pi d \sigma_r^2 = 4.02 \times 10^{-11}$ to 6.84×10^{-10} m^3. If we only consider the conduction only for the heat diffusion, then the equations at the equilibrium are

$$\begin{cases} K_0 \nabla^2 T + \dfrac{P}{V} = 0, & 0 < r < \sigma_r \\ \nabla^2 T = 0, & r > \sigma_r \end{cases}, \tag{3.6}$$

where $K_0 = 230\ \mathrm{W/(m)}$ is the thermal conductivity of Al. The radial analytical solution is

$$\begin{cases} T(r) = -\dfrac{P}{4K_0\pi d}\dfrac{r^2}{\sigma_r^2} + \dfrac{P}{2K_0\pi d}\ln\left(\dfrac{R}{\sigma_r}\right) + \dfrac{P}{4K_0\pi d} + T_0, & 0 < r < \sigma_r \\ T(r) = \dfrac{P}{2K_0\pi d}\ln\left(\dfrac{R}{\sigma_r}\right) + T_0, & r > \sigma_r \end{cases}, \tag{3.7}$$

where it is assumed that the edge of the Al foil connected to the CF35 flange is at the room temperature $T_0 = 293$ K with a radius $R = 10$ mm. The highest temperature is at the center of the foil $T(0)$ which is 447 K (392 K) for $\sigma_r = 1\ \mathrm{mm}$ ($\sigma_r = 2.5\ \mathrm{mm}$). The calculation actually says the Al foil is strong enough and won't melt.

However, to ensure everything functioning, CAFE sets a secure increase in temperature as 50 K, which requires external cooling. The 20 MeV proton beam with an average 5 μA current creates a 100 W head load. The convention-only cooling power $\dot{q}$ of the water is

$$\dot{q} = h_c \cdot S \cdot \Delta T, \tag{3.8}$$

where h_c is the convection heat transfer coefficient and S is the contacting surface area. For the Al dump (Al foil), $\dot{q} \approx 100$ (5.5) W and $S_{\mathrm{dump\ (foil)}} = 1.19 \times 10^{-3}$ m^2 requires $h_c > 1680\ (84)\ \mathrm{W/(m^2 \cdot K)}$, which can be easily reached by the adjusting the flow rate up to 400 cm^3/s of the water cooling system at CAFE.

Last but not least, my coworkers at CAFE helped to upgrade the PTFE sealing O ring to indium wire sealing which would have a better heat conductivity.

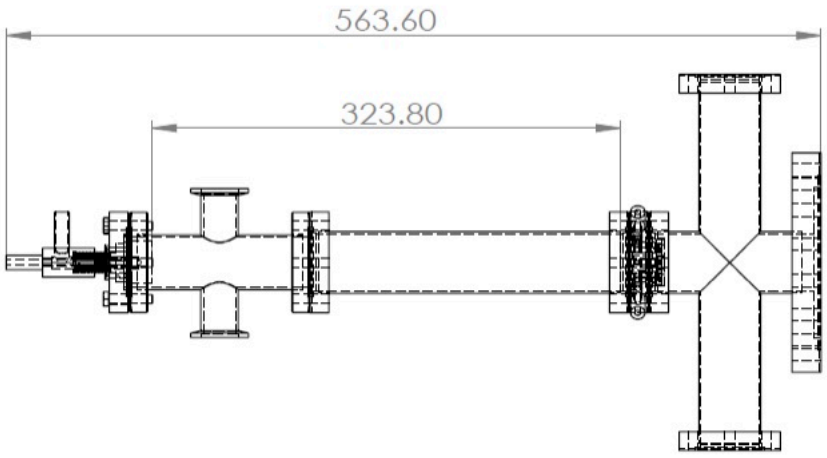

(a)

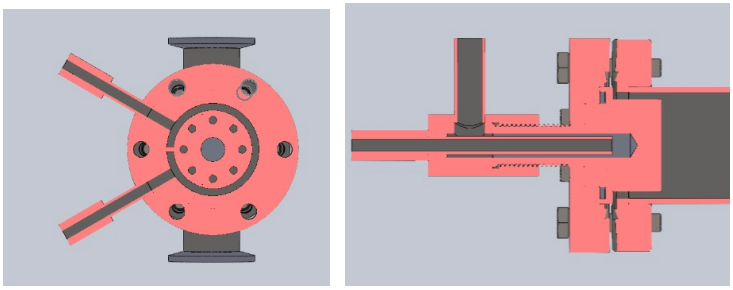

(b) (c)

Figure 3.8: (a) The design (marked size in millimeter) and zoom-in cross sections for (b) the Al window CF35 and (c) the CF35 connected to the Al dump.

3.2.1.3 CAFE target cell

Figure 3.8 shows the final design of the target cell with zoom-in cross sections for the Al foil CF35 holder and the CF35 connected to the Al dump which reveals the water cooling loop. The assembled target cell ready to be connected to the accelerator is shown in Fig. 3.9.

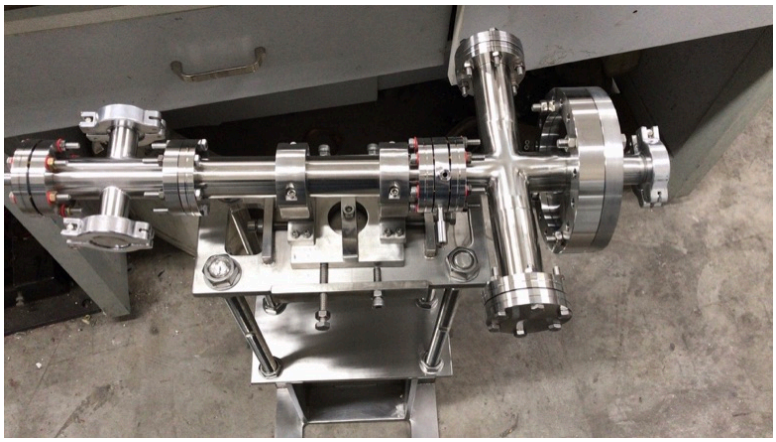

Figure 3.9: The assembled target cell for the 20 MeV proton bombardment.

3.2.2 Production

The experiment at CAFE was carried out on Dec. 2, 2018 to Dec. 7 2018 at CAFE with an average 1 μA 20 MeV proton beams. Multiple ^{83}Rb/^{83m}Kr sources from several kilo to mega Becquerel were obtained in the processing procedure. The Al window and the target chamber were washed by deionized water separately (the chamber was washed three times). The radioactivity ratio of the final zeolite samples is $1^{\text{st}} : 2^{\text{nd}} : 3^{\text{rd}} : \text{window} = 1 : 0.050 : 0.0032 : 0.052$. The transferring efficiency of the main target chamber in one wash was determined to be 90% as before. The strongest ^{83}Rb/^{83m}Kr source obtained is approximately 10 MBq.

The initial proton energy calculated with the time of incident protons flying through a 2.47 m vacuum chamber is 20.37 ± 0.03 MeV. The 1.4 MeV proton energy loss in the 25 cm target cell filled with 1.1 bar krypton gas dominates the energy spread in Fig. 3.10.

We validate the systematic uncertainties by measuring the detecting efficiency of a millimeter-scale source. Compared to the rubidium sources, the cylindrical shaped calibration source with a 3 mm radius and 6 mm height is small enough to be regarded as a point source. The typical size difference among the ^{83}Rb/^{83m}Kr sources is 3 cm. According to the measurements with

the calibration source, a 3 cm horizontal deviation to the surface center reduces the detecting efficiency to 60% and a 3 cm vertical deviation to 40%. Therefore, the systematic uncertainties are set to 60% in Fig. 3.10.

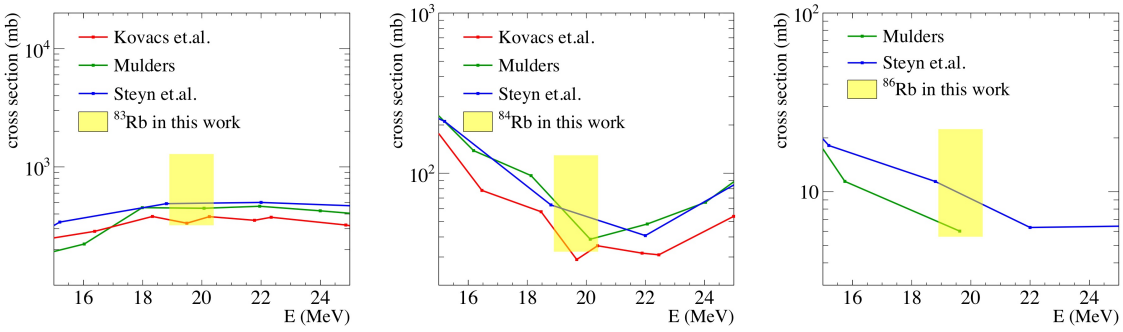

(a) (b) (c)

Figure 3.10: Comparison of the (a) ^{nat}Kr(p, xn)^{83}Rb, (b) ^{nat}Kr(p, xn)^{84}Rb and (c) ^{nat}Kr(p, xn)^{86}Rb cross sections at 20 MeV between this work and previous measurements [30, 31, 32].

3.3 Contamination tests before injection

We made a calibration module, consisting of 30 Bq ^{83}Rb absorbed by 1 g zeolite and a SS chamber with three standard CF35 flange connections with two mounted by 0.2 μm membrane filters (Merck, FGLP01300) for injection, and the other one by a 0.1 mm SS filter for pumping. The location of the module in the PandaX-II circulation loop is shown in Fig. 3.11 and marked with the dash line. There are two by-passes (V14 and V15). One is used for vacuum pumping because both ends of the ^{83}Rb/^{83m}Kr source have 0.2 μm filters. The other is used for by-passing the total calibration module in the LOOP2. The ^{83m}Kr-carried xenon flows into the detector directly after passing the heat exchanger, guided by the blue arrow route in Fig. 3.11.

Two kinds of contaminations can be potentially brought into the detector by the rubidium sources. One is the radioactivity due to rubidium leakage, which can cause ER backgrounds for

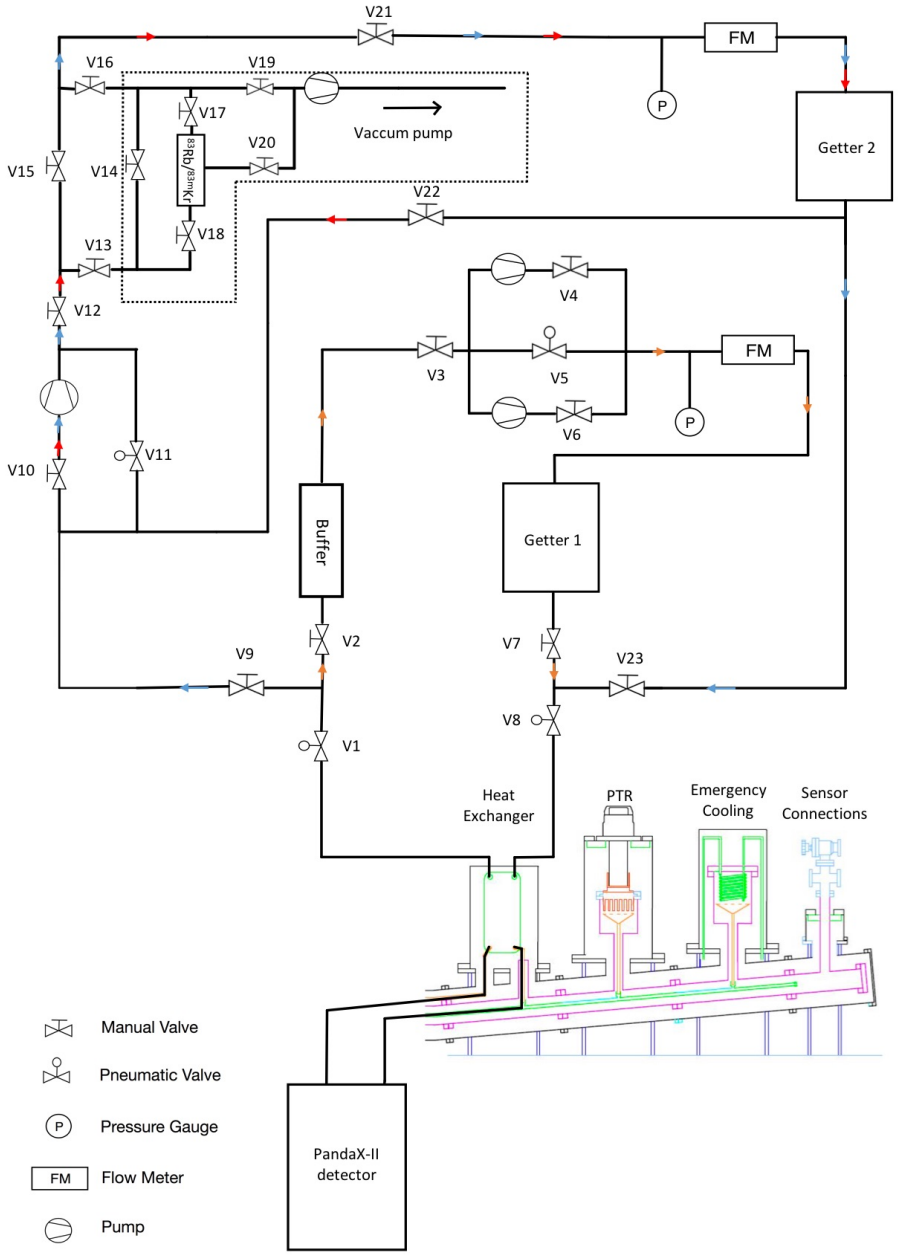

Figure 3.11: The schematic of the purification system for PandaX-II. The orange arrows indicate the purification LOOP1 for daily purification. The blue arrows show the LOOP2 which induces ^{83m}Kr into detector. The red arrows form a self-circulating route in LOOP2, reducing electro-negative gases released by the source before injection with the help of Getter 2. The black dash line marks the calibration module.

months. The other is the electronegative impurities in the zeolite beads, which may result in a significant drop of the electron lifetime in LXe.

To keep the radioactivity contamination in the acceptable range, flushing and vacuuming tests are designed to validate a ten-hour safe injection for the 30 Bq ^{83}Rb source. To prevent a significant drop of the electron lifetime, the residues of zeolite under vacuuming must meet the inlet requirements of the Getter used to purify the electronegative impurites.

3.3.1 Radioactivity contamination test

When xenon passes through the calibration module, it may wash off rubidium atoms, carrying them into the detector, resulting in ER backgrounds. In our recent published paper [34], the total ER backgrounds in the PandaX-II detector in the WIMP search window ($0 \sim 10$ keV) is 0.79 ± 0.16 mDRU ($1\ \mathrm{mDRU} = 10^{-3}$ events/day/kg/keV). We set 0.1 mDRU as the maximum acceptable contamination from ^{83}Rb.

We use a Monte Carlo (MC) simulation program with GEANT4 package to estimate the contamination of rubidium isotopes in the PandaX-II detector. Based on this, we calculated the acceptable level of the calibration module and conducted flushing and vacuuming tests to check.

The PandaX-II detector is breifly summarized here again for a quick view, and more details can be found in Chapter 2. The detector contains a dodecagonal time projection chamber (TPC), which has two arrays of photomultiplier tubes (PMTs), one in the gas phase on the top and the other immersed in the LXe at the bottom. The TPC is surrounded by PTFE walls, inside which there is the sensitive volume of the detector. A typical radioactive event in the LXe generates photons detectable by the PMTs promptly. Ionized electrons drift upward through a vertical electric field (400 V/cm), and produce the second scintillation signal under the extracting electric field (4.4 kV/cm) over the liquid surface. The first scintillation signal is noted as $S1$, and the

ionization signal is $S2$.

The MC simulation program with the PandaX-II detector geometry is used to simulate the energy depositions of the leaked rubidium isotopes. Uniformly distributed ^{83}Rb, ^{84}Rb and ^{86}Rb in the LXe are used in the simulation according to the injection procedure. The energy depositions in the fiducial volume (FV) of the PandaX-II detector are studied, which corresponds to a cocentric cylinder with a height from 3.3 cm to 58.3 cm below the liquid surface and a radius of 268.3 mm.

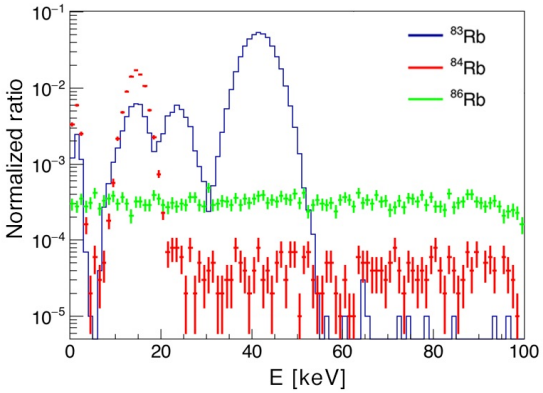

Figure 3.12: The simulated energy spectrum before reclustering of ^{83}Rb, ^{84}Rb and ^{86}Rb in the PandaX-II fiducial volume after normalization. The isotopes are assumed to be uniformly distributed in the LXe.

The normalized energy spectra of the three isotopes with 10^5 events simulated for each, are shown in Fig 3.12. The part in 0$\sim$10 keV$_{\rm ee}$ is integrated, and regarded as the low energy fraction. The fractions for ^{83}Rb, ^{84}Rb and ^{86}Rb are 0.84%, 1.7% and 0.33%, respectively. The systematic uncertainties could come from the clustering algorithm and detetor response time which are not calibrated before getting the real data, but should be consistent with one order. The peaks for ^{83}Rb and ^{84}Rb smaller than 5 keV$_{\rm ee}$ are not visible in the real data (details in section 3.4). Instead of getting multi-peaks for Auger electrons, a typical ^{83m}Kr event has one combined $S2$ for the whole 41.5 keV and two $S1$s for the separate transitions (32.1 keV and 9.4 keV). Taking 0.1 mDRU as

the requirement of the contamination below 10 keV_{ee}, we can calculate the radioactivity tolerance in LXe as $r(^{83}\text{Rb}) < 0.50$ mBq, $r(^{84}\text{Rb}) < 0.24$ mBq, $r(^{86}\text{Rb}) < 1.28$ mBq.

When the rubidium source is produced, the ratio of ^{83}Rb:^{84}Rb:^{86}Rb was $1 : 0.10 : 4.1$. After two months, the ratio became $1 : 0.05 : 0.71$ because of the decay of the isotopes. Considering the simulation results, the most dangerous isotope is ^{83}Rb for a two-month old source. Therefore, the upper limit should be validate to be smaller than 10^{-3} % with a 10 h injection for ^{83}Rb.

A flushing test for our calibration module is carried out, even though the Merck filters have been tested to have an upper limit of the Rb isotopes 1.3×10^{-10} %/h (2.4 μBq/h for a 1.8 MBq ^{83}Rb/^{83m}Kr source) [172]. The vacuuming test in the literature does not validate the movement of the zeolite powder under flushing in the real injection procedure.

In our flushing test, a ^{228}Th zeolite source is used instead of a ^{83}Rb one. Our rubidium absorbed zeolite beads are not radioactive enough for the test purpose because the sensitivity of the germanium detector is limited to $\sim 10^{-4}$ Hz/keV. If the leakage is less than 1% for the Rb zeolite samples, we need more than a month to validate the leakage level. Therefore, we made a strong ^{228}Th ($T_{1/2} = 1.9$ y) source by putting zeolite into thorium nitrate solution. The 238 keV gamma peak of the ^{228}Th with the highest statistics is used to test the leakage (the blue line in Fig. 3.13).

The first leakage test (Fig. 3.14) was done by flushing the zeolite with nitrogen (N_2). We blew N_2 into the ^{228}Th zeolite chamber which was followed by the 0.2 μm filter (Fig. 3.14). The filter was clamped to a CF35 flange with a PTFE gasket. At the downstream of the filter, a piece of mask cloth was used to trap the zeolite powder leaked out. The test lasted for 3.5 d with the flow rate varying between 0.6$\sim$2.0 SLPM. The pressure of the N_2 at the inlet varied from 1 to

2 barG, creating a pressure drop larger than that in the real injection.

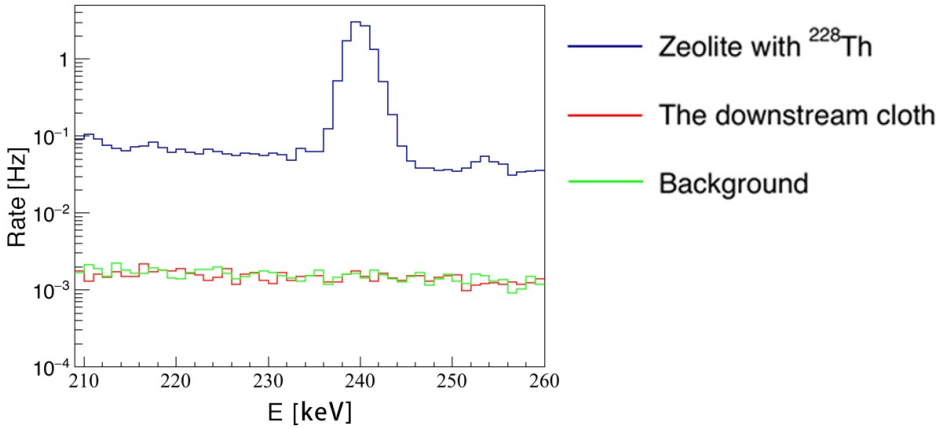

Figure 3.13: The blue line is the energy spectrum of the ^{228}Th zeolite source. The red and green lines are the spectra of the cloth and the background respectively.

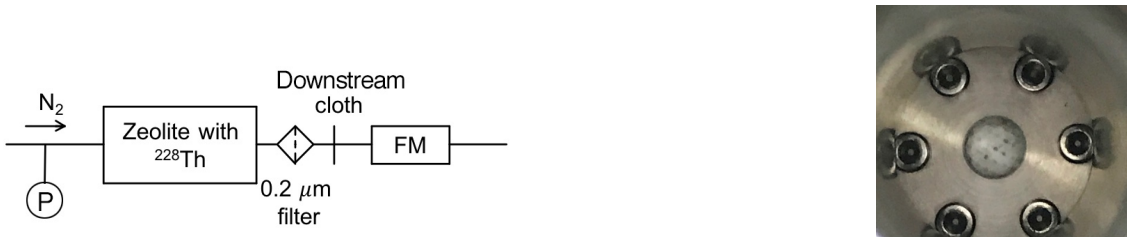

(a) (b)

Figure 3.14: (a) The N_2 flushing test arrangement for radioactivity leakage concern. (b) The 0.2 μm filter with a custom holder to stop zeolite powder to enter the detector.

The radioactivity of the cloth was measured by the germanium detector for 15.1 h after N_2 blowing. Compared to the background spectrum (Fig. 3.13), no noticeable radioactivity was detected. The test energy window for the 238 keV peak of ^{228}Th is chosen as [235, 246] keV. The counts in the energy window for the cloth (the red line in Fig. 3.13) is 962. Regarding these as backgrounds, at a 90% C.L., the number of the ^{228}Th decays n_s is smaller than 39.7 in the energy window. It corresponds to a rate $r_s < 7.3 \times 10^{-4}$ Hz. The ^{228}Th zeolite source has an integrated rate $r_0 = 10.2$ Hz in the window, and therefore, the upper limit of the leakage was

$r_s/r_0 = 8.5 \times 10^{-5}$ %/h.

Besides the flushing test, a vacuuming test (Fig. 3.15) was also done. Using the same strategy in the flushing test, we put another piece of cloth at the downstream of the filter and measured it after 3.5 d pumping. The upper limit of vacuuming leakage is 1.1×10^{-4}%/h at 90% C.L..

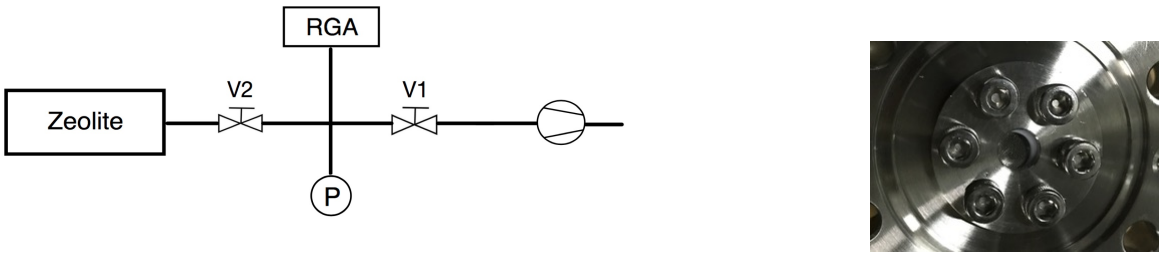

(a) (b)

Figure 3.15: (a) The vacuuming test arrangement which is also used for zeolite residue test. (b) The filter to stop zeolite powder for pumping.

Considering the results of these two tests and the simulation, we conclude thatå the 30 Bq ^{83}Rb zeolite source induces less than 0.1 mDRU ER backgrounds in 20 h.

3.3.2 Electronegative impurity test

Zeolite is a porous material which traps electronegative gases. If these electronegative impurites are brought into the LXeD through flushing, the ionization signals, $S2$s, will be affected for days. Free electrons generated by recoiling events can be absorbed by electronegative impurities in LXe during the drifting. Therefore, for the same ionization depositions, $S2$s are smaller with longer drifting time. The attenuation of ionization signals is characterized by the drifting time, or the electron lifetime in LXe, when the amount of electrons becomes e^{-1} of the original. The electron lifetime can reflect the concentration of the electronegative impurities in LXe.

The out-gassing of the zeolite is studied with the setup illustrated in Fig. 3.15. A SS filter (0.1 mm) is used to prevent the zeolite powder from damaging the pump Fig. 3.15. The out-gassing effect is measured with V1 closed (Fig. 3.15).

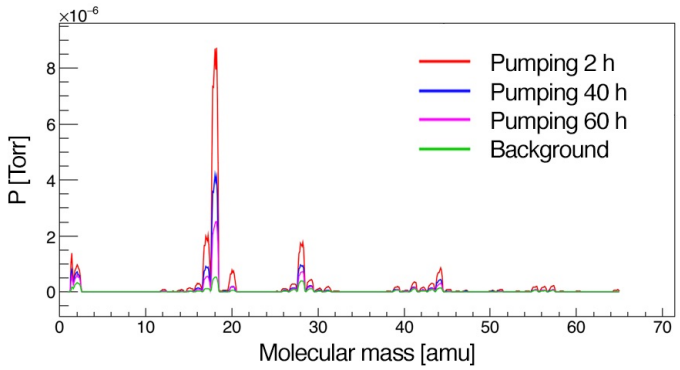

Figure 3.16: The spectrum of the residues with different pumping time. The background is measured with V1 closed in Fig. 3.15.

The residues in the zeolite chamber are measured by residue gas analyzer (RGA) in Fig. 3.16, which are dominant by water, and the others are normal. As the gas is purified by the Getter 2 (PS4-MT50-R-2, SAES company) in the LOOP2 (Fig. 3.11) before the injection. If all the residues meet the inlet requirements of the Getter, the impurities should be effectively reduced by three orders of magnitude in one circulation. After 40 h pumping, the final pressure in the source chamber measured with V1 closed for half an hour is smaller than 0.1 Pa, causing less than 1 ppm impurities into 1 bar xenon. Therefore, the electronegative residues meet the requirements [173].

3.4 Brief data analysis of ^{83m}Kr events in PandaX-II

After the contamination tests, the 30 Bq ^{83}Rb source module is ready for injection. The ^{83m}Kr gas is loaded through the blue route in Fig. 3.11 into the PandaX-II detector which contains 1.1 ton xenon in total and 580 kg in the TPC.

In this section, the details of the ^{83m}Kr injection are described. Then the signal analysis is presented including the waveforms, the energy spectrum and the lifetime of the ^{83m}Kr states. Finally, the upper limit of the radioactive contamination and the impact on the electron lifetime following the injection are analyzed.

3.4.1 ^{83m}Kr injection process

The location of the ^{83}Rb/^{83m}Kr source module has been mentioned before in Fig. 3.11. Before the injection, the zeolite chamber was pumped for 60 h at 80°C (The heating temperature was limited by the rubber used in the KF25 connection). The final vacuum reached 5.8×10^{-4} Pa. After pumping, the ^{83m}Kr was mixed with xenon, and the mixed gas was purified in LOOP2 by the Getter 2 for 24 h before injection, which follows the self-circulating route marked with red arrows in Fig. 3.11 .

The ^{83m}Kr injection was carried out on Sept 12, 2018 for about 10 h for the first time. Following this, we stopped injection for 12 h to check if there was significant rubidium leakage. After checking the contamination level, more injections were made, and the total injection time is 34.15 h.

3.4.2 ^{83m}Kr event analysis

As shown in Tab. 3.2 ([1]), the decay from ^{83m}Kr to ^{83}Kr is mainly through conversion electrons. The direct decay mode from 41.5 keV to the ground state is suppressed due to a large difference in the spin of the states.

In the standard data processing procedure for the PandaX-II experiment [141], an event

Table 3.2: Decay channels of the ^{83m}Kr isotope [1].

Transition energy	half-life	Decay mode	Branching ratio
32.1 keV	1.83 h	e(30 keV)+e(2 keV)	76%
		e(18 keV)+e(10 keV)+2e(2 keV)	9%
		e(18 keV)+X(12 keV)+2e(2 keV)	15%
9.4 keV	155.1 ns	e(7.6 keV)+e(1.8 keV)	95%
		γ	5%

consists of one or more ionization signals identified as $S2$, proceeded by one or more scintillation signals identified as $S1$s. ^{83m}Kr decays via an intermediate state of 9.4 keV with a halflife of 155 ns. The $S2$s of the two transitions, which typically span several microseconds, can hardly be separated in our data as in Fig. 3.17. But for $S1$s, sometimes the two transitions can be separated. The waveforms for $S1$s with the two transitions separated or mixed are compared in Fig. 3.18.

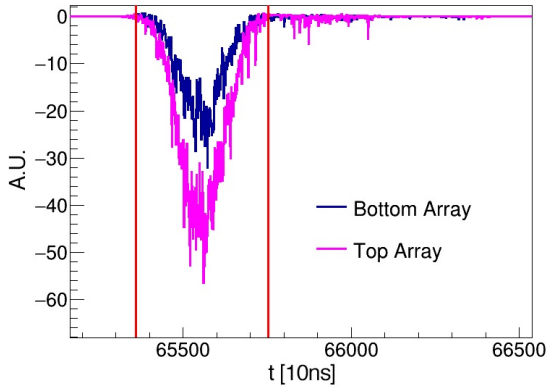

Figure 3.17: A typical $S2$ waveform for ^{83m}Kr decays. The red line indicates the $S2$ time window according to the standard data processing. The blue line is the summed waveforms of the bottom PMT array, and the magenta line is of the top PMT array.

In the data processing for the WIMP search, one identifies an event with only the maximum $S1$ and $S2$ in the triggered time window (1 ms). Our typical ^{83m}Kr events are shown in Fig. 3.19, where we observe two peaks of ^{83m}Kr share the same $S2$ but different $S1$s. In the left peak, the $S1$ only records the scintillation of 32.1 keV$_{\mathrm{ee}}$, and in the right one, the total scintillation of the

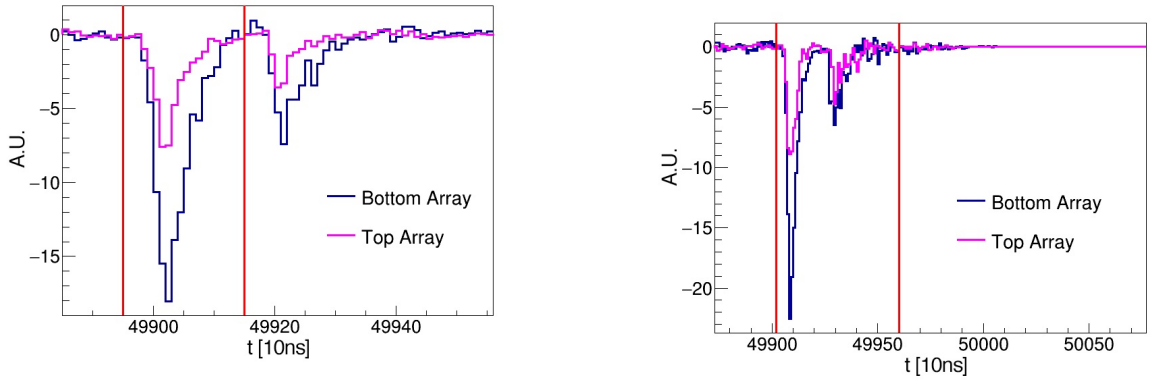

(a) (b)

Figure 3.18: (a) The waveform with the two $S1$ separated for ^{83m}Kr decays. (b) The waveform with the two $S1$ mixed. The red lines indicate the $S1$ time window according to the standard data processing. The blue lines are the summed waveforms of the bottom PMT array, and the magenta lines are of the top PMT array.

41.5 keV$_{ee}$ transition is included.

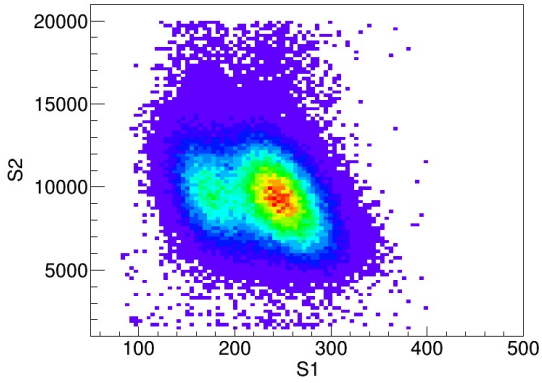

Figure 3.19: Typical ^{83m}Kr events with the data processing algorithm for WIMP search.

In order to select the pure ^{83m}Kr events, we limit $80\ \mathrm{PE} < S1 < 400\ \mathrm{PE}$ and $1500\ \mathrm{PE} < S2 < 20000\ \mathrm{PE}$. Furthermore, the drifting time is limited between [20, 350] μs, which corresponds a cut from 3.3 cm to 58.3 cm below the liquid surface in the TPC, including 532 kg LXe. The regions near the gate and cathode are excluded for a lower background level. The additional background rate is subtracted by comparing the data during calibration to that before. The ^{83m}Kr

radioactivity is 4.92 ± 0.01 Bq with these cuts. The rate of ^{83m}Kr is slightly underestimated as the long tail outside of the $S1$ and $S2$ selection window cannot be accounted. Fig. 3.20(a) indicates that the activity level during the injection. The turning point of the $r_{^{83m}Kr}$ at about 10 h marked the stop of the injection. The data after the injection is used to check the decay of ^{83m}Kr. The fitting function in Fig. 3.20(b) is $r_{^{83m}\mathrm{Kr}} = p0 \cdot \exp(\frac{-\ln 2 \cdot t}{p1}) + p2$, where $p0$ and $p2$ have unit of Bq, and $p1$ has unit of hour. Our result $p1 = 1.89 \pm 0.02$ h is consistent with the data in [1].

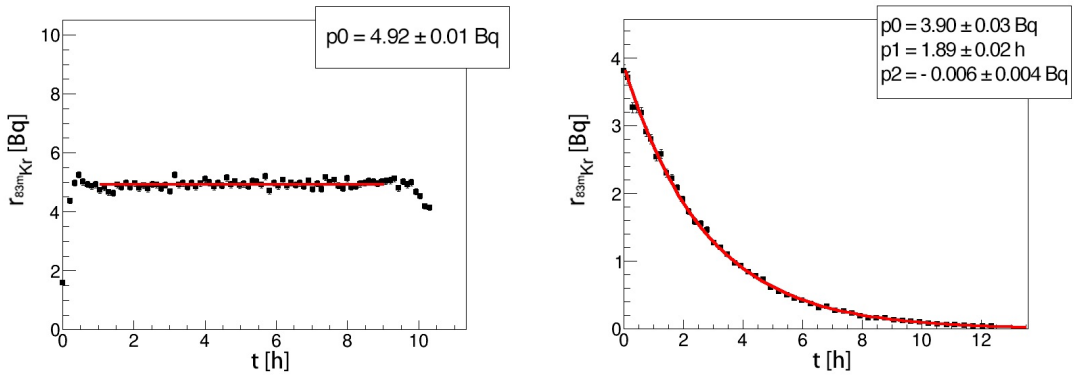

(a) (b)

Figure 3.20: (a) The rate of ^{83m}Kr during injection including 532 kg LXe. In the fitting, $p0$ is the rate of ^{83m}Kr with backgrounds subtracted. (b) The decay of ^{83m}Kr after injection. The fitting function is $r_{^{83m}\mathrm{Kr}} = p0 \cdot \exp(\frac{-\ln 2 \cdot t}{p1}) + p2$, where $p0$ and $p2$ have unit of Bq, and $p1$ has unit of hour.

Besides the halflife of the 41.5 keV$_{\mathrm{ee}}$ state, we can also measure the halflife of the 9.4 keV$_{\mathrm{ee}}$ intermediate state. The $S1$ waveform with the two transitions separated or mixed is shown in Fig. 3.18. The time interval of the two $S1$s, if well separated, could be used to fit the half-life of the first excited state of ^{83m}Kr as shown in Fig. 3.21. From fitting the tail with Δt larger than 120 ns, we obtained a half-life of 154.5±0.6 ns, which is consistent with the theoretical value.

The energy spectrum of ^{83m}Kr events is shown in Fig. 3.22. The relation between the

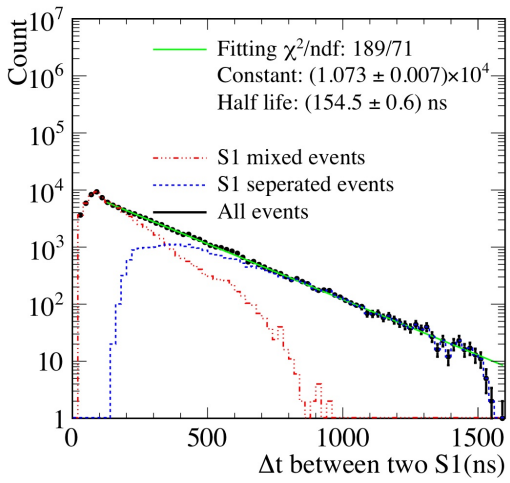

Figure 3.21: The fit of the halflife ($p1$) for the first excited state of ^{83m}Kr.

energy and the photon-electron signals is

$$E = 0.0137 \text{ keV}_{\text{ee}} \cdot (S1_{\text{tot}}/G1 + S2/G2), \tag{3.9}$$

where $S1_{\text{tot}}$ is the total scintillation photon elctrons from the 41.5 keV$_{\text{ee}}$ state to the ground state, $G1 = 0.1134$ and $G2 = 0.577 \times 23.9$ (see details in [34]) . The background events have been subtracted. A FV cut mentioned in section 3 was used to achieve a lower background level. Fig. 3.22 shows the energy resolution of the PandaX-II detector is 8.0% at 40 keV$_{\text{ee}}$. The mean of the peak E_0 is 40.6 keV$_{\text{ee}}$, slightly smaller than the value provided in [1], which can be further used to calibrate the detector response. Considering the $\pm 1\sigma_E$ integral including 68.2% events and the scaling from the FV to the sensitive volume, the ^{83m}Kr activity level was estimated to be 4.80 ± 0.02 Bq in 580 kg xenon.

Averaging the two estimates above, the ^{83m}Kr activity level in the TPC was 5.1 ± 0.4 Bq. If ^{83m}Kr uniformly distributed in the 1.1 ton LXe, the total ^{83m}Kr injected would be 9.7 ± 0.8 Bq. Since the ^{83m}Kr mixed Xe first flows into the TPC, the actual activity level might not be uniform

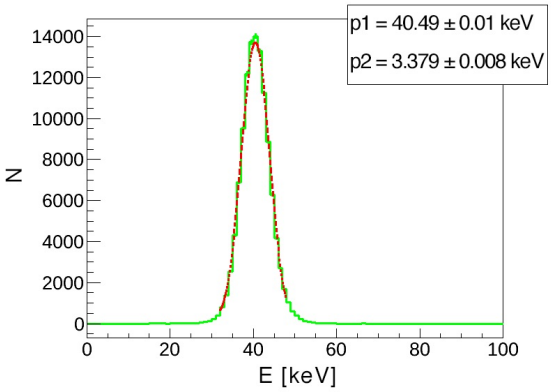

Figure 3.22: The energy spectrum of ^{83m}Kr with backgrounds subtracted. The fitting function is $N = \frac{p0}{\sqrt{2\pi}p2} \cdot \exp[-\frac{(E-p1)^2}{2 \cdot p2^2}]$

throughout the detector. The number 9.7 Bq above represents an upper limit.

Considering the ^{83m}Kr activity level of the source is 22 Bq ($30 \times 74\%$ Bq), the injection efficiency of ^{83m}Kr is 44% if ^{83m}Kr is uniform in the whole 1.1 ton xenon and 23% if only ^{83m}Kr in the TPC volume is considered.

3.4.3 Contamination analysis

The injection of ^{83m}Kr may induce two kinds of contamination into the detector. One is ER backgrounds due to rubidium isotopes, and the other is the electronegative impurities from the zeolite beads.

For the radioactive contamination, we did not see any noticeable radioactivity of the rubidium isotopes after total 34 h ^{83m}Kr injection. The upper limit of the leakage rate is determined based on the Feldman and Cousin's method [174].

To estimate the radioactivity level of ^{83m}Kr events, the double-S1 characteristic as in Fig. 3.18 is used. By constraining the range of the $S2$ and the first $S1$ as shown in Fig. 3.19, the second $S1$ to 28.5 PE and 85.5 PE (the $S1$ for the 9.4 keV transition) and the time difference

between the two $S1$s smaller than 1600 ns in the FV, we get 20.95% of the total ^{83m}Kr events during calibration. This cut is very powerful to suppress the influence of other events. In the 7480.42 h dark matter runs before the ^{83m}Kr injection, there are only 20 coincident events left with the cuts. We check 204.77 h dark matter runs after the injection in which only 1 event survives the strict cut. According to the Feldman and Cousin's method [174], we get an upper limit $s = 3.6$ events with 90% C.L. in the $t_0 = 204.77$ h run. Thus the upper limit of ^{83}Rb in the detector is

$$\begin{aligned} r_{^{83}\mathrm{Rb}} &< \frac{s}{t_0} \cdot \frac{1}{20.95\% \times \frac{380\,\mathrm{kg}}{580\,\mathrm{kg}} \times \frac{5.1\,\mathrm{Bq}}{30\,\mathrm{Bq}}} \\ &< 0.38\ \mathrm{mBq}, \end{aligned} \tag{3.10}$$

where 380 kg is the xenon mass in the FV, 580 kg is for the sensitive volume, 5.1 Bq is the ^{83m}Kr radioactivity during injection in the sensitive volume and 30 Bq is the ^{83}Rb radioactivity.

As the total injection time of ^{83m}Kr was $t_{in} = 34.15\ h$, the upper limit of the leakage rate of ^{83}Rb is

$$l_{^{83}\mathrm{Rb}} = \frac{r_{^{83}\mathrm{Rb}}}{t_{in}} < 5\ \mu\mathrm{Bq/h}. \tag{3.11}$$

To check the impact of electronegative impurities induced by ^{83m}Kr injection, the electron lifetime is measured by mono-peak events in the TPC. For normal WIMP search runs, we use the $S2_b$, the ionization signal from the bottom PMT array, of ^{222}Rn to fit the electron lifetime. $S2_b$ is used instead of the whole $S2$ to avoid the PMT saturation effect. In the ^{83m}Kr injection period, the events of ^{83m}Kr are used.

The electron lifetime before injection (Sep 9 - 11, 2018) was fitted in Fig. 3.23 a), where $\tau_e = 1/p1 = 1968 \pm 174\ \mu$s. In the first injection on Sep 12, 2018, the electron lifetime became

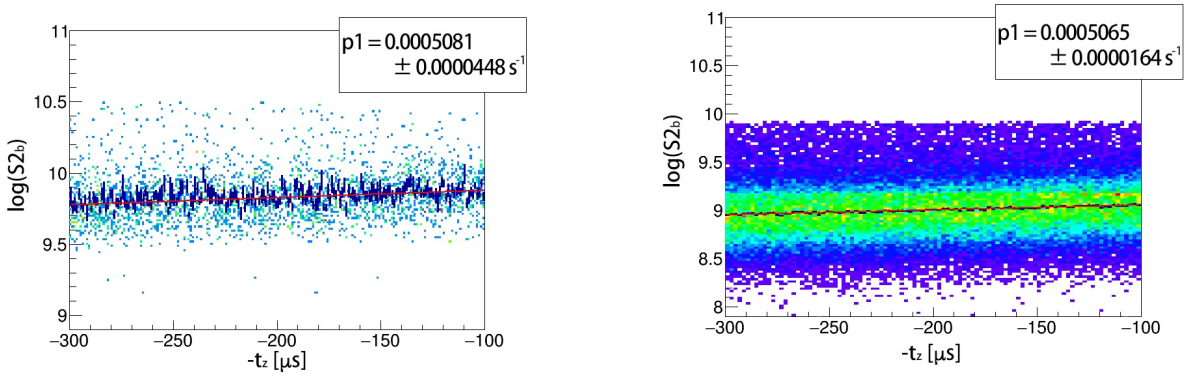

(a) (b)

Figure 3.23: (a) The electron lifetime before ^{83m}Kr injection checked by $\log S2_b$ of ^{222}Rn. $\tau_e = 1/p1$ is the electron lifetime . (b) The electron lifetime during ^{83m}Kr injection checked by $\log S2$ of ^{83m}Kr, $\tau e = 1/p1$ was the electron lifetime. In both (a) and (b), t_z is the drifting time of the electrons. The dark blue dots with error bars show the profiled average of the vertical axis, $\log S2_b$ for (a) and $\log S2$ for (b). The red lines are the fittings of the first order polynomial ($\log(S2_b)$ or $\log(S2) = p0 + p1 \cdot (-t_z)$), where $p1$ has the unit of μs^{-1}.

$\tau_e = 1/p1 = 1974 \pm 64$ μs (Fig. 3.23 b). No significant drop of the electron lifetime is detected in our detector. The result validates the previous injection preparation.

The $S1$ waveform with the two transitions separated or mixed is shown in Fig. 3.18. The time interval of the two $S1$s, if well separated, could be used to fit the half-life of the first excited state of ^{83m}Kr as shown in Fig. 3.21. From fitting the tail with Δt larger than 120 ns, we obtained a half-life of 154.5$\pm$0.6 ns, which is consistent with the theoretical value.

Chapter 4: Horizontal position reconstruction algorithms in PandaX-II

The spatial information of the events plays an important role in understanding the recoiling events and suppressing backgrounds. For instance, with the scattering angles of the mono-energetic incoming neutrons known, nuclear recoil energy calibration is pushed down to 1 $\mathrm{keV_{nr}}$ in the LUX experiment [25, 175]. More importantly, the spatial information suppresses the gamma and neutron backgrounds coming from outside of the sensitive region because the shielding effect of noble liquids leads to a strong spatial dependence in these backgrounds [58, 155]. Similarly, the surface backgrounds due to radioactivities attached to the materials can also be suppressed with positions known [58]. Therefore, a more accurate position reconstruction brings potentials to improve the sensitivity of dark matter searching.

This work focuses on the horizontal position reconstruction in the PandaX-II detector where Hamamatsu-R11410 3-inch photomultiplier tubes (PMTs) are used as light sensors. The vertical vertexes, reconstructed using the delay time of $S2$, can reach a resolution of a few millimeters with a drifting field $\sim \mathcal{O}(100)$ V/cm [128]. To reach a horizontal position resolution comparable to the vertical one, simple reconstruction using the center position of the hottest PMT is not sufficient because the PMTs are at least 8 cm apart. Sophisticated algorithms based on the distribution of the $S2$ collected by the PMTs are applied.

We develop two algorithms in this work based on the photon acceptance functions (PAFs),

η, which describe the light fraction collected by light sensors for one event as introduced in the literature [176]. PAF is a function of light sensor index, i, and position of events (x, y, z), because of the change in the solid angle subtended by the ith light sensor to (x, y, z). It can be evaluated as

$$\eta_i(x, y, z) = \frac{\text{photons detected by sensor}_i \text{ for an event happens at } (x, y, z)}{\text{total photons detected for the event happens at } (x, y, z)}. \tag{4.1}$$

During modeling, the functions are usually built with analytical models [177, 178] or Monte Carlo simulations [179, 180, 181], and trained with calibration data. Generally, a better agreement between the model and reconstructed data PAFs leads to a better position reconstruction.

To optimize the models, calibration events with positions or distributions known and energies close to WIMP searches are favored. In the PandaX-II liquid xenon detector, we use ^{83m}Kr isotopes released by the customized ^{83}Rb ($T_{1/2} = 86.2$ d) sources and flushed into our TPC, which has been introduced in the last chapter. The ^{83m}Kr isotopes are uniformly distributed in the detector because of a long enough lifetime ($T_{1/2} = 1.83$ h) to mix with xenon. In addition, the ^{83m}Kr events provide signals close to a typical WIMP search window $\sim \mathcal{O}(10)$ keV$_{\text{ee}}$. ^{83m}Kr isotopes released by ^{83}Rb decay into the ground state with two successive transitions of 32.1 keV$_{\text{ee}}$ and 9.4 keV$_{\text{ee}}$. Because separating the two with a 154 ns intervening half-life is difficult, we use the sum of the transitions.

Our developments on analytical and simulation-based PAFs are both tuned with ^{83m}Kr calibration data. The detailed geometry of the PandaX-II detector is described in [153]. The sensitive volume is surrounded by a dodecagonal polytetrafluoroethylene (PTFE) surface, and covered with 55 PMTs at the bottom and on the top, respectively, with the same alignment. In the

analytical algorithm, we extend the single-variable PAF based on ZEPLIN III's work to correct the light reflection effect because of the PTFE surface [177]. In the simulation-based algorithm, We tune the vertical vertexes of $S2s$ in the gas phase as a function of the horizontal position to make the simulation agree with calibration data.

We reach comparable quality in the two algorithms for the WIMP search purpose with $S2 \in (100, 10000)$ photoelectron (PE). With respect to uncertainties, the analytical algorithm is better for $S2s$ with several thousand PEs in the PandaX-II TPC, but becomes slightly worse than the simulation-based one for $S2$s with several hundred PEs as studied by the surface events from the PTFE panels surrounding the sensitive region. The uncertainties in the center region of the TPC are 3.4 (3.9) mm in the analytical (simulation-based) algorithm as estimated by the radioactivities on the gate grid wires with $S2s$ larger than 1000 PE. Apart from the uncertainties, the analytical algorithm presents slightly better uniformity, which is evaluated by the radial distribution of ^{83m}Kr events. But for robustness, the simulation-based algorithm is more stable when handling inhibited PMTs.

In this chapter, the content largely follows the publication [182] where the author is one main contributor. In section 4.1, we demonstrate the procedure to reconstruct positions with PAFs. In section 4.2 and section 4.3, we present the setup of refined analytical and simulation-based PAF with ^{83m}Kr events in the PandaX-II detector sequentially. Finally, in section 4.4, we compare the two algorithms in the gate events and surface events besides ^{83m}Kr events.

4.1 Reconstruction procedure with PAF

PAF$_i$, describing the light fraction detected by the ith PMT in one event, is a function of the 3D scintillation position. In a TPC as Fig. 4.1, the functions depend on two-dimensional (2D) horizontal positions because $S2s$ are all generated at the liquid-gas interface. We note the PAF$_i$ as $\eta_i(x, y)$ where x and y represent the horizontal vertexes, where i only includes the top PMT array close to the interface.

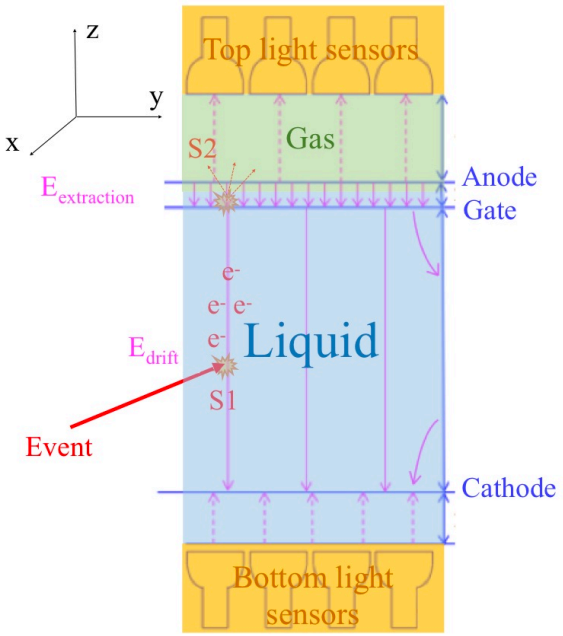

Figure 4.1: Sketch of a dual-phase nobel gas TPC. The two arrays of light sensors collect both prompt $S1s$ and delayed $S2s$. E_{drift} and $E_{\text{extraction}}$ with their directions indicated by the magenta arrows are established with the electric potential differences among the anode, cathode and gate electrode. More complicated designs for a real TPC are not included in this sketch. The Cartesian coordinate marked on the upper-left corner is used throughout this work where z is for vertical vertexes and (x, y) for horizontal ones.

Modeling of the PAFs is the first step. We define two groups of PAFs, which are the

model, $\eta_{i,\text{model=ana or simu}}(x,y)$, and data, $\eta_{i,\text{data}}(x_{\text{rec}},y_{\text{rec}})$, PAFs. Analyitcal and simulation-based algorithms both model PAFs with some adjustable parameters. The data PAFs can only be calculated with x_{rec} and y_{rec} reconstructed. The parameters are optimized for a better agreement between the model and data PAFs.

After the model building, we construct the likelihood function which is maximized by scanning possible x and y to infer the position of an event. The likelihood function should reflect how charges statistically distribute among the PMTs. More specifically, in each PMT, the photons collected follow a Poisson distribution. The total likelihood function is a multiplication of a series of the Poisson distributions as a function of x and y.

The statistical inference of the position with input photons of an event is done by maximum likelihood (ML) estimation. As deduced in the literature [176, 177], maximizing the total likelihood function is equivalent to maximizing the simplified log likelihood,

$$\ln L(x,y) = \sum_i S2_i \cdot \ln \frac{\eta_{i,\text{model = ana or simu}}(x,y)}{P(x,y)}, \tag{4.2}$$

where $P(x,y) = \sum_i \eta_{i,\text{model = ana or simu}}(x,y)$, and the summation includes all the top PMTs turned on. The $\ln L$ is maximized by scanning x and y in every event with the $S2$ charges collected by PMT$_i$, $\{S2_i\}$, as inputs.

4.2 Refined analytical PAF

To model the PAFs analytically, PAFs were simplified as a single-variable function of the distance to the center of the PMT, ι, in [177, 183]. Qualitatively, a PAF is a monotonically decreasing function of ι. PAFs are Gaussian distributions with the first-order corrections in [183].

ZEPLIN-III's work combines Cauchy and Gaussian distributions in modeling PAFs for a better agreement [177]. Later, LUX proposed a more sophisticated analytical model with x and y as variables based on the simulation of detector geometry and accounts asymmetries of the PMT positions according to the layout of PMTs and the horizontal boundary shape [178]. Because of a different detector geometry and PMT layout, we cannot use their modeled functions directly. Instead, we develop an extended single-variable model based on ZEPLIN-III's work [177].

4.2.1 Extended single-variable PAF

The single-variable PAF used in ZEPLIN-III is kept as the basic analytic form [177],

$$\eta^0_{i,\mathrm{ana}}(\iota_i) = A_i \cdot \exp\left(-\frac{a_i \cdot \frac{\iota_i}{r_i}}{1+(\frac{\iota_i}{r_i})^{1-\alpha_i}} - \frac{b_i}{1+(\frac{\iota_i}{r_i})^{-\alpha_i}}\right), \tag{4.3}$$

where i indicates the PMT index. The parameters, including A_i, α_i, r_i, a_i and b_i, are fitting parameters. The ι_i is the distance of the scattering point to the center of the PMT$_i$,

$$\iota_i(x,y) = \sqrt{(x-X_i)^2+(y-Y_i)^2}, \tag{4.4}$$

where (X_i, Y_i) is the center of PMT$_i$.

ZEPLIN's model which uses Eq. 4.3 as $\eta_{i,\mathrm{model}}$ causes problem at the large radius area for the PandaX-II detector. Without further adjustment, the model causes the events close to the PTFE surface to be congregated at the outermost PMT center which is around 3 cm away from the authentic surface. This inward bias is similar to the center-of-gravity algorithm due to non-optimized weights for $S2s$ collected by different PMTs.

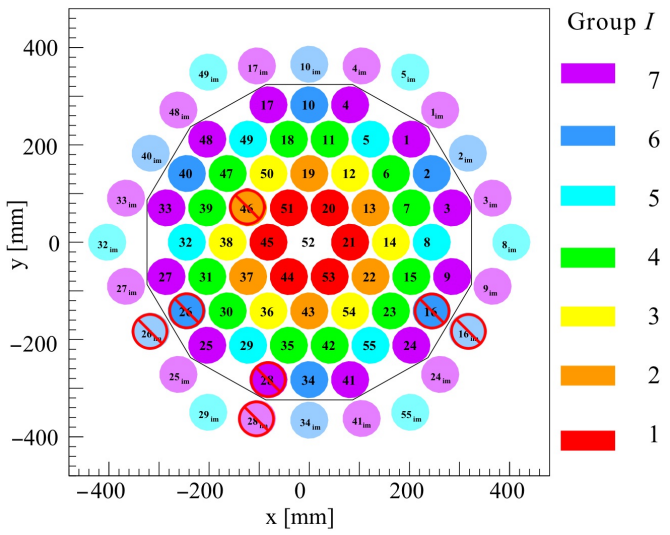

Figure 4.2: The arrangement of the top PMTs in the PandaX-II detector. The distance between two closest PMTs is 81.5 mm. The average diameter of the detector is 658 mm. The ones marked as banned are not included in the position reconstruction, those with semi-transparent color are image PMTs to account for the reflections on the PTFE field cage wall surfaces.

To fix this problem and correct the asymmetry brought by the PTFE reflection at the border, we introduce the image PMTs using the similar concept of 'image charge', which change the weights in the ML estimation (Fig. 4.2). The $\eta^0_{i,\mathrm{ana}}(\iota_i)$ is separated into two parts, the reduced object, $\eta_{i,\mathrm{ana}}(\iota_i)$, and the corresponding image, $\eta_{i,\mathrm{ana,im}}(\iota_{i,im})$. Mathematically, we add two groups of parameters, $\{w_I\}$ and $\{\rho_I\}$,

$$\begin{aligned} \eta_{i,\mathrm{ana}}(\iota_i) &= \frac{1}{1+w_I}\cdot(1-\rho_I)\cdot\eta^0_{i,\mathrm{ana}}(\iota_i), \text{ and} \\ \eta_{i,\mathrm{ana,im}}(\iota_{i,im}) &= w_I\cdot\eta_{i,\mathrm{ana}}(\iota_{i,im}), \end{aligned} \tag{4.5}$$

where I indicates the group number of the PMT, which is determined by the distance to the center of the TPC as in Fig. 4.2. The factor before $\eta^0_{i,\mathrm{ana}}(\iota_i)$ in Eq. 4.5 suggests that the light collected by the edge PMT is shared with the image PMT. The $\{w_I\}$ is only nontrivial for the PMTs next

to the boundary and zero for the inner PMTs. We reduce $\{w_I\}$ to one parameter w_e, which is the same for all the three outmost groups ($I = 5, 6, 7$) in the PandaX-II detector. The other parameter group, $\{\rho_I\}$, is nontrivial for each I which helps to correct the global reflection effect. The minus sign before the ρ_I in Eq. 4.5 represents a cut-off correction.

To include the image PMTs in the likelihood function, we modify Eq. 4.2 as follows,

$$\begin{aligned}\ln L(x,y) = &\sum_{\text{edge}} \left(\frac{1}{1+w_e} \cdot S2_i \cdot \ln \frac{\eta_{i,\text{ana}}(\iota_i)}{P(x,y)} \right. \\ &\left. + \frac{w_e}{1+w_e} \cdot S2_i \cdot \ln \frac{\eta_{i,\text{ana,im}}(\iota_{i,\text{im}})}{P(x,y)} \right) \\ &+ \sum_{\text{inner}} S2_i \cdot \ln \frac{\eta_{i,\text{ana}}(\iota_i)}{P(x,y)},\end{aligned} \tag{4.6}$$

where $P(x,y) = \sum_i (\eta_{i,\text{ana}} + \eta_{i,\text{im,ana}})$.

4.2.2 Model training with ^{83m}Kr in PandaX-II

We scan the group parameters, $\{w_e, \rho_I\}$, to optimize the analytical model. The fitting parameters of all the PAFs, $\{A_i, \alpha_i, r_i, a_i, b_i\}$, are initially set the same for each PMT$_i$ and then updated with iterative fittings. The quality of each group parameter is evaluated after reaching stable fitting results.

We parametrize $\{\rho_I\}$ for more efficient training. The required computational resources increase exponentially with the number of the groups, N_g, because we have to scan parameters in $N_g + 1$ dimensions. Therefore, we further parametrize ρ_I according to the group number and

reduce the number of parameters to two in $\{\rho_I\}$ by requiring

$$\rho_I = \begin{cases} c \cdot (\frac{R_i}{R_{\max}})^4, I = 1,2,3 \\ d \cdot (\frac{R_i}{R_{\max}})^4, I = 4,5,6,7 \end{cases}, \; R_i = \sqrt{X_i^2 + Y_i^2}, \tag{4.7}$$

where R_i is the distance of the PMT$_i$ center to the TPC center, and $R_{\max}$ (294 mm) is R_7. In fact, the set $\{\rho_I\}$ is a higher order correction of the $\eta^0_{i,\text{ana}}$, which can be expanded as Taylor series. We have tried different positive power numbers in the modeling. The uniformity of ^{83m}Kr is used to evaluate the quality similar to the parameter optimization procedure discussed later in this section. The R_i^4 dependence is selected for application in the PandaX-II detector. .

We tune the outer and inner parameters sequentially based on the uniformity of ^{83m}Kr. We scan d and w_e first as they have a larger effect on the uniformity. The initial fitting parameters of all the PAFs are set as the same. An example is $A_i = 0.4$, $a_i = -0.47$, $b_i = 6$, $\alpha_i = 2.3$, $r_i = 95$ mm. A_i is the maximum of the PAF$_i$ at $\iota_i = 0$, r_i reflects the size of the PMT and the other parameters are more phenomenological. Different initial values can be used as long as the fittings converge. With set group parameters and initial fitting parameters, the initial $\eta_{i,\text{ana}}$ are set, and we can reconstruct positions by ML in Eq. 4.6. Instead of initializing coordinates with arbitrary numbers, we take the positions reconstructed by the center-of-gravity algorithm as initial positions, which makes the ML estimation faster and avoids taking local maxima for most events. After the first reconstruction, the new coordinates of ^{83m}Kr are used to generate a data PAF as

$$\eta_{i,\text{data}}(x_{\text{rec}}, y_{\text{rec}}) = \frac{\overline{S2_i}}{S2_{\text{top}}}(x_{\text{rec}}, y_{\text{rec}}), \tag{4.8}$$

where $S2_{\text{top}} = \sum_i S2_i$ and the summation only includes the top PMTs. As 4 out of 55 PMTs

are turned off due to sparkings and afterpulses (Fig. 4.2), 51 PMTs are in the summation. The overline means averaging over the events in the same $x_{\rm rec}$-$y_{\rm rec}$ bin. The $\eta_{i,\rm data}(x_{\rm rec}, y_{\rm rec})$ fit to the next $\eta^0_{i,\rm ana}(\iota_i)$ in Eq. 4.3. An example of the extended PAF fitting for PMT$_7$ is shown in Fig. 4.3[1], where $\eta^0_{7,\rm ana}(\iota_7)$ in Eq. 4.3 is fitted to the ^{83m}Kr data with $(x_{\rm rec}, y_{\rm rec})$. $R_{\rm rec}$ (=$\sqrt{x^2_{\rm rec} + y^2_{\rm rec}}$) in Fig. 4.3 goes through the TPC center $(0, 0)$ and the PMT$_7$ center $(X_7, Y_7) = (204, 71)$ mm. The five fitting parameters for each PMT$_i$ are updated in the new fitting and used to generate new positions with Eq. 4.6. Six iterations can reach consistent fitting results within a 1 mm difference, which takes several hours in total for one (c, d, w_e).

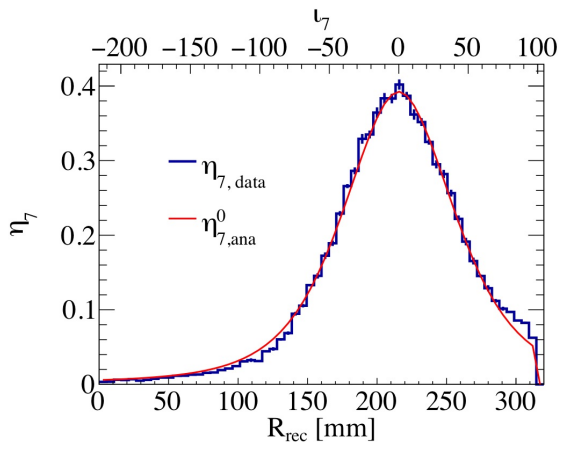

Figure 4.3: An example of the extended PAF in PMT$_7$ in Fig. 4.2. The blue line is the $\eta_{7,\rm data}$ along the line from the origin to the center of PMT$_7$, $(X_7, Y_7) = (204, 71)$ mm, and the red line is the fitted $\eta^0_{7,\rm ana}$.

Following this, we estimate the quality of the reconstruction with the spatial distribution of the ^{83m}Kr events. Another intuitive choice is the PTFE surface events like ^{210}Po which may reflect the main problem. However, there is a risk of pushing the surface events to the PTFE position and causing a strong distortion in the reconstruction. Therefore we use the uniformity in the binned and normalized $R^2_{\rm rec}$ distribution, $P(R^2_{\rm rec})$, of the ^{83m}Kr data. Only ^{83m}Kr events with

[1]Practically, a 2D fitting with (x, y) is done, but to make it more understandable, the 1D comparison is presented.

$R_{\rm rec} < R_{\rm crit}$ are used in the evaluation, and $R_{\rm crit}$ is determined by

$$P|_{R^2_{\rm rec}=R^2_{\rm crit}} = 0.2 \cdot P|_{R^2_{\rm rec}=0}, \tag{4.9}$$

which corresponds to the bin where the normalized distribution falls to 20% of its central value.

The relative standard deviation (RSD) in $P(R^2_{\rm rec})$ with $R_{\rm rec} < R_{\rm crit}$ is calculated after binning. Specifically, we set the binning as

$$R^2_{\rm rec} = 1200 \cdot n \ {\rm mm}^2, \ 0 \leq n \leq 100. \tag{4.10}$$

The RSD is calculated as follows,

$$\begin{aligned} {\rm RSD} &= \frac{\sqrt{\overline{P(n)^2} - [\overline{P(n)}]^2}}{\overline{P(n)}}, \quad \text{where} \\ \overline{P(n)} &= \frac{\sum_{n=0}^{n_{\rm max}} P(n)}{n_{\rm max}}, \ \ \overline{P(n)^2} = \frac{\sum_{n=0}^{n_{\rm max}} P(n)^2}{n_{\rm max}} \end{aligned} \tag{4.11}$$

and $n_{\rm max}$ corresponds to $R_{\rm crit}$. For different group parameters, the center of the TPC share similar $R^2_{\rm rec}$ distribution where the reflection has little influence. RSD quantifies the uniformity extended to the edge but not influenced by a small amount of events reconstructed extremely outward. In general, the smaller the RSD is, the more uniform the $R^2_{\rm rec}$ distribution. In Tab. 4.1, the RSD with $c = 1$, and $(d, w_e) = (0.20, 0.015)$ leads to the best performance. Then, the parameter c in Eq. 4.7 is tuned with d and w_e slightly modified.

RSD is minimized when $c = 1.0$, $d = 0.20$, $w_e = 0.015$. If we change the calculation criteria of RSD such as the binning of $R^2_{\rm rec}$ and choice of $n_{\rm max}$, the best parameters will be

Table 4.1: Values of RSD with $c = 1$ and different w_e and d.

dRSDw_e	0.010	0.015	0.020
0.15	0.146	0.160	0.152
0.20	0.123	0.115	0.143
0.25	0.126	0.127	0.134

slightly different, and cause around 1 mm difference in the reconstructed positions, which is minor compared to other uncertainties (see section 4.4). The final $\{\rho_I, w_I\}$ for different groups is shown in Tab. 4.2.

Table 4.2: Tuned group parameters.

I	1	2	3	4	5	6	7
ρ_I	0.0059	0.0532	0.0946	0.0580	0.0958	0.1703	0.2
w_I	0	0	0	0	0.015	0.015	0.015

A modification is required to place surface events at the physical wall as discussed in [184]. A stretching factor of 1.07 is further applied on $(x_{\rm rec}, y_{\rm rec})$. This might bring potential distortion in the reconstruction but is not significant compared to the local uncertainties (section 4.4). The $R^2_{\rm fRec}$ distributions of ^{83m}Kr data with four inhibited PMTs is shown as the blue line in Fig. 4.4, where the 'fRec' subscript stands for the final stretched reconstructed positions. The RSD$_f$ in $R^2_{\rm fRec}$ achieves 4.3% as calculated by Eq. 4.10 after replacing $R_{\rm rec}$ with $R_{\rm fRec}$ and $n_{\rm max}$ with $n_{f,\rm max}$ corresponding to $R^2_{\rm fRec} = 1 \times 10^5$ mm^2. The peaks along the $R^2_{\rm fRec}$ distribution are caused by reconstructed events gathering at the center of the PMTs, which is a minor problem as discussed in section 4.4 (Fig. 4.9).

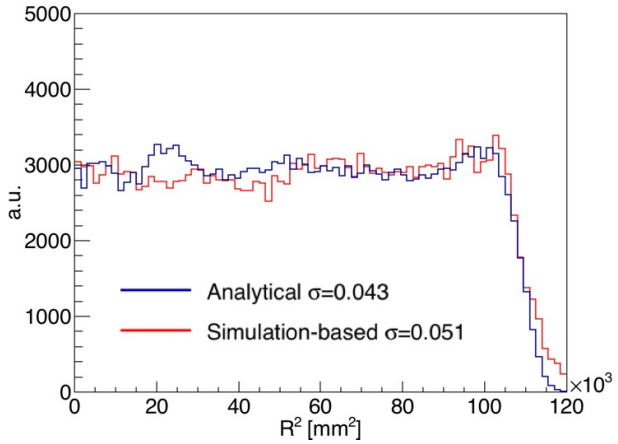

Figure 4.4: R^2_{fRec} distribution of ^{83m}Kr along R^2_{fRec} using the analytical (blue) and simulation-based (red) algorithms. The dashed black line is $0.2P|_{R^2_{\mathrm{rec}}=0}$ used in the analytical algorithm. The peaks along R^2_{fRec} in the analytical algorithm corresponding to the PMT centers (see Fig. 4.10(a)).

4.3 Simulation-based PAF

BambooMC, a Monte Carlo simulation, including event generator, light propagation, and signal reconstruction, is developed using the GEANT4 package for the PandaX-II detector [153, 185]. The event generator is a point source in the gas-phase immediately above the liquid and the photon numbers of the events follow Gaussian distribution. We fix the mean of the distribution as 10000 PE and sigma as 5000 PE to cover the region of interest.

The geometry follows the description in [153], and many parameters can be tuned for the light propagation, including the absorption length of photons in xenon, Rayleigh scattering length in xenon, reflection of the PTFE wall, etc. The output of this light simulation is the number of photons detected by each PMT for each event.

To generate smooth PAFs, several hundred thousand events should be simulated uniformly

at the liquid-gas interface, and the PAF_i is evaluated using a formula similar to Eq. 4.8,

$$\eta_{i,\mathrm{simu}}(x,y) = \overline{\frac{S2_{i,\mathrm{simu}}}{S2_{\mathrm{top,simu}}}}(x,y), \tag{4.12}$$

where $S2_{\mathrm{top,simu}} = \sum_i S2_{i,\mathrm{simu}}$ and the summation only includes top PMTs. The overline averages out the statistical fluctuation of the events in the same x-y bin. An example of the simulation-based PAF_7 is shown in Fig. 4.5. As the diameter of the PandaX-II detector is 658 mm (Fig. 4.2), for a 5 mm wide square bin, half million events are required for about 25 events in each bin.

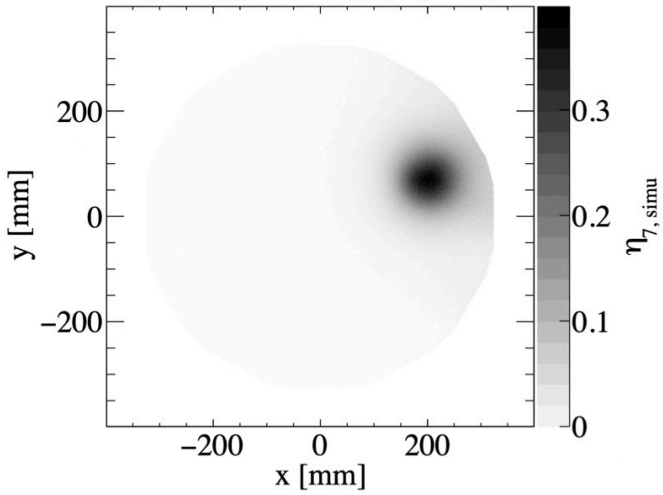

Figure 4.5: An example of simulation-based PAF in the PandaX-II detector with half-million events. The maximum of $\eta_{7,\mathrm{simu}}$ is at the center of PMT_7 in Fig. 4.2.

It takes several hours to generate simulation-based PAFs for one set configuration and reconstruct positions according to Eq. 4.2. If there are enough computation resources, we can simulate all the possible configurations, and select the one with the best quality.

However, as mentioned before, computation requirement grows exponentially with the

number of light propagation parameters. To find the most effective parameters within tolerable time, we focus on events at specific positions, the PMT centers. We select the ^{83m}Kr events with the maximum of the normalized $\{S2_i\}$ hit pattern detected by the top PMTs larger than a preset value for each PMT$_i$. The equivalent cut is $\eta_{i,\mathrm{data}} > t_i$, where t_i is the preset value for PMT$_i$ and typically ranges from 0.3 to 0.5. The surviving events have the highest light fraction in the PMT$_i$. We assume that these events are under the center of the PMT$_i$ which generate an averaged data template at $(x_{\mathrm{rec}}, y_{\mathrm{rec}}) = (X_i, Y_i)$ without any reconstruction. With the simplification, we only need to simulate 100 events at each (X_i, Y_i). Considering 51 PMTs are used (4 turned off), around five thousand events are enough for each configuration in the PandaX-II case.

After many trials, we find that the light emission point of $S2$ in the gas phase, as a function of horizontal position, is an effective parameter to make the simulation agree with the data templates. The vertical position, z, directly changes the angular coverage in the PMTs, which is more effective than the tuning of the reflectivity of the PTFE, the Rayleigh scattering length and absorption length. However, z does not represent the real average positions of the proportional scintillation in the gas phase, as discussed in more detail at the end of this section.

The optimization of z at a specific (X_i, Y_i) is done with χ^2 minimization,

$$\chi^2(z, X_i, Y_i) = \sum_j \frac{[\eta_{j,\mathrm{simu}}(X_i, Y_i|z) - \eta_{j,\mathrm{data}}(X_i, Y_i)]^2}{\sigma_{j,\mathrm{data}}(X_i, Y_i)^2}, \tag{4.13}$$

where j is the PMT index. Because the (X_i, Y_i) position is fixed, $\eta_{j,\mathrm{simu}}$ is tuned as a function of z. The uncertainty $\sigma_{j,\mathrm{data}}$ is evaluated as

$$\sigma_{j,\mathrm{data}}(X_i, Y_i) = \sqrt{\overline{(S2_j/S2_{\mathrm{top}})^2} - \left(\overline{S2_j/S2_{\mathrm{top}}}\right)^2}, \tag{4.14}$$

where the overline represents the average over the events selected at the center of PMT$_i$.

An example of tuning at the center of PMT$_7$ is plotted in Fig. 4.6. The ^{83m}Kr events are selected by constraining $\eta_{7,\mathrm{data}} > 0.4$. The $\sigma_{j,\mathrm{data}}(X_7, Y_7)$ is shown as error bars in the black histogram. In this example, $z = 6$ mm is the one with the minimum χ^2, and the liquid-gas interface corresponds to $z = 0$. Moreover, compared to z, the reflectivity, r, is of a higher order as in Tab. 4.3. In this GEANT4 simulation example, the reflectivity of the PTFE surface is modelled using a 'ground' PTFE surface, 'dielectric_metal' interface and 'SigmaAlpha=0.1' under the 'unified' mode. The meanings of the keys are defined in the literature [186, 187]. Because r is a higher order effect, we use our measurement of the PTFE material reflectivity, 0.95, in the simulation [138].

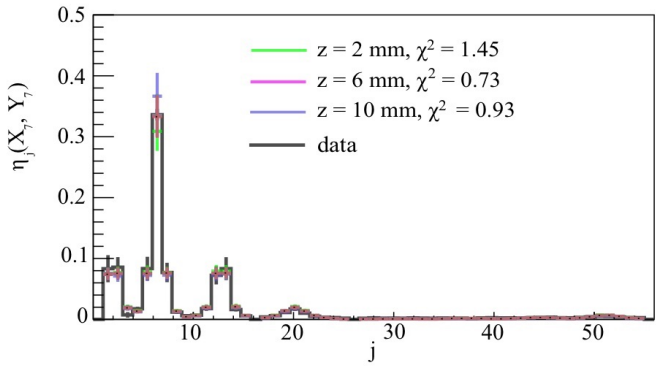

Figure 4.6: An example of the data and simulation η_j comparison at the center of PMT$_7$, $(X_7, Y_7) = (204, 71)$ mm. The simulation templates are generated with different z heights for the light emission..

Table 4.3: The χ^2 dependence on the reflectivity r with $z = 6$ mm at (X_7, Y_7).

r	0.25	0.50	0.75	1.00
χ^2	0.75	0.74	0.73	0.78

However, the optimization of z at the PMT centers is not enough for the area close to the PTFE surface at large R. A iterative tuning is performed. Starting with z at the liquid-gas

interface, we simulate half-million events horizontally uniformly distributed in the gas phase to generate PAFs, and they are used to reconstruct the calibration data. Following this, a set of target positions which are marked as red circles in Fig. 4.7, $\{(x_k, y_k)\}$, is chosen to represent the local behaviors. For each (x_k, y_k), 100 ^{83m}Kr events reconstructed closest to it are averaged to represent the reconstructed data. Then, the simulation at the same (x_k, y_k) position with different z are done. The new z with the best agreement to the data is updated for each target position. Two or three iterations are enough to find the optimized $z(x_k, y_k)$. After optimizing the z at different points, we use 2D linear interpolation to generate the mapping, $z(x, y)$, as in Fig. 4.7. We generate the final half million events in the gas phase with the optimized surface of $z(x, y)$.

The shape of $z(x, y)$ reveals some physical effects on the PAFs. The reflection of the PTFE surface leads to a small increase in z at the border. The center region has a highest z which may be caused by larger $E_{\text{extraction}}$ due to the deformation of the electrodes. Nevertheless, the deformation of the grid wires on the gate electrode should be sub-milimeter as suggested in another simulation [138]. Moreover the distance between the gate and anode is 11 mm which is smaller than the z-parameter at the center. Therefore, z are not the real positions of $S2s$. A more reasonable explanation is that the non-uniform $E_{\text{extraction}}$ results in different $S2$ responses horizontally even for mono-energetic gammas [34, 40], and the PAFs are different correspondingly.

A stretching factor, 1.06, determined by the PTFE surface events in [184], is applied to the original reconstructed positions. The factor is slightly different from the analytical algorithm because the two present different radial bias as in Fig. 4.9(b). The R^2_{fRec} distribution of the ^{83m}Kr data with four PMTs turned off are shown in Fig. 4.4. A 5.3% RSD$_{\text{fRec}}$ in the R^2_{fRec} distribution of the ^{83m}Kr data is reached in $R^2_{\text{fRec}} < 1 \times 10^5$ mm^2.

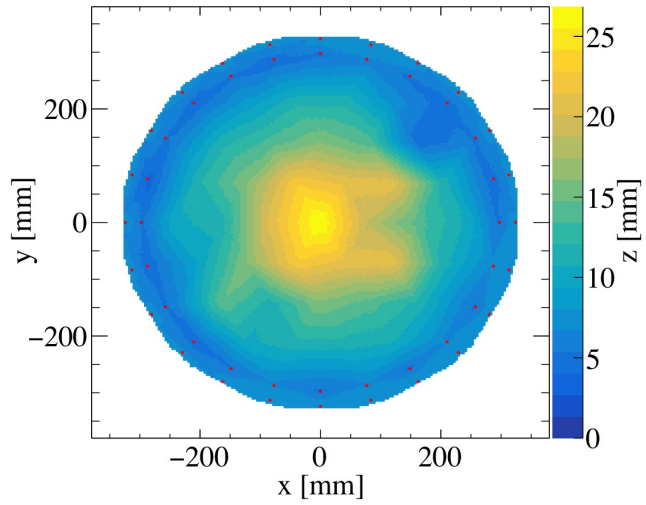

Figure 4.7: The optimized surface of $z(x, y)$ (the effective vertical position of $S2$ emissions) for the PandaX-II detector with 2D linear interpolation applied. The red circles are $\{(x_k, y_k)\}$ which used to optimize $z(x, y)$ at the edge.

4.4 Comparison

In this section, we compare the position reconstruction algorithms regarding uniformity, robustness and uncertaitnties. Before the comparison, we first estimate the best performance of the ML (Eq. 4.2 in section 4.1) by using simulation-based PAFs to reconstruct the corresponding simulation data. The uniformity and robustness are evaluated with ^{83m}Kr events. We calculate the uncertainties in the center area by the radioactivities on the gate electrode. The uncertainties at the border are estimated by the PTFE surface events as in [184].

4.4.1 Simulation event

As the simulation data have known positions, the uncertainties can be directly evaluated by the difference between the reconstructed position $(x_{\rm rec}, y_{\rm rec})$ and the origin $(x_{\rm true}, y_{\rm true})$ as

$|\Delta R| = \sqrt{(x_{\rm rec} - x_{\rm true})^2 + (y_{\rm rec} - y_{\rm true})^2}$. The PAF is constructed by Eq. 4.12, and the position is reconstructed by ML defined in Eq. 4.2. The total deviation, ΔR, is plotted as functions of R^2 in Fig. 4.8(a), and $\overline{\Delta R}$ is 2.2 mm including all simulated data. The radial deviation, $\Delta R_r = \sqrt{x_{\rm rec}^2 + y_{\rm rec}^2} - \sqrt{x_{\rm true}^2 + y_{\rm true}^2}$, in Fig. 4.8(b) shows a systematic inward deviation at large R. The best performance is limited by the hardware setup, including the horizontal distances among PMT centers and the vertical distance from the liquid-gas interface to the top-array PMTs. The border area performs worse because of a less angular coverage.

The total deviation between the two algorithms in the reconstructed real ^{83m}Kr events,

$$|\Delta R_{\rm fRec}| = \sqrt{(x_{\rm fRec,ana} - x_{\rm fRec,simu})^2 + (y_{\rm fRec,ana} - y_{\rm fRec,simu})^2}, \tag{4.15}$$

is shown in Fig. 4.9(a). The average total deviation, $\overline{|\Delta R_{\rm fRec}|}$, throughout the plane is (5.2 ± 3.6) mm, which reflects the propagated errors of the local uncertainties in the two algorithms and the distortion due to the surface events stretching. Similar to Fig. 4.8, the outer part is worse. Moreover, the clustering of events under the PMT centers in the analytical algorithm is reflected in the fluctuation along $R^2_{\rm fRec,ana}$, which is minor compared to the absolute deviation. The radial deviation is calculated as

$$\Delta R_{r,\rm fRec} = \sqrt{x^2_{\rm fRec,simu} + y^2_{\rm fRec,simu}} - \sqrt{x^2_{\rm fRec,ana} + y^2_{\rm fRec,ana}}. \tag{4.16}$$

The $\Delta R_{r,\rm fRec}$ distribution along $R^2_{\rm fRec,ana}$ in Fig. 4.9(b) reveals that the simulation-based algorithm reconstructed events slightly more outward in $(30000, 11000)$ mm^2 with a peak around 50000 mm^2.

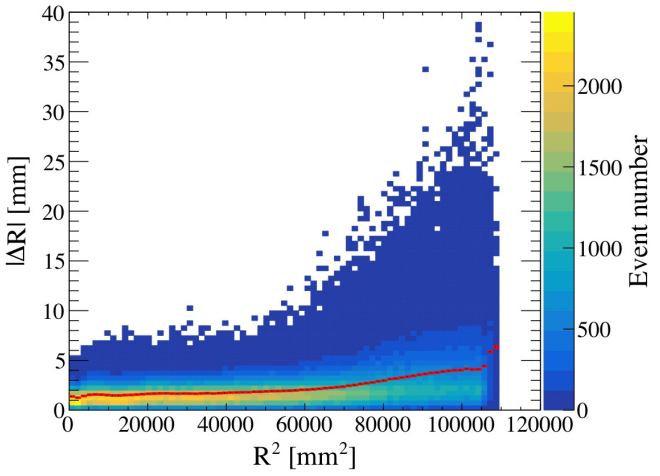

(a)

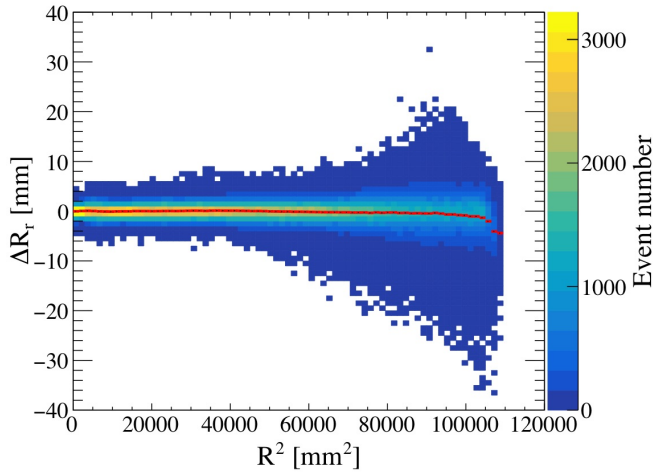

(b)

Figure 4.8: The deviation between ML reconstructed (Eq. 4.2) and true positions using simulated data (mean $S2$ at 10000 PE with a 5000 PE sigma) with corresponding simulated PAF, (a) Total deviation, $|\Delta R|$, vs R^2 (b) Radial deviation, ΔR_r, vs R^2. The red line represents the mean deviation, and therefore serve as an estimate of the intrinsic uncertainty of the ML fit.

4.4.2 ^{83m}Kr event

The uniformity comparison in the R_{fRec} distributions of the ^{83m}Kr events is shown in Fig. 4.4, where the analytical algorithm wins over the simulation-based slightly. In the x_{fRec}-y_{fRec} distribution (Fig. 4.10), the average of the number of ^{83m}Kr events over the bins within the

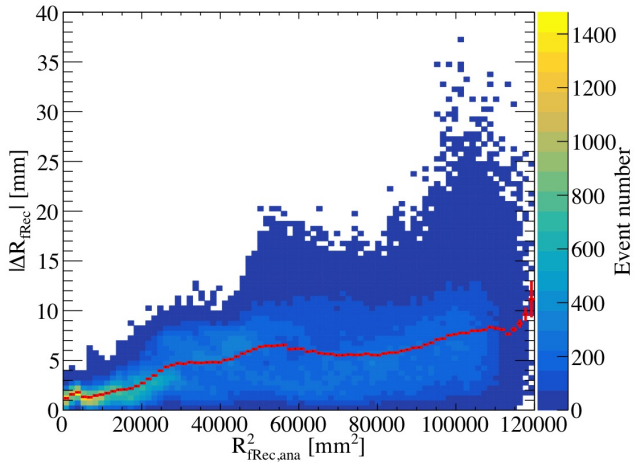

(a)

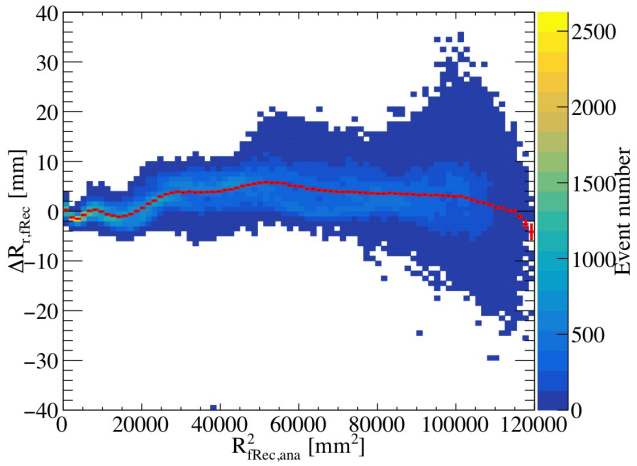

(b)

Figure 4.9: The total deviation between the reconstructed positions obtained by the two algorithms for the ^{83m}Kr events. (a) Total deviation, $|\Delta R_{\mathrm{fRec}}|$, vs $R^2_{\mathrm{fRec,ana}}$. (b) The radial deviation, $\Delta R_{r,\mathrm{fRec}}$, $R_{\mathrm{fRec,simu}} - R_{\mathrm{fRec,ana}}$, vs $R^2_{\mathrm{fRec,ana}}$. In both figures, the x-axis, $R^2_{\mathrm{fRec,ana}}$, is calculated with the analytical algorithm. The red line again represents the mean deviation.

detector boundary (black line) is 49.4 ± 13.4 (48.9 ± 14.1) for the analytical (simulation-based) algorithm. The standard deviations of the event numbers are taken as uncertainties in the average. The 2D uniformity of ^{83m}Kr is consistent with the R_{fRec} distribution.

The robustness in the simulation-based algorithm is slightly better than the analytical one. The average of the ^{83m}Kr event number calculated similarly for the third quadrant in Fig. 4.10

where two close PMTs are turned off is 48.8 ± 14.3 (48.4 ± 13.9) for the analytical (simulation-based) algorithm. The change of standard deviations suggests that the simulation-based algorithm is more stable when handling inhibited PMTs.

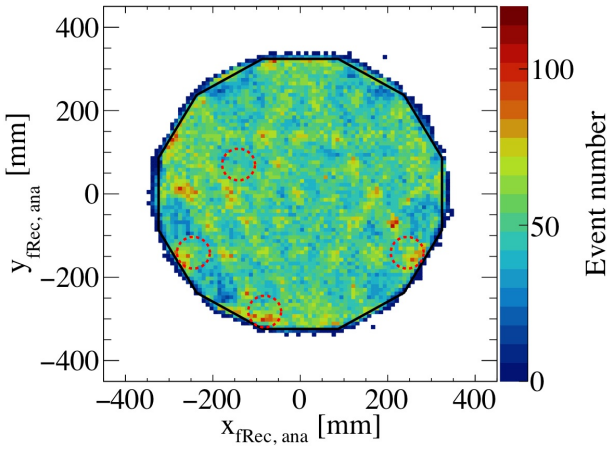

(a)

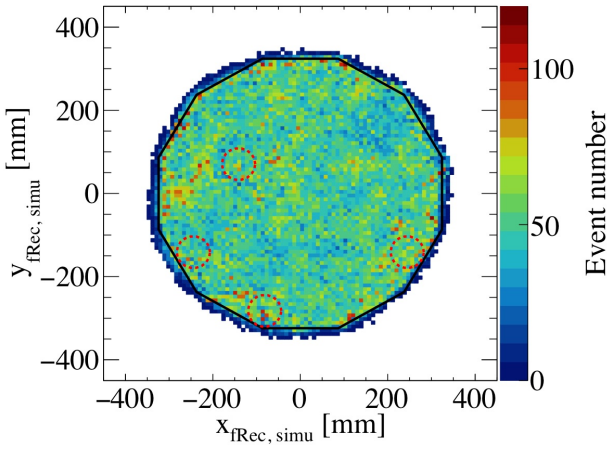

(b)

Figure 4.10: $x_{\text{fRec}} - y_{\text{fRec}}$ ^{83m}Kr event distribution using the (a) analytical and (b) simulation-based algorithms. The four red circles mark the inhibited PMTs.

4.4.3 Gate event

With the known geometry of the gate electrode wires (Fig. 4.11), we can use the gate events to estimate the uncertainties in the horizontal position reconstruction. These events are likely to come from radioactive isotopes attached to the grid wires. Because the electric field close to the wires is quite different from the bulk sensitive region, we lack enough information to identify the dominant isotopes. The gate events can be selected with the characteristic drifting time (2-4 μs). We select the $S2$ from 1000 to 20,000 PE to avoid the statistic uncertainty dominance and sufficient coverage for WIMP search purpose.

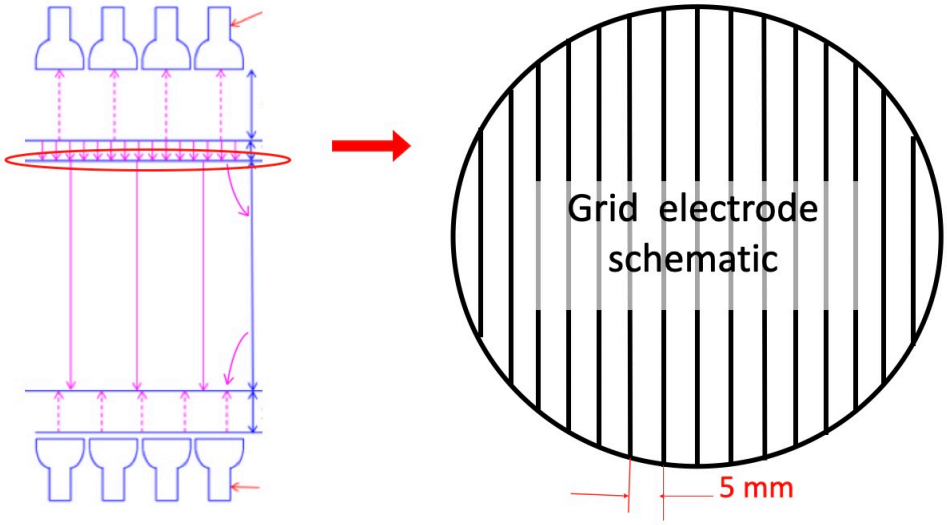

Figure 4.11: The sketch of the gate electrode geometry.

The 2D distribution of the gate events for the two algorithms can be found in Fig. 4.13. The grid wires are parallel to the x-axis and 5 mm apart along the y-axis. The gaps normally are not recognizable as shown by the events with $y_{\mathrm{fRec}} \in (-50, 0)$ mm in Fig. 4.13. For clarity, the peaks in the simulation-based algorithm in this region are caused by the binning of the 2D PAFs. Occasionally, due to some local defects, larger gaps can be seen. The red stars mark the

local minima of the event distribution, where only the events with $R < 300$ mm are included. We use Tab. 4.4 to compare the two algorithms, but the uncertainties in the local minimums are not the uncertainties in the position reconstruction algorithms similar to the argument that the uncertainties in the measured mean value of N measurements is smaller than the uncertainties in each measurement ($\sigma/\sqrt{N}$ vs. σ). The standard deviations in the local minimums can only serve as the lower bound of the uncertainties in the position reconstruction.

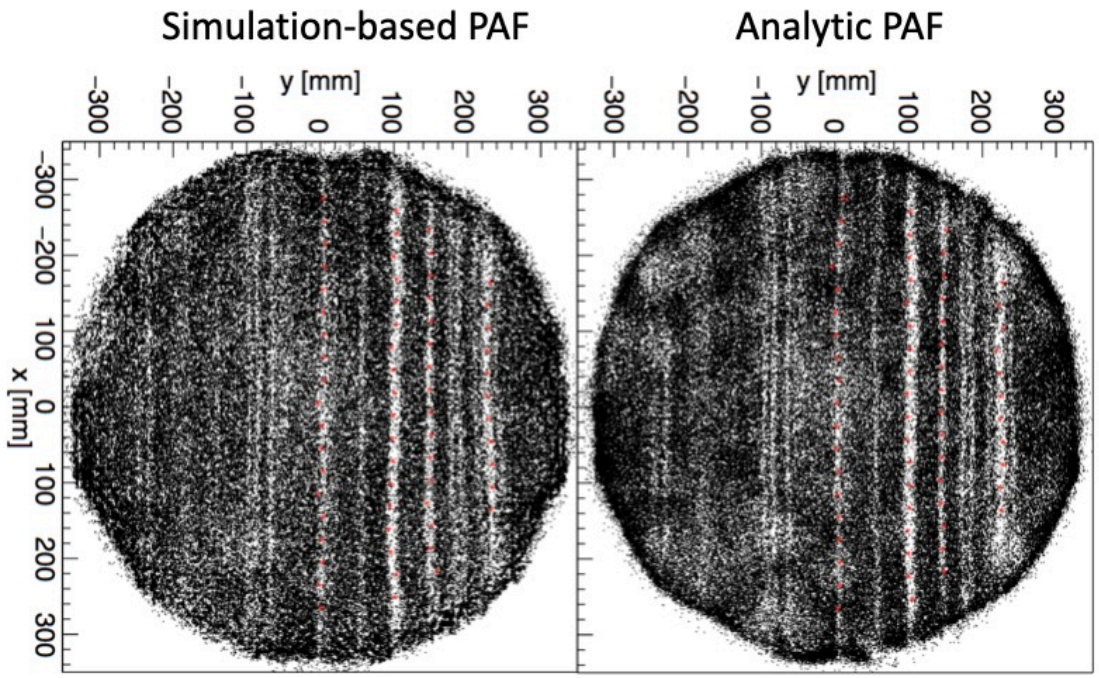

Figure 4.12: The positions of gate events reconstructed with the analytical (left) and simulation-based (right).

Table 4.4: The position of selected gaps in the gate events and standard deviations.

Gap No.	Simulation-based	Analytical
$y_1 \pm \sigma_{y_1}$	2.4±2.7	3.4±3.3
$y_2 \pm \sigma_{y_2}$	99.1±3.2	100.1±2.0
$y_3 \pm \sigma_{y_3}$	149.6±2.6	145.3±2.1
$y_4 \pm \sigma_{y_4}$	229.2±2.7	224.5±2.8

The projected y_{fRec} distributions of the gate-electrode events can also be used to study the uncertainties in the center of the detector. In Fig. 4.13, we also apply a spatial cut, $R^2_{\mathrm{fRec}} < 72000$ mm^2, to suppress backgrounds from the surface and outside the detector. This fiducial radius cut is the same as the WIMP search in PandaX-II [34]. We identify the malfunctioning grid wires according to the troughs and fit the y_{fRec} distribution with Eq. 4.17, where p_0 is constrained to the peak within $(-95, -85)$ mm, σ_{gate} represents the uncertainties in the position reconstruction, d_0 is the reconstructed gap between grid wires, and N_1 to N_6 are the fitted event numbers on the corresponding grid wires. The three troughs in Fig. 4.13 at -95 mm, -85 mm and -65 mm correspond to the Gaussian functions skipped for the centers at $p_0 - 1d_0$, $p_0 + 1d_0$ and $p_0 + 5d_0$, respectively. At these sites, the grid wires may be sagging or have poor electrical connections with their holder in -100 °C liquid xenon.

$$
\begin{aligned}
f = {} & \mathrm{Gaus}(y_{\mathrm{fRec}}, p_0, \sigma_{\mathrm{gate}}) \cdot N_1 + \\
& \mathrm{Gaus}(y_{\mathrm{fRec}}, p_0 - 2d_0, \sigma_{\mathrm{gate}}) \cdot N_2 + \\
& \mathrm{Gaus}(y_{\mathrm{fRec}}, p_0 + 2d_0, \sigma_{\mathrm{gate}}) \cdot N_3 + \\
& \mathrm{Gaus}(y_{\mathrm{fRec}}, p_0 + 3d_0, \sigma_{\mathrm{gate}}) \cdot N_4 + \\
& \mathrm{Gaus}(y_{\mathrm{fRec}}, p_0 + 4d_0, \sigma_{\mathrm{gate}}) \cdot N_5 + \\
& \mathrm{Gaus}(y_{\mathrm{fRec}}, p_0 + 6d_0, \sigma_{\mathrm{gate}}) \cdot N_6,
\end{aligned}
\tag{4.17}
$$

and the Gaus is the Gaussian function,

$$
\mathrm{Gaus}(x, \mu, \sigma) = \frac{1}{\sigma\sqrt{2\pi}} \exp\left[-\frac{(x-\mu)^2}{2\sigma^2}\right]. \tag{4.18}
$$

The best-fitting parameters are shown in Tab. 4.5. As the diameter of the wires (100 μm) is much smaller than the σ_{gate}, the dispersion represents the local uncertainties. $\overline{|\Delta R_{\text{fRec}}|}$ in Fig. 4.9(a) (5.2 ± 3.6 mm) is consistent with the propagated uncertainty $\sqrt{\sigma^2_{\text{gate,ana}} + \sigma^2_{\text{gate,simu}}} = 5.2$ mm. In principle, the event numbers, from N_1 to N_6, should be the same regardless of the reconstruction algorithms. $N_{1,2,6}$ for the two algorithms are consistent within the fitting errors. However, because we use three Gaussian functions for a single peak in $(-85, -65)$ mm to constrain d_0 better, which brings too many degrees of freedom, the differences in $N_{3,4,5}$ are larger.

Table 4.5: The results of fitting Eq. 4.17 with the y_{fRec} of the gate events reconstructed with the two algorithms.

	σ_{gate} [mm]	d_0 [mm]	p_0 [mm]			
	3.36 ± 0.10	5.33 ± 0.04	-90.2 ± 0.2			
Analytical	N_1	N_2	N_3	N_4	N_5	N_6
	135 ± 7	192 ± 8	57 ± 8	165 ± 9	100 ± 10	175 ± 7
	σ_{gate} [mm]	d_0 [mm]	p_0 [mm]			
	3.94 ± 0.16	5.58 ± 0.07	-91.7 ± 0.3			
Simulation-based	N_1	N_2	N_3	N_4	N_5	N_6
	119 ± 7	173 ± 9	84 ± 10	125 ± 10	60 ± 10	176 ± 7

A double check of the invisibility of the gaps with a 3 mm position resolution can be done with a toy MC where the events are smeared manually with a 2D Gaussian with a σ as 3 mm which is plotted in Fig. 4.14.

4.4.4 Surface event

We use the PTFE surface events to study the upper bound of the uncertainties with different $S2$s [184]. Moreover, the uncertainties in the position reconstruction is tightly related to the probability distribution function (PDF) of surface backgrounds. This section presents the procedure

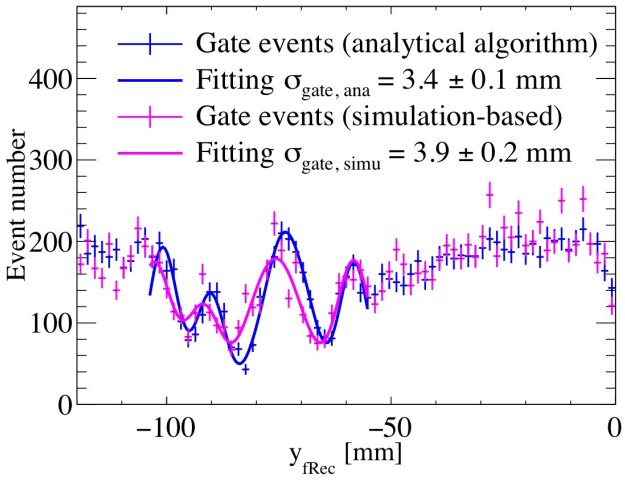

Figure 4.13: The gate events y_{fRec} distribution projected along the grid wires with the analytical (blue) and simulation-based (magenta) algorithms. The solid lines are the corresponding fittings to the y_{fRec} distribution by six Gaussian functions with the same width.

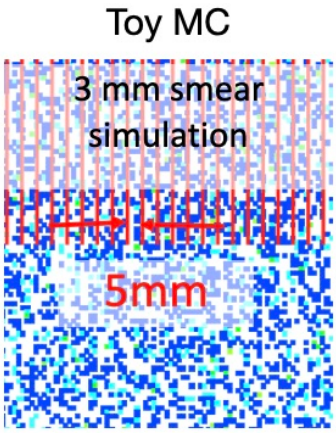

Figure 4.14: The toy gate events smeared with a 3 mm 2D Gaussian.

of the PDF construction of surface backgrounds where the analysis of the uncertainties is included.

Before diving into the details, let's discuss the general properties of the surfaces events. If we loose the FV cut, the surface backgrounds become the dominant backgrounds, indistinguishable with the other survived events if the spatial information is not preserved. Surface events are dominant by β decays and ^{206}Pb released by the α-decay of ^{210}Pb in the ^{238}U decay chain in the

region of interest (ROI) as plotted in Fig. 4.15. The β-decay has an energy end-point of 63.5 keV and a half-life of 22.2 y. As discussed in [188], many surface events have only part of the $S2$s can be collected in the surface events, which causes a lower $S2/S1$ compared to normal ERs.

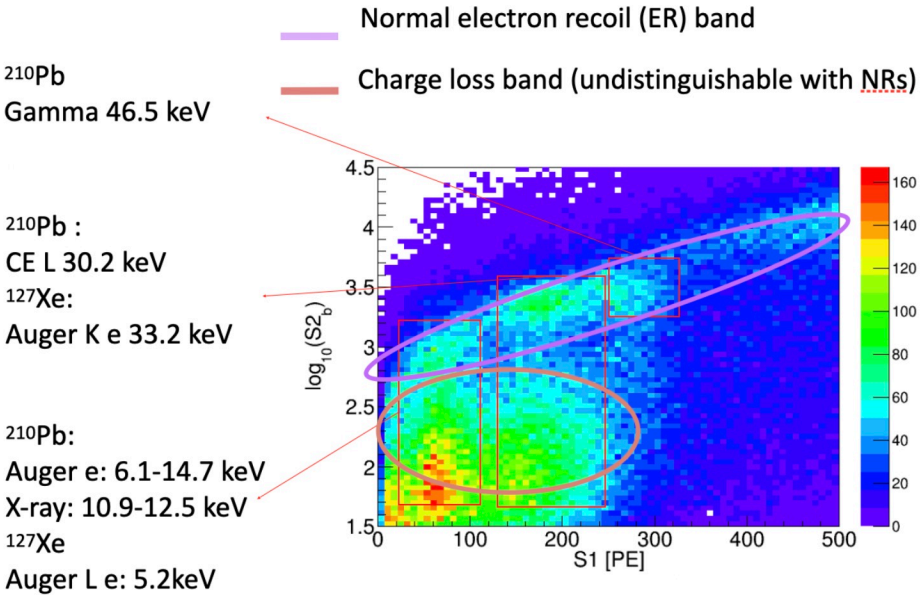

Figure 4.15: The $\log_{10}(S2/S1)$ vs $S1$ for the surface events in PandaX-II.

The properties of surface backgrounds in the ROI can be studied with events outside the ROI. The data with nominal reconstructed positions outside the border of our detector can represent the properties of surface events contribute to the backgrounds because the percentage of the bulk events are negligible in these surface events. An exception of the properties is the radial position uncertainties because the horizontal position reconstruction algorithm and the radial electric field result in asymmetric position uncertainties for events inside and outside the nominal border of our detector. Therefore, the estimation of surface backgrounds is factorized into two parts, one describing the radial position uncertainties and the other including other properties.

Besides the parameters used in the old PDFs of backgrounds, $S1$ and $S2$, and the radius of the recoiling events, the vertical position, z, can be implicitly included in the surface-background

PDF. Because the marginal effect of the electric field, the distortion of the field close to the wall, and a non-uniform WIMP-search cut efficiency along z, including the vertical information more accurately construct the PDF of the surface events.

The surface-background PDF is factorized into two independent parts, one for the radius distribution, noted as P_R, and the other for $S1$, $S2$ and z, denoted as P_d. To parameterize the former part, data with $S1$ larger than the ROI but the same $S2$ are used. We first define the nominal border of our detector, termed as the soft wall, by the median positions of the surface events with different z and azimuth angles. Then, P_R is parameterized as a function of $S2$ and the distance to the soft wall, r_w. For the latter part, P_d, a data-driven histogram related to $S1$, $S2$, and z, is fitted with kernel density estimator (KDE) [189], a statistic tool smoothing out the distribution. The final PDF model is

$$P_{b,\mathrm{wall}}(r_w, \mathrm{S1}, \mathrm{S2}, \mathrm{z}) = \mathrm{P_R}(\mathrm{r_w}, \mathrm{S2}) \times \mathrm{P_d}(\mathrm{S2}, \mathrm{S1}, \mathrm{z}). \tag{4.19}$$

To find the median radial positions of the surface events, data with $S1$s from 50 to 500 PE are used, which are outside of the ROI. The surface events in this range are dominant by the decays of ^{210}Pb and ^{210}Bi in the ^{238}U decay chain. With the flat distribution inside the detector subtracted, the median of the 1D event distribution along radius for different z and azimuth angles is set as the border of our detector. Then, the average on the radius of the soft wall is stretched to be the same as the solid boundary of our TPC (329.7 mm). The original reconstructed positions have all been horizontally stretched 7% and 6% for the analytical and simulation-based PAF algorithm, respectively. The stretched soft walls and the corresponding inward 1σ fluctuations are shown in Fig. 4.16, which indicate the uncertainties in different position reconstruction

algorithms.

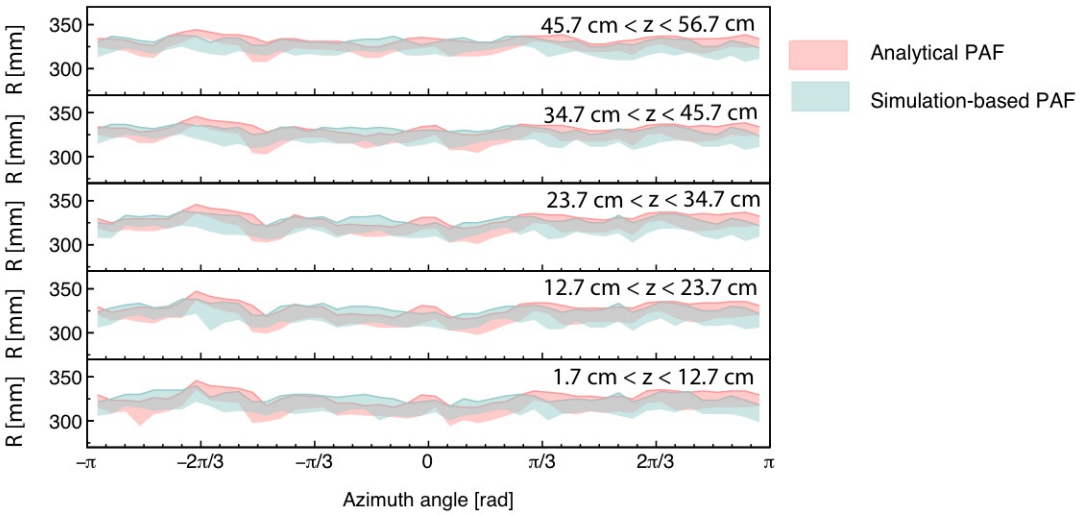

Figure 4.16: The stretched soft walls and 1σ inward fluctuation bands with analytical and simulation-based PAF algorithms. The vertical range is bounded from $z = 0$ (the bottom of the TPC) to $z = 60$ cm (the liquid surface).

The equivalence of different position reconstruction algorithms is shown in Fig. 4.17, which is determined by requiring the same amount of surviving events with the same cuts. The cuts used, excluding the radial cut, are the same as mentioned in Ref. [34] except for the $S1$-$S2$ cut, because the statistics will otherwise be too small. In Fig. 4.17, the dashed blue line marks the solid boundary (329.7 mm), and the solid blue line indicates the old FV cut, $R^2 < 7.2 \times 10^4$ mm^2 and $1.7\,\mathrm{cm} < \mathrm{z} < 56.7\,\mathrm{cm}$, for the former analysis in Ref. [34]. The red and green dashed lines are the stretched soft walls averaged over azimuth angle of the analytical and simulation-based PAF algorithms, respectively. The corresponding equivalent radial cut, $r_w < -64.8$ mm / $r_w < -63.9$ mm for the analytical / simulation-based PAF algorithms, is drawn in a dashed line with the same color. In the old FV cut, the dependence on z is neglected, which is included in the parameter r_w in the new FV cuts. The conversion between z and the drifting time, Δt_z, is done with known drifting velocity of free electrons during Run 10, $v_e = 1.7$ mm/μs [34].

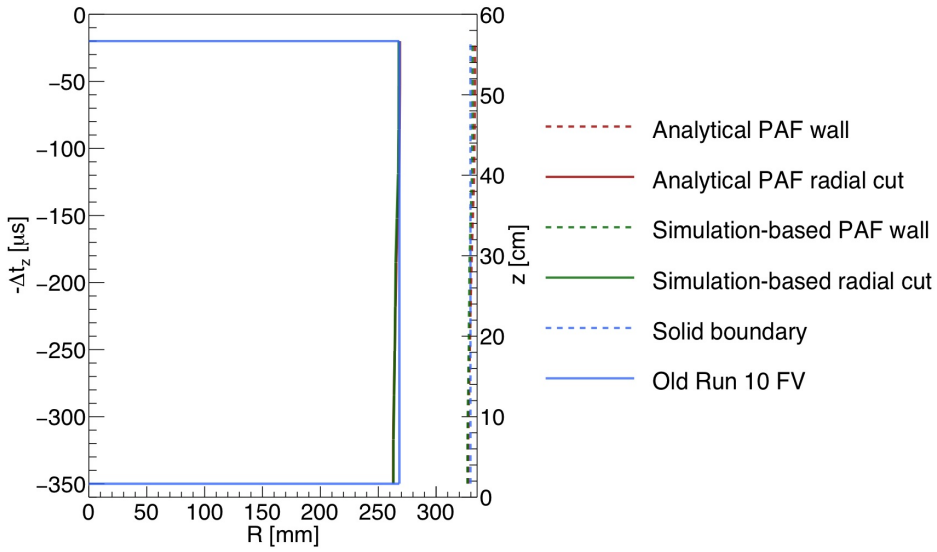

Figure 4.17: The soft walls and equivalent radial cuts with different position reconstruction algorithms. The radius of the solid boundary (329.7 mm) and the old FV cut used in Run 10 [34] are drawn for reference.

After defining the soft walls, $P_R(r_w, \mathrm{S2})$ is built with the same data used in the soft-wall construction, which describe the radius distribution inside the soft wall. The surface-background distributions with different $S2$s and position reconstruction algorithms are shown in Fig. 4.18, where the negative sign of r_w represents inward fluctuation. Larger $S2$s have smaller fluctuation in the radius, which agrees with our statistical intuition. Due to the asymmetry in the radial position uncertainties, only the events with negative r_w are used to construct P_R.

We use normal functions to fit the inward fluctuation of surface events for different $S2$s, which means P_R can be modeled as

$$P_R(r_w, \mathrm{S2}) = \frac{1}{\sqrt{2\pi\sigma_\mathrm{r}(\mathrm{S2})^2}} \cdot \exp(-\frac{\mathrm{r_w^2}}{2\sigma_\mathrm{r}(\mathrm{S2})^2}). \tag{4.20}$$

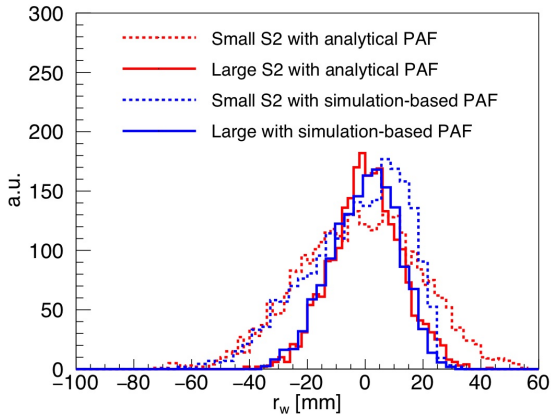

Figure 4.18: Run 10 surface-background distribution with different $S2$ ranges and different position reconstruction algorithms with all cuts applied in Ref. [34] except the $S1$-$S2$ and FV cut. Small $S2$ is for 200 to 250 PE, and large $S2$ for 900 to 1100 PE. The inner flat event distribution has been subtracted.

The fitted standard deviations, $\sigma_{\rm surf}$, shown in Fig. 4.18 are further parameterized as an analytic function of $S2$,

$$\sigma_{\rm surf}(\mathrm{S2}) = \frac{1}{\mathrm{p0} - \mathrm{p1}\cdot\log_{10}\mathrm{S2} + \mathrm{p2}\cdot(\log_{10}\mathrm{S2})^2}\,\mathrm{cm}, \quad \mathrm{S2} <= 3000\ \mathrm{PE}, \tag{4.21}$$

When $\mathrm{S2} > 3000$ PE, the uncertainties in the position reconstruction algorithms start to dominate instead of the statistical uncertainties, which can serve as a conservative estimation of the uncertainties as shown in Fig. 4.19.

P_d is constructed independently, to reflect the properties of the surface events other than the radial position uncertainties. The data used to derive P_d are the events survived the WIMP-search cuts in Run 10 except the radius in the FV cut. The events with $r_w > 0$ is used to suppress all the other contributions to a negligible level. We inherit the $S1$ and $S2$ from old PDFs which present strong signal discrimination power over ER backgrounds. The z distribution of the surface events is non-trivial. In Fig. 4.20, the decrease of surface backgrounds for events with drifting time

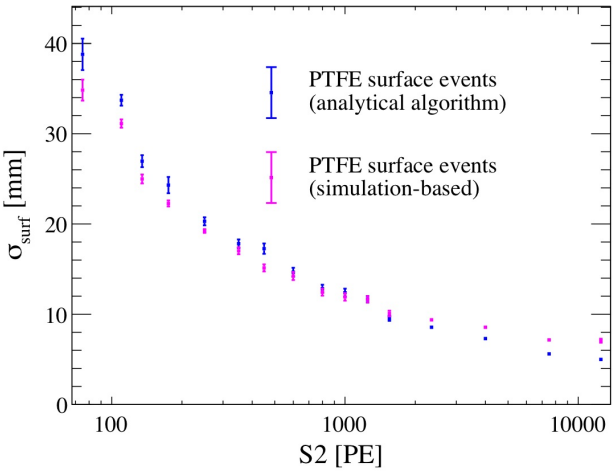

Figure 4.19: The change of σ_{surf} as a function of $S2$ in a wide range.

longer than 200 μs is because of marginal effect of the electric field. The electrons are drifted towards the wall where the radial fraction of the electric field points out, and no $S2$ will generate. In the data with smaller drifting time, the efficiency of WIMP-search cuts causes irregularity. Therefore, besides r_w and old parameters, z is also included in the new PDF. The original event distribution as a function of $S1$, $S2$ and z is smoothed with KDE integrated in Python. Because it is difficult to visualize four-dimensional PDFs according to Eq. 4.19, the PDFs are projected as in Fig. 4.21.

4.5 Summary

To reach a millimeter level resolution in the horizontal position reconstruction for a TPC mounted with 3-inch PMTs, we develop two algorithms based on the previous works. In the analytical algorithm, we introduce two groups of parameters to extend the axially-symmetric PAF for non-negligible reflection. In the simulation-based one, we tune the light emission points in the gas phase as a function of x and y. Both algorithms are trained with ^{83m}Kr data. The

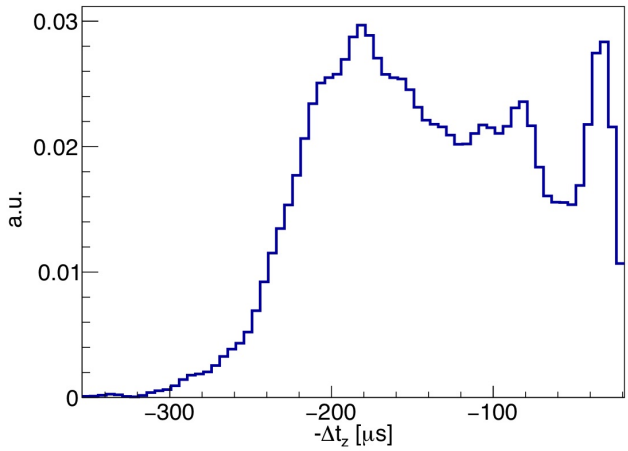

Figure 4.20: The Δt_z distribution of the Run 10 surface events after applying the WIMP-search cuts excluding the radial cut. Other dimensions are integrated. The drifting time from 20 to 350 μs corresponds to z from 56.7 to 1.7 cm

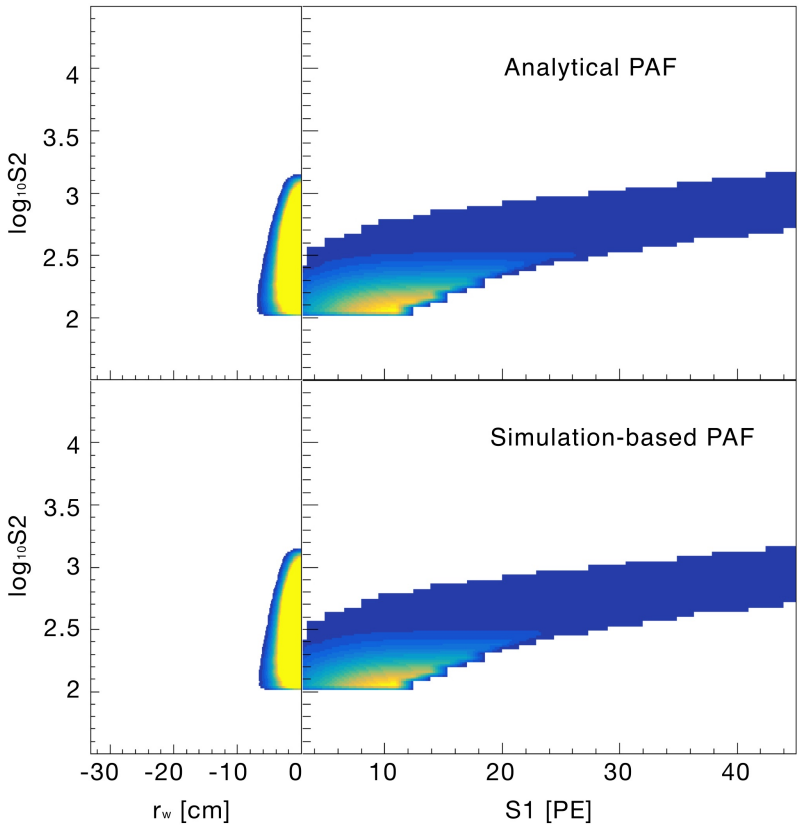

Figure 4.21: The projections of $P_{b,\text{wall}}$ onto different axes. The top / bottom panel is for the analytical / simulation-based PAF algorithm respectively. The left panels integrate the other two dimensions ($S1$ and z), and the right panels only integrate events in the corresponding FV.

reconstructed horizontal positions are stretched radially by a factor of 1.07 (1.06) in the analytical (simulation-based) algorithm to make the mean radius of the surface-event positions agree with the solid boundary.

Applying both algorithms to the PandaX-II detector, the uniformity of the $R^2_{\rm fRec}$ distribution of ^{83m}Kr reaches 4.3% (5.3%) in the analytical (simulation-based) algorithm within $R^2_{\rm fRec} < 1\times10^5$ mm^2, and the average difference in the reconstructed positions between the two algorithms is 5.2 ± 3.6 mm. Using the gate events, the uncertainties are 3.4 mm $(3.9$ mm) for the analytical (simulation-based) algorithm when $S2s$ are of several thousand PEs. For $S2s$ with several hundred PEs, the uncertainties are several centimeters near the PTFE surface.

As two algorithms are comparable in uncertainties in the WIMP search $S2$ region, we decide to apply the simulation-based algorithm in the final analysis of PandaX-II because of the robustness, and preserve the analytical algorithm as a crosscheck.

Chapter 5: Overview of PandaX-4T experiment

This chapter briefly reviews the subsystems of PandaX-4T experiment and the Run 1 data for spin-indepedent (SI) WIMP-nucleus scattering search.

5.1 Subsystems

PandaX-4T preserves the designs of previous dual-phase liquid xenon time projection chambers (LXeTPCs) and scales up to hold 5.6 ton xenon in the pressure vessel where 3.7 ton xenon is in the sensitive region viewed by PMTs. The infrastructure and subsystems are up-scaled accordingly to reach the running condition requirements. The layout of the main workspace can be seen in Fig. 5.1, where the TPC sits at the center of the water shielding tank. The data acquisition (DAQ) system is right above the detector in the clean room. The cryogenics and main circulation system are in the Class 1000 clean room. The new distillation tower is right outside the clean room and connected to the circulation system, which can be turned on for online purification.

5.1.1 TPC and electrodes

The stainless steel (SS) inner vessel (IV) (1.3 m diameter, 1.8 m height) is separated from the outer SS vessel (OV) with a 12.5 cm vaccum jacket. All the cables, tubes and feedthroughs

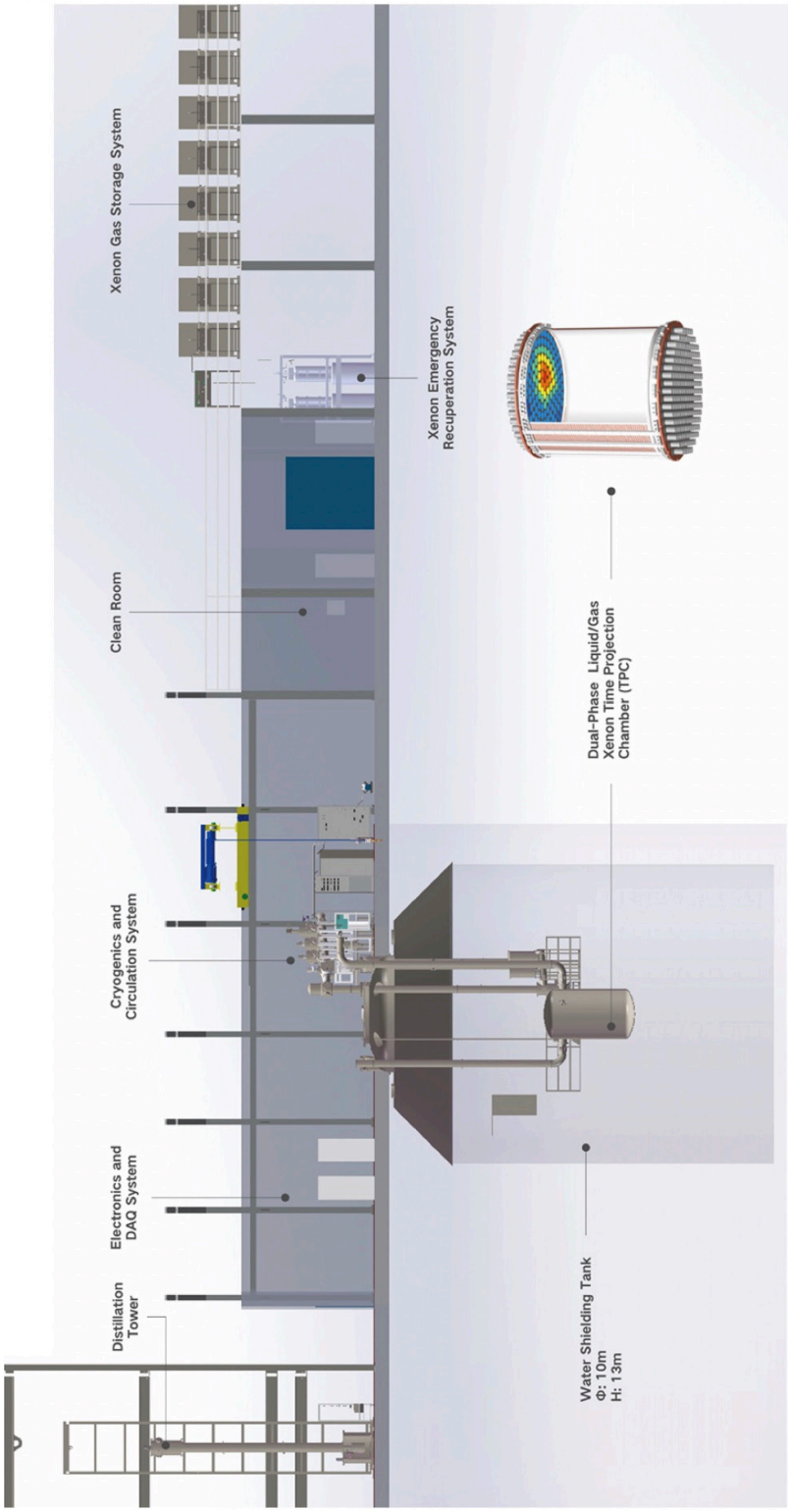

Figure 5.1: Overview of the PandaX-4T experiment

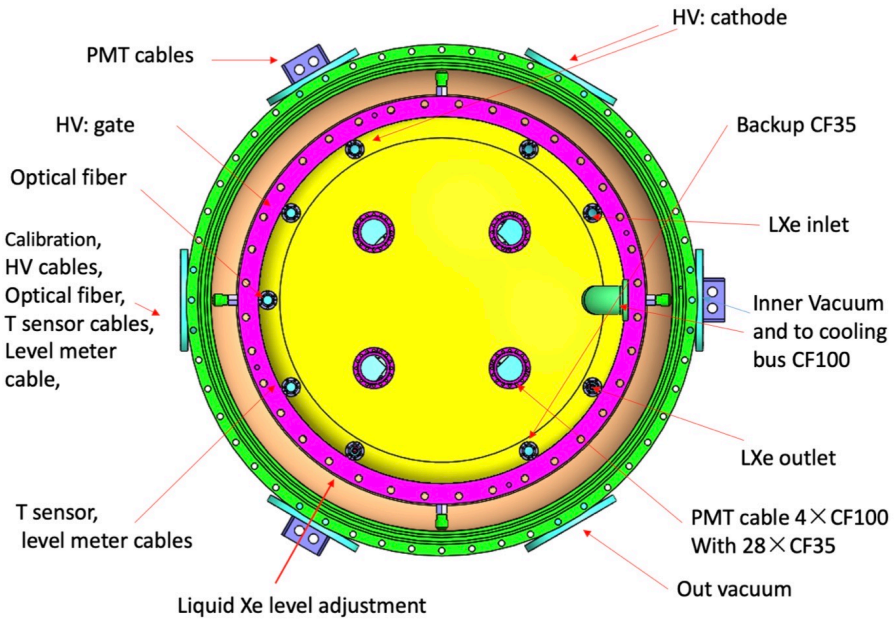

Figure 5.2: The arrangement of the ports for the IV and OV of PandaX-4T.

are guided to the top of the IV with the layout as shown in Fig. 5.2. The PandaX-4T TPC is a 24 polygon cylinder surrounded by the polytetrafluoroethylene (PTFE) panels with a 1.2 m diameter whose cross-sectional view can be found in Fig. 5.3(a), about 7 cm away from the wall of IV. The two copper (Cu) boards with a diameter 1 cm smaller than that of the IV are connected by 24 PTFE supporting rods. The side of the Cu boards facing the sensitive region has a layer of PTFE reflector mounted for a higher photon collection efficiency. The 2 cm thickness of the Cu boards is optimized for the buoyancy.

Four main electrodes are mounted in PandaX-4T detector (Fig. 5.3(b)) on the TPC, including the anode (grounded), gate electrode (about -5 kV), cathode (-15 to -50 kV) and screening electrode (grounded). The liquid-gas interface is between the anode and gate electrode separated by 10 mm. The drifting region is 1185 mm, referring to the distance between the gate and cathode. The distance between the cathode and the screening electrode to protect the bottom PMT array is

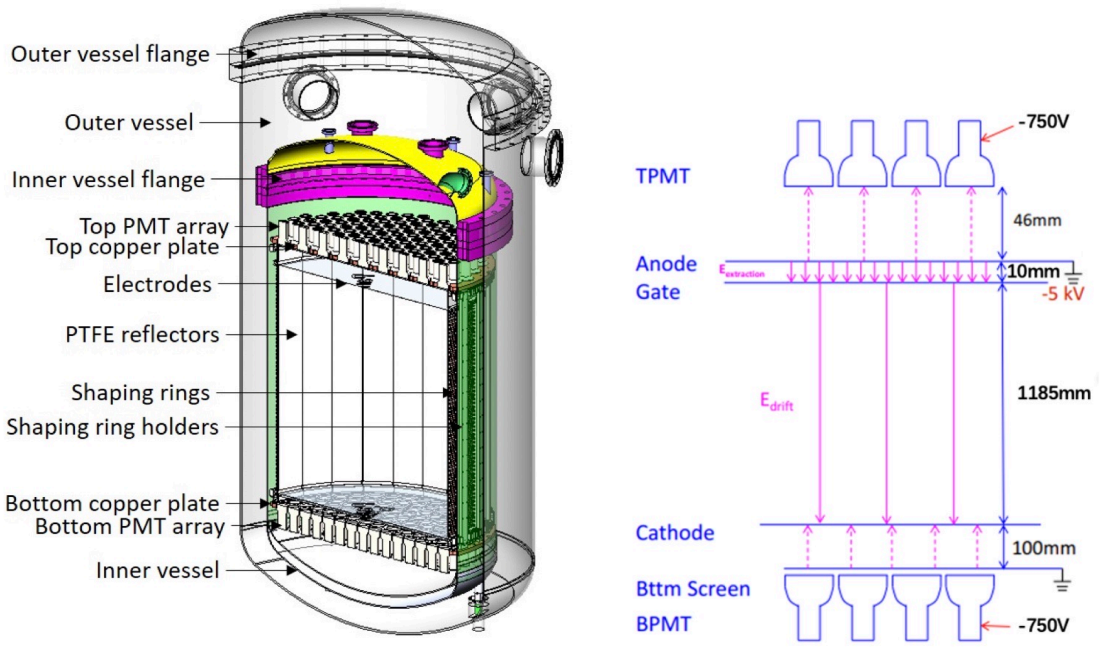

(a) (b)

Figure 5.3: (a) A cross-sectional view of the PandaX-4T detector. (b) The layout of the four main electrodes in PandaX-4T.

100 mm. The anode and gate electrode are manufactured with meshes (Fig. 5.4(a)) with $3\ \mathrm{mm} \times 3\ \mathrm{mm}$ holes and 190 μm SS wires. The cathode and screening electrode are made of 200 μm grid wires (Fig. 5.4(b)) aligned with 5 mm separation. In general, the grids are preferred for higher transmittance of light (96%) compared to the meshes (86%) for our electrodes. Furthermore, grids can in principle hold higher voltages. However, it's more complicated to manufacture the grid electrodes.

The field cage is guided with 58 loops of Cu shaping rings (Fig. 5.5). Each loop has 24 Cu rods whose shape has been optimized for a more uniform electric field with COMSOL simulation. The Cu rods in the two bottom layers have a width of 4 mm, and the others 3 mm. The whole TPC is connected to the IV lid with six SS screws. The resistors (1 GΩ for each) welded on a Kapton sheet set the potential gradients over the shaping rings. Two parallel series of resistors

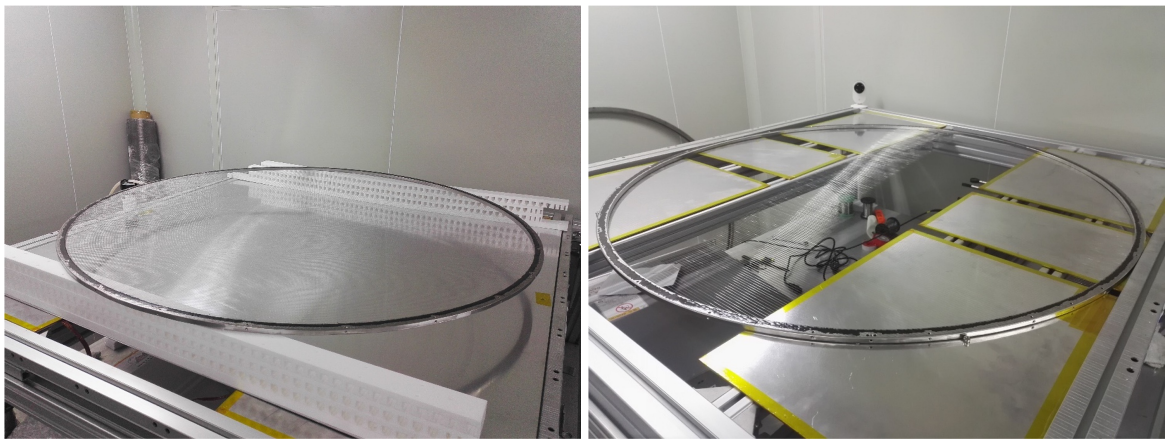

(a) (b)

Figure 5.4: (a) The gate electrode in PandaX-4T (b) The cathode in PandaX-4T.

are used to avoid failure due to an unexpected open circuit.

Figure 5.5: The front view of the PandaX-4T TPC.

A couple of other components are mounted in the TPC including light emitting diodes

(LEDs), the overflow chamber and different sensors. PandaX-4T has 4 optical fibers connected to the LEDs for PMT gain calibration. PTFE caps (Fig. 5.6(a)) are used to diffuse the photons. The 30 L overflow chamber shown in Fig. 5.6(d) is at the bottom of the detector to adjust the liquid-gas level (Fig. 5.6(c)) and also serves as the outlet of the IV, connecting to circulation system for purification. To balance the pressure in the overflow chamber, besides the two tubes mentioned before, the third one is connected to the gaseous xenon. In the detector, two long 0.6 m level meters are mounted to monitor the xenon levels during filling, and three 1 cm level meters (Fig. 5.6(b)) are used to monitor the change of the liquid-gas interface. Customized level meters are used where the capacitance change converts to the liquid level. In addition, five PT-100 temperature sensors are mounted on the top of IV, on the upper and lower Cu board, at the middle of a PTFE supporting rod and in the overflow chamber, and another four are put on the outside of the IV.

5.1.2 PMT, readout electronics and DAQ system

Both PandaX-II and PandaX-4T detectors use Hamamatsu R11410 3-inch PMTs to detect scintillation photons in the sensitive region. PandaX-4T increases the number of the top array from 55 to 169 and the bottom array from 55 to 199. In the veto region between the TPC and the wall of IV, 1-inch R8520-406 PMTs are mounted (48 used in PandaX-II and 105 used in PandaX-4T). The quantum efficiency is approximately 30-35% for 175 nm (xenon scintillation light) as shown in Fig. 5.7.

Photoelectrons at the entrance photo-cathode of the PMTs are amplified through dynodes (DYs) and the anode. In PandaX-II (preserved in PandaX-4T), 12 dynodes were used between

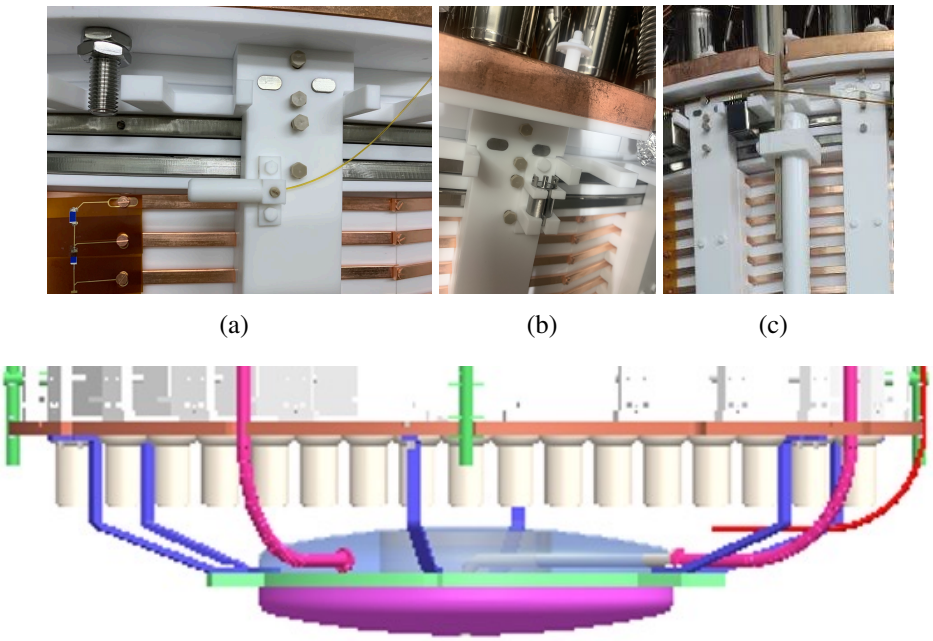

Figure 5.6: (a) The blue LED covered with a PTFE diffuser. (b) The short level meter. (c) The overflow port at the liquid-gas interface. (d) The overflow chamber at the bottom of the IV.

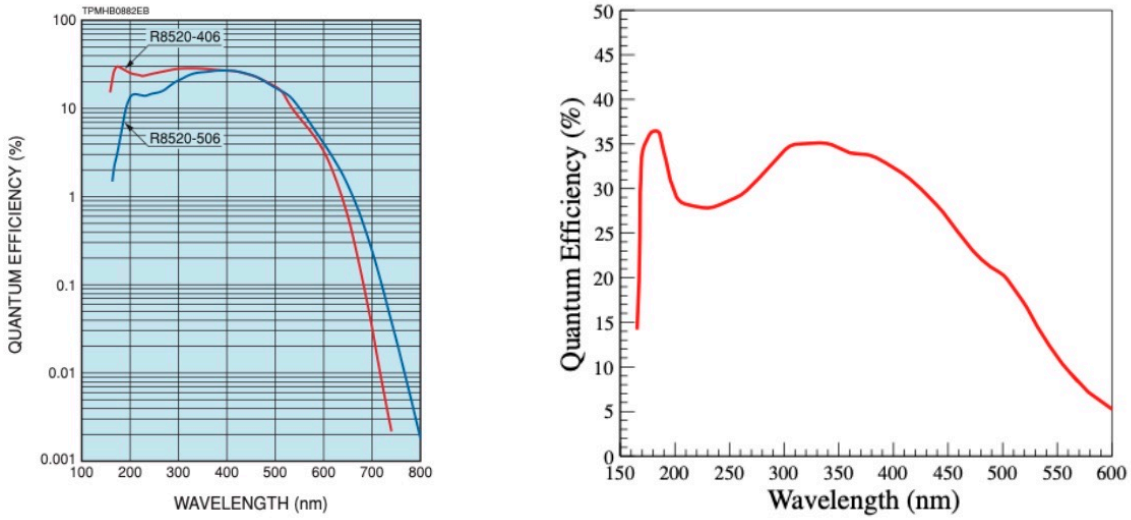

Figure 5.7: The quantum efficiency of R8520 (left) and R11410 (right) PMTs used in PandaX-II and PandaX-4T as a function of scintillation wavelength .

cathode and anode to reach a typical 5.5×10^6 (2.3×10^6) gain for the 3-inch (1-inch) PMT with 1500 V difference. Resistors in the circuit determine the voltages over different DYs. A split positive and negative HV scheme is adopted to reduce the discharging probabilities among the feedthrough pins which are separated by several millimeters. Initially, the PMTs started with $\pm$750 V where each PMT has an individual channel for the positive HV supplier, and 8 PMTs share a negative one. Behaviors of some PMTs deteriorate gradually over time, including severe afterpulses and lower gains due to lower HV to stop discharges. Some PMTs are turned off to preserve the quality of data. In PandaX-4T commissioning data released, 9 PMTs are turned off for malfunctional base connections, and 4 for large noises. The average dark rate is about 100 Hz per channel. It is worthwhile to mention that new readout base boards with an extra readout at Dy8 to mitigate PMT saturation in the high energy range $\mathcal{O}(1)$ MeV [35] are applied in PandaX-4T (Fig. 5.8).

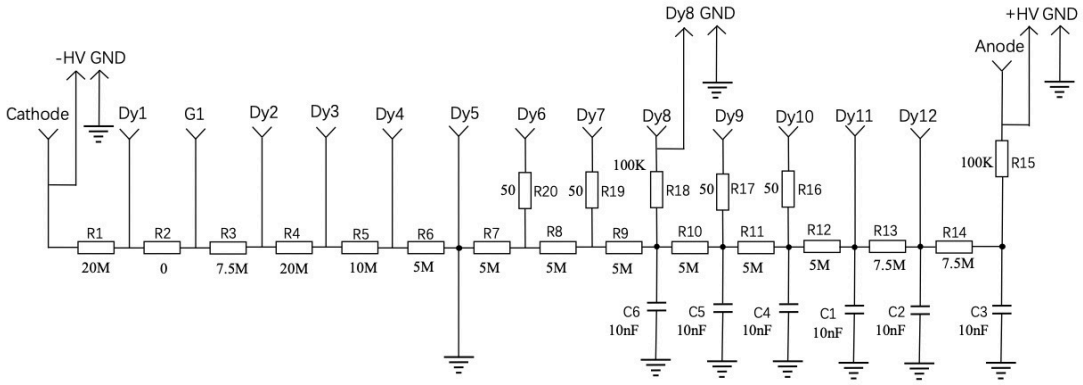

Figure 5.8: The PMT readout in PandaX-4T with a new readout at DY8 for MeV-scale analysis [35].

The schematics of the overall readout electronics and DAQ system of PandaX-4T is shown in Fig. 5.9 [36]. Firstly, the anode signals from PMTs are transmitted to the decoupling and

amplification modules to extra out and amplify the pulsive signals. The customized decoupling and amplifying circuits can be found in Fig. 5.10. The low-noise linear amplifers give a gain of 1.5 and 5 for the 3-inch and 1-inch PMTs used, respectively. Secondly, the decoupled and amplified signals are transmitted to digitizers (CAEN V1725B, 250 MS/s sampling rate) where one ADC count corresponds to 0.122 mV. Each digitizer has 16 channels, and in total 32 are used. In PandaX-4T, a single photoelectron (SPE) signal in the 3-inch PMTs typically has an amplitude about 7 mV and the pulse width 20–30 ns. Finally, the digitized data are transmitted to DAQ servers (Dell R730) with a rate up to 85 MB/s for each digitizer (one server for 8 digitizers and 4 servers in total). The acquired data are transferred to another data server (Dell R930) by an optical fiber (10 Gbps) which are raw data ready for further software processing and analysis. More details can be found in Ref. [36].

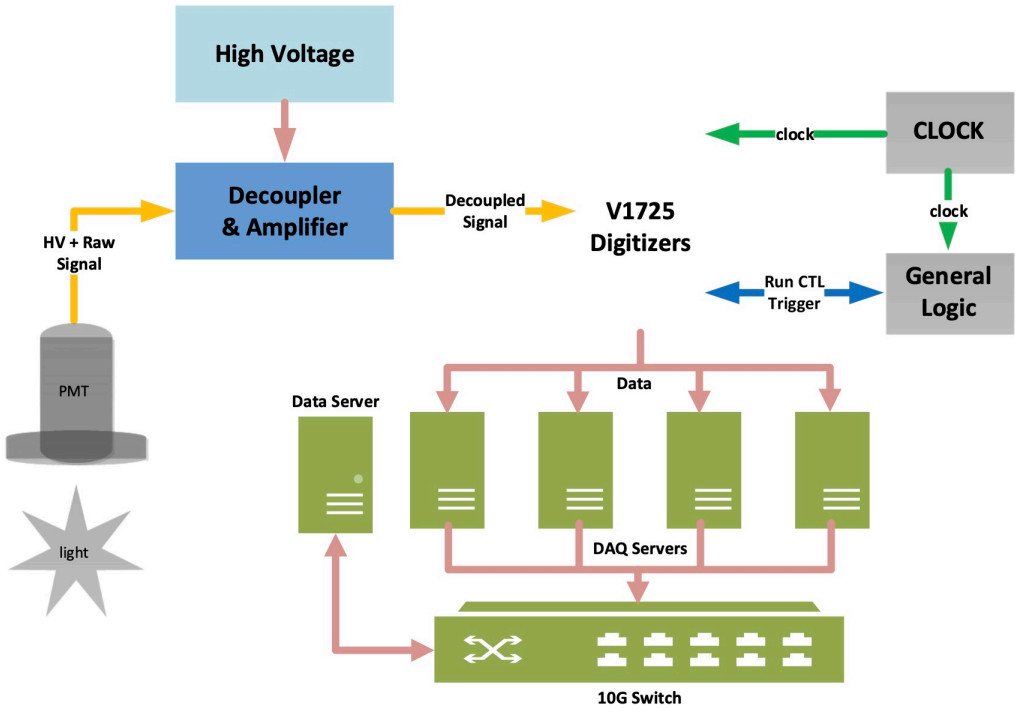

Figure 5.9: The overivew of PandaX-4T readout electronics and DAQ system [36].

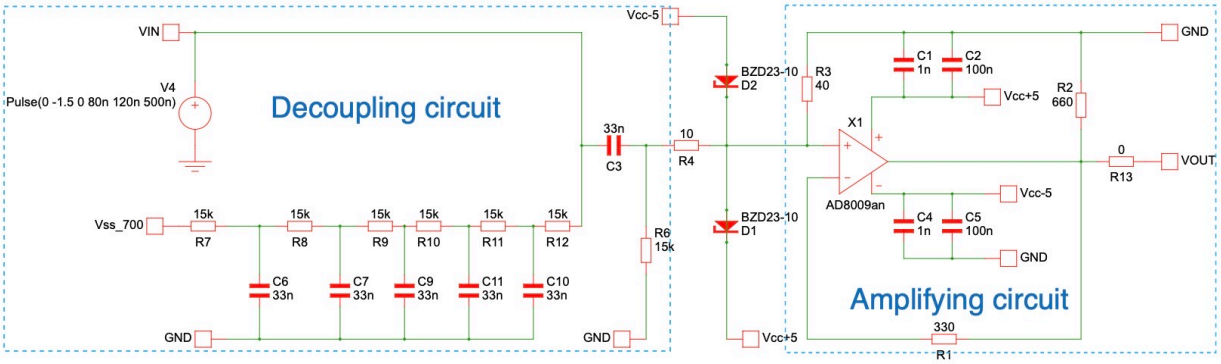

Figure 5.10: The decoupling circuit and amplifying circuit [36].

5.1.3 Cryogenics, circulation system and distillation tower

With the experience on the previous cooling bus in PandaX-I and PandaX-II, the new cryogenic system includes three coldheads which can reach 580 W cooling power at 178 K [37]. The maximum total purification speed of two circulation loops is up to about 155 SLPM. As shown in Fig. 5.11, the cooling bus has a single stage Gifford McMahon (GM) RDK-500B, a PTR PT-90 and a PTR PC-150. A liquid nitrogen (LN2) sorption pump is included for emergency cases, such as power-off or malfunctioning of pumps. A cooling SS tube in a coil shape is installed in the cooling tower of RDK-500B, going through inner and outer chamber with access to LN2. The LN2 pump can be turned on manually for some other uses like retrieving xenon or speeding up the filling. The xenon filling rate for PandaX-4T commissioning with LN2 pump turned on can be found in Fig. 5.12. Before starting to fill the IV, it was pre-cooled with 1.5 barG xenon gas filled for 2 days.

The cooling bus is part of the circulation system, which also includes the heat exchangers (HE), circulation pumps, hot purifiers and other attachable modules like the calibration panel and the distillation tower. Similar to PandaX-II, two parallel loops (LOOP1 and LOOP2) with hot

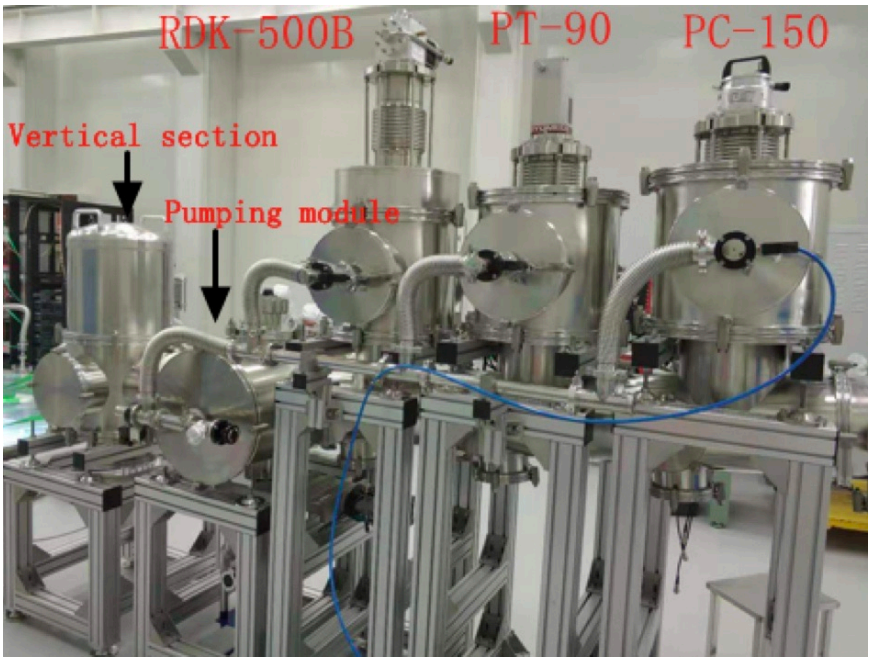

Figure 5.11: The cooling bus of PandaX-4T [37].

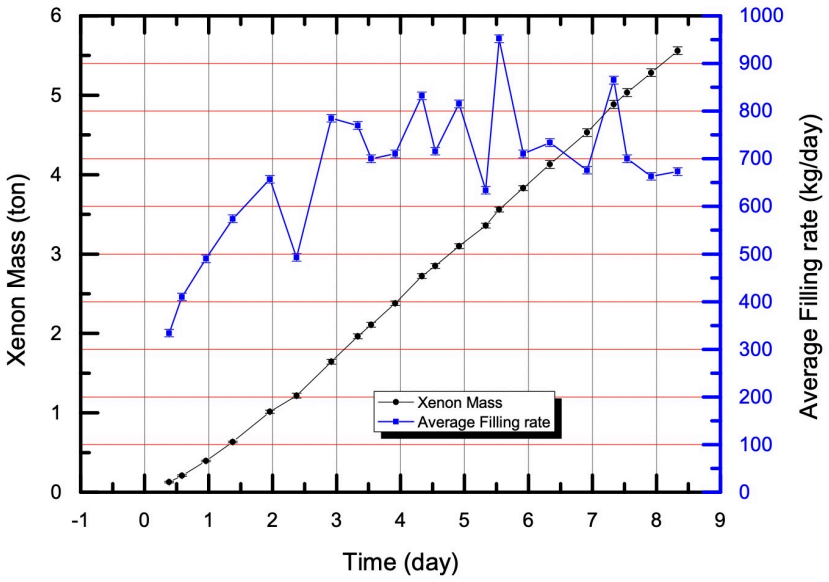

Figure 5.12: The flow rate of xenon filling with the cooling bus for PandaX-4T [37].

metal getter manufactured by SAES (Fig. 5.13) are implemented in PandaX-4T. In PandaX-4T, the tested maximum total flow rate reaches 155 SLPM, and stable daily flow rates are 80 SLPM and 30 SLPM for the too loops.

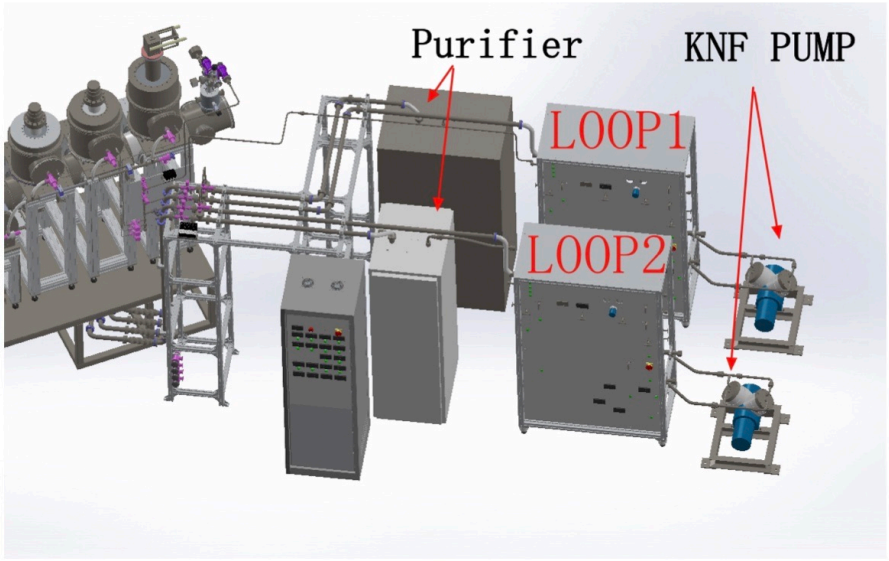

Figure 5.13: A sketch of the two circulation loops with hot purifiers [37].

The distillation tower in PandaX-4T (Fig. 5.14) is designed to reduce ^{85}Kr or ^{222}Rn with both offline and online modes, which has also been used to remove tritium in xenon [38, 145]. Xenon bought commercially has 0.5 ppm $^{\mathrm{nat}}$Kr. The distillation tower takes advantage of different boiling points (under standard pressure) among krypton (120 K), radon (211 K) and xenon (165 K). During the krypton distillation operation, krypton is enriched in the gaseous phase. Reversely, radon will be enriched in the liquid phase. Practically, in PandaX-4T commissioning run, the $^{\mathrm{nat}}$Kr level is determined as 0.33 ± 0.21 ppt with $\beta - \gamma$ coincident events in ^{85}Kr decay. Distillation makes ^{85}Kr sub-dominant ER backgrounds in PandaX-4T, which is a great success. However, the online mode for krypton removal brought noticeable ^{222}Rn to the detector, and only offline mode is used afterwards.

Figure 5.14: The PandaX-4T distillation tower [38].

5.1.4 Background control

Without a lower background level, the increase of exposure won't bring enough sensitivities to search for dark matter. In PandaX-4T, a ultra-pure water shielding is used to reduce ambient radioactivities. The class 1000 clean room is built inside a class 10,000 clean room with air purified by a radon removal system with activated charcoal. Moreover, materials are monitored carefully before mounting, and surface treatment procedures are investigated to further suppress radioactive background [190].

5.1.4.1 Water shielding

Although the cosmic rays are well-stopped by Jinping mountain, long-lived radioactive isotopes like ^{40}Kr, ^{238}U and ^{232}Th are universal in the materials. Neutrons can be generated via fission of heavier nuclei and (α, n) processes, and γs are also penetrable and common in the long decay chains. Radon isotopes in the ^{238}U decay chain are flying radioactive sources.

In PandaX-4T, a commercial ultra-pure water shielding system (Fig. 5.15(a)) is used to stop the ambient radioactivities. The resistance of the purified water reaches 18 MΩ·cm, and the highest flow rate is 10 ton/h. The water tank (Fig. 5.15(b)) with a 10 m diameter and 13 m height is filled with the purified water with 1 m on the top filled with nitrogen. As measured by the inductively coupled plasma mass spectrometry (ICP-MS) [190], ^{232}Th and ^{238}U in the water sample is 0.0029 ± 0.0007 ppt and is 0.0019 ± 0.0005 ppt, respectively. The ^{222}Rn in the water is 15.8 ± 4.4 mBq/kg as measured by a high purity germanium (HPGe) detector at CJPL.

(a) (b)

Figure 5.15: (a) A photo of the water purification system. (b) A side view of the water tank.

5.1.4.2 Radon reduction in the clean room

A commercial radon reduction system from ATEKO with activated charcoal (AC) is used to reduce the ^{222}Rn in the air at least by a factor of 1000 with a 230 m^3/h flow rate at room temperature with the ambient pressure at CJPL (85 kPa). The purified air is sent into the Class 10000 clean room. The whole system can be seen in Fig. 5.16, where the two AC columns are in black. The air is precooled to -50°C before entering the AC columns.

Figure 5.16: The radon removal system for the clean rooms.

5.1.4.3 Material screening and surface treatment

A couple of technologies are used in PandaX-4T for material screening, including two HPGe counting stations (JP-I and JP-II), ICP-MS, neutron activation analysis (NAA), radon emanation measurement systems, krypton assay station and alpha detection system. An example of the HPGe measurement can be found in chapter 3 for the ^{83m}Kr sources. ICP-MS measures the intrinsic radioactivity of materials based on their mass-to-charge ratios, and in PandaX-4T, the ICP-MS assays are performed in a Class 10 cleanroom facility utilizing an Agilent 7900

spectrometer. Three radon emanation measurement systems are built where a chamber with a negative HV applied PIN diode is used to collect the positively charged ions of radon daughter nuclei and measure energy deposit of α particles in the decay. Natural krypton assay station is constructed at CJPL to measure the krypton concentration in xenon target with a cold trap which has a sensitivity at 8 ppt, and the $^{\mathrm{nat}}$Kr in PandaX-4T is smaller than 8 ppt. A commercial alpha detection system fabricated by ORTEC is used to measure the surface radioactivity of the samples, which helps to improve the surface cleaning procedure. NAA analyzes the elemental composition of a sample material using neutron activation, which is used to screen PTFE in PandaX-4T. For complete information, please check out the reference [190].

5.1.5 Calibration

An ideal calibration system should cover a wide energy window of interest ($\mathcal{O}(1-10^4)$ keV$_{\mathrm{ee}}$) and different scattering types (ER and NR), and not affect the detector operation in the long run. To understand the responses of the growing larger LXeTPCs, short-lived gaseous radioactive sources, including ^{83m}Kr and ^{220}Rn (ER calibration sources), have been injected into the PandaX-4T detector through the circulation system. Figure 5.17 presents the calibration panel connected to the main loop with V1 as the inlet and V3 as the outlet, and the two chambers marked as 'Rn' and 'Kr' can be seen. The development of ^{83m}Kr sources is discussed in details in chapter 3, and ^{220}Rn development has been overviewed in chapter 2.

Three polyvinyl chloride (PVC) tubes are mounted on the inner side of OV as shown in Fig. 5.18. The inner side of the PVC is air and has PTFE coated SS ropes to guide through the calibration sources including ^{60}Co (ER), ^{137}Cs (ER), ^{232}Th (ER), and AmBe (NR). The working

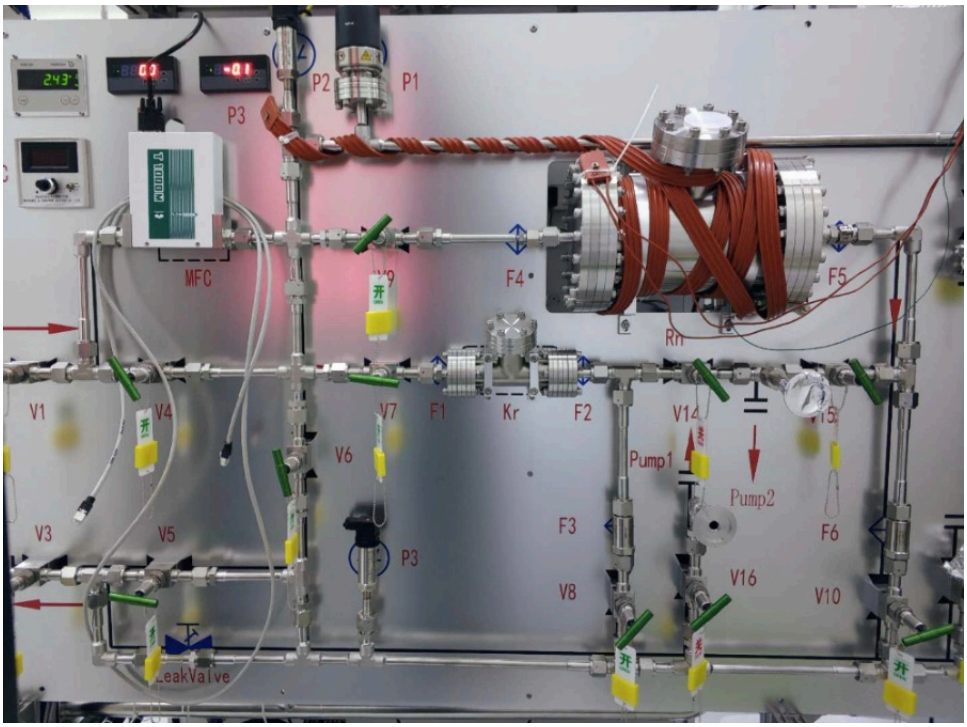

Figure 5.17: The calibration system connected to the PandaX-4T circulation system.

port for the calibration sources can be found in Fig. 5.18.

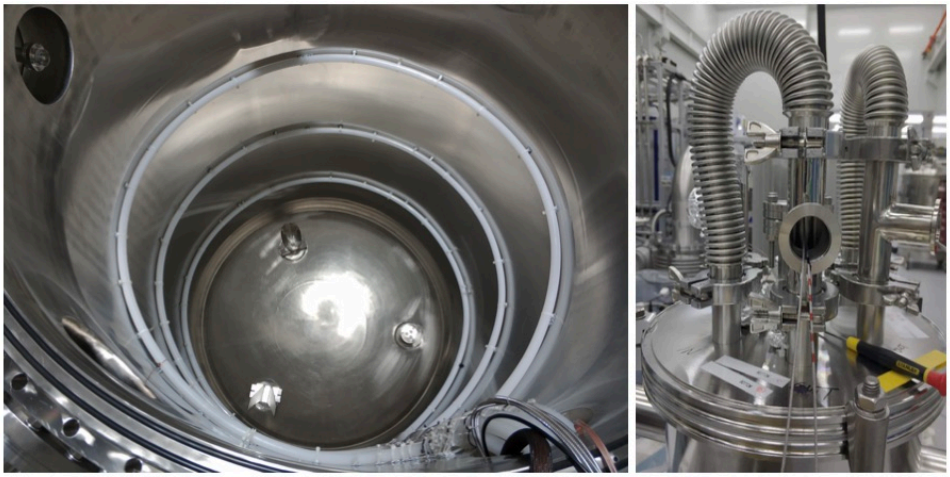

Figure 5.18: The three PVC calibration tubes attached to the OV (left) and the handling port (right) to load the calibration sources in the workspace.

Figure 5.19 outlines the tunnel welded on the outer side of OV to guide the neutrons into the detetor which are from the deuteron-deuteron (DD) fusion generator. Mono-energertic neutrons

(2.2 MeV and 2.45 MeV) are provided by the DD generator according to the scattering angles (π and $\pi/2$, respectively).

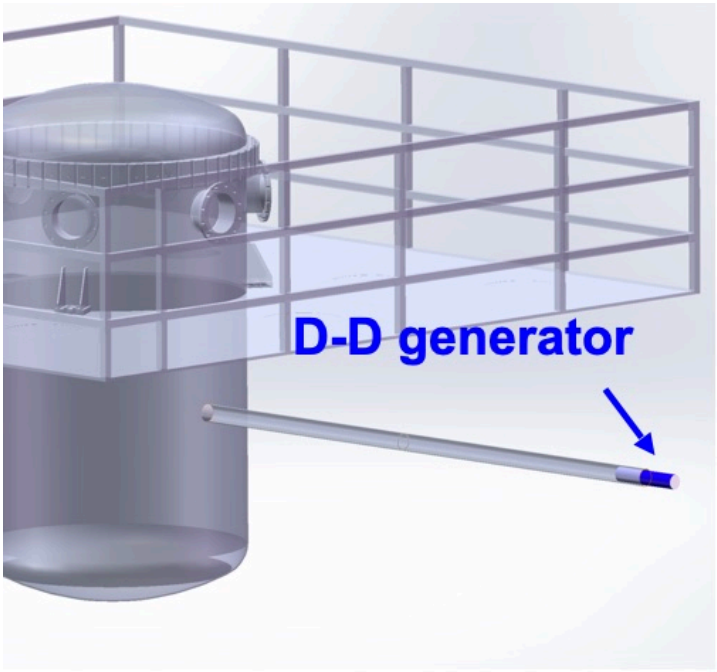

Figure 5.19: The sketch of the tunnel welded to the OV for DD fusion neutrons for NR calibration.

5.1.6 Slow control

Our slow control system (SCS) is responsible for monitoring the status of the facility remotely and generate alarms in case abnormal status is detected [39, 191]. The signals from sensors are digitalized with DAM-8082 if needed. All the digital data are transmitted to the slow control computers via RS-232 or RS485 protocol, which limits the physical distance between the computer and the digitizer to 20 m. The program for data collection from sensors is written in Python3 which can be easily packed and used. The data are fetched periodically and written to the remote InfluxDB database. The data visualization is implemented with the open source Chronograf (v1.7.7). The anomaly detection function is provided by Kapacitor (v1.5.2). A

schematic view of the integration of the SCS and the subsystems is shown in Fig. 5.20.

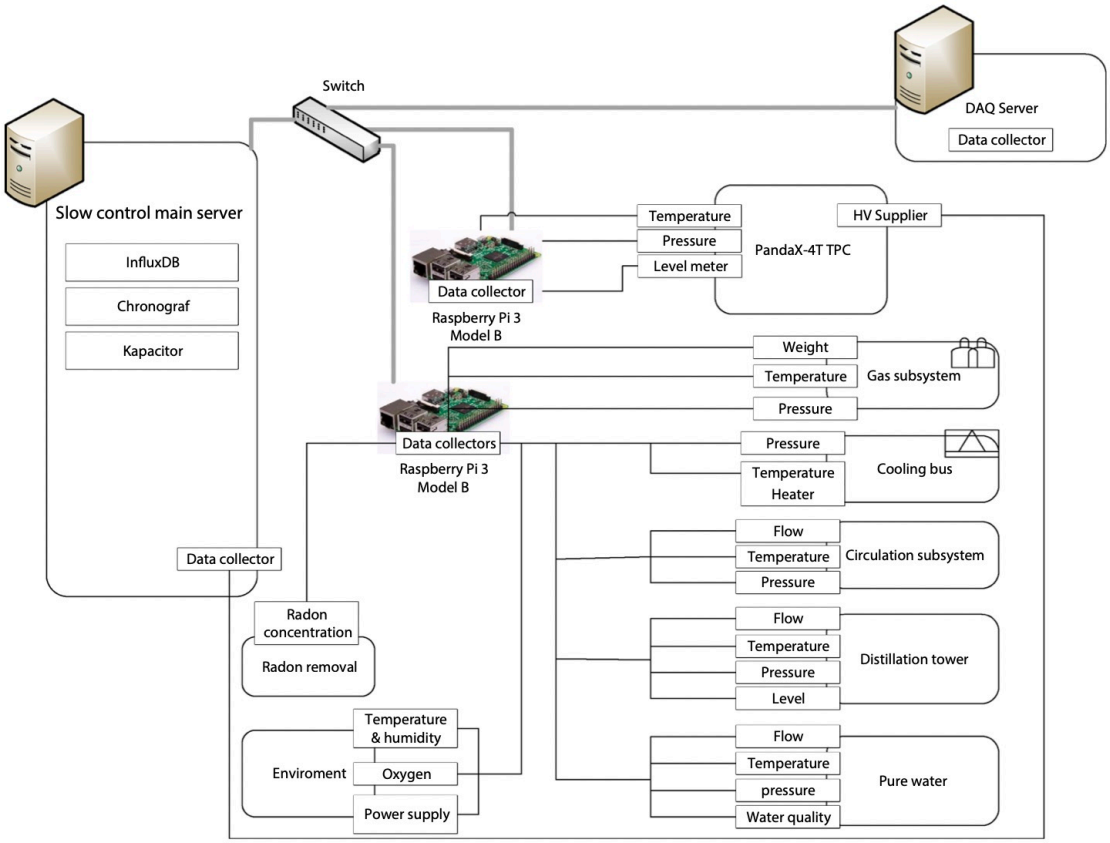

Figure 5.20: The schematics of the slow control system of PandaX-4T [39].

5.1.7 Data processing and reconstruction

The main functions required in the data processing in PandaX-4T (P4-chain) are similar to PandaX-II [141], but modified for an easier reach to different data stages. C++11 is used for the data processing with self-developed Bamboo-Shoot 3 library integrated where data are saved with 'bsd' extension abbreviated for Bamboo-Shoot data. All different stages of data are defined under the structure of Bamboo-Shoot 3. The algorithms and definitions in the processing chain may be modified for different physics purposes. The philosophy of the P4-chain design is to pack actions

with classes and objects defined in the same way as Python. After the data processing chain, The 'bsd' files are converted into ROOT files (**AnaData**) for conveninece which is more widely used in the field of high energy physics. More corrections and quality cuts can be developed in this step for a better clustering, the spatial uniformity correction and cutting off outliers. More details are provided later in section 5.2.

5.1.8 Detector simulation

In PandaX-4T, a GEANT4-based Monte Carlo package, BambooMC, is used to predict the energy depositions of the physics events [185, 192]. Noble element simulation techniques (NEST) are applied to predict the detector responses from the energy depositions to the main observables $S1$ and $S2$ with viable waveform simulation mode [193, 194].

The program of BambooMC performs MC simulation for different types of detectors in PandaX experiments with a modular architecture, in which the different geometry, physics scattering processes, event generators and data analysis can be integrated with a configuration file provided by the user. The basic function of BambooMC is to predict how the particles scatter with a nucleus or an electron after being released by the decays of radioactive isotopes in the detector materials including neutron, alpha, beta and gammas particles. The radioactivities of the main materials, including SS, PTFE, PMTs and the printed circuit boards, are measured with the HPGe detector. An application of BambooMC optical simulation is available in chapter 4 for improving the quality of horizontal position reconstruction.

The detector response is modeled with the help of NEST for fast detector simulation with different detector parameters. A detailed description of the tuned NEST model in PandaX-4T is

provided in chapter 6. Waveform simulation takes longer time, and is not included in our fast detector simulation. A self-developed waveform simulation without NEST is used to estimate the cut efficiencies in PandaX-4T.

5.2 Run 1 for WIMP search

The first result of PandaX-4T has been published in the summer of 2021 for the search on SI WIMP-nucleus scattering, with a lowest excluded cross section (90% C.L.) of 3.8×10^{-47} cm^2 at a dark matter mass of 40 GeV/c^2 reported [2]. The basic information of the Run 1 data can be found in Tab. 5.1.

Set	1	2	3	4	5
Duration (days)	1.95	13.25	5.53	35.58	36.51
$\bar{\tau}_e$ (μs)	800.4	939.2	833.6	1121.5	1288.2
$dt_{\max}$ (μs)	800	810	817	841	841
V_{cathode} ($-$kV)	20	18.6	18	16	16
V_{gate} ($-$kV)	4.9	4.9	5	5	5

Table 5.1: Basic information of Run 1 data of PandaX-4T experiment.

The data analysis can be divided into four main parts as following.

1. Interpret the waveform scientifically with P4-chain. P4-chain is setup with calibration data to extract out useful information and prepare the candidates for DM search.

2. Estimate the backgrounds. A blind analysis requires independent estimations of the backgrounds to avoid cognitive biases. For our Run 1 data, because of the unexpected tritium background, the whole data analysis is not fully blinded, but all the other backgrounds have independent estimations.

3. Model the hypothetical signal. With the calibration data, energy responses can be studied, and then, the observable of the hypothetical signal can be predicted.

4. Report an excess or set a limit on the DM search. If an excess reaches 5σ significance, it can be claimed as a discovery. Suspicious excesses with a global significance over 3σ will be interesting for discussion. Otherwise, a limit with a 90% or 95% confidence level (C.L.) is often reported.

5.2.1 P4-chain

The correlation between the Bamboo-Shoot data and the actions can be seen in Fig. 5.21. The meanings of different stages under the Bamboo-Shoot frame work are:

RawData Waveforms are saved by the DAQ system with event structure provided by CAEN V1725 [195];

GroupData The initial PMT waveform segments (self-triggered and individually saved for each PMT channel) are grouped by a 2 ms coincidence time window, and saved as 'bsd' files;

CalibData The PMT gains calibrated by blue LEDs are used to convert the unit of the waveforms from ADC (mV) to PE;

HitData A single hit corresponds to a single segment with the information calculated which are briefly explained in Tab. 5.2;

SignalData A signal consists of a group of clustered hits. The clustered signals are categorized as $S1$, $S2$, noise, sparking or unknown, which is done by a decision tree. The properties of

a signal are saved in a 'paired' way with a key and value, including the horizontal position, the total top/bottom charge, widths with different definitions and etc;

PhysicalEventData The $S1$ and $S2$ are paired with an allowed time separation, which depends on the drifting time under different drifting electric fields. The paired event is categorized according to the number of qualified $S1$ and $S2$ in the cluster as single scattering, $S1$-only, $S2$-only and multi scattering.

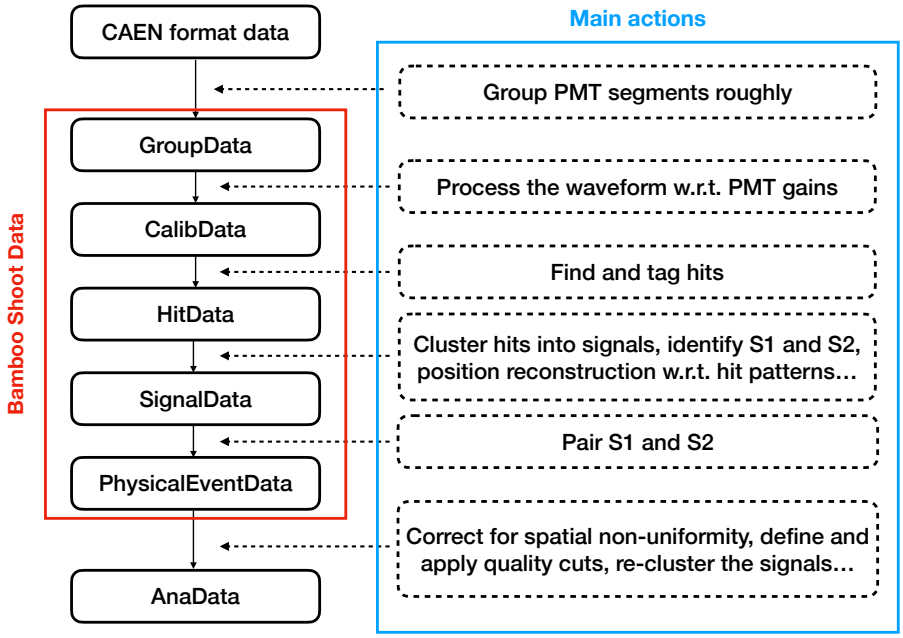

Figure 5.21: Flow chart of P4-chain. Not all the actions in the chain are listed.

5.2.1.1 PMT calibration

As mentioned before, four blue LEDs are mounted in the IV to calibrate the PMT gains. Voltages from 5 V to 10 V are applied on the LEDs for PMTs at different locations in the detector.

Name	Unit	Explanation
channelNumber	N/A	PMT index
threshold	ADC	Default value is 20 ADC
startTime	sample	Time tag rising above the threshold
peakTime	sample index	Time tag of the highest point
height	PE	Value at peakTime
width	sample	Sample number above the threshold
area	PE	Integral of the waveform above the threshold
pre/post_baseline	PE	Average of 10 samples below the threshold at both ends
rms_pre/post_baseline	PE	Standard deviation of pre/post_baseline
HitType	N/A	NOISE or SATURATE or BASELINE or NORMAL
CalibPmtSegment	PE	Waveform after PMT gain calibration saved as a vector

Table 5.2: A single hit defined. One sample in a waveform corresponds to 4 ns.

Most of the charge signals should be white noises and SPEs to extract out the PMT gains which are used to convert the RawData in a unit of ADC to PE. A typical example of LED calibration is shown in Fig. 5.22.

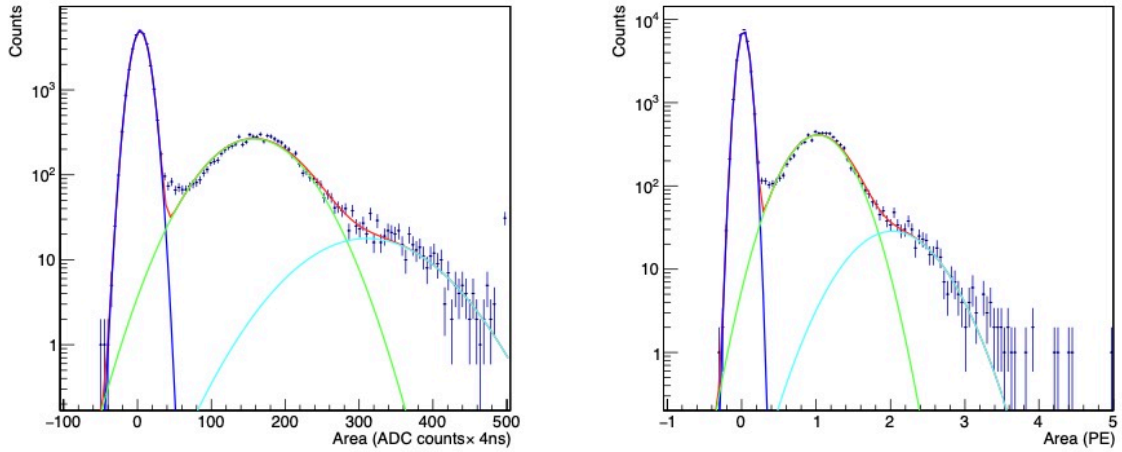

Figure 5.22: An example of the LED calibration of one PMT with the integrated area of the waveform before correction in unit of ADC (left) and after correction in unit of PE (right). The 4 ns refers to the sampling width of the waveforms

Besides the gain, another important parameter in PMT is the probability to generate a second photoelectron while only one hits the photo-cathode. This double photoelectron emission (DPE) probability for the xenon scintillation light at 178 nm is provided as 22.5% for our 3-inch

PMTs. Because DPE is an input parameter for the detector response simulation, it is specifically calibrated with the smallest $S1$ (expected to be single photon hit) in the AmBe neutron data and ^{83m}Kr calibration data. The DPE is determined to be 22.8% with AmBe and 23.9% with ^{83m}Kr as shown in Fig. 5.23.

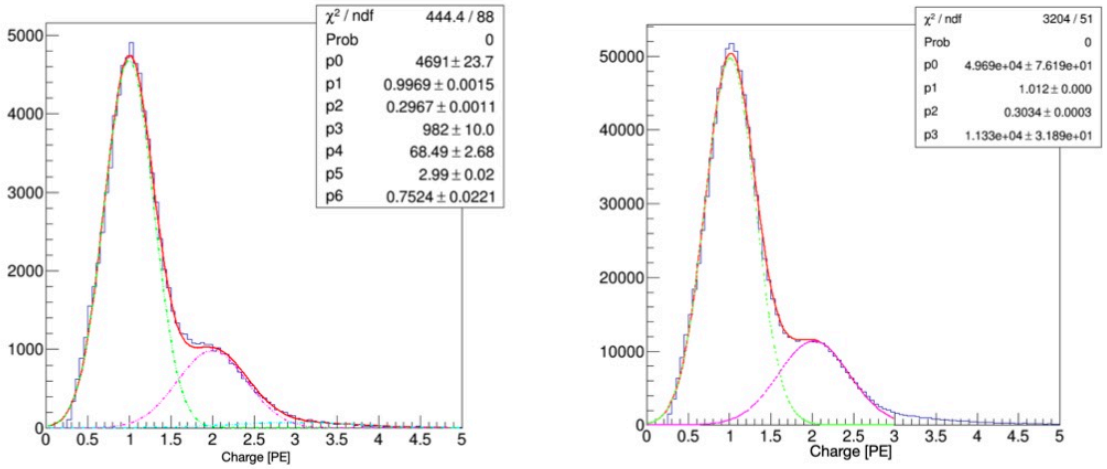

(a) ^{241}Am-^{9}Be (b) ^{83m}Kr

Figure 5.23: Estimation of the double photon emission probability with AmBe neutron (left) and ^{83m}Kr (right) events.

5.2.1.2 Position reconstruction

The vertical position is calculated with the drifting time of the electrons and the drifting velocity which can be identified with the events from cathode (1185 mm drifting distance). The vertical uncertainty is conservatively estimated as 3.0 mm. The horizontal position is inferred with the $S2$ collected by the top PMT array. After clustering the hits and reaching to SignalData,

fast horizontal position reconstruction is done with the center-of-gravity (COG) algorithm as

$$\begin{aligned} x_{\mathrm{COG}} &= \sum_i (X_i \times q_i) / \sum_i q_i \\ y_{\mathrm{COG}} &= \sum_i (Y_i \times q_i) / \sum_i q_i \end{aligned}, \tag{5.1}$$

where i is the index of PMTs, (X_i, Y_i) is the known position of the ith PMT and q_i is the charge collected by the ith PMT. The algorithm is known for inward bias due to non-optimized weights. More sophisticated algorithms including template matching with light simulation of the detector and analytical photon acceptance function setup with calibration data (^{83m}Kr events) are applied later on with $(x_{\mathrm{COG}}, y_{\mathrm{COG}})$ as inputs. Only the first half (width-based definition) of $S2$ charge is used for a smaller uncertainty, reaching 3.0 (8.2) mm for 1000 (100) PE evaluated by the difference between the two algorithms. The PAF algorithm is introduced in detail in chapter 4.

5.2.1.3 Uniformity correction

For the same physics signal, $S1$ and $S2$ signals are different in different parts of the detector. Figure 5.24(a) and Fig. 5.24(b) show the difference in the light yield $S1/E_{\mathrm{ee}}$ and charge yield $S2_b/E_{\mathrm{ee}}$ for ^{83m}Kr events ($E_{\mathrm{ee}} = 41.5$ keV$_{\mathrm{ee}}$) in the detector. Taking the mono-energetic ^{83m}Kr events as an example, as shown in Fig. 5.24(a), the total reflection at the liquid-gas interface ($z = 0$ mm) will reduce the total amount of $S1$ collected. A smaller $S1$ is also observed with a larger radius which can also be understood with the reflection happened at the LXe-PTFE surface. The z non-uniformity of $S2$ is mainly caused by the loss of electrons during the way drifting upward due to electron-negative impurities. The evolution of electron lifetime, τ_e, which quantifies the loss over the increase of the drifting time can be found in Fig. 5.24(c) for the

PandaX-4T commissioning run which is tracked by α events in $5.5-6$ MeV and the 164 keV_{ee} de-excitation of ^{131m}Xe. The maximum drifting time for set 4 and 5 is 840 μs (800 μs for set 1). The horizontal non-uniformity in $S2_b$[1] is calibrated by ^{83m}Kr events (Fig. 5.24(b)).

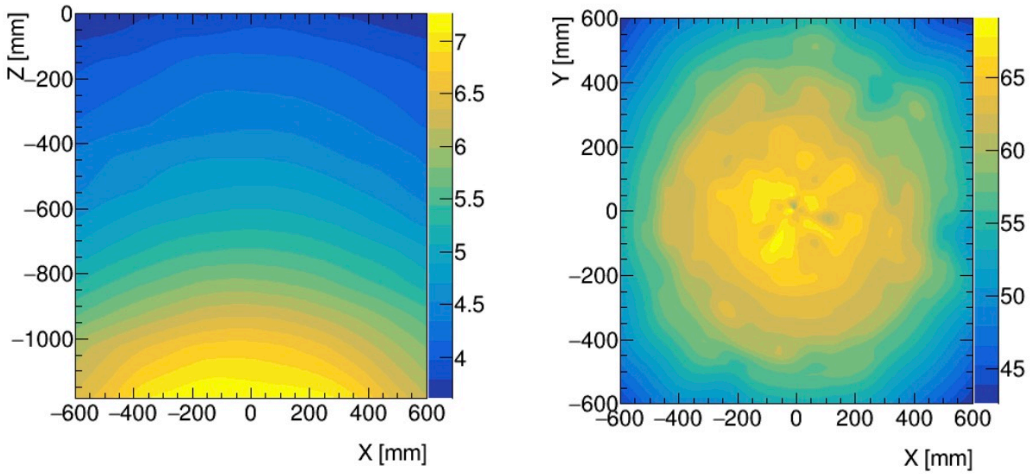

(a) (b)

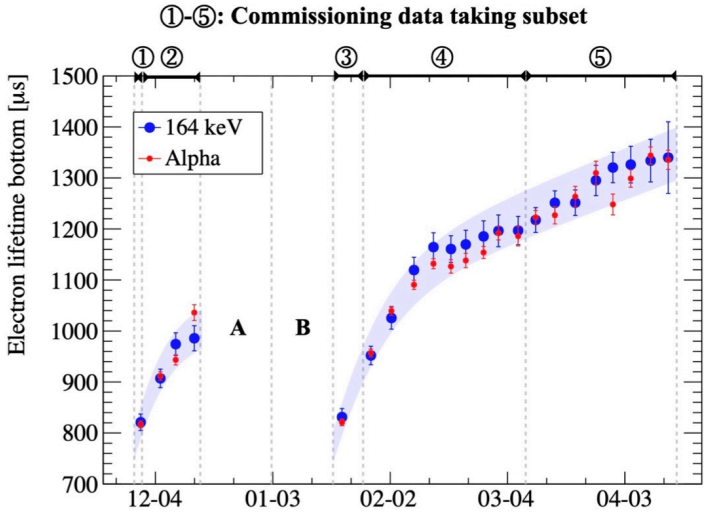

(c)

Figure 5.24: (a) $S1$ uniformity map (Z vs. X) calibrated with ^{83m}Kr where the color bar means the light yield $S1/E_{\text{ee}}$. (b) $S2_b$ uniformity map (Y vs. X) calibrated with ^{83m}Kr where the color bar means the charge yield $S2_b/E_{\text{ee}}$. (c) The electron lifetime for z correction in $S2_b$ traced with ^{131m}Xe (164 keV_{ee}) and α events ranges in $5.5-6$ MeV. 'A' marks for the HV training of the electrodes, especially the cathode, and 'B' for a circulation pump replacement.

[1]The subscription b in $S2_b$ stands for the $S2$ collected by the bottom PMT array.

5.2.1.4 Main quality cuts

The live time of data taking is confined by two cuts other than the hardware downtime. One is to require the candidate to be separated by 22 ms from a previous event to avoid contamination, which cut the live time off by 7.3%. The other is a limit on the isolated $S1$ rate of the data file to avoid excessive discharges, which reduce the live time by 2.3%. The total live time before accounting for other quality cuts is 86.0 day.

With the help of ER/NR calibration events, quality cuts are further developed which are mainly based on the definition of $S1$s and $S2$s to reduce noises and outliers.

1. Requirements on clean $S1$s: (a) an upper limit on the number of peaks in the waveform; (b) outlier cut with both upper and lower limits on the top-bottom asymmetry (TBA) of $S1$, $(S1_t - S1_b)/(S1_t + S1_b)$), as a function of the z vertex; (c) outlier cuts on the $S1_t$ and $S1_b$ patterns to suppress extra charges due to PMT after pulses.

2. Requirements on clean $S2$s: (a) upper limits on the number of noises and single-electron $S2$s; (b) outlier cuts on TBA of $S2$ as a function of $S2$; (c) outlier cuts on the goodness-of-fit of horizontal position reconstruction which reflect whether the $S2_t$ pattern is reasonable, an upper limit on the deviation between the template matching and PAF horizontal position reconstruction algorithms and another upper limit on the root-mean-square (RMS) of the $S2_t$ pattern; (d) outlier cuts on $S2$ shape correlated to the height, width and charge.

3. Outlier cuts on diffusion of the electron clouds (width of $S2$ as a function of z), which is the most important quality cut to suppress the accidental backgrounds.

5.2.2 Main backgrounds and fiducialization

The main backgrounds are summarized in Tab. 5.3. The 'flatER' contains the contributions of ^{222}Rn daughters (^{214}Pb β-decay mainly), ^{85}Kr (β-decay), material ER, solar neutrino and two-neutrino double beta decay of ^{136}Xe. Instead of summing up the individual estimation of each component, a side-band estimation with data in $18 - 30$ keV$_{\rm ee}$ is taken for 'flatER' because of a smaller uncertainty. The event numbers of tritium in the data sets are floating. ^{127}Xe L-shell electron capture with cascade ER signals summed to 5.2 keV$_{\rm ee}$ is estimated by the theoretical ratio to the K-shell electron capture (33.2 keV$_{\rm ee}$), which limits the upper bound of $S1$ (135 PE) used for the search. Neutron backgrounds are estimated with three different algorithms [155, 196]. ^{8}B neutrinos from the sun can scatter with xenon nuclei via coherent elastic neutrino-nucleus scattering predicted by the standard model. Surface background refers to the radioactivities happened on the PTFE surface surrounded the sensitive region but shows up in the data set because of the uncertainties in the horizontal position reconstructions which is estimated similar to PandaX-II (see chapter 4 for details). Accidental background due to randomly paired $S1$ and $S2$ whose rates are estimated by the time windows where negligible physics events appear. Reference [2] provides more details on the background estimation.

Table 5.3 summarizes the background contribution with a pre-defined fiducial volume and parameter space defined by $S1$ and $S2$. The fiducial volume is optimized by the minimization on the figure of merit defined as the square root of background events per unit xenon mass. The spatial distribution of background events are generated by BambooMC simulation if needed. The final optimized fiducial volume (FV) contains 2.67 ± 0.05 tonne xenon as marked by the red lines in Fig. 5.25.

	Set 1	Set 2	Set 3	Set 4	Set 5	Total	Below NR median	Best fit
Rn	6.9±3.8	42.8±23.5	22.7±12.5	162.0±88.9	112.1±61.5	346.5±190.2	1.42±0.78	-
Kr	1.1±0.7	7.7±4.9	3.2±2.1	20.4±13.1	20.9±13.4	53.3±34.2	0.21±0.13	-
Material	0.8±0.1	5.7±0.7	2.4±0.4	15.2±1.9	15.6±1.9	39.7±5.0	0.16±0.02	-
Solar ν	0.8±0.2	5.4±1.1	2.3±0.5	14.3±2.9	14.6±2.9	37.4±7.5	0.16±0.03	-
^{136}Xe	0.7±0.1	4.6±0.9	1.9±0.4	11.8±2.4	12.1±2.4	31.1±6.2	0.05±0.01	-
Flat ER (data)	4.0±2.9	54.5±10.5	12.2±4.9	240.5±21.8	180.9±18.9	492.1±31.2	2.06±0.14	509.6±22.8
CH_3T	17±5	88±11	21±6	258±24	148±17	532±32	5.1±0.3	532±32
^{127}Xe	0.19±0.04	1.08±0.25	0.96±0.22	3.99±0.92	1.91±0.44	8.13±1.07	0.12±0.02	8.41±2.08
Neutron	0.02±0.01	0.15±0.08	0.07±0.03	0.45±0.22	0.46±0.23	1.15±0.57	0.69±0.35	0.82±0.41
^{8}B	0.01±0.01	0.05±0.03	0.03±0.02	0.26±0.13	0.29±0.15	0.64±0.32	0.62±0.31	0.61±0.17
Surface	0.01±0.01	0.07±0.02	0.03±0.01	0.18±0.05	0.18±0.05	0.47±0.13	0.42±0.12	0.44±0.11
Accidental	0.04±0.01	0.32±0.05	0.03±0.01	0.99±0.18	1.05±0.21	2.43±0.47	0.80±0.15	2.31±0.45
Sum	21±6	144±15	34±8	504±32	333±25	1037±45	9.8±0.6	1054±39
Data	21	148	34	496	359	1058	6	

Table 5.3: The main backgrounds for the WIMP-nucleus scattering search [2].

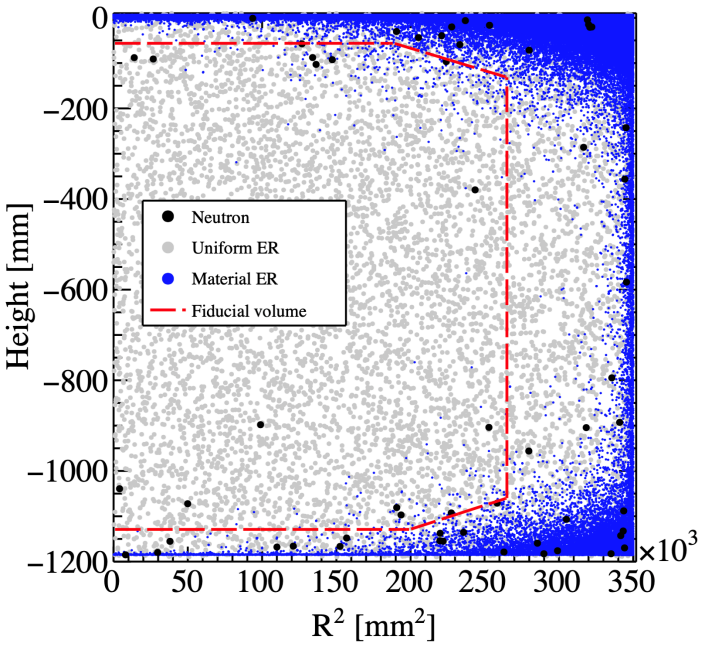

Figure 5.25: The optimization of fiducial volume of PandaX-4T Run 1 data with simulation events. The amount of uniform ER are scaled with summation of tritium, flat ER and ^{127}Xe. The spatial distributions of neutron and material ER contribution are generated by BambooMC, and the event numbers are scaled with independent estimations, respectively.

The signal region of interest for the GeV-scale WIMP search covers $S1$ from 2 PE to 135 PE for single scattering events (single $S1$ and single $S2$). There is another lower limit on $\log_{10}(S2_b/S1)$ vs. $S1$ as a 99.5% NR acceptance cut (Fig. 6.12). The survived DM candidates

can be found in Fig. 5.26.

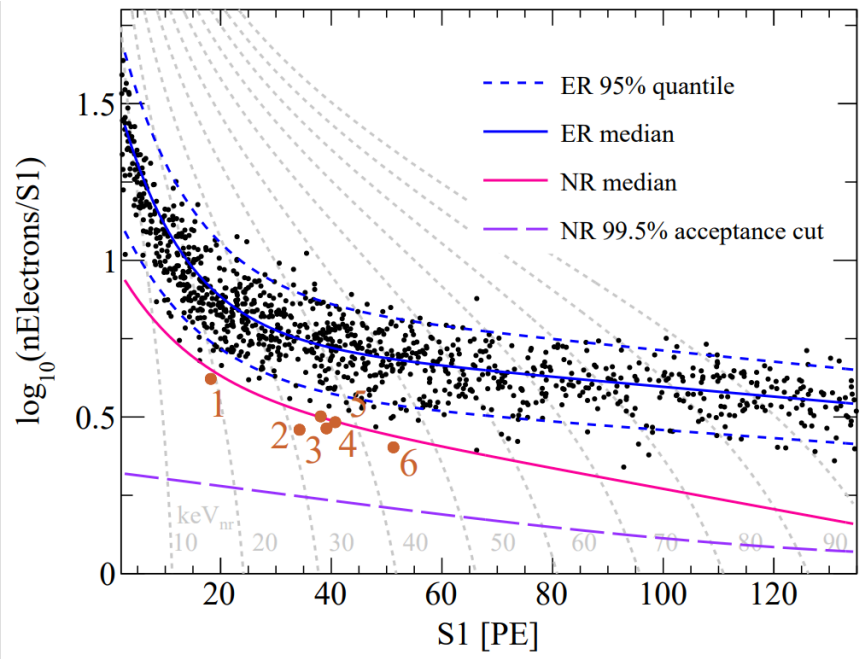

Figure 5.26: Dark matter candidates survived the quality cuts and showing up in the region of interest. The region below NR median and above the NR acceptance can be taken as a golden signal search window for an intuitive cut-and-count analysis. Compared to the 'below NR median' background estimation in Tab. 5.3, Run 1 data present a downward fluctuation.

It's worthwhile to discusse the below-NR-median (BNM) leakage ratio of ER events. Our ^{220}Rn ER calibration data gives a 0.43% ER leakage, however tritium is about 1%. This is because the smaller the energy is, the worse the energy resolution. The ER leakage ratio as BNM background is between 0.5%-1%.

5.2.3 Signal modeling and limit setting

The exotic WIMP events are expected to be uniformly distributed in the sensitive region, with a theoretical event energy spectrum of SI WIMP-nucleus scattering following

$$\frac{dR}{dE_R} = N_T n_\chi \sigma_A^{SI} F(q) \int_{v_{\min}(E_R)}^{v_{\max}(E_R)} f(v) v d^3\vec{v}, \tag{5.2}$$

where E_R is the nuclear recoiling energy that could be detected by our detector and σ_A^{SI} can be connected to σ_n^{SI} (WIMP-nucleon scattering cross ssection) in Eq. 1.6 which is used to compare WIMP searches with different targets. The right side the of equation sums up all the possible scattering cases for the same E_R. The smallest speed, $v_{\min}$, of incoming WIMP corresponds to the back-scattering case with maximum energy transfer that can generate the E_R. The largest speed, $v_{\max}$, is for the case that reaches the galactic escape velocity (544 km/s). The v distribution in the lab frame, $f(v)$, follows Figure 1.2, and the galactic-frame velocity distribution should follow Maxwell distribution. $N_T = N_0/A$ is the number of nuclei per gram of xenon (N_0 is the Avogadro's number), and $n_\chi = \rho_\chi/m_\chi$ is the number density of DM (ρ_χ is the local DM density and m_χ is the WIMP mass). $F(q)$ is the nuclear form factor as a function of the momentum transfer $q = \sqrt{2m_A E_R}$ (m_A is the nucleus mass), which confines the effective range of q for coherence scattering ($1/q$ shouldn't be too small compared to the nucleus size to preserve coherence) [197]. An example of Eq. 5.2 with $m_\chi = 100$ GeV/c^2 is given in Fig. 5.27.

To predict the observable of the signal, we rely on the energy calibration of detector response, where NEST model is used (more details in chapter 6). Before calibrate the NEST model, the energy response in a wider range compared to the signal region is done first to extract

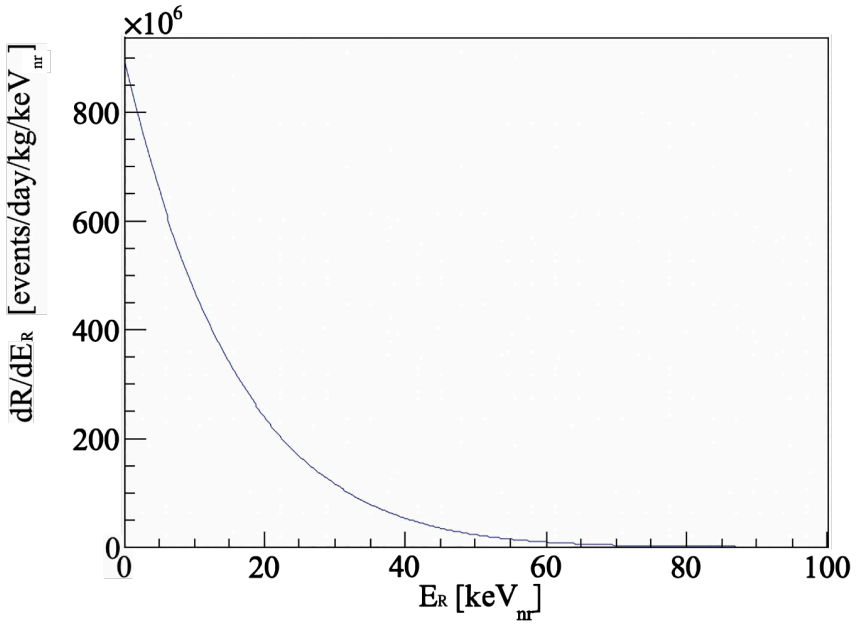

Figure 5.27: An event energy spectrum example of SI WIMP-nucleon scattering in xenon detector with $m_\chi = 100$ GeV/c^2 and $\sigma_n^{SI} = 1 \times 10^{-31}$ cm^2.

out some universal detector parameters.

Doke plot is used to build the equivalent ER energy reconstruction by a linear fit of charge yield (CY) as a function of light yield (LY) with a group of mono-energetic ER peaks. ERs are expected to deposit most of the signals in scintillation and ionization, quantifying as LY (scintillation quantas generated in unit energy) and CY (ionization quantas generated in unit energy), respectively (negligible phonons). Even if the LY/CY is a non-linear function of energy deposition, the total quantas should be the same for a unit energy deposition. In the PandaX-4T commissioning run, ^{83m}Kr (41.5 keV$_{\rm ee}$), ^{131m}Kr (163.9 keV$_{\rm ee}$), ^{129m}Xe (236.2 keV$_{\rm ee}$) and ^{127}Xe (408 keV$_{\rm ee}$) are used to find out the basic parameters, including $G1$ and $G2_b$, in the ER equivalent

energy reconstruction

$$E_{\rm ee} = W \times (\frac{S1}{G1} + \frac{S2_b}{G2_b}), \tag{5.3}$$

where W is the work function of LXe, $G1$ and $G2_b$ are the two parameters in the linear energy reconstruction valid for a wide energy range (see Fig. 6.15). $G1$ represents the photo detection efficiency (PDE). $G2_b$ equals to EEE $\times$ SEG$_b$, where EEE is electron extraction efficiency, and SEG$_b$ stands for the single electron gain for a single electron extracted out from the liquid. SEG can be found with the smallest $S2$ in the calibration events (Fig. 5.28). As $S2_b$ is used for energy reconstruction in PandaX-4T, SEG$_b$ is scaled by $S2/S2_b$ found with calibration data (AmBe neutron events) as shown in Fig. 5.29. EEE can also be inferred with the shape of SEG as introduced in Ref. [198], providing a crosscheck on the $G2$. A summary of the basic parameters of Run 1 can be found in Tab. 5.4.

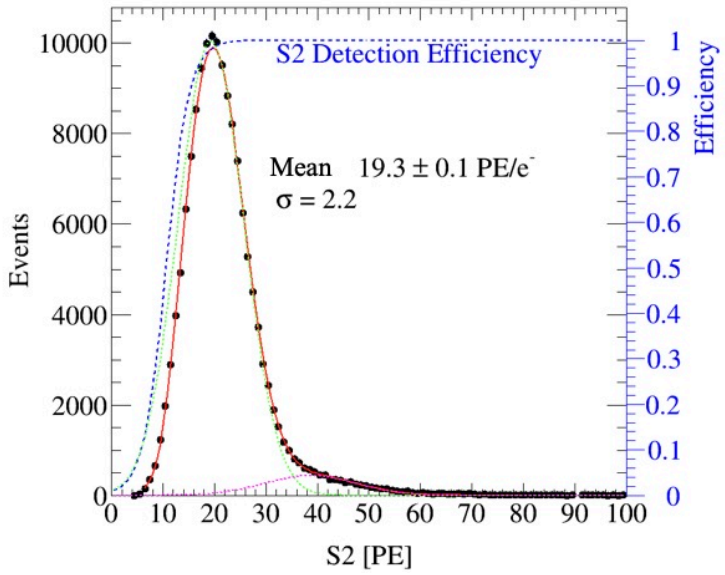

Figure 5.28: Single electron gain in $S2$ with the small $S2$s under $V_{\rm gate} = -5$ kV (if $S2_b$ is used, the $S2/S2_b$ can be used to find SEG$_b$ as shown in Fig. 5.29). The total fitting function (red line) is the summation of the Gaussians as a function of $S2$ for single and double electrons convoluted with a Fermi-Dirac function for efficiency (blue dashed line).

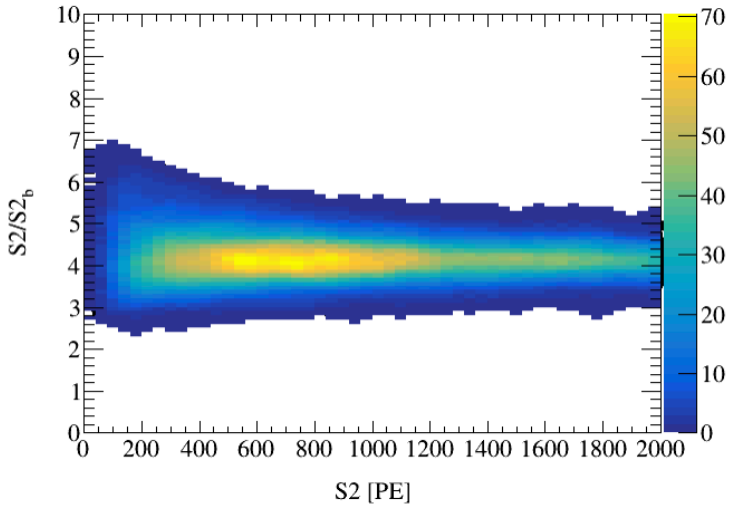

Figure 5.29: $S2/S2_b$ of AmBe neutron events with $V_{\mathrm{gate}} = -5$ kV.

Set	1, 2	3, 4, 5
PDE (%)	9.0 ± 0.2	9.0 ± 0.2
EEE (%)	80.2 ± 5.4	92.6 ± 5.4
SEG$_b$ (PE/e)	3.8 ± 0.1	4.6 ± 0.1

Table 5.4: A summary of the basic detector parameters for PandaX-4T Run 1.

The further calibration in the signal region for both ER/NR events are presented in detail in chapter 6 with the help of NEST. The prepared background probability distribution functions (PDFs) w.r.t. to $S1$ and $S2_b$ can be found in Fig. 6.25 and Fig. 6.28. With the calibrated fast detector simulation, Figure 5.30 predicts the PDF of WIMP ($m_\chi = 100$ GeV/c^2) for Run 1 set 4 or 5.

As no excess is found in our data, the result is reported with limits and sensitivities, which is set with profile likelihood ratio analysis explained in chapter 6. The published result is provided for reference (Fig. 5.31).

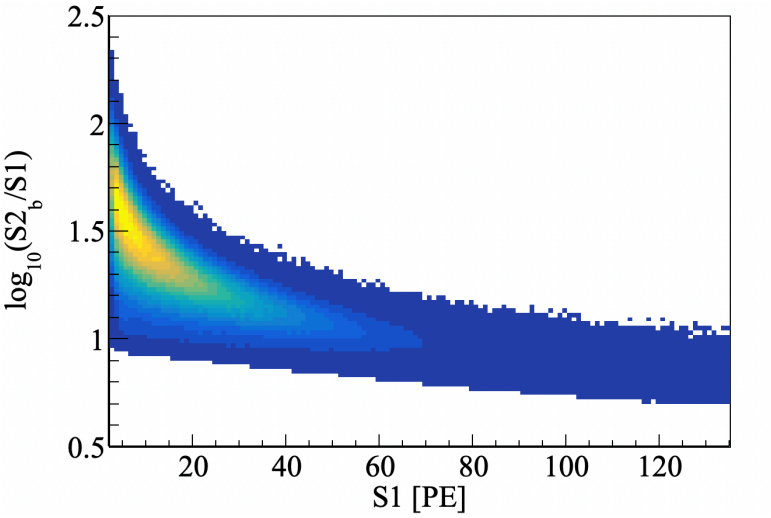

Figure 5.30: A prediction of WIMP PDF ($m_\chi = 100$ GeV/c^2) for Run 1 set 4 or 5 with the calibrated fast detector simulation.

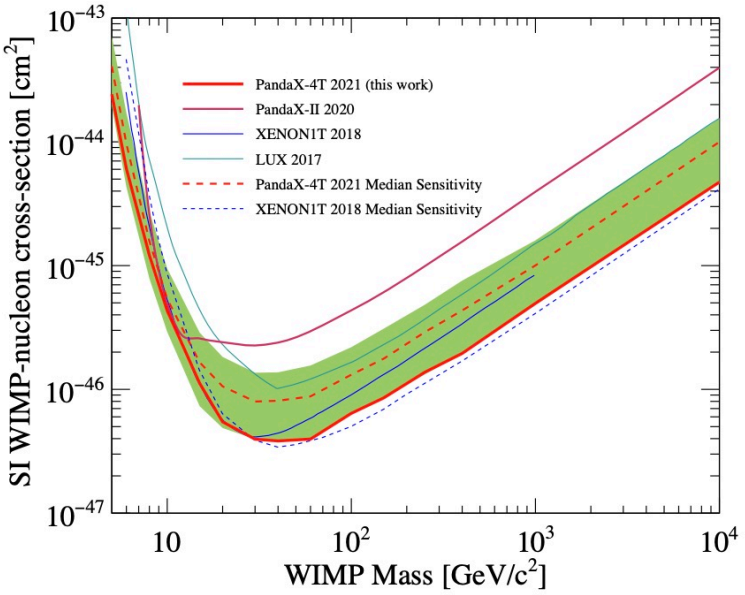

Figure 5.31: The 90% C.L. exclusion limit and 1σ sensitivity band of spin-independent WIMP-nucleus scattering reported with PandaX-4T Run 1 data.

Chapter 6: Signal model with reweighting Monte Carlo in limit setting

Profile likelihood ratio (PLR) analyses have been widely used to interpret the data of direct DM searches in the last decade [34, 55, 60, 117]. Firstly, the likelihood approach has a strong discrimination power by virtue of the knowledge on probability densities of backgrounds and signals. Secondly, the PLR avoids filp-flopping between an upper limit and a signal interval, similar to the Feldman-Cousins-approach [199]. Thirdly, the construction of likelihood can include statistical and systematic uncertainties which are reflected in the sensitivities and confidence intervals. Therefore, this frequentist approach is recommended by a number of direct DM search collaborations to report the results [4].

Template morphing is conventionally used in the PLR with likelihood functions (LHFs) defined in a multi-dimensional parameter space [179]. The LHF includes probability distributions of the expected dark matter signal and backgrounds as functions of observable(s) with a strong discrimination power. The probability distribution functions (PDFs) are often prepared as histograms filled by millions of Monte Carlo (MC) simulation events. The main parameters in the simulation include cross sections, DM mass and mediator mass if applied. The other nuisance parameters free in the likelihood maximization are profiled in the analyses. A running time generation of PDFs with conventional MC simulations is not practical because many fitting algorithms fail due to statistical fluctuations. Markov Chain Monte Carlo (MCMC) can avoid the failure [200],

but is too time-consuming because hundreds of likelihood maximization are needed in the PLR analysis. Templates at discrete points of the parameter space are often prepared, and PDFs at arbitrary points are interpolated linearly or with other techniques [201].

This work applies reweighting MC on the profile likelihood ratio method without conventional templates, re-using the simulation events to generate PDFs. The approach has historically been used to study the ising model close to the phase transition, improve the lattice QCD simulations and extend the parameter space to search new physics theories at the large hardronic colliders [202, 203, 204]. In this application, reweighting MC makes it possible to use fast extremum finding algorithms like Newton-CG, Powell or MINUIT [205, 206, 207] because the same statistical fluctuations cancel out in the maximization of the LHF (ML). The reweighting strategy provides an independent estimation of the uncertainties introduced by the template morphing method. More importantly, by avoiding an exponential increase in the memory cost while the number of parameters increases linearly, reweighting MC brings potential to handle more parameters and interpret uncertainties in the PLR analyses more accurately.

We apply the reweighting MC technique search for the WIMP-nucleus scattering with the latest released data by Particle and astrophysical xenon experiment (PandaX)–PandaX-4T Run 1 [2]. In our previous analysis for PandaX-4T, the PDF templates are prepared for different WIMP masses and two nuisance parameters counting the uncertainties in the detector response for ERs which dominate the systematic uncertainties. The comparison with PandaX-4T data between the two methods focuses on the effects of nuisance parameters instead of the best fits in the ML. For the main parameters, including cross-section and WIMP mass, the best fits have a zero-signal number in either method with the downward fluctuation in the signal region for the mass range from 5 to 10,000 GeV/c^2.

The chapter is organized as following. We first introduce the basic idea of reweighting MC in section 6.1. Then in section 6.2, we summarize the fast detector simulation procedure and present where the reweighting strategy can be applied to generate PDFs of NR and ER events. Section 6.3 presents the application of reweighting MC on the preparation of the PDFs in PandaX-4T WIMP search. In section 6.4, we present the application on the PLR analysis with PandaX-4T data for WIMP search, and compare the reweighting MC approach with the template morphing method.

6.1 Probability distribution functions with reweighting Monte Carlo

PDFs of different compositions including signals and backgrounds are often presented after being projected onto the observable variables with the best discrimination power to separate signals from backgrounds. In the construction of the PDFs, even with a simplified fast simulation, many implicit parameters will play important roles such as the drifting electric field $E_{\rm drift}$, the light yields and the recombination ratio of the initial ionization, which are usually hidden if they are fixed in the later likelihood analysis to set the limit and sensitivity. For clarification, the PDF is usually written as a function of variables ($\rm var_*$) and parameters ($\rm par_*$) with a line separated them as

$$\mathrm{PDF} = P(\{\mathrm{var}_*\}|\{\mathrm{par}_*\}). \tag{6.1}$$

However, the expression sometimes becomes ill-defined if an intermediate step of the simulation of an event i is scrutinized, because the parameters might be a function of some variables before this step. For example, the recombination ratio is a function of energy E, and E_i is required to calculate the recombination ratio in the random generation. In this case, we put the required

inputs including parameters and variables of the intermediate step on the right side of the line '|', and the variable follow the P as a result of the random generator on the left side of the line '|'.

6.1.1 Principle

Reweighting MC reuses a pool of simulation events saved ahead of time together with intermediate random $\mathrm{var}_{i,*}$ drawn from par_* for each event i. The reweighted pseudo events construct the new PDFs with analytically calculated new weights. A new weight of the saved event i is computed as the product of probability density ratios of all related intermediate steps. To make the reusage effective, the initial pool should cover the variables used to store the simulation results with enough statistics for each step.

Before presenting the examples, we introduce two random processes commonly used in our detector simulation following Gaussian distribution $G(x, \mu, \sigma)$ and binomial distributions $B(n, N, p)$

$$\begin{aligned} G(x, \mu, \sigma) &= \frac{1}{\sigma\sqrt{2\pi}} \exp\left[-\frac{(x-\mu)^2}{2\sigma^2}\right] \quad \text{and} \\ B(n, N, p) &= \frac{\Gamma(N+1)}{\Gamma(n+1)\Gamma(N-n+1)} p^n (1-p)^{N-n}, \end{aligned} \tag{6.2}$$

where Γ is the Gamma function

$$\Gamma(n) = (n-1)!. \tag{6.3}$$

The variables start with n or N are integers, which will be valid to the rest of this chapter.

6.1.2 Example

In an example with two MC simulation steps with an initial variable x_I, an intermediate variable x_M and a final variable x_F, the probability (density) function of x_F can be expanded as

$$P(x_F|x_I) = \begin{cases} \int_{x_M} P_2(x_F|\Theta_2, x_M) P_1(x_M|\Theta_1, x_I) dx_M, & \text{for continuous } x_M \\ \sum_{x_M} P_2(x_F|\Theta_2, x_M) P_1(x_M|\Theta_1, x_I), & \text{for discrete } x_M \end{cases}, \tag{6.4}$$

where Θ_1 represents the parameter(s) for the first simulation step, and Θ_2 for the second. When we use P to represent the probability density/mass functions, the functions are normalized to 1.

6.1.2.1 Step function reweighting

Let's start with step functions in P_1 and a Gaussian or Binomial in P_2 as

$$\begin{aligned} P_1 &= \frac{1}{|\Theta_1|} \cdot H(x_M + x_I) \cdot H\big(|\Theta_1| - (x_M + x_I)\big) \\ P_2 &= G\big(x_F, \mu(x_M, \boldsymbol{\Theta}_2), \sigma(x_M, \boldsymbol{\Theta}_2)\big) \end{aligned}, \tag{6.5}$$

where H is the unit step function

$$H(x) = \begin{cases} 1, x \geq 0 \\ \\ 0, x < 0 \end{cases}. \tag{6.6}$$

In step P_1, for simplicity, we fix $x_{I,i} = 0$ for every event i, and start from a pool with $\Theta_{1,\text{pool}}$

large enough to cover x_M of interest (see Fig. 6.1). The ith event will hold an original density as

$$\rho_{\text{pool},i} = \frac{1}{|\Theta_{1,\text{pool}}|}. \tag{6.7}$$

A target distribution with $\Theta_{1,\text{target}} = 0.5\Theta_{1,\text{pool}}$ will give a new density to the ith event as

$$\rho_{\text{target},i} = \frac{2}{|\Theta_{1,\text{pool}}|} \cdot H(0.5\Theta_{1,\text{pool}} - x_{M,i}). \tag{6.8}$$

The weight applied on the ith event to generated the distribution of target variable distribution is

$$w_i = \frac{\rho_{\text{target},i}}{\rho_{\text{pool},i}}. \tag{6.9}$$

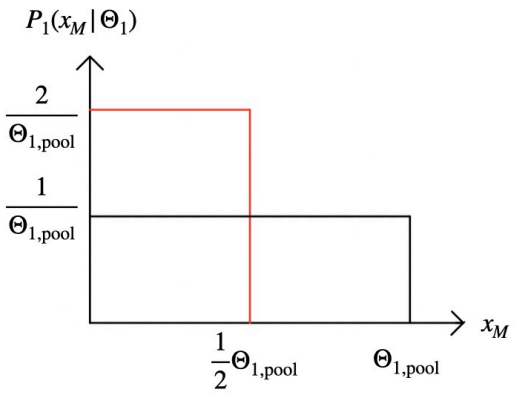

Figure 6.1: The step function example of P_1 in Eq. 6.5 with different Θ_1 as in Eq. 6.7 and Eq. 6.8.

6.1.2.2 Gaussian reweighting

Let's discuss the reweighting according to different Gaussian distributions to present the importance of covering the region of interest in the pool. In Fig. 7.9(a), we present a qualified

pool covers the target by minor statistic sacrifice around the peak region of the target Gaussian distribution, and presents smaller uncertainties where $\rho_{\text{target},i} \ll \rho_{\text{pool},i}$. On contrary, Fig. 7.9(b) is an unqualified pool that fails to reconstruct the target distribution. We suggest that the pool of the Gaussian reweighting should satisfy

$$\begin{aligned} &\mu_{\text{pool}} \sim \bar{\mu}_{\text{target}} \text{ and} \\ &\sigma_{\text{pool}} \geq \max\{|\Delta_{\mu\text{target}}| + \sigma_{\text{target}}\}. \end{aligned} \tag{6.10}$$

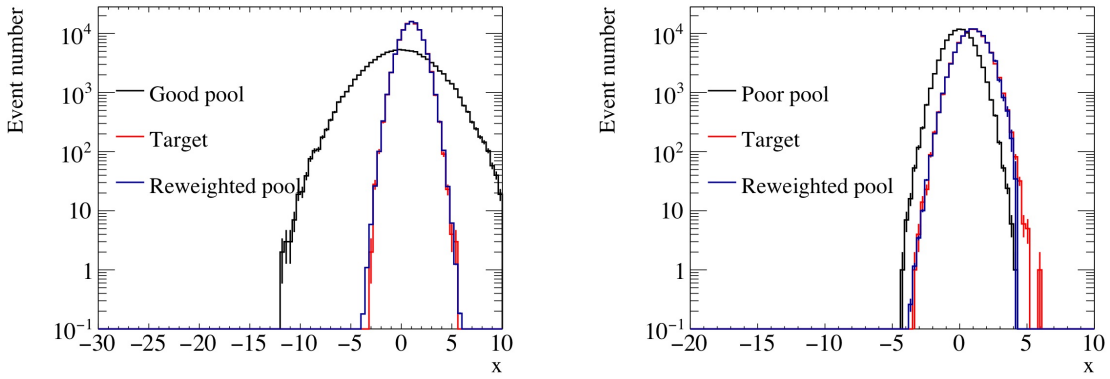

Figure 6.2: The reweighting example of one-dimensional Gaussian distributions for a target $G(x, \mu = 1, \sigma = 1)$. The red line is generated with conventional MC. (a) Reweighting with a qualified pool $G(x, \mu = 0, \sigma = 3)$, (b) Reweighting with an unqualified pool $G(x, \mu = 0, \sigma = 1)$.

6.1.2.3 Binomial reweighting

Because the pool only needs to remember the variables and the corresponding probability density in the related random processes, it is unnecessary to use the same generator in the pool as the target. It is better to prepare a pool for a binomial distribution target with a truncated Gaussian function generator for a better coverage of the variables as shown in Fig. 6.3. For

a target distribution of n following $B(n, N, p)$, the expectation and standard deviation of the distribution is Np and $\sqrt{Np(1-p)}$. To cover the n of interest, a pool with $G(n, \mu_{\rm pool}, \sigma_{\rm pool})$ should satisfy

$$\begin{aligned} \mu_{\rm pool} &= \overline{Np}, \\ \sigma_{\rm pool} &\geq \max\{\Delta(Np) + \sqrt{Np(1-p)}\}. \end{aligned} \tag{6.11}$$

Together with the requirement of n being an integer of an event i in the MC simulation, a $\rho_{{\rm pool},i}$ with the choice of μ and σ holding dependence on N_i is evaluated as

$$\begin{aligned} \rho_{{\rm pool},i}(n_i|\mu_{{\rm pool},i}, \sigma_{{\rm pool},i}) &= \int_{n_i-0.5}^{n_i+0.5} G(x, \mu_{{\rm pool},i}, \sigma_{{\rm pool},i})dx \\ &= 0.5 \cdot \left({\rm Erf}(\frac{n_i + 0.5 - \mu_{{\rm pool},i}}{\sqrt{2} \cdot \sigma_{{\rm pool},i}}) - {\rm Erf}(\frac{n_i - 0.5 - \mu_{{\rm pool},i}}{\sqrt{2} \cdot \sigma_{{\rm pool},i}}) \right), \end{aligned} \tag{6.12}$$

where ${\rm Erf}$ is the error function as

$${\rm Erf}(x) = \frac{2}{\sqrt{\pi}} \int_0^x \exp(-x^2)dx. \tag{6.13}$$

The target distribution will present a new density according to

$$\rho_{{\rm target},i}(n_i|N_i, p_{\rm target}) = B(n_i, N_i, p_{\rm target}). \tag{6.14}$$

The new weight of the ith event is

$$w_i = \frac{\rho_{{\rm target},i}}{\rho_{{\rm pool},i}}. \tag{6.15}$$

Technically, $\log\left(B(n_i, N_i, p_{\text{target}})\right)$ is calculated due to finite scope allowed for integers when we calculate $\Gamma(x)$.

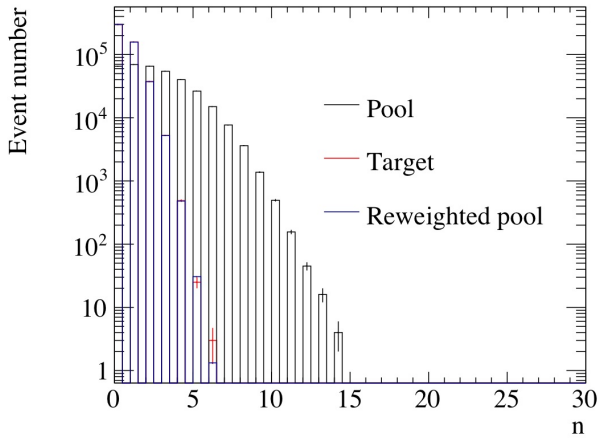

Figure 6.3: Reweighting example for one-dimension binomial distribution target $B(n, N = 10, p = 0.05)$ with a pool (black line) prepared by truncating a Gaussian $G(x, \mu = 1, \sigma = 0.9)$ with $x > -0.5$ and rounding x to integers n. The red line is generated with conventional MC.

6.1.3 Uncertainties

In the example presented in section 6.1.2.1 (Fig. 6.1), the target variable generation can be directly sampled with $\Theta_{1,\text{target}}$ without reweighting, yielding $\sqrt{2}$ smaller statistical uncertainties on average with the same amount of events initially generated. The ratio of the statistical uncertainty in each event i increased or decreased according to the pooling choice is $\sqrt{\rho_{\text{target},i}/\rho_{\text{pool},i}}$. It won't be appropriate to estimate the overall uncertainty difference between reweighting with a pool and direct generation by averaging $\{\sqrt{\rho_{\text{target},i}/\rho_{\text{pool},i}}\}$. It is preferred to have a right size of the pool and large enough number of events to make the statistical uncertainties in the simulation insignificant in the region $\rho_{\text{target},i} > \rho_{\text{pool},i}$. The extra uncertainties in reweighting MC only makes the PLR analyses more conservative compared to an ideal PDF prepared analytically or

with infinitely many simulation events, but makes the analyses more robust with less marginalization of the systematic uncertainties.

6.1.4 Brief summary

A more realistic detector simulation often contains more than two steps. Each step plays a role in the probability function requiring the pool to save a $\rho_{*,\mathrm{pool},i}$ and related variables $\mathrm{var}_{*,\mathrm{i}}$. The new weight $w_{\mathrm{tot},i}$ according to different steps will be a product of the $\{w_{*,i}\}$.

$$w_{\mathrm{tot},i} = \prod_{*} w_{*,i}, \tag{6.16}$$

Each $w_{*,i}$ is related to one or more $\mathrm{var}_{*,i}$ and par_{*}.

6.2 Fast detector simulation

Noble Element Simulation Techniques (NEST) provide a phenomenological model to do fast detector simulations for low energy NRs, ERs, α events and etc. in a LXeTPC. By including different experimental measurements, a canonical calibration is constructed in NEST which could be further adjusted according to some detector effects like the photon detection efficiency (PDE), single electron gain (SEG), electron extraction efficiency (EEE) and etc. As our data should be comparable to the other LXeTPCs, the modification of the canonical NEST should be a higher order effect, and

The procedure of the fast simulation follows the schematics shown in Fig. 6.4. Starting from the energy depositon of the event, the initial ionization and scintillation yields are calculated where the heat/phonons are quenched and not detected in a LXeTPC. Then, the recombination

ratio of the electron-ion pairs are evaluated with part of the initial ionization recombining and producing $S1$. The survived free electrons leads to the amount of $S2$.

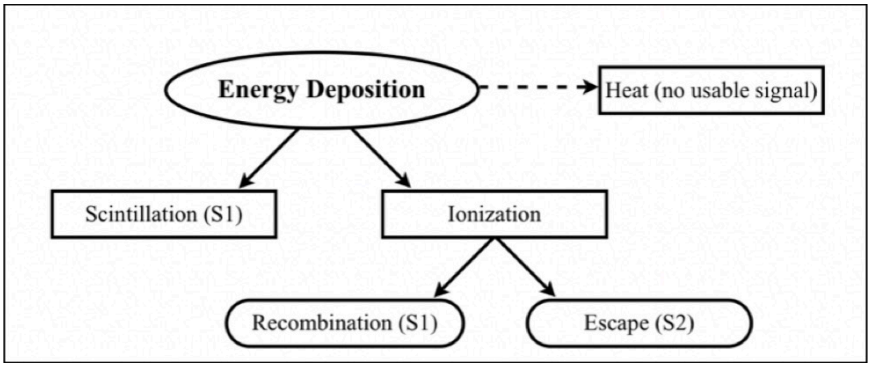

Figure 6.4: The schematics of the fast detector simulation with NEST.

In WIMP search, we focus on the NRs and ERs below 100 keV_{ee}. More detailed random generators related to the NR/ER simulation are summarized in Tab. 6.1 where the canonical NEST2 (v.2.2.1) is used if not marked by '$\star$' or explained. The 'canonical' means no waveform simulation included, and the summed charges of $S1$ and $S2$ are directly simulated without hits generated one by one. Each P indicates an individual random generator, and f means an analytical calculation. Some minor differences lie in different truncation choices at physics borders, which may lead to slightly different efficiencies (expected to be smaller than 0.5%). The choices of Gaussian or Binomial generator for some intermediate steps may also cause differences at the energy threshold. But the degrees of freedom we add into the original NEST2 are enough to mitigate the differences and present successful calibration with a combined fit of the radon (^{220}Rn) low-energy ER progenies, AmBe neutrons and DD fusion neutrons.

In this chapter, the main degrees of freedom to modify the canonical NEST are added on the median and fluctuation in the recombination ratio calculation which are parameterized in $\mathbf{p}_{\text{extra}}$ that are enough to reflect the medians and spreading of the $S2$ and $S1$ responses for

No.	Brief description	Generator or calculator NR	Generator or calculator ER	Pool
1	Energy deposition E	$P(E)$		Both
2	Total effective quanta N_q	$P(N_q\|E)^\star$	$P(N_q\|E, E_{\rm drift})$	ER
3	Ionization and scintillation quanta n_q	$P(n_q\|N_q, E)^\star$	$n_q = N_q$	N/A
4	Initial ionization quanta $n_{\rm ion}$	$P(n_{\rm ion}\|n_q, E, E_{\rm drift})$	$P(n_{\rm ion}\|n_q, E)$	NR
5	Number of electrons $n_{\rm ele}$ and photons $n_{\rm pho}$ with recombination rate $r_{\rm rec}$	$P(r_{\rm rec}\|E, E_{\rm drift}, \mathbf{p}_{\rm extra})$ $P(n_{\rm ele}\|n_{\rm ion}, r_{\rm rec})$ $n_{\rm pho} = N_q - n_{\rm ele}$		Both
6	Vertical vertex of the recoiling z	GEANT4 simulated distribution or uniform in ($t_{z,\rm min}, t_{z,\rm max}$)		Both
7	From $n_{\rm pho}$ to $S1$			
7.a	Detected hit number $n_{\rm hit1}$	$P(n_{\rm hit1}\|n_{\rm pho}, \bar{g}_1, z)$		Both
7.b	Double photon emission	$P(n_{\rm extra1}\|n_{\rm hit1})$		N/A
7.c	$S1_{\rm ori}$ with single photoelectron resolution	$P(S1_{\rm ori}\|n_{\rm hit1}, n_{\rm extra1})$		N/A
7.d	Baseline suppression (Fig. 6.10(a))	$P(S1_{\rm det}\|S1_{\rm ori})$		N/A
7.e	Reverse correction of z dependence	$S1_{\rm cor} = f(S1_{\rm det}, z)$		N/A
7.f	Extra noise smearing	$P(S1\|S1_{\rm cor})$		N/A
8	From $n_{\rm ele}$ to $S2_b$			
8.a	Electron number in the gas phase $n_{\rm eGas}$ with electron lifetime τ_e (Fig. 6.11)	$P(n_{\rm eGas}\|n_{\rm ele}, z, \tau_e, v_e, \rm EEE)$		Both
8.b	The original hit number of $S2_b$, $n_{\rm hit2}$	$P(n_{\rm hit2}\|n_{\rm eGas}, \rm SEG)$		Both
8.c	Extra hit similar to 7.b	$P(n_{\rm extra2}\|n_{\rm hit2})$		N/A
8.d	$S2_{b,\rm ori}$ similar to 7.c	$P(S2_{b,\rm ori}\|n_{\rm hit2}, n_{\rm extra2})$		N/A
8.e	Charge loss in $S2_{b,\rm ori}$ (Fig. 6.10(b))	$P(S2_{b,\rm det}\|S2_{b,\rm ori})$		N/A
8.f	Reverse correction of z similar to 7.e	$S2_b = f(S2_{b,\rm det}, z, \tau_e, v_e)$		N/A

Table 6.1: Brief summation of the simulation steps in the fast detector simulation. The step with a star mark ($\star$) means a different parameterization is used compared to NEST2.

Name	Value
E_{drift} [V/cm]	127.4, 115.6, 109.7, 92.8, 92.8
v_e [mm/μs]	1.481, 1.463, 1.450, 1.409, 1.409
$t_{z,\text{min}}$ [μs]	38.0, 38.5, 38.9, 40.0, 40.0
$t_{z,\text{max}}$ [μs]	761.0, 770.5, 777.2, 800.0, 800.0
NoiseLinear	0.028
SPEres [PE]	0.3
DPE [%]	22
$\tilde{G1}$ [%]	9.0(0.2)
SEG [PE]	3.8(0.1), 3.8(0.1), 4.6(0.1), 4.6(0.1), 4.6(0.1)
σ_{SEG}/SEG	0.27
EEE [%]	90.2(5.4), 90.2(5.4), 92.6(5.4), 92.6(5.4), 92.6(5.4), 92.6(5.4)
z_{max} [mm]	1185
Density of LXe [g/cm^3]	2.8611

Table 6.2: The detector simulation parameters for the 5 sets in PandaX-4T Run 1. The main uncertainties of the parameters are shown in the round brackets. The rows with only one value have the 5 sets sharing the same parameter.

low energy NRs and ERs. The other parameters in the simulation marginalized as constants are not listed in Tab. 6.1, but are summarized in Tab. 6.2. These parameters can be added as extra degrees of freedom in the future to include the uncertainties related to the detector responses after the consistency check with the template morphing method which limits the number of detector parameters to two or three.

For reference, we present more details in the simulation step by step.

1. The energy deposition of either ER or NR, E, is sampled according to the expected energy spectrum

$$P(E) = \frac{dR}{dE}(E). \tag{6.17}$$

2. The total quanta number N_q follows a Gaussian random generator

$$P\left(N_q|E,(E_{\text{drift}})\right) = G\left(N_q, \mu_q, \sqrt{\text{Fano}\cdot\mu_q}\right), \tag{6.18}$$

where $\mu_q = E/W$ is the mean of total quanta number generated, and W is the work function to generate a quanta [193, 194]. The Fano factor is for the theoretical irreducible uncertainty which depends on $E_{\rm drift}$ for ER (Fig. 6.5) [208].

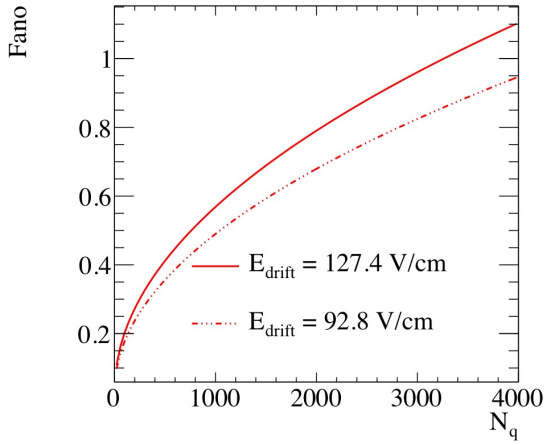

Figure 6.5: The Fano factor dependence on the total quanta number N_q for ER under different electric fields.

3. The detectable quanta number n_q is generated with

$$P(n_q|N_q, E) = B(n_q, N_q, L(E)), \tag{6.19}$$

where L is the Lindhard factor[209]. The L is 100% for ER but for a 50 keV$_{\rm nr}$ energy deposition, about 80% of the energy is quenched into heat and other losses which are not detectable in a LXeTPC. The '$\star$' in Tab. 6.1 is for the difference of W in the NR simulation. We keep W of NR and ER the same (13.7 eV). The difference should only cause minor effects in the fluctuation of n_q because we follow the same parameterization of $\bar{n}_q$ dependence on E as

$$\bar{n}_q = W \cdot L(E) = 11 \cdot [E\ ({\rm keV_{nr}})]^{1.1}. \tag{6.20}$$

4. The initial ionization number, $n_{\rm ion}$, follows

$$P\left(n_{\rm ion}|n_q, E, (E_{\rm drift})\right) = B(n_{\rm ion}, n_q, p_{n_{\rm ion}}). \tag{6.21}$$

The $p_{n_{\rm ion}}$ presents the percentage of electron-ion pars generated, and the others are excitons, which is a function of E. For NR, $p_{n_{\rm ion}}$ depends on $E_{\rm drift}$ (Fig. 6.6). The initial number of electron-ion pairs is $n_{\rm ex} = n_q - n_{\rm ion}$.

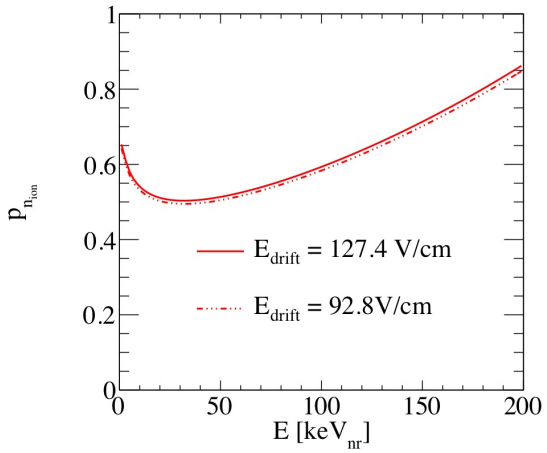

Figure 6.6: The probability of n_q to be an electron-ion pair instead of an exciton, $p_{n_{\rm ion}}$ for NR under different drifting electric fields.

5. The recombination rate of the electron-ion pairs, $r_{\rm rec}$, is randomly generated following

$$P(r_{\rm rec}|E, E_{\rm drift}, \mathbf{p}_{\rm extra}) = G(r_{\rm rec}, \mu_r, \sigma_r), \tag{6.22}$$

where both μ_r and σ_r are functions of E and $E_{\rm drift}$. We add four degrees of freedom in $\mathbf{p}_{\rm extra}$ such that the NEST model can agree with our calibration data . The modification on

the original $\mu_{r,0}$ is

$$\begin{aligned}\mu_r(E, p_0, p_1, p_2) =& \mu_{r,0}(E) + p_0 \cdot P_0\left(\frac{E}{E_{\text{norm}}}\right) + \\ & p_1 \cdot P_1\left(\frac{E}{E_{\text{norm}}}\right) + p_2 \cdot P_2\left(\frac{E}{E_{\text{norm}}}\right),\end{aligned} \tag{6.23}$$

where

$$\begin{cases} P_0(x) = 1 \\ P_1(x) = x \\ P_2(x) = 0.5 \cdot (3x^2 + 1) \end{cases}. \tag{6.24}$$

The normalization energy E_{norm} represents the energy window we are interested in, which is 50 keV$_{\text{ee}}$ (150 keV$_{nr}$) for ER (NR). The $\sigma_{r,0}(E)$ is modified with a scaling factor

$$\sigma_r(E, p_f) = p_f \cdot \sigma_{r,0}(E)). \tag{6.25}$$

The covariance matrixs of $\mathbf{p}_{\text{extra}}$ in our calibrated detector simulation can be found in Fig. 6.7, which correspond to the calibrated μ_r and σ_r (the 1σ band is plotted with the red shades) in Fig. 6.8. Then, the survived free electron numbers, n_{ele}, follows

$$P(n_{\text{ele}}|n_{\text{ion}}, r_{\text{rec}}) = B(n_{\text{ele}}, n_{\text{ion}}, 1 - r_{rec}). \tag{6.26}$$

The total photon number is $n_{\text{pho}} = n_q - n_{\text{ele}}$.

6. Sample vertical vertexes z according to different sources. For calibration events, ^{220}Rn is uniformly distributed. The z-distributions of neutron events require the GEANT4 simulation

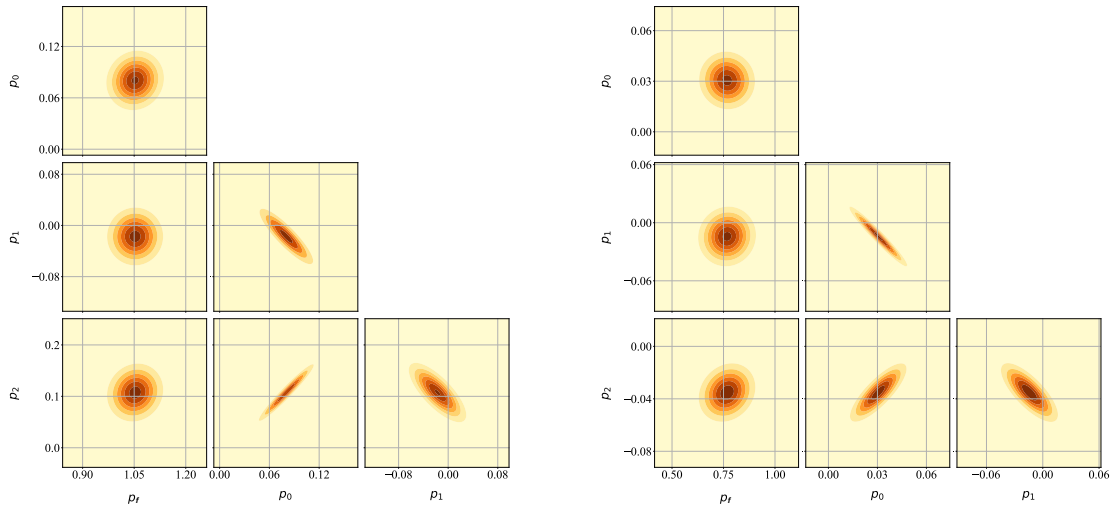

(a) (b)

Figure 6.7: Covariance matrix of $\mathbf{p}_{\text{extra}}$ for ER (a) and NR (b).

(BambooMC) ahead of this detector simulation as a reference for the vertical distribution. The allowed z satisfies

$$t_{z,\min} < \frac{z}{v_e} < t_{z,\max}, \tag{6.27}$$

where v_e is the drifting velocity of free electrons in the LXe. The minimum (maximum) drifting time, $t_{z,\min}(t_{z,\max})$, is related to the fiducial volume defined for each set which can be found in Tab. 6.2.

7. The generation from n_{pho} to $S1$.

   a The original hit number of $S1$, n_{hit1}, follows

$$P(n_{\text{hit1}}|n_{\text{pho}}, \bar{G1}, z) = B\left(n_{\text{hit1}}, n_{\text{pho}}, \frac{G1(z)}{1+\text{DPE}}\right), \tag{6.28}$$

   where DPE stands for the double photoelectron emission probabilities, describing

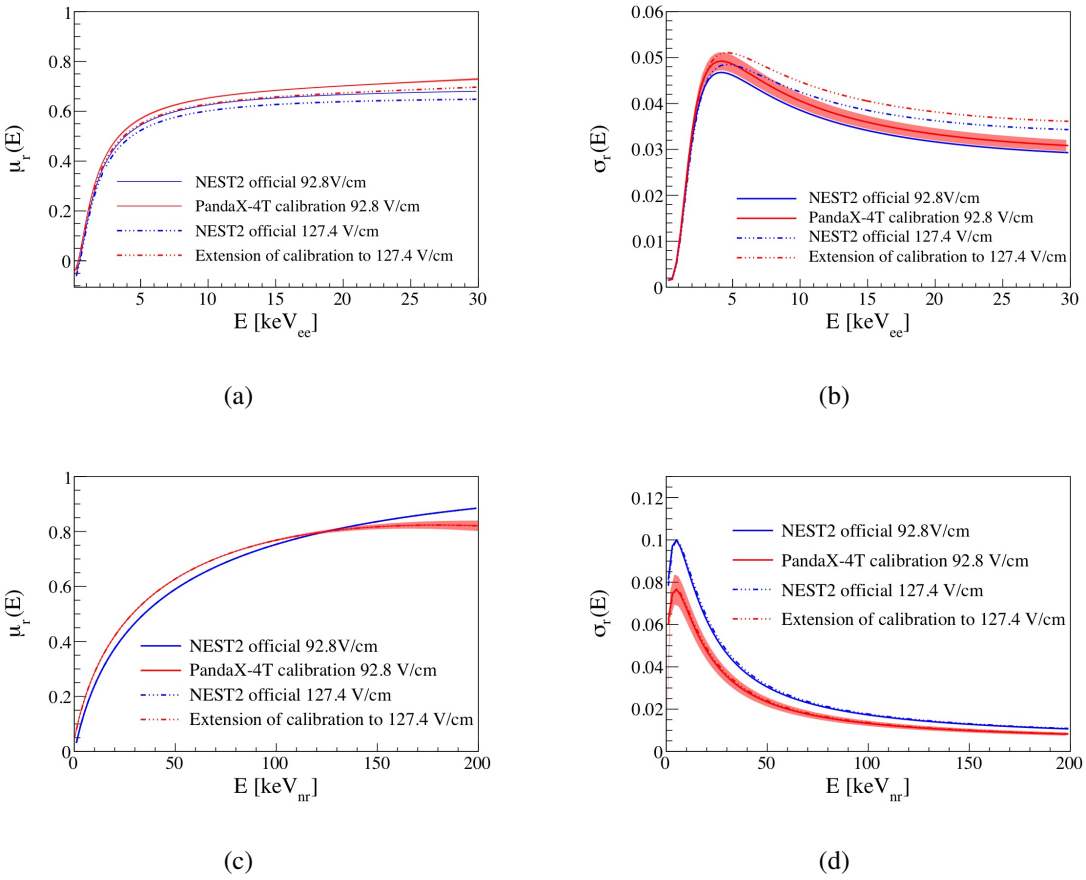

Figure 6.8: (a) ER recombination ratio mean. (b) ER recombination ratio standard deviation. (c) NR recombination ratio mean. (d) NR recombination ratio standard deviation. The deviation of the $\mu_r(E)$ and $\sigma_r(E)$ calibrated with data taken under $E_{\text{drift}} = 92.8$ V/cm for ER (^{220}Rn) and NR (DD and AmBe sources) respectively. The extensions to 127.4 V/cm are also plotted. The transparent red band is the 1σ band of the

the probabilities for the PMTs to emit two photons from the photocathode with one single incoming photon. The photon detection efficiency, $G1$, depends on z. The $r_{G1}(z)$ is parameterized with a polynomial function of degree 3 as shown in Fig. 6.9 for the PandaX-4T Run 1, and the mean $\bar{G}1$ can be found in Tab. 6.2. The horizontal dependency is not included in the simulation but corrected in the data processing.

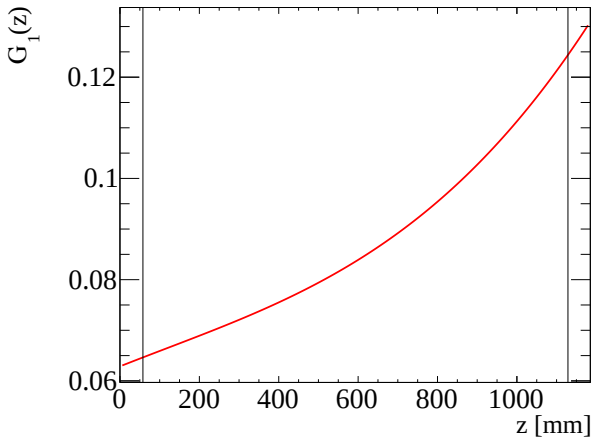

Figure 6.9: The dependence of photon detection efficiency $G1$ on z calibrated by the 164 $\mathrm{keV_{ee}}$ peak of ^{131m}Xe. The $z = 0$ accords to the liquid-gas interface. The black lines mark the vertical fiducial cuts to avoid excessive cathode events and gate events.

b The extra hit number because of DPE follows

$$P(n_{\mathrm{extra1}}|n_{\mathrm{hit1}}) = B(n_{\mathrm{extra1}}, n_{\mathrm{hit1}}, \mathrm{DPE}). \tag{6.29}$$

The detected hit number is $n_{\mathrm{hit1,sum}} = n_{\mathrm{hit1}} + n_{\mathrm{extra1}}$.

c The $S1_{\mathrm{ori}}$ is generated with

$$P(S1_{\mathrm{ori}}|n_{\mathrm{hit1}}, n_{\mathrm{extra1}}) = G(S1_{\mathrm{ori}}, n_{\mathrm{hit1,sum}}, \mathrm{SPEres} \cdot \sqrt{\mathrm{n_{hit1,sum}}}), \tag{6.30}$$

where SPEres is the single photoelectron resolution (PandaX-4T Run 1 in Tab. 6.2).

d The charge loss, BLS_i, due to the baseline suppression (BLS) firmware is sampled with a data driven calibration for different $S1_{\mathrm{ori}}$. The PandaX-4T BLS mapping is shown in Fig. 6.10(a) [210]. Then, $S1_{\mathrm{det}} = \mathrm{BLS} \cdot S1_{\mathrm{ori}}$.

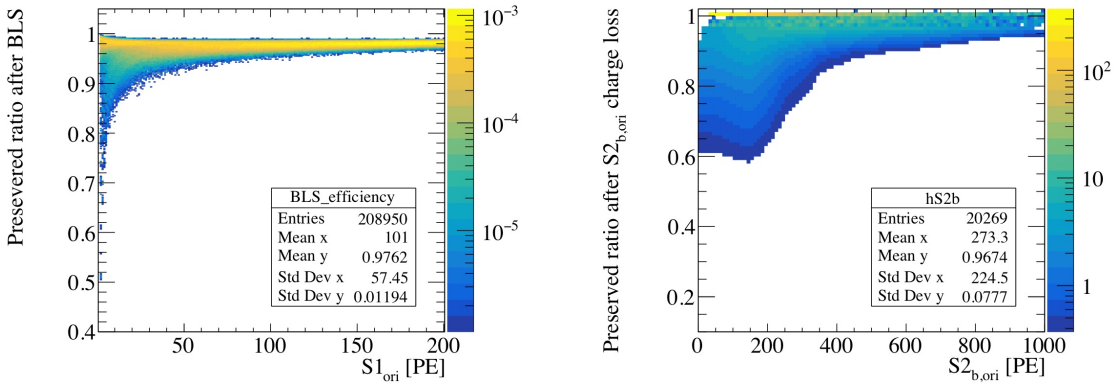

(a) (b)

Figure 6.10: The data calibration nonlinear charge losses in the reconstruction: (a) BLS of $S1_{\rm ori}$ and (b) charge loss of $S2_{b,{\rm ori}}$. The color bar represents the distribution of the probability but with non-normalized scale.

e Correct the z dependency in $G1$ with

$$f(S1_{\rm det}, z) = S1_{\rm det} \cdot \bar{G1}/G1(z). \tag{6.31}$$

f Finalize the $S1$ generation by further accounting for the noise in the detection with

$$P(S1|S1_{\rm cor}) = G(S1, S1_{\rm cor}, {\rm noiseLinear} \cdot S1_{\rm cor}), \tag{6.32}$$

where the linear noise parameter (noiseLinear) can also be found in Tab. 6.2.

8. The generation from $n_{\rm ele}$ to $S2_b$, where the subscript of b means only the photoelectrons collected by the bottom PMT array is used in the following analysis.

a The electron lifetime, τ_e, is found for each set by the 164 $\rm keV_{ee}$ deexcitation peak of ^{131m}Xe (Fig. 6.11). It can be randomly generated according to the histograms or directly assigned to the events with the duration as the ratio. The survived electrons

in the gaseous xenon $n_{\mathrm{eGas},i}$ follows

$$P(n_{\mathrm{eGas}}|n_{\mathrm{ele}}, z, \tau_e, v_e, \mathrm{EEE}) = \mathrm{B}(\mathrm{n_{eGas}}, \mathrm{n_{ele}}, \mathrm{EEE} \cdot \exp(-\mathrm{z}/(\mathrm{v_e} \cdot \tau_\mathrm{e}))), \quad (6.33)$$

where the EEE is the electron extraction efficiency at the liquid-gas interface.

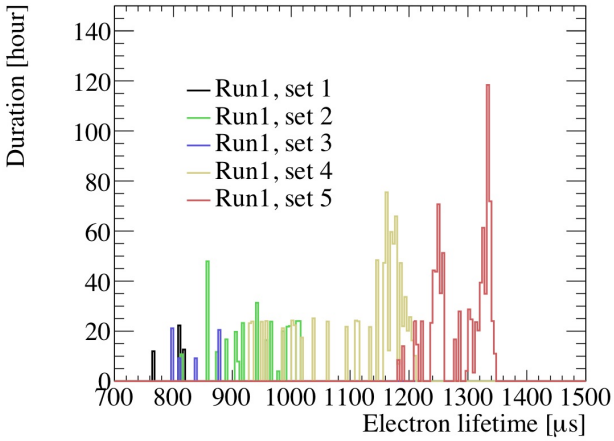

Figure 6.11: The elifetron lifetime τ_e for the five subsets in the PandaX-4T commissioning run.

b The original hit number of $S2_b$, n_{hit2}, is generated with

$$P(n_{\mathrm{hit2}}|n_{\mathrm{eGas}}, \mathrm{SEG}) = G(n_{\mathrm{hit2}}, \mathrm{SEG} \cdot n_{\mathrm{eGas}}, \sigma_{\mathrm{SEG}} \cdot \sqrt{n_{\mathrm{eGas}}}), \quad (6.34)$$

where SEG stands for the single electron gain calibrated with the smallest $S2$ found in the data with uncertainty σ_{SEG}, and the ratio $S2_b/S2$ for the events can be used to found SEG_b. SEG reflects the electroluminescence amplification which depends on the extraction electric field, gaseous xenon pressure and the photon detection efficiency in $S2_b$ (geometric reasons).

c Similar to $S1$ generation from the step 7.c to 7.f, the generation of $S2_b$ accounts for

the DPE, BLS and z dependency. The difference is that the z dependence is corrected with a factor

$$f(S2_{b,\mathrm{det}}, z, \tau_e, v_e) = S2_{b,\mathrm{det}} \cdot \exp(z/(v_e \cdot \tau_e)). \tag{6.35}$$

With a step-by-step simulation explained ahead, let's discussed the efficiencies included. The efficiencies on the simulated events depend on the cuts developed in the software data processing chain, and will by no means be the same among different detectors. The signal reconstruction efficiencies and detector efficiencies are integrated into the simulation as

1. $n_{\mathrm{hit1}} > 2$, which means at least two PMTs are fired for $S1$.

2. $S1 > 2$ PE, which is the $S1$ threshold.

3. $n_{\mathrm{hit2}} > 0$, because the SEG fluctuation is modeled as a Gaussian function which may cause nonphysical events in Eq. 6.34.

4. $S2_{b,\mathrm{ori}} > 21.6$ PE, which is the threshold on $S2_b$ before the reverse correction of τ_e.

5. $\log_{10}(S2_b/S1) > \mathrm{Acceptance}(S1)$ for 99.5% NR acceptance (purple line in Fig. 6.12).

The quality-cut efficiencies are parametrized as functions of $S1$ and $S2_b$ because the data selection is made in the two quantities. The efficiencies are estimated by left-over ratios of the β-decays in the ^{220}Rn progenies for ER, and neutrons generated by DD fusion and AmBe (α, n)-reactions for NR as functions of $S1$ and $S2_b$ with outliers excluded by 5%-95% quantiles. The cut efficiencies related to $S1$ and $S2_b$ can be found in Fig. 6.13(a) and Fig. 6.13(b), where we don't include the efficiency of the diffusion cut (95%) on the width of the S2 charges as a function of the drifting time. The quality-cut efficiencies should be the same for ERs and NRs measured under

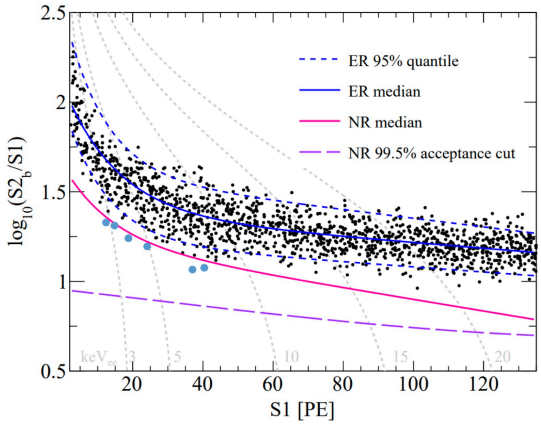

(a) ^{220}Rn

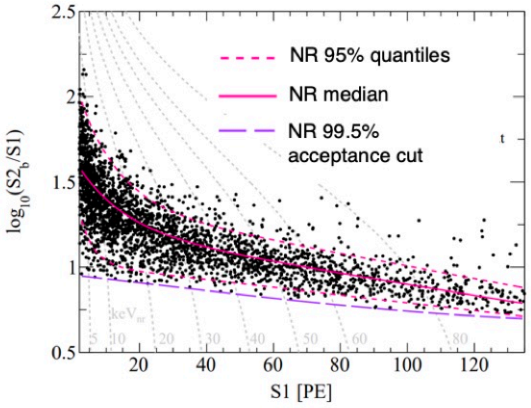

(b) DD

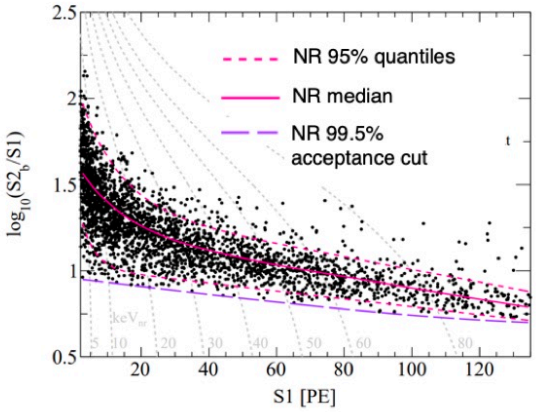

(c) AmBe

Figure 6.12: Calibration data taken under 92.8 V/cm

the same detector parameters, but could be different for different calibration conditions. ^{220}Rn calibration data with a high event rate causes difference in the data acquisition present a different dependency on the quality-cut efficiencies, which is not plotted here but should be kept in mind. While calibrating the detector simulation with degrees of freedom added with $\mathbf{p}_{\mathrm{extra}}$, we fixed the quality cut efficiencies on $S1$ and $S2$ to the center because they are highly correlated at the energy threshold. The $\mathbf{p}_{\mathrm{extra}}$ will absorb the uncertainties in the efficiencies except a constant efficiency factor on the total observed event number. Extra efficiencies are from the $S1$ window (2-135 PE)

for the WIMP search in PandaX-4T Run 1, and 99.5% NR acceptance cut as shown in Fig. 6.12.

The total efficiencies of ER and NR with all cuts is shown in Fig. 6.14.

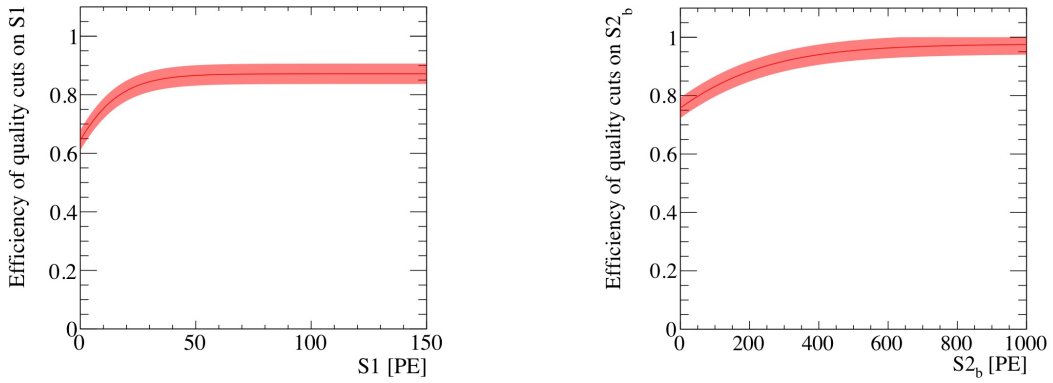

(a) $S1$ efficiency (b) $S2_b$ efficiency

Figure 6.13: Quality-cut efficiencies on $S1$ and $S2_b$ except diffusion band cut (95%) according to data in Fig. 6.12 before calibrating the detector simulation. The interpretation in the region of $S1 < 2$ PE and $S2_b < 20$ PE is not valid as no calibration data cover this region. NEST at the threshold already ensures a 0 efficiency at 0 PE, the quality-cut efficiencies on $S1$ and $S2$ are added onto NEST which is fine if it's not 0 at 0 PE in the parameterization.

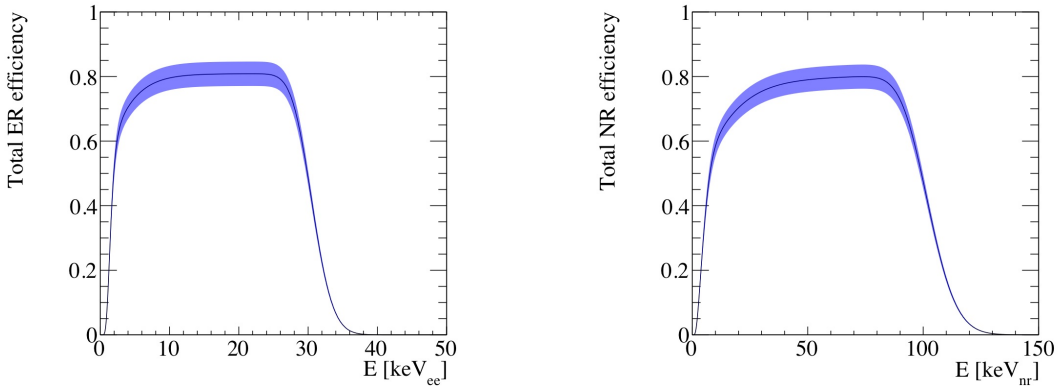

(a) Total ER efficiency (b) Total NR efficiency

Figure 6.14: Efficiencies of ER and NR due to pre-calibrated quality cuts and detector simulation integrated cuts. For reference, the total efficiencies reach 50% at 1.95 keV$_{ee}$ for ER and 7.65 keV$_{\rm nr}$ for NR.

The detector parameters in step 7 and 8 of Tab. 6.1 is well-constraint by calibrations on $G1$ and $G2_b$ ($=$ EEE $\times$ SEG$_b$) with mono-energetic peaks as shown in Fig. 6.15. The tuning of the

canonical NEST2 mainly lies in step 5 of the recombination ratio with $p_{\rm extra}$. The comparison of the fitted NEST model and calibration data can be found in Fig. 6.17. The difference in the observable $(S1, S2_b)$ between the original NEST2 and the calibrated can be seen in Fig. 6.16 where we used a flat ER and 10 TeV WIMP energy spectrum.

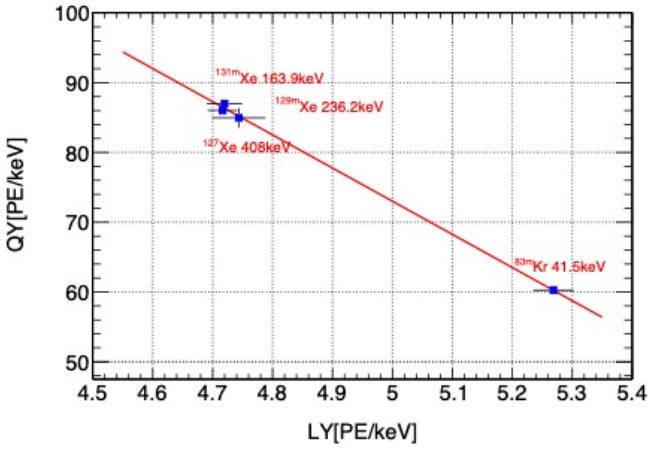

Figure 6.15: Charge yield vs. light yield in PE/keV and the linear fit with uniformly distributed ER peaks, ^{131m}Xe (164 keV$_{\rm ee}$), ^{129m}Xe (236 keV$_{\rm ee}$), ^{127}Xe (408 keV$_{\rm ee}$), and ^{83m}Kr (41.5 keV$_{\rm ee}$), which are used in the detector parameter fit of $G1$ and $G2_b = \text{EEE} \times \text{SEG}_b$ listed in Tab. 6.2.

6.3 Reweighted probability distribution functions

After introducing the reweighting MC and fast detector simulation, more practical examples of preparing PDFs are presented in this section for the following profile likelihood analysis (PLR). Besides the reweighting techniques, sometimes it is better to prepare different pools for a large difference in the detector parameters like different $E_{\rm drift}$ and τ_e in different data sets. It is a waste to have too many events in the pool generated with parameters that not used in any data set.

We have tried two ways to prepare the pool. One is to minimize the number of the pools that different pools are prepared only for the large difference in the energy spectrum and every

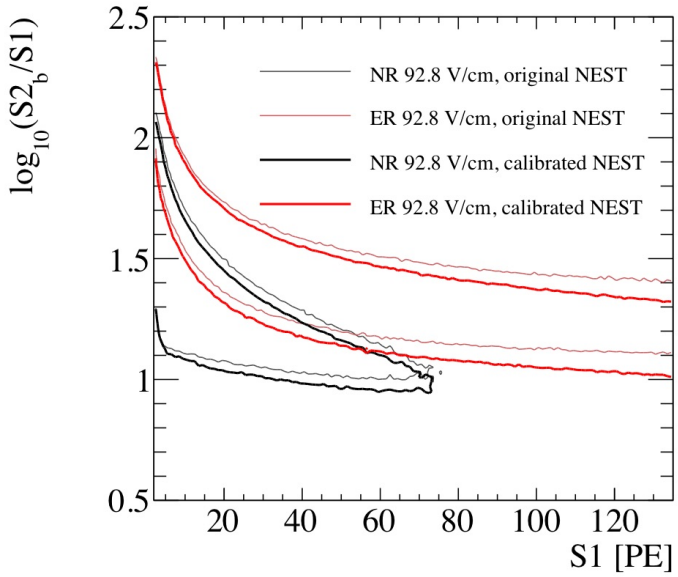

Figure 6.16: The comparison of the original NEST2 and the calibrated version with observable $(S1, S2_b)$. A flat energy spectrum is used for ER, and 10 TeV WIMP for NR. The contour lines correspond to 10% of the largest probability.

data set shares the same pool. The other is to add more pools for different data sets. It turns out the latter is more effective and has a smaller statistical uncertainties with the same amount of total events in the pool for this practical application with 5 data sets in Run 1, but the former one is discussed in details for pedagogical reasons.

6.3.1 Major detector parameters

To prove viability, we keep tracking the uncertainties in two detector parameters as what used with template morphing in Ref. [2] which preserves the two most important parameters related to $\mathbf{p}_{\text{extra}}$ in the modification of recombination ratio of the initial ionization for ERs as described in step 5. The p_f to scale $\sigma_{r,0}(E)$ is preserved directly, and a principle component analysis is done for (p_0, p_1, p_2) to cast the major parameter $p_0^{'}$ along the 'long axis'. More

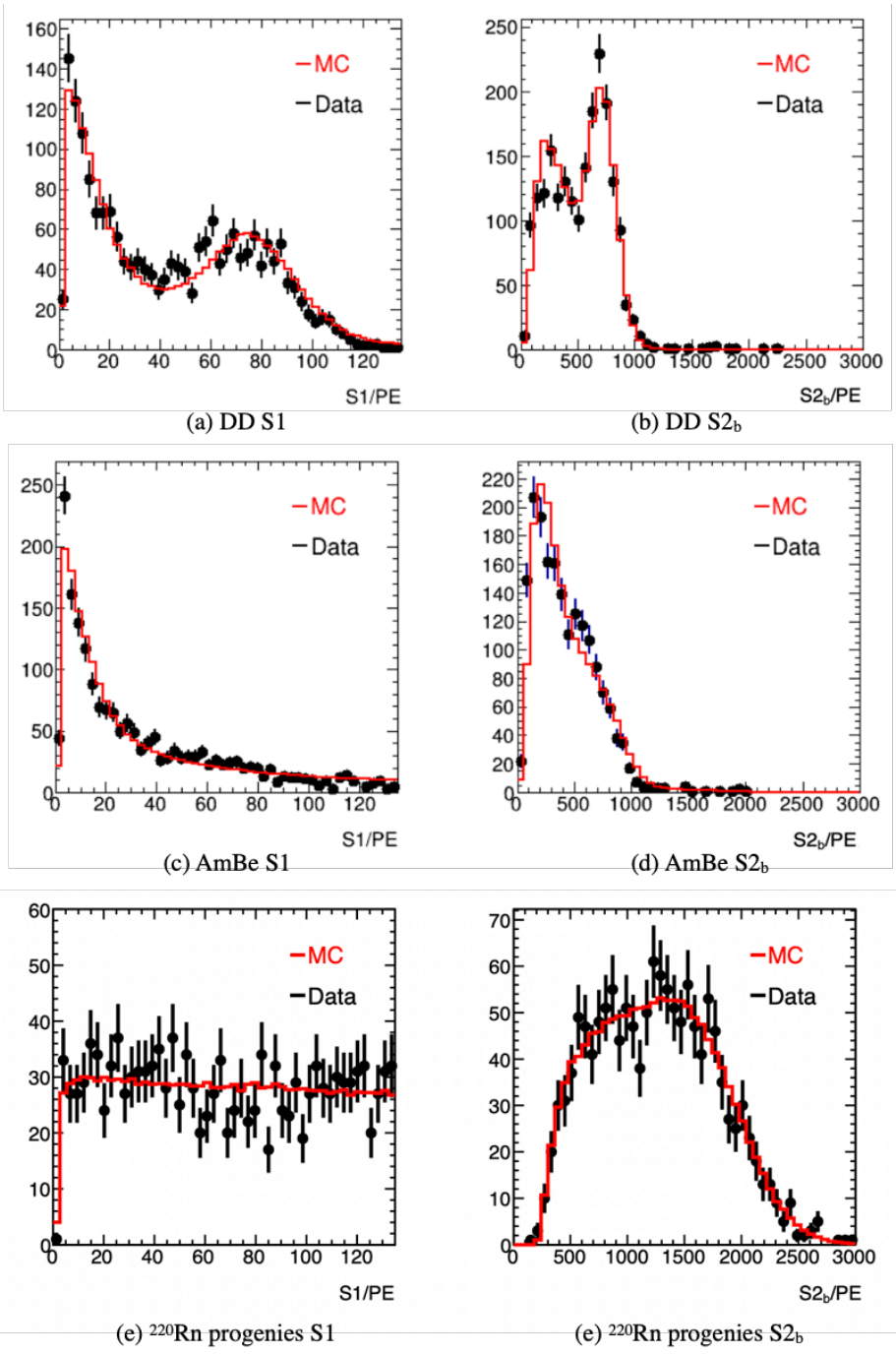

Figure 6.17: The tuned NEST model compared to calibration data with projections on $S1$ and $S2_b$ for DD neutron (NR), AmBe neutron (NR) and ^{220}Rn progenies in the low-energy window (ER).

specifically, the rotational matrix $R_{3\times3}$ is found

$$\begin{pmatrix} p_0^{'} \\ p_1^{'} \\ p_2^{'} \end{pmatrix} = R_{3\times3} \begin{pmatrix} p_0 \\ p_1 \\ p_2 \end{pmatrix} \tag{6.36}$$

such that the uncertainties in (p_0, p_1, p_2) (Fig. 6.7) are mainly absorbed in $p_0^{'}$. The $p_1^{'}$ and $p_2^{'}$ are marginalized to the best fit.

$$\begin{aligned} \mu_r(E) =& \mu_{r,0}(E) + (0.0786p_0^{'} + 0.0170) \\ &+ (-0.0735p_0^{'} + 0.00661) \times \frac{E}{10\ \text{keV}} \\ &+ (0.0224p_0^{'} + 0.000519) \times \left(\frac{E}{10\ \text{keV}}\right)^2, \\ \sigma_r(E) =& p_f \cdot \sigma_{r,0}(E) \end{aligned} \tag{6.37}$$

where $\mu_{r,0}$ and $\sigma_{r,0}$ are the original median and fluctuation of the recombination ratio of the electron-ion pairs in the NEST2.

Now let's prepare one pool for the 'flatER'. Using the $\mu_{r,\text{pool}}(E)$ with the $\mu_r(E)$ in Eq. 6.37 where $\mu_{r,0}(E)$ under $E_{\text{drift}} = 92.8$ V/cm is used because more than 80% data were taken under the electric field in Run 1. The $\sigma_{r,\text{pool}}(E) = (1.5 \text{ to } 2.0)\sigma_r(E)$ will cover enough parameter space, including the variation of $(p_0^{'}, p_f)$ as indicated in the best fit (see Fig. 6.7 for the 1σ variation) and the change of $\mu_{r,0}(E)$ and $\sigma_r(E)$ under E_{drift} from 127.4 V/cm to 92.8 V/cm as plotted in Fig. 6.8. For each event i in the pool, only the following intermediate variables need to be recorded: $r_{\text{rec},i}$ and $\rho_{\text{rec,pool},i}$ besides the observable variables like $S1_i$ and $S2_{b,i}$. The pool

doesn't need to remember the median or sigma in the Gaussian function to generate the events but does need to record the corresponding probability density $\rho_{\mathrm{rec,pool},i}$ and E_i which are required to calculate the new weight of the event i.

Later on, while the $(p^{'}_{0,\mathrm{pool}}, p_{f,\mathrm{pool}})$ are updated to $(p^{'}_{0,\mathrm{target}}, p^{'}_{f,\mathrm{target}})$. The new probability density $\rho_{\mathrm{target},i}$ of the event i will be calculated as

$$\rho_{\mathrm{target},i} = G\big(r_{\mathrm{rec},i}, \mu_{r,\mathrm{target}}(E_i), \sigma_{r,\mathrm{target}}(E_i)\big), \tag{6.38}$$

where E_{drift} is an implicit parameter in the functions of μ_r and σ_r. The new weight of event i again follows Eq. 6.9. Figure 6.18 plots the example of one pool (Fig. 6.18(a)) of events reweighted for set 1 (Fig. 6.18(b)) and set 4, 5 (Fig. 6.18(c)) for ER events. PDFs prepared are normalized versions of the frequency distributions and filled with the new weights onto axses with respect to $S1$ and $S2_b$ instead of r_{rec} and E.

6.3.2 Other detector parameters

As summarized in the last column of Tab. 6.1, many intermediate steps can be included if the detector parameters in Tab. 6.2 vary in the target parameter space. Follow the steps in Tab. 6.1, the possible applications of reweighting techniques on the step 1, 7.a, 8.a and 8.b are discussed. The possibilities of step 2 and 4 are not discussed which will be very similar to what we have discussed in section 6.3.1, and the dependence on E_{drift} for these two steps is solved by preparing different pools for different sets. The possible z-distribution reweighting in step 6 can be implicitly included in 7.a and 8.a.

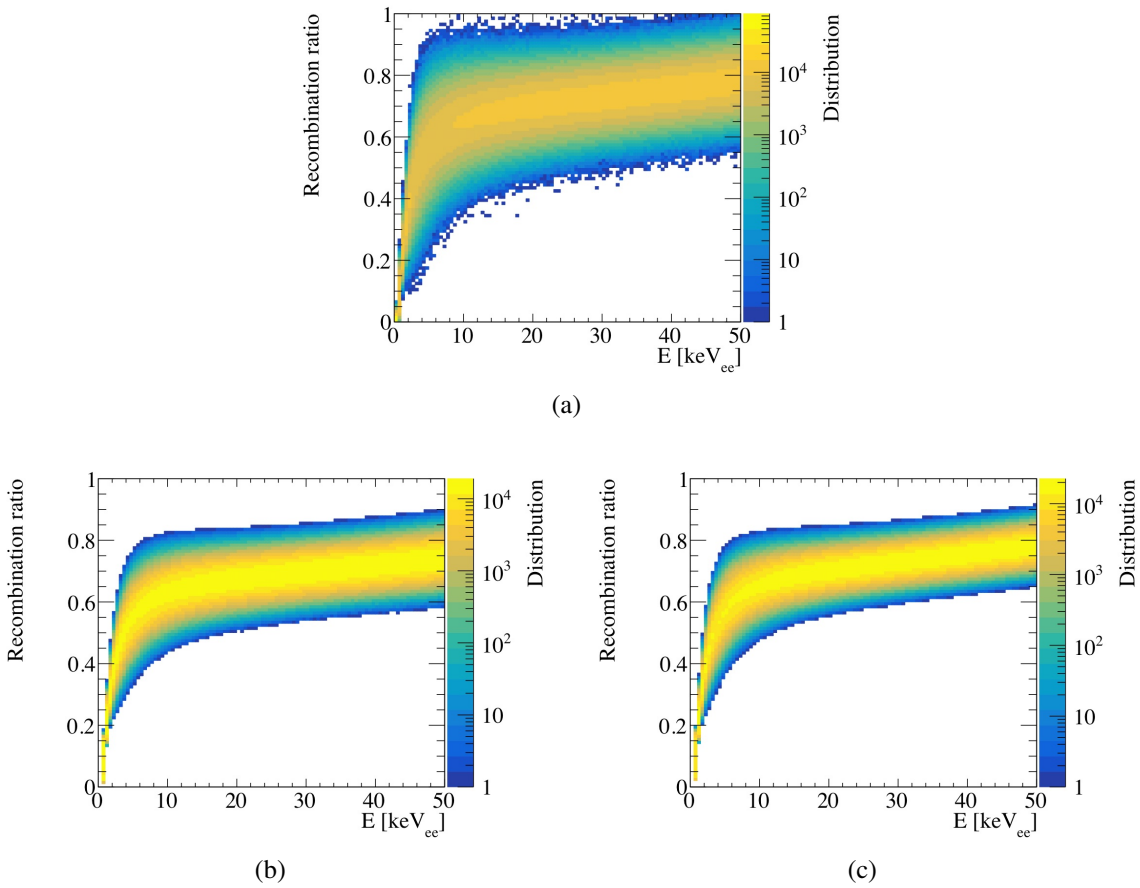

Figure 6.18: The recombination ratio r_{rec} prepared in a pool (a) reweighted with new parameters $(p_0^{'}, p_f)$ and for set 1 (b) with $E_{\mathrm{drift}} = 127.4$ V/cm and set 4, 5 (c) with $E_{\mathrm{drift}} = 92.8$ V/cm in Run 1.

6.3.2.1 Energy spectrum

If the energy spectra of different compositions contributing to the data overlap on the order of $\mathcal{O}(10\%)$ or more, sharing a pool can be an effective way to reduce the pooling event number. As indicated in Eq. 6.17, the event spectrum is interpreted as a probability density function in the simulation. For the event i, only E_i and $\rho_{E,i}$ need recording in the pool. A intuitive reweighting example of tritium events with a 'flatER' pool is presented in Fig. 6.19. Comparing the error bars on the histogram of the 'target' generated by a direct MC simulation to the 'reweighting' one, it's

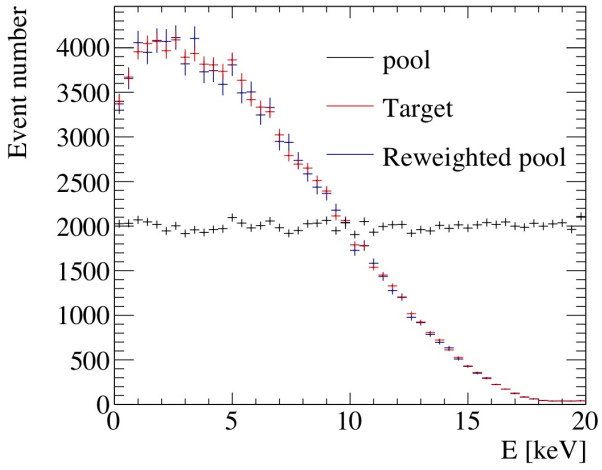

Figure 6.19: Energy spectrum reweighting example with a 'flatER' pool and a tritium target.

clear that in the region $E \gtrsim 10$ the 'reweighting' distribution has smaller uncertainties with the same amount of simulation event number.

6.3.2.2 Photon detection efficiency

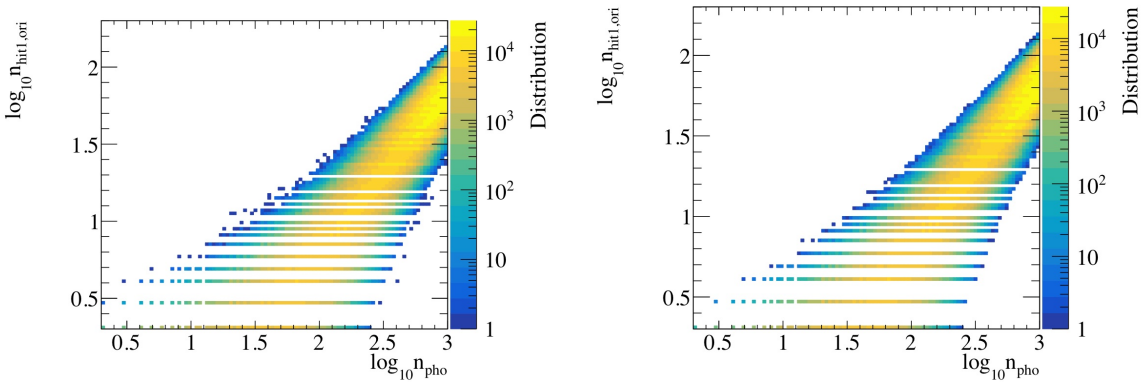

Figure 6.20: Distributions of $\log_{10} n_{\text{hit1,ori}}$ vs. $\log_{10} n_{\text{pho}}$ in the pool (a) prepared by a roundoff and truncated Gaussian and (b) the reweighted target for the nominal $\bar{G}_1$ in Tab. 6.2.

Equation 6.28 describes the related variables and parameters in step 7.a related to PDE ($G1$). To make the reweighting effective, at least $n_{\text{hit1},i}$, $n_{\text{pho},i}$ and $\rho_{G1,\text{pool},i}$ are saved. A roundoff

and truncated Gaussian is used to prepared the pool as in the 1D example of section 6.1.2.3, and Eq. 6.28 is used to calculate $\rho_{G1,\text{target},i}$. If the pool is shared among targets with different z-distribution, then, z_i should be saved as well. In Tab. 6.2, different sets share the same $\bar{G}_1$ because it is a highly geometry dependent parameter and $G1$ changes insignificantly while E_{drift} changes. The distributions filled in $\log_{10} n_{\text{hit1,ori}}$ vs. $\log_{10} n_{\text{pho}}$ for the pool (a roundoff and truncated Gaussian) and the reweighted target with the nominal $\bar{G}_1$ in Tab. 6.2 are plotted in Fig. 6.20. The $\mathcal{O}(1)\%$ uncertainty in $\bar{G}_1$ is not very noticeable from Fig. 6.20(a) to Fig. 6.20(b).

6.3.2.3 Electron lifetime and electron extraction efficiency

In step 8.a, the percentage of electrons survived into the gaseous xenon (Eq. 6.33) is correlated to z_i, τ_e, i (following the distrbution in Fig. 6.11), and EEE (see Tab. 6.2). This Binomial generator step is also prepared with a truancated Gaussian in Fig. 6.21 where n_{eGas} is confined between n_{ele} and 0. The example presented is still for sharing the same pool among different data sets so that Fig. 6.21(a) should well cover the union of Fig. 6.21(b) and Fig. 6.21(c).

6.3.2.4 Single electron gain

The preparation for the SEG is a simplified version of the last one correlated to τ_e and EEE in one step. In Eq. 6.34, SEG in Tab. 6.2 is different among sets and has an uncertatinty on the order of $\mathcal{O}(1\%)$ as well. Figure 6.22 presents the pool and targets for set 1 and set 4, 5. With the increase of n_{eGas} (actually the increase of E), the responses start to diverge, and the $\mathcal{O}(1\%)$ uncertainties won't make the two different bands overlap. This example explains why preparing different pools for different data sets is more economic.

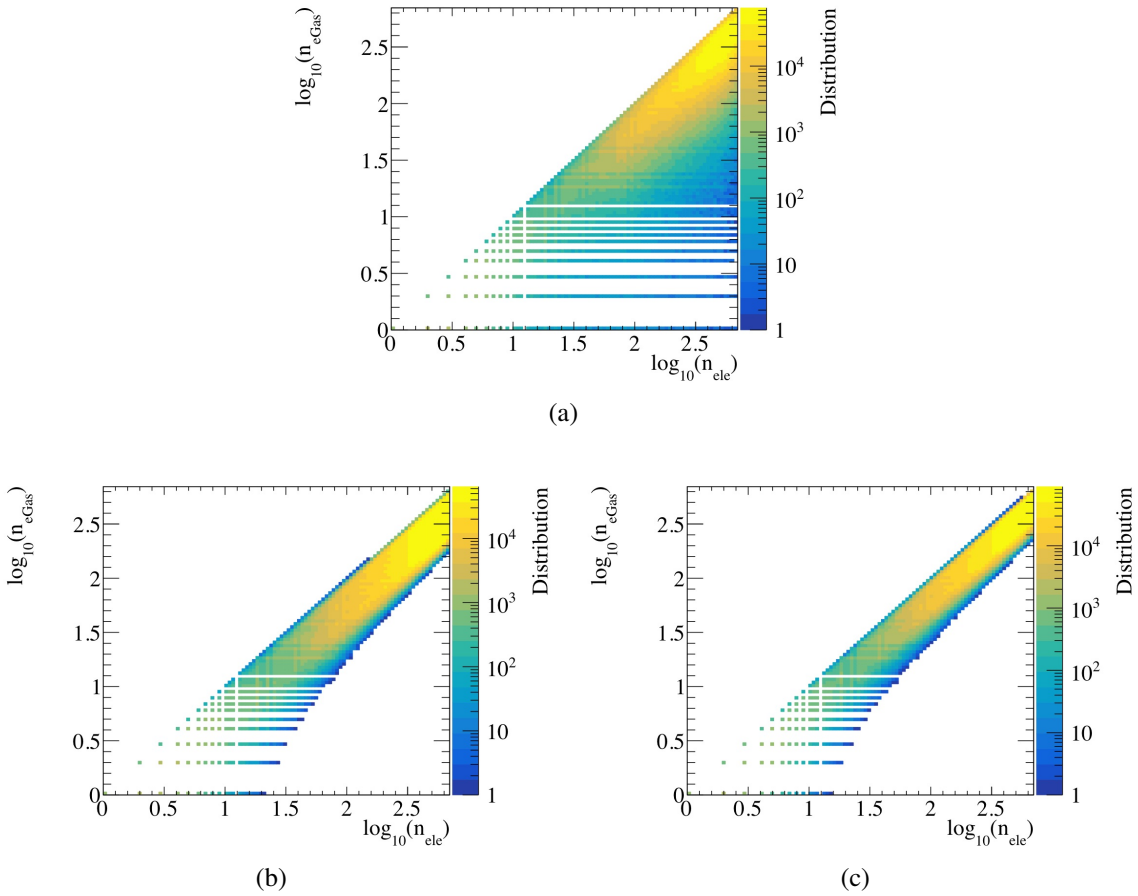

Figure 6.21: Distributions of $\log_{10} n_{\mathrm{eGas}}$ vs. $\log_{10} n_{\mathrm{ele}}$ in the pool (a) prepared by a roundoff and truncated Gaussian and the reweighted target for (b) set 1 and (c) set 4 with different electron lifetimes (Fig. 6.11) and the nominal EEE for different data sets in Tab. 6.2.

6.4 Application on WIMP search in PandaX-4T

We apply the reweighting MC on WIMP search with PandaX-4T Run 1 data to include the uncertainties of $p_* = (p_0', p_f)$ (template) or $p_* = (p_0, p_1, p_2, p_f)$ (reweighting) in ER detector simulation. The PLR analysis starts with the definition of LHF where we use an unbinned one. The test statistics with the likelihood ratio is then used to interpret the agreement between the data and the hypothesis with different WIMP masses and cross sections of the spin-independent WIMP-nucleus scattering. Following the frequentists hypothesis test, toy MC events are generated

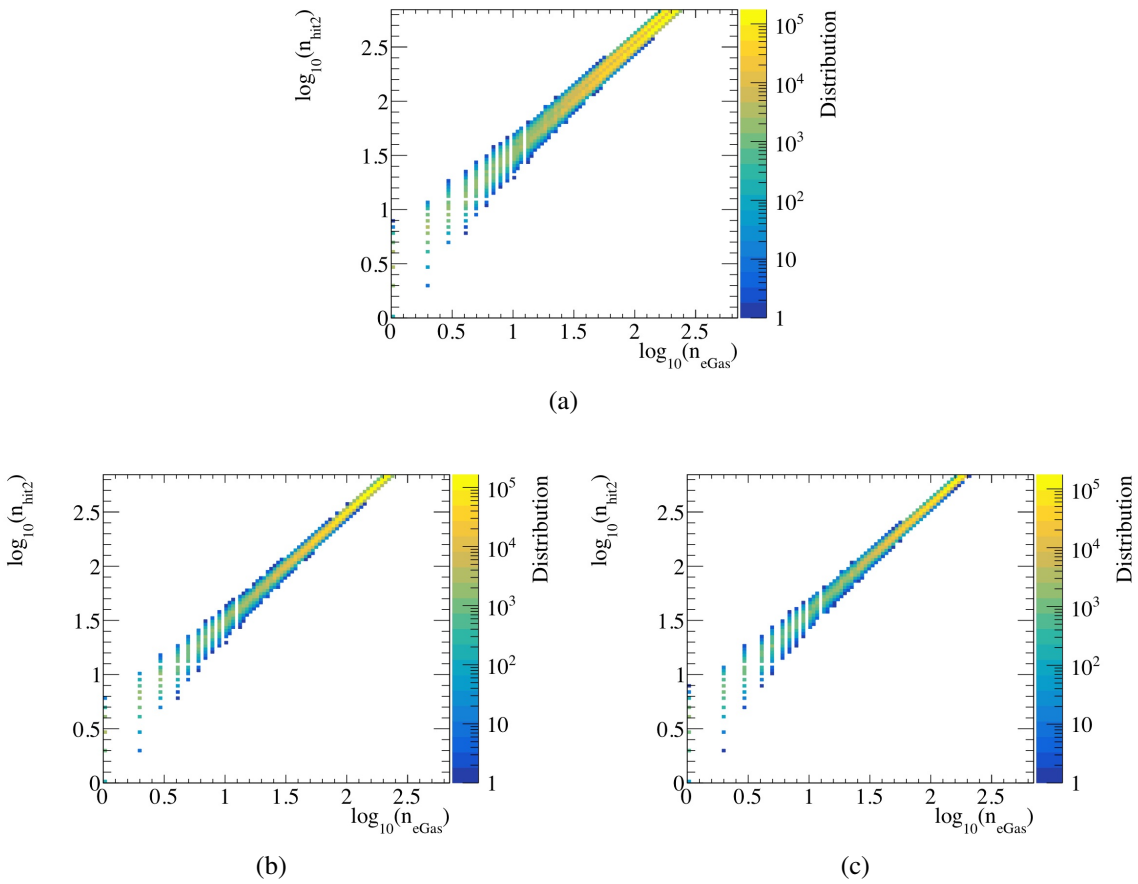

Figure 6.22: Distributions of $\log_{10} n_{\text{hit2}}$ vs. $\log_{10} n_{\text{eGas}}$ in the pool (a) prepared by a roundoff and truncated Gaussian and the reweighted target for (b) set 1 and (c) set 4, 5 with different nominal SEGs in Tab. 6.2.

as pseudo data to build the expected distribution of the test statistics w.r.t. the signal model. The p-value is calculated for different signal models tested to represent the agreement level. Finally, the limit will be set according to the confidence level (C.L. $= 1 - p$). Details on the procedure of PLR analyses are presented in this section for completeness.

The unbinned LHF is defined as

$$\mathcal{L}_{\text{tot}}(\mu) = \Big[\prod_{n=1}^{\text{nset}} \mathcal{L}_n\Big] \times \Big[\prod_{b} G(\delta_b, 0, \sigma_b)\Big] \times \Big[\prod_{p_*} G(\delta_{p_*}, \mu_{p_*}, \sigma_{p_*})\Big] , \tag{6.39}$$

where $\mathcal{L}_n$ is the unbinned likelihood for each data set n,

$$\begin{aligned}\mathcal{L}_n = \quad & \text{Poiss}(N^n_{\text{meas}}|N^n_{\text{fit}}) \times \left[\prod_{i=1}^{N^n_{\text{meas}}} \left(\frac{N^n_\mu \epsilon^n_\mu(p_*) P^n_\mu(S1^i, S2^i_b|\{p_*\})}{N^n_{\text{fit}}} \right.\right. \\ & + \sum_{b(\text{ER})} \frac{N^n_b \epsilon^n_b(p_*)(1+\delta_b) P^n_b(S1^i, S2^i_b|\{p_*\})}{N^n_{\text{fit}}} \\ & \left.\left. + \sum_{b(\text{not ER})} \frac{N^n_b (1+\delta_b) P^n_b(S1^i, S2^i_b)}{N^n_{\text{fit}}} \right) \right], \end{aligned} \tag{6.40}$$

$$N^n_{\text{fit}} = \quad N^n_\mu \epsilon^n_\mu(p_*) + \sum_{b(\text{ER})} N^n_b \epsilon^n_b(p_*)(1+\delta_b) + \sum_{b(\text{not ER})} N^n_b(1+\delta_b). \tag{6.41}$$

The PDFs of the backgrounds and dark matter are noted as P^n_b and P^n_μ respectively, where the uncertainties of the detector nuisance parameters δ_{p*} on the ER compositions are constraint by the Gaussian penalty terms $G(\delta_{p_*}, 0, \sigma_{p_*})$. The uncertainties σ_{p_*} are treated as the systematic uncertainties marginalized from the ER calibration. The measured data number for each set N^n_{meas} is compared to the Poisson distribution with a median as the total expected observed event number N^n_{fit}, summing the observed signal ($N^n_\mu \epsilon^n_\mu$) and background event numbers ($N_b \epsilon^n_\mu$ or N_b) confined by penalty terms with uncertainties σ_b as shown in Fig. 6.23. For ER compositions, the efficiencies $\epsilon_{b,\mu}(p_*)$ related to the detector nuisance parameters are required to calculate the observed event numbers. The tritium radioactivities are not independently estimated which is floated in the fitting and marked with an infinitely large σ_b.

The procedure of PLR analyses is briefly summarized in section 6.4.1 has been widely discussed in the literature [4]. In section 6.4.2, we discuss some subtle details not well-defined. We compare the best fits and limits between template morphing and reweighting in section 6.4.3.

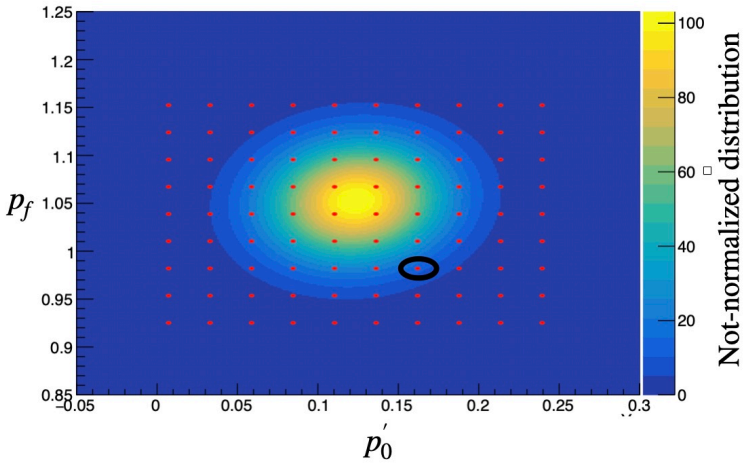

Figure 6.23: The 2D Gaussian penalty of $(p_f, p_0^{'})$ with the color bar showing the probability constraints (not-normalized). The red points indicate the templates prepared for the publication in Ref. [2]. The black circle marks the one for the best fit of $(p_f, p_0^{'})$ by the template morphing methode with Run 1 data.

6.4.1 Profile likelihood ratio analysis

The procedure of PLR analyses is included for reference. With the LHF defined as Eq. 6.39. The test statistics q_μ is defined as

$$q_\mu = -2 \log \frac{\mathcal{L}_{\text{tot}}(\text{data}|\mu, \{\widehat{\widehat{\delta}}_b\})}{\mathcal{L}_{\text{tot}}(\text{data}|\widehat{\mu}, \{\widehat{\delta}_b\})}, \tag{6.42}$$

where in the denominator, the $\{\widehat{\mu}, \{\widehat{\delta}_b\}\}$ is the set of signal significance parameter μ and nuisance parameters leading to the global maximum value of the $\mathcal{L}_{\text{tot}}$ with a specific $\{\text{data}\}$ input. In the numerator, the μ is fixed to the signal hypothesis waiting to be tested (excluded or accepted), and $\{\widehat{\widehat{\delta}}_b\}$ leads to a local $\mathcal{L}_{\text{tot}}$ maximum. The definition assures that $q_\mu \geq 0$ forever. According to the definition in Eq. 6.42, The smaller the q_μ is, the better agreement between the data and tested signal model μ.

The q_μ can be intuitively understood as the extension of χ^2 from 'Gaussian region' to

'Poisson region'. If the $\mathcal{L}_{\rm tot}$ is a Gaussian function, the distribution of q_μ will follow χ^2 distribution with one degree of freedom which comes from the cross section, and other degrees of freedom cancel out after profiling. However, the hypothesis tests for rare-event experiments are often in the 'Poisson region' because the detector is designed to reach a background-free channel.

6.4.1.1 Limit setting

1. Find the test statistic of the observed real data, $q_{\mu,\rm obs}$ for a chosen μ. Put the real data into Eq. (6.42), and get $q_{\mu,\rm obs}$. The $q_{\mu,\rm obs}$ vs σ_μ for $m_\chi = 40$ GeV/c^2 is shown in Fig. 6.24. At the same time, we get the best fitted nuisance parameters. **The $\{\hat{\hat{\delta}}_{b1}\}$ in the numerator are used in the following toy MC simulations.** Different μ result in different $\{\hat{\hat{\delta}}_{b1}\}$ because the increase of fixed signal number will suppress the other backgrounds contributions like neutron.

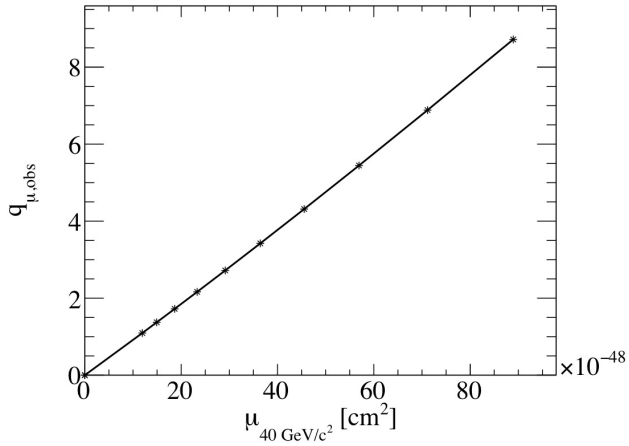

Figure 6.24: An example of $q_{\mu,\rm obs}$ vs. cross sections $\mu_{40\ \rm GeV/c^2}$ for $m_\chi = 40$ GeV/c^2 in PandaX-4T Run 1.

2. Conduct toy MC simulations. To find the test statistic distribution with μ scenario ($q_{\mu,1}$ distribution), we need a lot of toy data sets (use $N_{\rm toy} = 1000$ as an example).

In a jth simulation,

$$N^n_{\mu\text{eff},j} = \text{Poiss.Generator}(\text{N}^\text{n}_\mu \epsilon^\text{n}_\mu), \tag{6.43}$$

and similarly,

$$N^n_{b\text{eff},j} = \text{Poiss.Generator}\big(\text{N}^\text{n}_\text{b} \epsilon^\text{n}_\text{b} \cdot (1 + \hat{\hat{\delta}}_{\text{b1}})\big). \tag{6.44}$$

The systematic uncertainties could result in different ϵ for different detector simulation parameters, which in the end are accounted in the limits and sensitivities.

3. Find $q_{\mu,1}$ distribution. We have 1000 $q_{\mu,1}$ by putting the toy pseudo-runs into Eq. (6.42), and then we can get the distribution of $q_{\mu,1}$, $f_1(q_\mu)$ with the example in Fig. 6.30. The distribution should generally gather close to 0 because we use data generated by μ signal hypothesis to test μ, and the local maximized $\mathcal{L}_\text{tot}$ with fixed μ is close to the global maximized $\mathcal{L}_\text{tot}$.

4. Calculate the p-value by

$$p_\mu = \frac{\int_{q_{\mu,\text{obs}}}^{\infty} f_1(q_\mu) dq_\mu}{\int_0^\infty f_1(q_\mu) dq_\mu}, \tag{6.45}$$

5. Set the limit. Usually, the limit is set on the cross section or coupling constant for a specific scattering including DM particles. The μ is a function of the cross section or coupling constant, and so is p_μ. Under 90% C.L., the μ is excluded if $p_\mu < 0.1$. It is hard to hit the μ with exactly $p_\mu = 0.1$. Several p_μ need to be calculated close to $p_\mu = 0.1$, and we use the following function to fit the μ_critical,

$$p_\mu = (1 - \text{C.L.}) \cdot \exp[z_0 \cdot (\mu - z_1)], \tag{6.46}$$

where z_0 and z_1 are fitting parameters, and when $\mu_{\rm critical} = z_1$, $p_\mu = 1 - {\rm C.L.}$.

6.4.1.2 Sensitivity band setting

The sensitivity band is found by treating the background-only toy data as the real data, and find the limit following the procedure in Sec. 6.4.1.1, and then calculate the 1σ or 2σ center band with the $N_{\rm pseudo}$ limits (use 2000 as an example). Strictly speaking, for the kth background-only toy data set, the $\{\hat{\hat{\delta}}_{b,k}\}$ is different in each toy limit setting, and each $f_k(q_\mu)$ distribution should be calculated individually . In this way, $N_{\rm pseudo} \times N_{\rm toy}$ toy MCs are required, which usually takes too long a computational time.

The simplified method is to neglect the change in the $f_k(q_\mu)$, and choose one background-only toy data to generate a $f_2(q_\mu)$ with $\{\hat{\hat{\delta}}_{b,2}\}$, which is different from $f_1(q_\mu)$. The scanning of μ (in this chapter, μ is the cross section tested) to calculate the sensitivity band should cover the fluctuation of the background-only limits.

1. Prepare 2000 background-only toy data sets. We fit the real data to the background-only model in the Eq. (6.42) to get $\{\hat{\hat{\delta}}_{b,{\rm only}}\}$ (set $\mu = 0$). The jth toy background-only data is generated as

$$N^n_{b{\rm eff},j} = {\rm Poiss.Generator}({\rm N^n_b}\epsilon^{\rm n}_{\rm b} \cdot (1 + \hat{\hat{\delta}}_{\rm b,only})). \tag{6.47}$$

   These background-only toy data sets can be shared in search different theoretical scenarios.

2. Find the $\{\hat{\hat{\delta}}_{b,2}\}$. Use the most probable number of backgrounds to generate one background-

only data without Poisson random generator.

$$N^n_{b\text{eff,mean}} = \text{int}(N^n_b \epsilon^n_b \cdot (1 + \widehat{\widehat{\delta}}_{b,\text{only}})), \tag{6.48}$$

where 'int' means round off. The pseudo-data set $\{N^n_{b\text{eff,mean}}\}$ is treated the same as data in Eq. (6.42) to find the $\{\widehat{\widehat{\delta}}_{b,2}\}$. $\{\widehat{\widehat{\delta}}_{b,2}\}$ **is generally different from** $\{\widehat{\widehat{\delta}}_{b,1}\}$.

3. Calculate the $q_{\mu,\text{obs,k}}$ for the kth pseudo-data with Eq. (6.42), and get the 2000 groups of $q_{\mu,\text{obs,k}}$.

4. Repeat the step 2 and 3 in Sec. 6.4.1.1 to find $f_2(q_\mu)$.

5. Find the limits. Calculate the $p_{\mu,k}$ similar to the step 4 Sec. 6.4.1.1. Fit the limit in the kth simulation use the Eq. (6.46).

6. Using the distribution of the limits the find the 1σ and 2σ bands.

6.4.1.3 Look elsewhere effect

If a local excess is found for a specific dark matter mass, look elsewhere effect (LEE) should be checked to test the global significance and the degeneracy of the possible signal hypotheses, avoiding an overestimated local significance. Taking WIMP search on the parameter space of (μ_χ, m_χ) as an example, for a large enough μ_χ (the statistics becomes Gaussian-like but not Poisson-like), one-dimensional χ^2 test with fixed m_χ can serve as an approximation for the local, and two-dimensional χ^2 test with both μ_χ and m_χ floating for the global. A $q_{\mu,\text{obs}} = 2.71$ accords to $p = 0.1$ ($Z = 1.28$) with a one-dimensional χ^2 distribution as an approximated $f(q_\mu)$, and $p = 0.26$ ($Z = 0.64$) with a two-dimensional χ^2 distribution. The significance level Z can be

converted from p by

$$Z = \sqrt{2}\mathrm{Erf}^{-1}(1-2p), \tag{6.49}$$

with Erf defined in Eq. 6.13 for two-tailed tests.

LEE is suggested in Ref. [4] for a local excess approaching or exceeding 3σ ($p_0^{\mathrm{local}} \lesssim 0.00135$). The same N_{toy} toy MC used for sensitivity band setting can be used but testing for q_0 (q_μ are tested before). The denominator part of Eq. 6.42 will be different for different m_χ if the signal PDFs are not degenerate, which results in a different $f(q_0(m_\chi))$ for different m_χ. Technically, for each m_χ, the N_{toy} $q_0(m_\chi)$ gives the distribution of $f(q_0(m_\chi))$. For each toy MC k, $q_{0,k}(m_\chi)$ has a corresponding $p_{0,k}(m_\chi)$ with $f(q_0(m_\chi))$. Then, the minimum of $p_{0,k}(m_\chi)$ is selected as $p_{0,k,\mathrm{min}}$ (the smaller the p is, the more likely a signal appears). The distribution $f(p_{0,\mathrm{min}})$ is constructed with $k = 1, 2, 3, ..., N_{\mathrm{toy}}$. Finally, the global $p_{0,\mathrm{obs}}^{\mathrm{global}}$ is found by

$$p_{0,\mathrm{obs}}^{\mathrm{global}} = \int_0^{p_{0,obs}^{\mathrm{local}}} f(p_{0,\mathrm{min}}) dp_{0,\mathrm{min}}. \tag{6.50}$$

6.4.2 Subtleties in the PLR analysis

The procedure of PLR analyses is usually well-defined, but some subtleties may cause differences on the order of $\mathcal{O}(10\%)$ in the limit and sensitivity. We discuss the effects of the binning in the PDF preparation, extrema finding algorithms and the toy MC sampling.

6.4.2.1 Binning effects

In the preparation of the PDFs, the binned histograms of the MC simulation events are often used, which leaves freedoms to choose the number of the simulation events and bins along the

observable axes. As discussed in Ref. [211], it is possible to calculate the probability densities analytically if the MC simulation can be broken down into multiple steps, and each step only connects two or three variable axes (variables refer to the properties of the ith simulation event like E_i, $n_{\mathrm{pho},i}$, $n_{\mathrm{ele},i}$) because the numerical integrals with gradients can be carried out without the use of MC, but the numerical step sizes and the start and end of the variables in the integral still depend on human choices. The analytical integral calculations of the probability densities is beyond the discussion of this dissertation, and we focus on the preparation with MC simulations.

The bin size should be small enough to fully use the discrimination power, but should be large enough to avoid too many simulation events required. Taking the WIMP search with the PandaX-II full exposure as an example, the PDFs are prepared in the $\left(\log_{10}(S2/S1), S1\right)$ space. While the bin size $\Delta\log_{10}(S2/S1)$ become smaller than 0.02 and $\Delta S1$ smaller than 1 PE, the discrimination becomes stable to separate the predicted WIMP signal (40 GeV/c^2 as a representative) from the backgrounds. But the argument needs to be checked for different data sets, especially if some steep structure appears in the observable parameter space such as the accidental background in the PandaX-4T Run 1 data. A binning difference in $\Delta S1$ as small as 0.01 will cause a visible difference larger than 10% in the 90% C.L. limit (sensitivity bands are often stable because the structure is often washed out). In this case, a non-uniform binning along $S1$ will be more suggestive (Fig. 6.25) to catch the change with more details, being more stable with the change in bin sizes.

It is also known that too small a the simulation event number will sacrifice the discrimination power with the statistical uncertainties in the simulation. More importantly, if the observed data locate at the edges of some background PDFs, such as the events at the border of ER and NR in $\log_{10}(S2/S1)$, the bins with less than 5 events will vary relatively dramatically from one

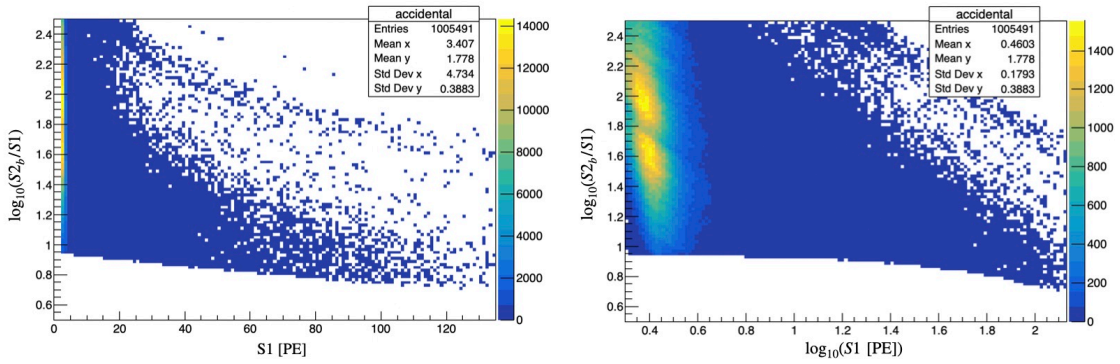

Figure 6.25: Accidental background PDF in PandaX-4T Run 1 prepared with equal bin size along $S1$ (left) and $\log_{10}(S1\ [\mathrm{PE}])$ (right).

simulation to another. The simulation event number has to be large enough to cover important regions which may become computationally expensive if these regions are at the tails of some major backgrounds. Using the PandaX-II full exposure example again and fixing the bin size as $\Delta \log_{10}(S2/S1) = 0.02$ and $\Delta S1 = 1$ PE, we compared the 90% C.L. limits with ER and NR PDFs prepared by 1×10^6 and 1×10^8 events as shown in Fig. 6.26. The right plot in Fig. 6.26 with 1×10^8 events satisfies our requirements to present a less than 10% variation in the 90% C.L. limit. A further reduction in the uncertainties in the reported limit can be done by averaging the results of different trials.

6.4.2.2 Extrema finding algorithms

We test the different extrema finding algorithms with the help of 'scipy' package in Python3. We choose MINUIT and Powell algorithms after testing with our unbinned likelihood Eq. 6.39. Both present competitive behaviors speaking of the accuracy of extrema [212]. In this analysis, Powell is 2 to 4 times faster than the MINUIT algorithm with no significance bias in the q_μ calculation. MINUIT is more helpful while the errors of the fitting are of interest. 'NewtonCG'

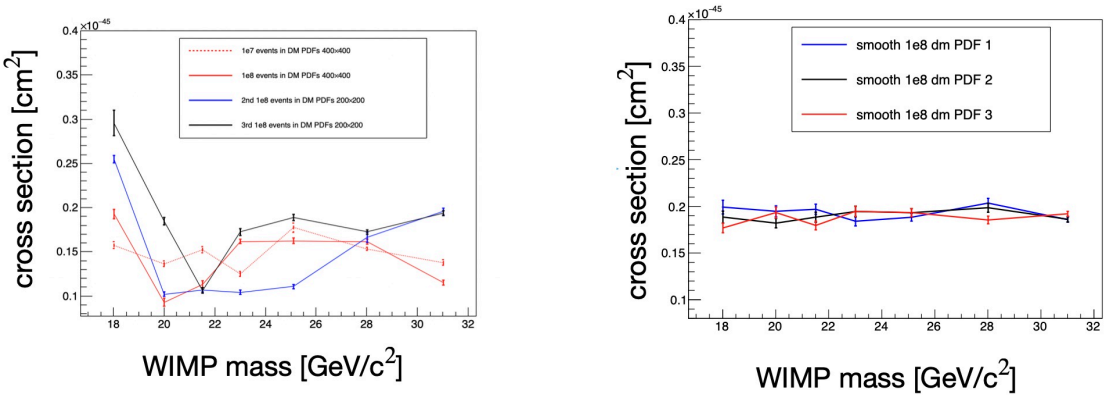

Figure 6.26: The 90% limits with three different trials of the same PDF generators with 1×10^6 (left) and 1×10^8 (right) simulation events. The limits are not the same as the publication in Ref. [40] because more conservative ER band widths are finally used. And these problems are found and fixed during the procedure of analysis

in 'scipy' also gives us stable results in finding maxima of the likelihood but takes too long to converge with the same accuracy reached compared to MINUIT and Powell. Many other options even cannot find the right maximum with a complicated function. Our conclusion agrees with the test on the website (Fig. 6.27).

6.4.2.3 'Systematic' uncertainties put in toy MC

We discuss the handling of the toy MC in Run 1 data of PandaX-4T in this part. The Poisson random generator accounts for the statistical uncertainties. The uncertainties in the best fit $\{\hat{\hat{\delta}}_{b1}\}$ is mainly limited by the statistics in the data, so if these uncertainties are included in the toy MC, we will be over conservative by double counting the uncertainties. But we preserve the uncertainties in p_* of the best fit (Fig. 6.29 for the reweighting method) as systematic uncertainties of the detector response simulations. In other words, the p_* in the toy MC is sampled with the covariance matrix constraint by the best fit of the data before calculating the related $N^n_{\mu,b}$.

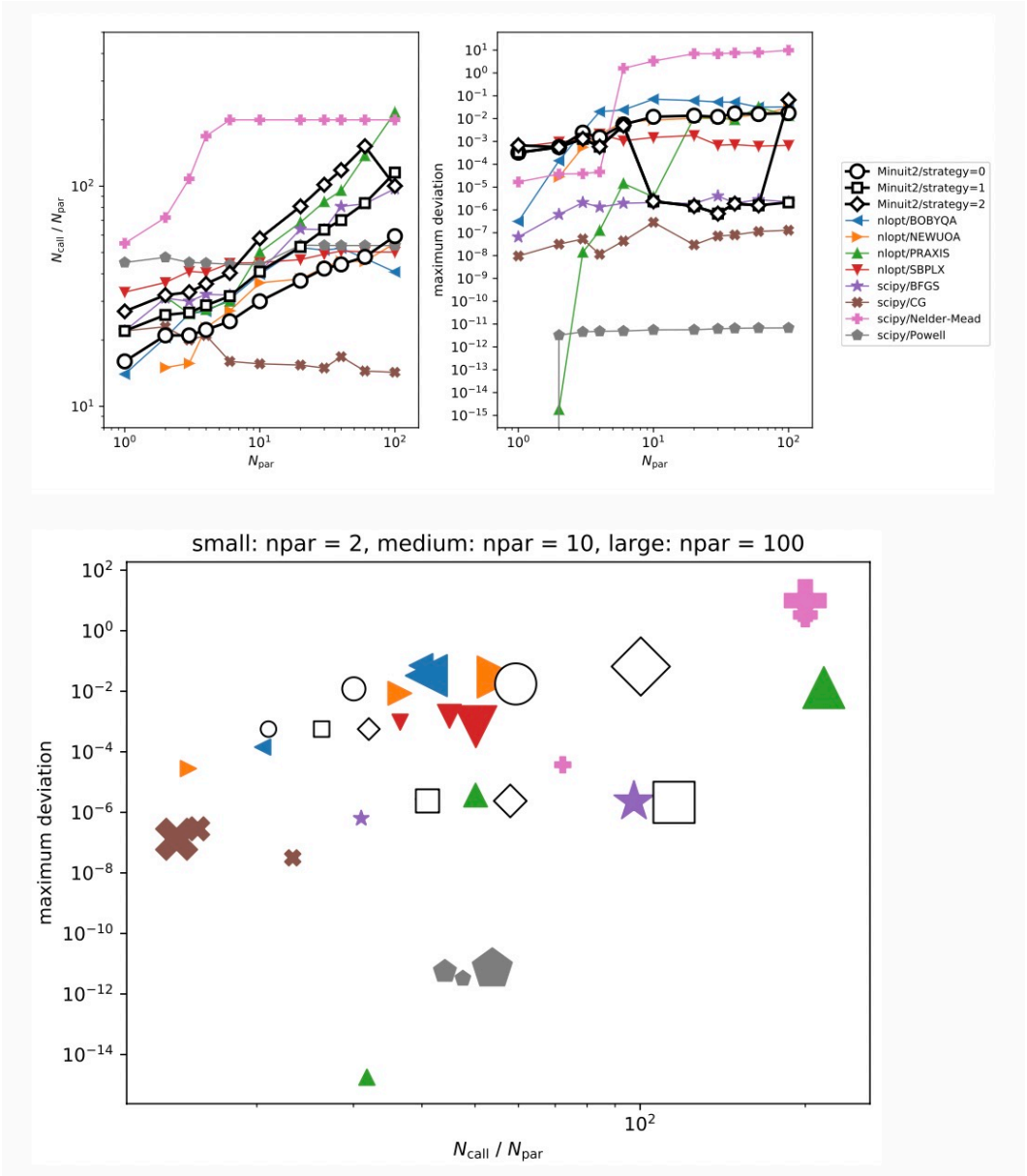

Figure 6.27: Performance of different extrema finding algorithms provided by 'scipy' [41]. N_{call} is the number of iteration (first-order and second-order derivatives of the function may need to be updated in one iteration). N_{par} is the number of fitting parameters.

6.4.3 Comparison with template morphing

For completeness, before discussing the differences in the template morphing and reweighting method, we present Run 1 set 4 (shared with set 5) examples of the binned PDFs of backgrounds

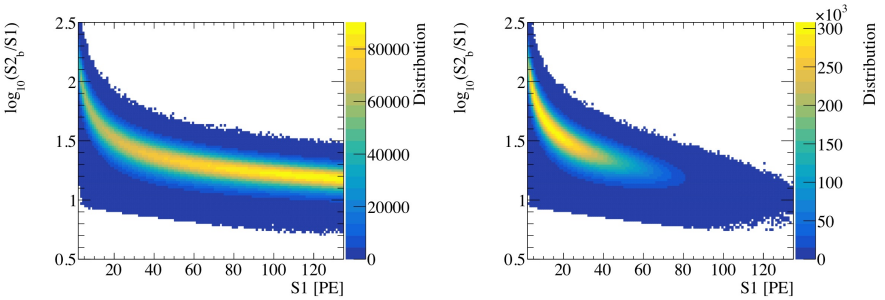

(a) Flat ER

(b) Tritium

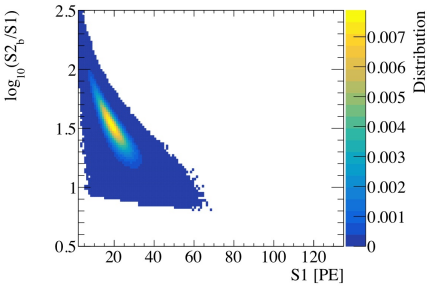

(c) Xe^{127} 5.2 keV_{ee}

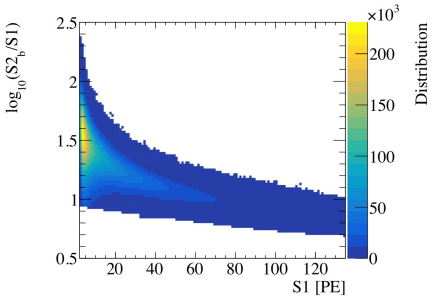

(d) Neutron

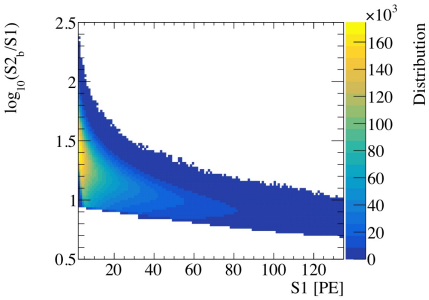

(e) NeutronX

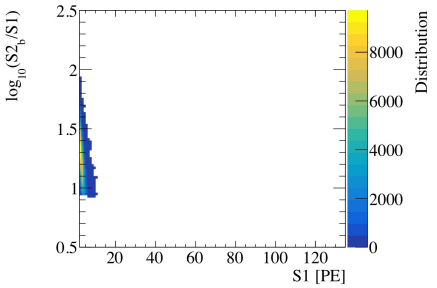

(f) B^8 coherent neutrino-nucleus scattering

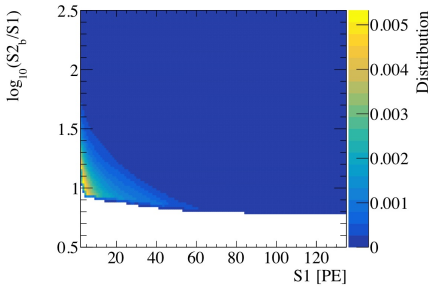

(g) Surface

Figure 6.28: Run 1 set 4 (or set 5) examples of the binned background PDFs. Accidental background is not in this plot, and ER backgrounds are plotted with the calibrated NEST p_*.

prepared with 2^{28} events with a $\Delta S1 = 1$ PE and $\Delta\big(\log_{10}(S2_b/S1)\big) = 0.01$ bin sizes. The nominal PDFs (except the accidental background) are shown in Fig. 6.28 with the ER components holding nominal p_*.

In the template morphing method, the ER PDFs prepared have $(p_0^{'}, p_f)$ as the red lattice marked on Fig. 6.23. If 8.4×10^6 (2^{23}) events is used, the best fit of $(p_0^{'}, p_f)$ is unstable for different signal hypotheses μ_s tested (different cross sections of the 40 GeV/c^2 WIMP as examples). After increasing the event number in the fast detector simulation to 2.7×10^8 (2^{28}), different signal hypotheses present a convergent best fit on $(p_0^{'}, p_f) = (0.162, 0.99)$ marked by the black circle on Fig. 6.23. If we rotate the $p_0^{'}$ back, it corresponds to $(p_0, p_1, p_2) = (0.098, -0.037, 0.14)$.

In the reweighting MC method, the covariance matrix in Fig. 6.8(a) is directly used as the penalty term of p_*. Using different pools for the 5 subsets in PandaX-4T Run 1 with 8.4×10^6 (2^{23}) events in total will be enough to reach a stable best fit on p_*. But it is still preferred to have more events for a lower statistical uncertainties in the test statistic q_μ. But limited by the requirement of the computational time, the maximum total simulation event number in the pool tried is 1.7×10^7 (2^{24}). The best fit $(p_f, p_0, p_1, p_2) = (1.01, 0.093, -0.041, 0.12)$ with the uncertainties is shown in Fig. 6.29 where the uncertainties in p_* is around half of Fig. 6.8(a) for more statistics. The template morphing best fit in p_* is consistent with the reweighting MC within the uncertainties.

With a consistent result on the best fit, the PLR analyses is done with 1000 toy sets according to the best fit for the q_μ distribution $f(q_\mu)$. In the PandaX-4T Run 1 example, the reweighting MC (2^{24} events in pool) appears to be 10% to 20% more conservative in the sensitivity than the template morphing (2^{28} events) which is checked with more efforts. By fixing all the non-ER PDFs to be the same and remove the p_* penalty term, it reveals that a $\mathcal{O}(10)$ times smaller statistics in the tritium and 'flatER' PDFs lead to a visible difference in the $f(q_\mu)$. Figure 6.30

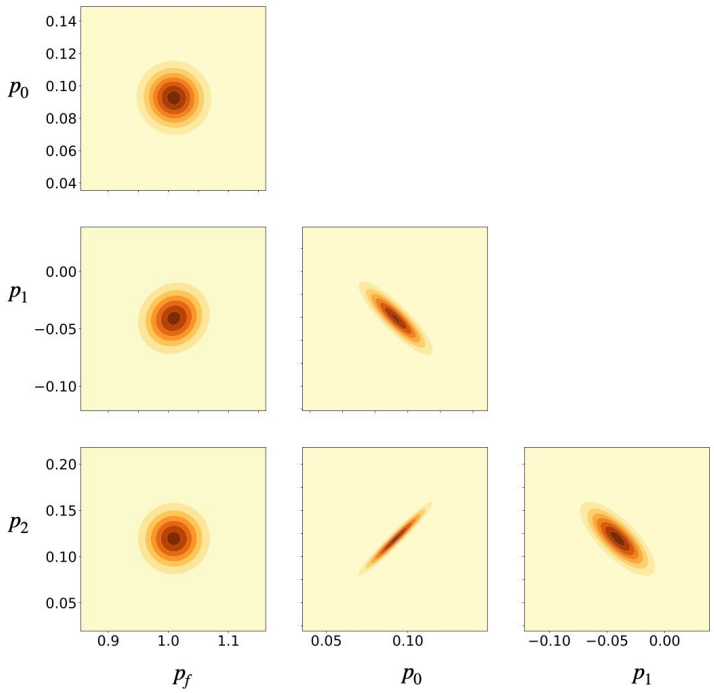

Figure 6.29: The best fit of (p_f, p_0, p_1, p_2) with Run 1 data using the reweighting MC.

shows that the reweighting method with a smaller statistics has a wider q_μ distribution which will lead to a more conservative sensitivity. A χ^2-distribution of one degree of freedom has the 90% cumulative probability at 2.71, which is used to check the deviation of the signal hypothesis μ_s (a 40 GeV/c^2 WIMP with a 2.6×10^{-47} cm^2 SI cross section with nucleus) from a 'Gaussian behavior'. This example is in the Poisson-like region with $\int_0^{2.71} f(q_\mu) dq_\mu = 97.5\ (95.6)\%$ for the template morphing (reweighting).

The differences between the template morphing and the reweighting in the 90% C.L. limit and the sensitivity band are show in Fig. 6.31. The main difference with the template morphing between Fig. 6.31 and what published in Ref. [2] is due to the binning effect of the accidental backgrounds as discussed in this chapter. But after applying power constraint, the limit and 1σ sensitivity will be consistent to Ref. [2] within 5%.

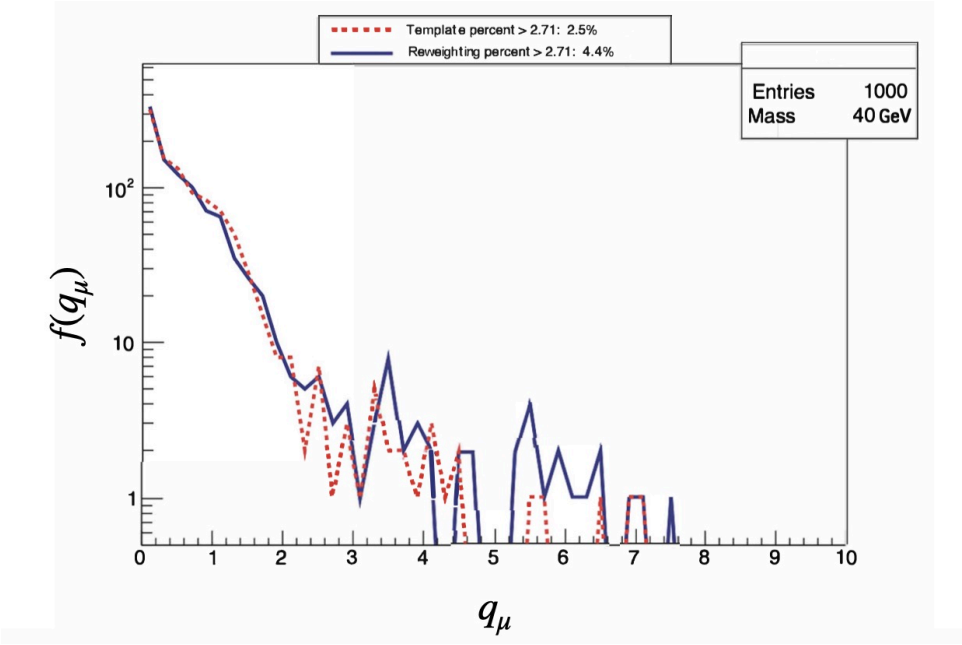

Figure 6.30: The $f(q_\mu)$ with the template tritium and 'flatER' PDFs (2^{28} events) and the reweighting ones (2^{24} events) generated with the signal hypothesis μ_s for a $40\ GeV/c^2$ WIMP with a 2.6×10^{-47} cm^2 SI cross section with nucleus.

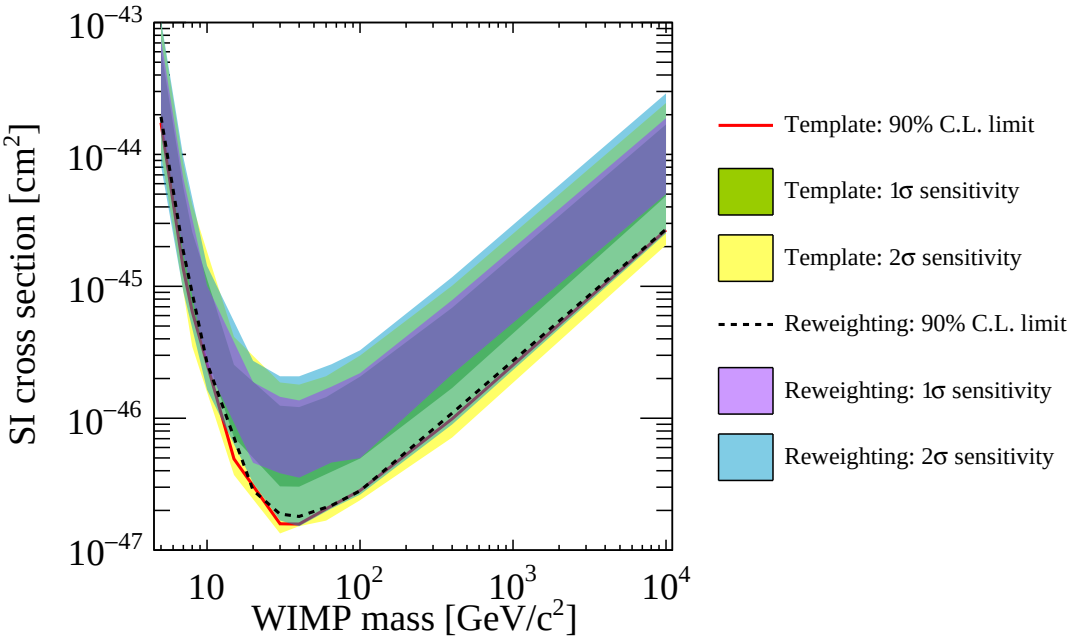

Figure 6.31: The comparison in the 90% C.L. limit and sensitivity band of SI WIMP-nucleus scattering cross section vs. the WIMP mass between the template morphing and the reweighting before applying power constraint.

Chapter 7: A Search for Light Fermionic Dark Matter Absorption on Electrons

GeV-scale weakly interacting massive particles (WIMPs) and QCD axions are the two top candidates searched with tailored experiments for decades because of the 'WIMP-miracle' [52, 75, 213] and the strong CP problem [214, 215, 216, 217, 218], respectively. However, the GeV-scale standard thermal WIMP is problematic for small scale observations [219, 220, 221, 222, 223], and QCD axions have the axion quality problem [224, 225].

With no solid evidence on searches for either WIMPs [2, 55, 56, 57, 58, 122, 226, 227, 228] or QCD axions [8, 110, 229], alternatives are studied, among which warm dark matter (WDM) represented by the keV sterile neutrino is a popular one because it mitigates the small scale problems with a larger free streaming scale [96, 230, 231], while maintaining excellent agreement with observations on the large scale. The keV-scale sterile neutrinos can also be made to connect to the neutrino mass origin and baryogenesis [66, 89, 90, 91]. Particular interests arose from the $\sim$3.5 keV unidentified excess in X-ray spectrum from satellites [42, 92, 93]. However, later analyses have challenged the sterile neutrino interpretation because no such excess is observed in some other X-ray data sets [94], and in tension with the DM profiles at the center of galaxies [95]. To date keV sterile neutrino dark matter with the standard Dodelson and Widrow production mechanism has been ruled out to make up the whole DM relic density by the structure formation and X-ray limits [97, 98, 99, 232], but it stays as a promising DM candidate with some other

production mechanisms like the Shi-Fuller resonant production [233] and the decays from heavier particles [234, 235].

Nevertheless, a more general light neutral fermionic particle can still be a warm or cold dark matter candidate, depending on the initial conditions in the thermal history. If such fermionic particles couple to neutrinos or charge leptons via a new kind of interaction, they can be probed experimentally via similar techniques as in the search for sterile neutrinos [45, 101, 236]. Specifically, in a dark matter direct detection experiment, sub-MeV fermionic DM (noted as χ hereafter) absorption on electron targets with an out-going active neutrino ($\chi e \rightarrow e\nu$) can be searched via a tree-level process predicted in an effective theory treatment, as the final state electron obtains a kinetic recoil through the mass of χ [45, 101]. Such a search becomes particularly attractive to direct detection experiments for vector (V) and axial-vector (A) interactions, where the satellite X-ray limits are the weakest since $\chi \rightarrow \nu\gamma$ can only be produced by two-loop diagrams due to the gauge symmetry and QED charge conjugation symetry. The absorption signal of a 60 keV/c^2 fermion DM on electron targets with a vector mediator can interpret the electron recoil excess in XENON1T [101]. In this work, we present the first experimental search on such a signal with recent data from the PandaX-4T experiment.

This chapter largely follows the script in Ref. [237], starting with an overview of keV sterile neutrino DM in section 7.1. Then, in section 7.2, we present the expected signals of the general light fermionic DM absorbed by electrons with an out-going active neutrino. More discussions on astrophysical and cosmological limits on the light fermionic DM are in section 7.3. Finally, the profile likelihood ratio analysis is briefly summarized in section 7.4. For clarification, as this work searches on a ER signal, the unit of energy deposition 'keV' is for 'keV$_{\rm ee}$'.

7.1 Overview on keV sterile neutrino

A well-motivated model of keV sterile neutrinos is the neutrino minimal standard model (νMSM) with three righted-handed neutrinos N_I ($I = 1, 2, 3$) added on to the SM to address the origin of DM, neutrino oscillations and baryon asymmetry together.

7.1.1 νMSM model

The interactions are described by the Lagrangian

$$\mathcal{L}_{\text{int}} = \mathcal{L}_{\text{SM}} + \overline{N}_I i\partial_\mu \gamma^\mu N_I - f_{Ia}\phi \overline{N}_I L_a - \frac{M_I}{2}\overline{N_I^c} N_I + h.c., \tag{7.1}$$

where L_a ($a = e, \mu, \tau$) are the lepton doublets, ϕ is the Higgs field ($\langle\phi\rangle = 174$ GeV), M_I are for the Majorana masses, and f_{Ia} are the Yukawa coupling constants. The active neutrino masses m_i ($i = 1, 2, 3$) are on the order of $f_{Ia}^2\langle\phi\rangle^2/M_I$. As there is no solid indication for f_{Ia} to be on order 1, the masses of M_I is not confined on the GUT scale ($10^{14} \sim 10^{16}$ GeV). To explain the two neutrino oscillations measured with type-I seesaw mechanism $\big(\Delta m_{\text{atm}}(= (7.53\pm0.18) \times 10^{-5}\ \text{eV}^2)$ and $\Delta m_{\text{sol}}(= (2.44\pm0.06) \times 10^{-3}\ \text{eV}^2)$ [50, 51, 91]$\big)$, two-sterile-neutrino beyond SM is viable which requires the lightest active neutrino mass eigenstate as $m_1 = 0$. Baryon asymmetry can be interpreted in the parameters for the CP-voilation phase(s) in the active neutrino oscillations (PMNS matrix) or the leptogenesis which is more correlated to the two sterile neutrinos working in the seesaw mechanism.

However, at least three sterile neutrinos are required to solve the DM origin and neutrino oscillations at the same time under the framework. With only two sterile neutrinos, lighter

massive active neutrino $m_{2,3}$ with a mass $\sqrt{\Delta m^2_{\rm atm}}$ will lead to an overabundance of the DM relic density Ω_c as pointed out in Ref. [91]. After adding a third sterile neutrino, only upper limits of m_1 for different production mechanisms are required which is allowed.

7.1.2 Free streaming scale

Free streaming (FS) length is a more well-defined concept in the freeze-out mechanism as

$$\lambda_{FS} = \int_0^{t_{eq}} \frac{v(t)}{a(t)} dt, \tag{7.2}$$

where $v(t) = c$ while the DM is relativistic, and t_{eq} is the time reaching mass-radiation equivalence in the thermal history. Before the DM becomes non-relativistic and stays similar to radiation, the primordial perturbations are washed out within the scale. The FS effect may violate the observations on the matter power spectrum. Lyman-α keeps updating on the lower constraint of the WDM mass with an upper limit on the free streaming length allowed.

For a different DM production mechanism, the free streaming effect will be different. An approximate estimation of λ_{FS} can be written as

$$\lambda_{FS} = 1.2\ {\rm Mpc} \left(\frac{\rm keV}{M_1}\right) \left(\frac{\langle p_1 \rangle}{3.15T}\right)_{T \approx {\rm keV}}, \tag{7.3}$$

where the average momentum $\langle p_1 \rangle$ depends on the production mechanisms as

$$\left(\frac{\langle p_1 \rangle}{3.15T}\right)_{T\approx \mathrm{keV}} \begin{cases} = 0.8 - 0.9, \text{ for DW} \\ \approx 0.6, \text{ for Shi} - \text{Muller} \\ \lesssim 0.2, \text{ for } \mathrm{T_{prod}} \gtrsim 100 \text{ GeV} \end{cases} . \tag{7.4}$$

'DW' stands for the Dodelson-Widrow mechanism where keV sterile neutrinos are non-resonantly generated through oscillations in the temperature lower than the QCD phase transition (200 MeV) but higher than the active neutrino decoupling and BBN (1 MeV). DW was once taken as the standard mechanism for the keV sterile neutrino but has been ruled out as the major DM to explain the whole relic density. 'Shi-Muller' mechanism produces keV sterile neutrinos resonantly near or during BBN epoch with the lepton number asymmetries. '$T_{\mathrm{prod}} \gtrsim 100\ GeV$' refers to the generation well above the QCD phase transition as early decoupled thermal relics, and the reduction of degrees of freedoms with SM heavy particles decaying away causes the red shift of the DM while reaching $T \approx 1$ keV. The recent limit from Lyman-α forest power spectrum on the DW sterile neutrino (early decoupled sterile DM not limiting to neutrinos) is $M_1 > 28.8\ (4.65)$ keV with a 95% C.L.

7.1.3 Controversial 3.55 keV excess

XMM-Newton and Chandra reported a 3.55 keV line excess in the X-ray spectrum of the Perseus (Fig. 7.1), Virgo cluster and the stacked one of other 69 clusters which could be explained by a 7.1 keV sterile neutrino decay ($\chi \to \nu\gamma$). The one-loop diagram shown in Fig. 7.2 is the leading term contributing to the indirect detection with X-ray telescopes.

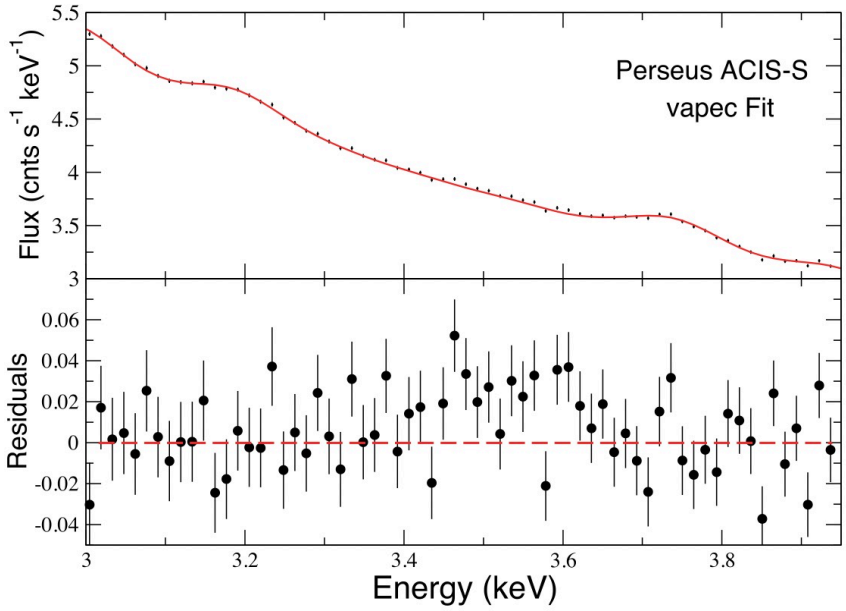

Figure 7.1: The 3.55 keV line excess reported in Ref. [42] with Perseus cluster as an example.

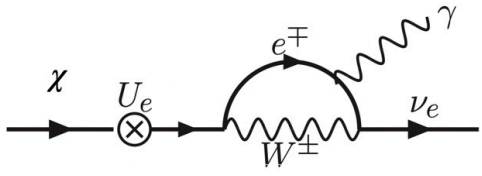

Figure 7.2: The Feynman diagram of the leading visible decay channel of keV sterile neutrino.

Some phenomenological production mechanisms may help to evade the strong constraints from Lyman-α forest. But the interpretation is in tension with other stacked X-ray spectra of more than 80 selected galaxies and galaxy groups after masking the central regions which have objects emit very little radiation above $\sim$2 keV [94]. The expected excess with the strength of 3.55 keV reported ahead should have presented at least 7.8σ for 89 galaxies from XMM-Newton or 2.7σ for 81 from Chandra but was not seen in either. Moreover, an analysis comparing the X-ray line emission and dark matter halo contour in a pixel-by-pixel way for the Galactic center and Perseus reveals that the radial and azimuthal distribution of the 3.55 keV emission is incompatible with a

dark matter origin for both [95]. But the interpretation of 3.55 keV line excess as part of the DM composition for some galaxies is still possible.

The strongest limit of the mixing angle between the keV sterile neutrino and active neutrinos is from the NuSTAR X-ray observations as shown in Fig. 7.3 overlain with the 7.1 keV sterile neutrino mixing angle for the 3.55 keV excess [43].

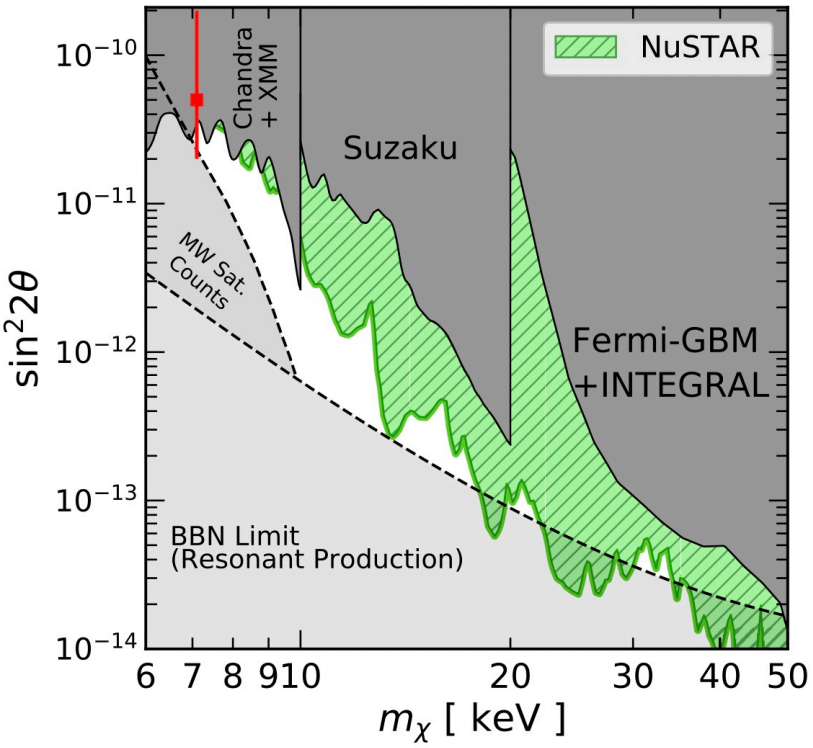

Figure 7.3: The 95% C.L. limit of the mixing angle vs. mass of keV sterile neutrino with X-ray telescopes [43]

.

7.2 A light fermionic dark matter search in direct detection

The keV sterile neutrino DM is one representative of a general light fermionic DM interacting with electrons and active neutrinos. Because of the viable one-loop diagram of the visible decay and the large exposure with the massive galaxy clusters which is searched by indirect detections,

DM direct detection experiments is orders less sensitive (Fig. 7.4).

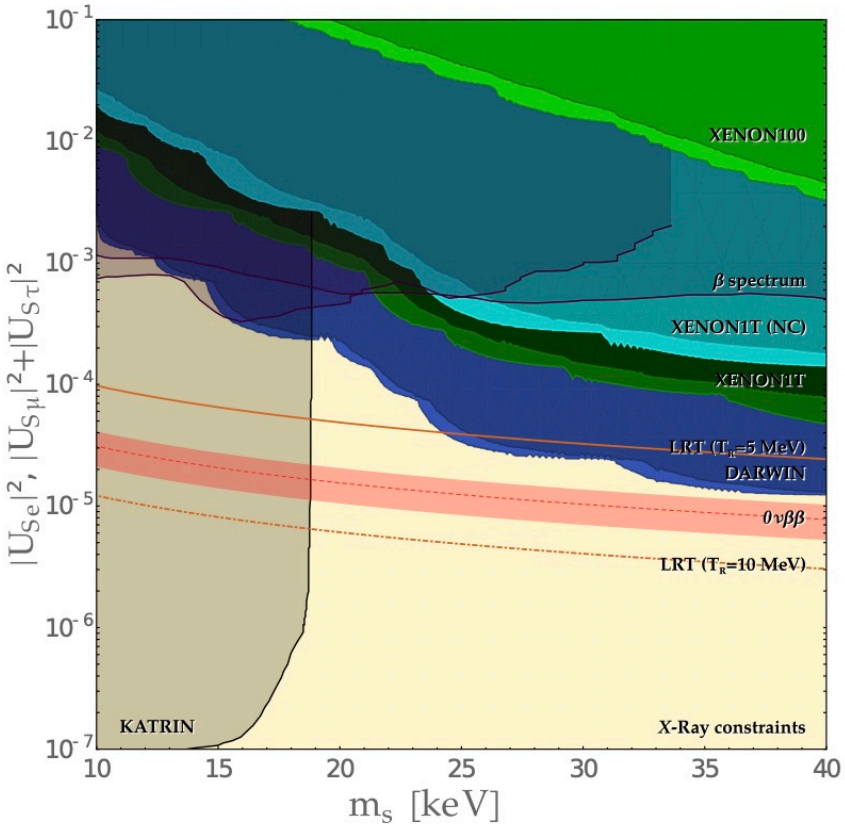

Figure 7.4: The projected sensitivity of the mixing angle vs. mass of keV sterile neutrino in XENON1T [44]. 'NC' stands for neutral current , and 'LRT' for low reheating temperature.

.

However, if a more general light fermionic DM interacting with SM particles via a new kind of interaction, how strong the astrophysical constraints limits are depends on the leading order visible decay channel, but the characteristic of such DM searched by direct detections via the tree-level scattering have less dependence on the interaction type. As studied systematically in Ref. [45], dimension-six operators involving χ, active neutrino ν and electron can be represented

by five independent operators as

$$\begin{aligned}
\mathcal{O}^{S}_{e\nu\chi} &= \frac{1}{\Lambda^2}(\bar{e}e)(\bar{\nu}_L\chi_R) \\
\mathcal{O}^{P}_{e\nu\chi} &= \frac{1}{\Lambda^2}(\bar{e}\gamma_5 e)(\bar{\nu}_L\chi_R) \\
\mathcal{O}^{V}_{e\nu\chi} &= \frac{1}{\Lambda^2}(\bar{e}\gamma_\mu e)(\bar{\nu}_L\gamma^\mu\chi_L) \quad , \\
\mathcal{O}^{A}_{e\nu\chi} &= \frac{1}{\Lambda^2}(\bar{e}\gamma_\mu\gamma_5 e)(\bar{\nu}_L\gamma^\mu\chi_L) \\
\mathcal{O}^{T}_{e\nu\chi} &= \frac{1}{\Lambda^2}(\bar{e}\sigma_{\mu\nu} e)(\bar{\nu}_L\sigma^{\mu\nu}\chi_R)
\end{aligned} \tag{7.5}$$

where the SM left-handed neutrino is taken, and the light DM χ is assumed to be a Dirac particle for convenience. The Λ has a mass dimension, reflecting the heavy mediator mass scaled with a dimensionless coupling constant.

7.2.1 Atomic form factor smearing

Absorption signals generally have distinguishable peak features in the energy spectrum because the outgoing active neutrino has negligible static mass compared to electrons and χ. Considering the local velocity of the DM halo, v_χ, is on the order $\mathcal{O}(0.001)$ and can be neglected, the energy conservation in $\chi e \to e\nu$ holds as

$$m_\chi - E_{nl} = |\mathbf{q}| + E_R, \tag{7.6}$$

where E_{nl} ($E_{nl} > 0$) is the binding energy of the initial electron on the state $|nl\rangle$, $|\mathbf{q}|$ is the outgoing neutrino energy and E_R is the detectable ionized electron energy. If the binding energy and atomic effects are omitted, $E_R = m_\chi^2/2(m_\chi + m_e)$. The expected event spectrum over the

recoiling energy E_R integrates all the possible $\mathbf{q}$ and sums the states $|nl\rangle$,

$$\frac{dR}{dE_R} = N_T \frac{\rho_\chi}{m_\chi} \sum_{nl} (4l+2) \frac{q}{16\pi m_e^2 m_\chi E_R} |M(\mathbf{q})|^2 K_{nl}(E_R, \mathbf{q}), \tag{7.7}$$

where N_T is the number of electron targets per unit mass and $\rho_\chi \sim 0.3$ GeV/cm^3/c^2 is the local DM density [4, 238]. The summation over the degenerate states of $|nl\rangle$ gives the factor $(2l+1)$ and another factor of 2 with the doublet. K_{nl} is the atomic K-factor [239] also known as the ionization form factor [101, 240]. $|M(\mathbf{q})|^2$ is the particle scattering amplitude with the leading term as

$$|M^{(S,V,A,T)}(\mathbf{q})|^2 = (1,1,3,12) \times \frac{16\pi m_e^2}{m_\chi} \sigma_e q, \ , \quad |M^P(\mathbf{q})|^2 = 4\pi \sigma_e q^3. \tag{7.8}$$

The σ_e is defined as $\frac{m_\chi^2}{4\pi\Lambda^4}$ with the same dimension as cross section, corresponding to the total cross section in a scattering between a free electron and χ while $m_\chi \ll m_e$ for $\mathcal{O}^S_{e\nu\chi}$ and $\mathcal{O}^V_{e\nu\chi}$. Two examples of the event spectrum with $m_\chi = 50, 130$ keV/c^2 for $\mathcal{O}^V_{e\nu\chi}$ are shown in the Fig. 7.5. The detector efficiency as a function of m_χ can be found in Fig. 7.6.

7.2.2 Detector response smearing

A typical energy threshold $\mathcal{O}(1)$ keV of a liquid xenon time projection chamber (LXeTPC) limits the conventional search of spin-independent (SI) WIMP-nucleus elastic scattering to a smallest mass about 5 GeV/c^2. However, the mass difference between the sub-MeV fermionic DM and out-going active neutrino overcomes the kinematic difficulty.

This work utilizes the data from the commissioning run released recently by PandaX-

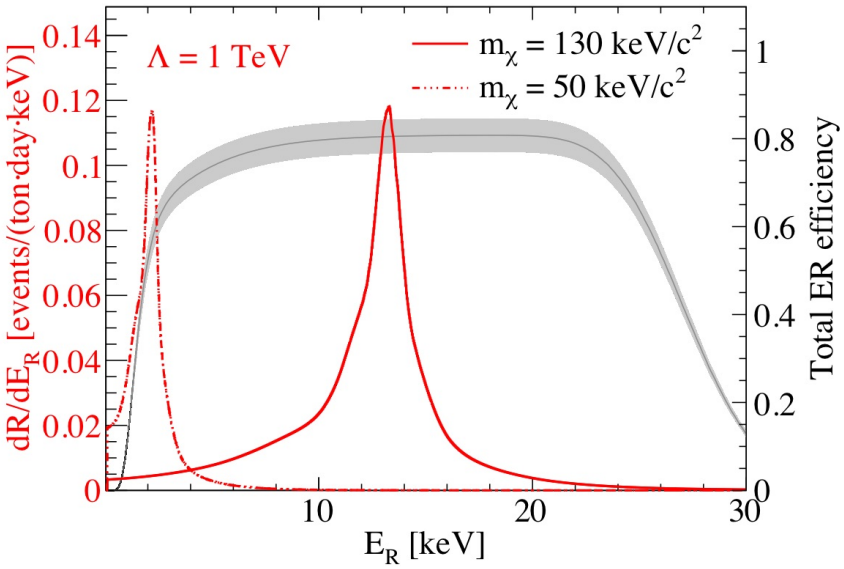

Figure 7.5: Total efficiencies (black line with gray shaded region representing the uncertainties) for ER signals, and event spectra of the fermionic DM absorption via a vector mediator on electron targets for $m_\chi = 50$ keV (dashed red line) and $m_\chi = 130$ keV (solid red line) with $\Lambda = 1$ TeV for $\mathcal{O}^V_{e\nu\chi}$. The left axis is for the total efficiencies and the right axis is for the event spectra.

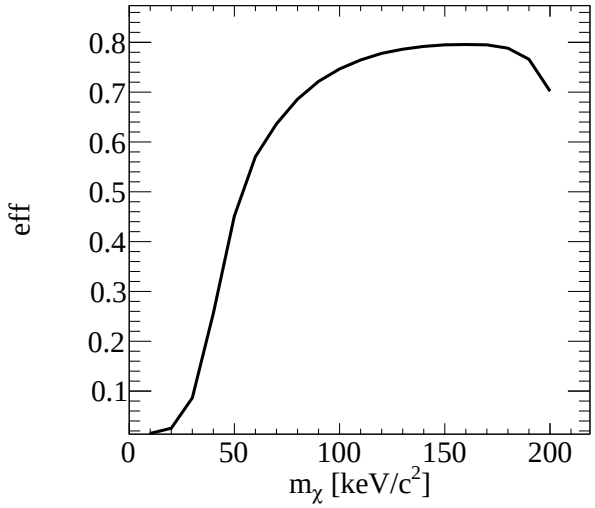

Figure 7.6: Efficiencies as a function of m_χ.

4T [2]. The summary of the hardware subsystems of PandaX-4T can be found in Chapter 5. A recoiling event generates the prompt scintillation photons ($S1$), and the delayed electroluminenscence photons ($S2$) amplified with the proportional scintillation. The commissioning data in the previous

work searches for SI WIMP-nucleus scattering with a 0.63 tonne-year exposure, corresponding to a fiducial volume (FV) with 2.67 ± 0.05 tonne xenon which is optimized by the spatial distribution of the expected backgrounds. The whole Run 1 data is divided into 5 subsets mainly because the cathode high voltage is lowered from -20 kV to -16 kV for avoiding excessive discharges. The adjustment on the liquid level and a online krypton distillation trial causes further separation of the data.

The electronic recoiling (ER) signal response model is constructed based on the noble element simulation techniques (NEST v2) [193, 194] and calibrated with the daughters of ^{220}Rn [241] injected into the detector at the end of Run 1. Only the essential related parts are briefly explained in this chapter, and more details can be found in Chapter 6. Before confronting the NEST model, the energy reconstruction related detector parameters are calibrated with a group of mono-energetic peaks first. The electron-equivalent energy of the event is

$$E_R = 0.0137\ \text{keV} \times (\frac{S1}{G1} + \frac{S2_b}{G2_b}), \tag{7.9}$$

where 0.0137 keV is the work function in the LXe. $G1$ is the photon detection efficiency (PDE), and $G2_b$ is conventionally defined as $\text{EEE} \times \text{SEG}_\text{b}$ which is directly calibrated where EEE and SEG_b are electron extraction efficiency and the single electron gain for $S2_b$ collected by the bottom PMT array in $S2$, respectively. These detector parameters are treated as nuisance parameters in the modeling of ER responses (see more details in chapter 6).

In the low-energy region ($E_R < 30$ keV) calibration of the NEST model, the main degree of freedoms are put on the median (μ_recomb) and fluctuation (σ_recomb) of the ionization recombination ratio with an add-on quadratic polynomial as a function of E_R and a multiplied constant scaling

factor, respectively. The NEST model parameters are marginalized to two main parameters. A linear combination of the three initial parameters in the quadratic function with matrix rotation marginalizes the uncertainties onto one major parameter p_0. The scaling factor (p_f) on the original fluctuation of the recombination ratio is preserved directly. The detector parameters uncertainties after the ER signal model calibration is summarized as σ_{p_*} in Tab. 7.1. With the calibrated NEST model, the predicted PDFs of signals ($\chi e \rightarrow e\nu$) for $m_\chi = 50, 130$ keV/c^2 can be found in Fig. 7.7.

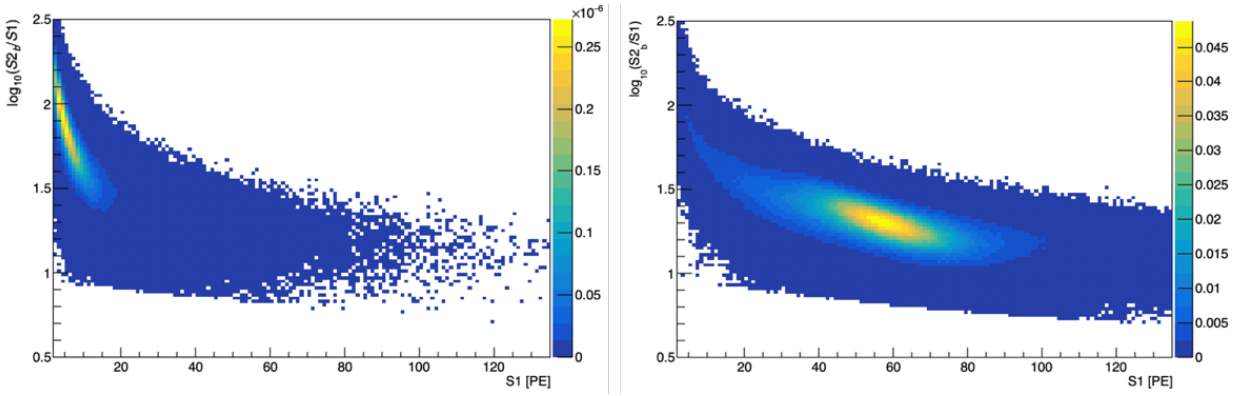

Figure 7.7: Predicted probability distribution functions of signals ($\chi e \rightarrow e\nu$) for $m_\chi = 50$ keV/c^2 (left) and $m_\chi = 130$ keV/c^2 (right).

The predicted ER center and width (10% and 90% quantiles along $\log_{10}(S2_b/S1)$) with the 1σ band according to the detector parameters (PDE, $G2_b$, SEG$_\mathrm{b}$, p_0, p_f) are compared with set 4 and 5 taking under 93 V/cm drifting electric field in Fig. 7.8. The efficiencies of ER events as a function of energy is shown in Fig. 7.5 which include the data quality-cut efficiencies pre-determined in the all-but-this way, the NEST model implied efficiencies at the energy threshold and the $S1$ window-cut efficiency ($2 - 135$ PE). With the calibrated NEST model under 93 V/cm drifting electric field, we extent the signal responses to different electric fields and predict the probability distribution functions (PDFs) for different sets.

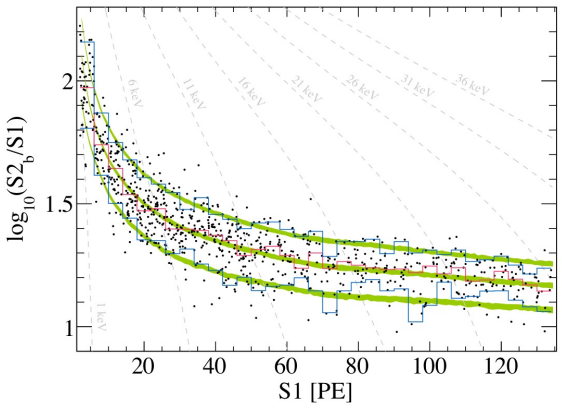

Figure 7.8: DM candidates (black dots with center markded as the red line, 10% and 90% quantiles marked as blue lins) for set 4 and 5 taking under the drifting electric field 93 V/cm compared with the calibrated NEST model (green bands represent the 1σ variation of the detector parameters summarized in Tab. 7.1) for the 90% quantiles, center and 10% quantiles from up to bottom. The dashed gray lines are the equal-energy lines for set 4 and 5.

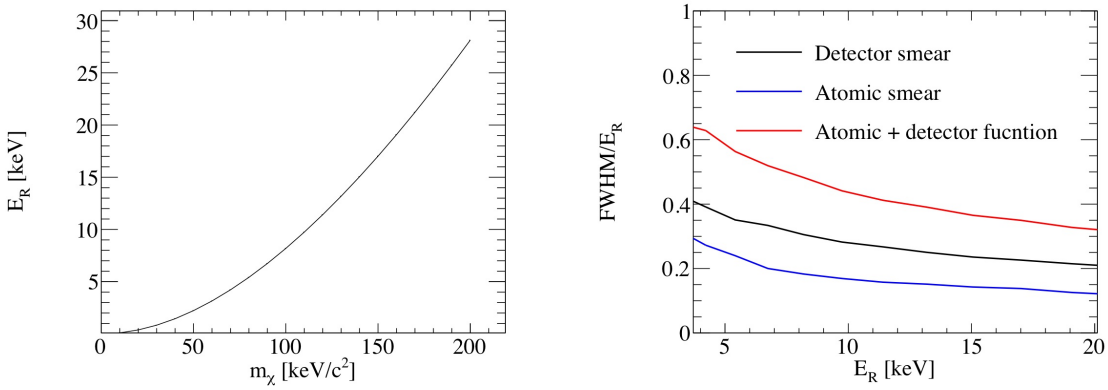

(a) (b)

Figure 7.9: (a) The map between the m_χ and the recoiling energy E_R :with a free electron in $\chi e \to e\nu$. (b) Energy resolution estimated with FWHM vs. E_R according to different effects (atomic smear and detector response).

Figure 7.9 presents the energy resolution estimated by the full-width-half-maximum (FWHM) for the detector response with a single energy value as the input energy spectrum (black) with nominal detector parameters as presented in Tab. 7.1. FWHMs of the light fermionic DM absorption on electrons with atomic effects before and after being smeared by detector effects are are overlain as the blue and red lines, respectively.

Name	Center of p_*	σ_{p_*}	Best fitted δ_{p_*}
PDE [PE]	0.0896	2%	$(-0.4 \pm 1.7)\%$
$G2_b$ set 1, 2 [PE]	3.5	6%	$(-0.8 \pm 1.2)\%$
$G2_b$ set 3, 4, 5 [PE]	4.3		
SEG_b set 1, 2 [PE]	3.8	2%	$(-1.1 \pm 0.7)\%$
SEG_b set 3, 4, 5 [PE]	4.6		
p_0	0.124	30%	$(9 \pm 29)\%$
p_f	1.05	4%	$(-4 \pm 3)\%$
Name	$N_b\epsilon_b$	σ_b	Best fitted observed event number
Signal ($m_\chi = 130$ keV/c^2)	float	N/A	47 ± 23
Tritium set 1	float	N/A	16 ± 4
Tritium set 2	float	N/A	84 ± 11
Tritium set 3	float	N/A	19 ± 6
Tritium set 4	float	N/A	249 ± 21
Tritium set 5	float	N/A	139 ± 17
Flat ER set 1, 2, 3, 5	251.6	9%	242 ± 16
Flat ER set 4	240.5	9%	219 ± 15
^{136}Xe	31.1	16%	32 ± 5
^{127}Xe (L-shell electron capture)	8.13	25%	8.5 ± 2.0
Accidental	2.43	20%	2.4 ± 0.5
Surface	0.47	25%	0.44 ± 0.11
Neutron	1.15	50%	1.4 ± 0.6
^{8}B	0.64	28%	0.60 ± 0.17
Total			1060 ± 46
Data			1058

Table 7.1: Summary of nominal values, uncertainties (fractional), and best fits for the detector response parameters p_* (upper), and signal and individual background components (lower). p_* include PDE, $G2_b$, SEG_b and ionization recombination parameters p_0 and p_f (see text for details). Similar to Ref. [2], the common DM signal and tritium background for each set are left float in the fit. The best fit values of the number of events have been corrected for their efficiencies.

The uncertainties in σ_{p_*} represent the adjustability of the calibrated signal model in the likelihood analysis. We have faced the difficulty that the fixed signal model calibrated by the short-period calibration events fail to predict the ER band width of the observed data spanning longer time [34, 40]. But in this work, the treatment of the detector parameters with nuisance parameters δ_{p*} in Eq. 7.10 gives the freedom to adjust the signal model automatically in the likelihood analysis which will be discussed in more details later, and solidly describes the allowance of the change with the penalty terms $G(\delta_{p*}, \sigma_{p_*})$ in Eq. 7.10. Handling the change of PDFs according to p_* is non-trivial because the conventional template method limits the number of detector parameters to two or three with an exponential increase in the computation resources required for more p_*. We utilize Monte Carlo reweighting technique [202, 203, 204, 242] that a group of simulation events (millions) are saved ahead of the likelihood analysis, and filled into the PDFs with new weights that are analytically calculated according to p_*. With the GPU accelaration, we are able to handle the five detector parameters in the likelihood analysis for the limit and sensitivity setting. Chapter 5 provides more details about the reweighting Monte Carlo technique.

7.3 Astronomical and cosmological limits

Any DM candidate should be consistent with the thermal relic density at the current epoch ($\Omega_c h^2 = 0.12$, where h has a unit of 100 km/s/Mpc). The interation $O_{e\nu\chi}$ will lead to the accumulation of χ while T drops below $2m_e$, and the rate of $\chi\nu \to e^+e^-$ is suppressed compared to $e^+e^- \to \chi\nu$. The conservative constraint to avoid the overproduction with an initial abundance of χ as 0 at a more earlier epoch is to calculated the yield of $e^+e^- \to \chi\nu$ from around 1 MeV

which stabelizes around 0.1 MeV. If such χ is mainly produced via the accumulation between 0.1-1 MeV, there should be a under-production limit. As shown in Fig. 7.12 (orange lines), the overproduction limit with the assumption χ making up all the DM thermal reclic is on the same level of PandaX-4T Run 1 data, which is the golden parameter space to explore because no extra production mechanism is required to generate Ω_c.

Another concern may be the temperature change of active neutrino in the production of χ. The radiation-to-photon ratio or N_{eff} at the recombination era is heavily constraint by the precise measurement of CMB temperature anisotropies. At the time while χ accumulates, the radiation density is on the same level of the matter density. With a much smaller static mass, the number density of radiation is much larger than matter. Therefore, the number of DM particles is much smaller than the number of active neutrinos that already exist, which avoid effecting the observations related to the recombination era.

The interaction of χ with electrons and neutrinos means unavoidable decay of χ which should be consistent with astronomical and cosmological observations. For a χ in the sub-MeV mass range, the decay with electrons on the final states do not spontaneously happen. The correlated leading order decays with photons and active neutrinos are summarized in Fig. 7.10. X-ray telescopes still put limits on the decay of such light fermionic dark matter with photon(s) on the final state. Large scale cosmological observations put limits on the decay of such light fermionic dark matter with only active neutrinos on the final states.

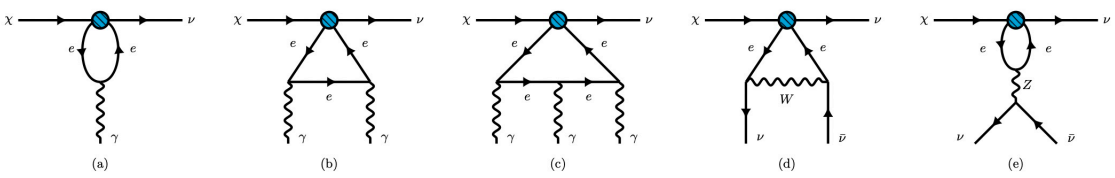

Figure 7.10: Related Feynman diagrams of the leading order decays of χ [45].

Type	Leading visible decay
Scalar	$\chi \to \gamma\gamma\nu$
Pseudoscalar	$\chi \to \gamma\gamma\nu$
Vector	$\chi \to \gamma\gamma\gamma\nu$
Axial-vector	$\chi \to \gamma\gamma\nu$
Tensor	$\chi \to \gamma\nu$

Table 7.2: The leading visible decay of χ.

Table 7.2 summarizes the leading visible decay channels for the five dimension-six operators. For the scalar, pseudo-scalar and axial-vector currents, the one-loop diagram of $\chi \to \gamma\nu$ is forbidden because of the QED charge conjugation symmetry which is the same for $\chi \to \gamma\gamma\nu$ with the vector current. It takes more calculation to understand the gauge symmetry prohibition of the one-loop diagram of $\chi \to \gamma\nu$ for the vector current as presented in the literature [45]. The astronomical constraints are the most important ones to check whether the direct detection searches are meaningful or not. With the prohibitions on the decay channels, we presented search on such a light fermionic DM for the vector and axial-vector operators because these two are the most loosely constraint cases with respect to the visible decays. For $\mathcal{O}^{A}_{e\nu\chi}$, the astrophysical constraint on the leading visible decay channel ($\chi \to \gamma\gamma\nu$) is overlain on the Fig. 7.12 (blue). The astrophysical upper limit with a 95% C.L. combines the contributions from the Insight-HXMT, NuSTAR/M31 and INTEGRAL/08 [45, 102, 243, 244]. The constraint on leading visible decay channel ($\chi \to \gamma\gamma\gamma\nu$) of $\mathcal{O}^{V}_{e\nu\chi}$ is not shown in the selected window. The constraints on other currents are not presented in our result where the X-ray constraints are much stronger.

The leading invisible decay is $\chi \to 3\nu$ for all the operators. Because non-relativistic matter and radiation have different equations of states (EoSs), large scale observations may be deviated too much due to the conversion of the matter into dark radiation (DR) in the thermal history. The theoretical uncertainties may change the cosmological limit by one order of magnitude. For

one thing, the divergence in the decay width calculation in the one-loop diagram of $\chi \to 3\nu$ requires approximation. For another thing, the decay width limit $\Gamma^{-1} \gtrsim 468$ Gyr from CMB, BAO and SNIa observations may be changed by a factor of 2 for this light fermionic dark matter. The reference constrains the decay width with the background evolution in the thermal history of one cold dark matter particle decaying into two DR particles. In general, different hypothetical DM decays in the thermal history require $\Gamma^{-1} \gtrsim 200$ Gyr [245]. Nevertheless, we include the cosmological limit according to the $\Gamma^{-1} \gtrsim 468$ Gyr limit as a reference in our result (magenta lines in Fig. 7.12).

7.4 Limit and sensitivity setting with PandaX-4T Run 1 data

This first experimental search on the absorption of a general light fermionic dark matter with an out-going active neutrino uses Run 1 data of PandaX-4T which is reviewed in Chapter 5. The data set used is exactly the same as the WIMP search presented in Chapter 6. The total exposure after fiducial volume cut is 0.63 tonne·year. The quality cuts yield a plateau efficiency at 78% for ER recoiling energy away from energy threshold ($E_R \gtrsim 10$ keV) which can be found in Fig. 6.14.

A profile likelihood ratio (PLR) analysis is used to place constraints on σ_e for different m_χ. The PLR method presents almost the best sensitivity with the PDFs for different compositions and meanwhile handling the uncertainties as the nuisance parameters with penalty terms. The likelihood function is constructed similarly to WIMP search with the same backgrounds but

different signal models (also noted as μ) as

$$
\begin{aligned}
\mathcal{L}_{\rm tot}(\mu) = \quad & [\prod_{n=1}^{\rm nset}\mathcal{L}_n] \times [\prod_b G(\delta_b,\sigma_b)] \times [\prod_{p_*} G(\delta_{p_*},\sigma_{p_*})]\,, \\
\mathcal{L}_n = \quad & {\rm Poiss}(N^n_{\rm meas}|N^n_{\rm fit}) \times \Bigg[\prod_{i=1}^{N^n_{\rm meas}}\Bigg(\frac{N^n_\mu\epsilon^n_\mu P^n_\mu(S1^i,S2^i_b|\{p_*\})}{N^n_{\rm fit}} \\
& + \sum_b \frac{N^n_b\epsilon^n_b(1+\delta_b)P^n_b(S1^i,S2^i_b|\{p_*\})}{N^n_{\rm fit}}\Bigg)\Bigg]\,, \\
N^n_{\rm fit} = \quad & N^n_\mu\epsilon^n_\mu + \sum_b N^n_b\epsilon^n_b(1+\delta_b).
\end{aligned}
\tag{7.10}
$$

The PDFs of the backgrounds and dark matter are noted as P^n_b and P^n_μ respectively, where the uncertainties of the detector nuisance parameters δ_{p*} on the ER compositions are constraint by the Gaussian penalty terms $G(\delta_{p_*},\sigma_{p_*})$ as summarized in Tab. 7.1. The uncertainties σ_{p_*} are treated as the systematic uncertainties marginalized from the ER calibration. The measured data number for each set $N^n_{\rm meas}$ is compared to the Poisson distribution with a median as the total expected observed event number $N^n_{\rm fit}$, summing the observed signal ($N^n_\mu\epsilon^n_\mu$) and background event numbers ($N_b\epsilon^n_\mu$ or N_b) confined by penalty terms with uncertainties σ_b as shown in the Tab. 7.1. For ER compositions, the efficiencies $\epsilon_{b,\mu}(p_*)$ related to the detector nuisance parameters are required to calculate the observed event numbers. The tritium radioactivities are not independently estimated which is floated in the fitting and marked with an infinitely large σ_b.

We only search for m_χ larger than 10 keV/c^2 and smaller than 180 keV/c^2 because the other regions are already heavily constraint by the DM abundance constrain, cosmological and astrophysical observations. The search region is well-covered by the Run 1 data released before [2]. The global best fit with $m_\chi = 130$ keV/c^2 shown in the Fig. 7.11 presents a 1.7σ local upward fluctuation (converted from p-value), and the fitted parameters are in the Tab. 7.1 ($\chi^2 = 27.7$),

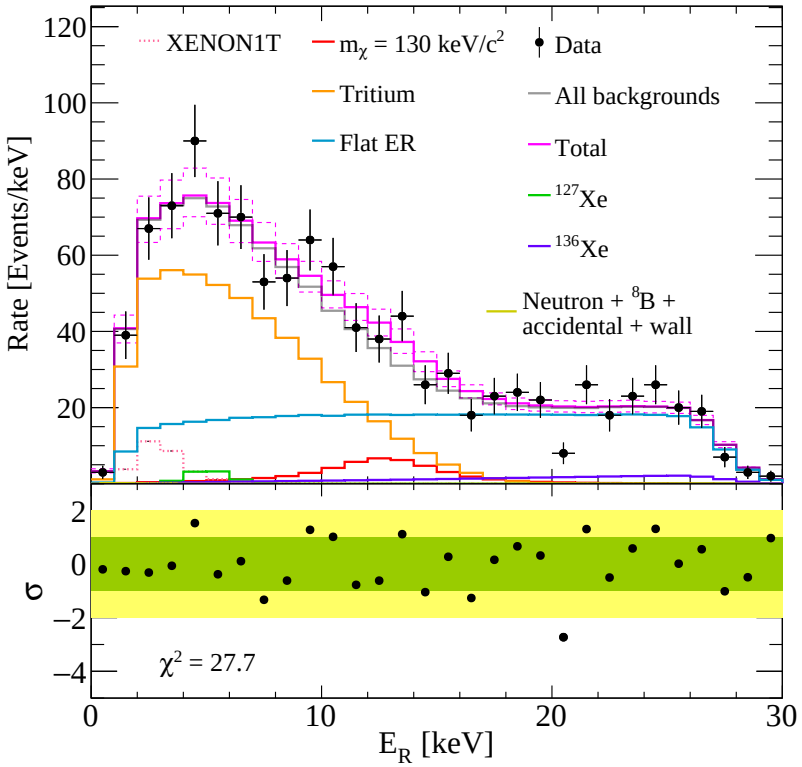

Figure 7.11: Upper: The recoiling energy spectrum E_R of data (black dots with uncertainty bars) campared to the best fit (solid magenta histogram) of the absorption fermionic dark matter signal model with $m_\chi = 130$ keV/c^2 (red histogram) and backgrounds as listed in Tab. 7.1. The dash solid lines mark the 1σ uncertainty band according the the best fitted detector parameters p_* taken as systematic uncertainties. Lower: the relative deviation of the data (black dots with uncertainty bars) compared to the total uncertainties (green band as $\pm1\sigma$ and yellow band as $\pm2\sigma$) in each energy bin (1 keV wide) where the statistic uncertainties are dominant.

but the local excess is mitigated to 0.6σ with the look elsewhere effect considered [4, 188] (also see section 6.4.1). The difference between the dashed magenta lines and the solid magenta line represents the $\pm1\sigma$ uncertainties in the fitted detector parameters p_* which is minor in the statistical uncertainties as presented in the lower panel of the Fig. 7.11. The best fitted p_f in the Tab. 7.1 suggests that the observed data presents a slightly narrower band than the ER NEST model calibrated with ^{220}Rn, which can be also checked in Fig. 7.8.

We follow the limit setting procedure of the PLR analysis as summarized in the literature

with power constraint applied for the part with a downward fluctuation stronger than 1σ [4, 246]. Pseudo-data based on the best fit of the testing signal hypothesis (m_χ, σ_e) are simulated to find the test statistics distribution, which is used as the criteria for limit setting with the observed data calculated test statistics. The sensitivity band is found by the limits of the pseudo-data generated with the best fit of the background-only hypothesis ($N_\mu = 0$). Figure 7.12 shows the limit (red line) and sensitivity band (green band for $\pm 1\sigma$ and yellow for $+2\sigma$) for the axial-vector and vector operators in the $\chi e \to e\nu$ with a 90% confidence level (C.L.). The limits are set on σ_e with the unit of cm^2. The leading order term of the axial-vector interaction is three-fold stronger than the vector interaction which leads to the difference in the limit and sensitivity band. Our dark matter direct detection data has presented competitive sensitivities in the mass region 25 to 55 keV/c^2. For clarification, we plotted the limit sensitivity for $m_\chi > 100$ keV/c^2 with dashed line because the ionization form factor of the non-relativistic atomic response becomes inaccurate. If our sensitivity becomes competitive for $m_\chi > 100$ keV/c^2 in the future, the relativistic effect can be included according to the literature [247].

To sum up, we present the first sensitive experiment search on the absorption signals of fermionic dark matter on electron targets which extends the m_χ to sub-MeV mass range with the LXeTPC. The XENON1T's ER excess interpreted with such light fermionic DM (60 keV/c^2) is only marginally allowed by our data. If the interaction in the absorption is mediated by an axial-vector or a vector with an out-going active neutrino, our data present the strongest constraints on the cross section for some mass range for the axial-vector operator and vector operator because the astrophysical constraints are alleviated when the leading decay channel has more than one photon. No significant dark matter signals are identified with the commissioning data of PandaX-4T. With lower backgrounds and larger exposure, more sensitive searches are on the horizon [57,

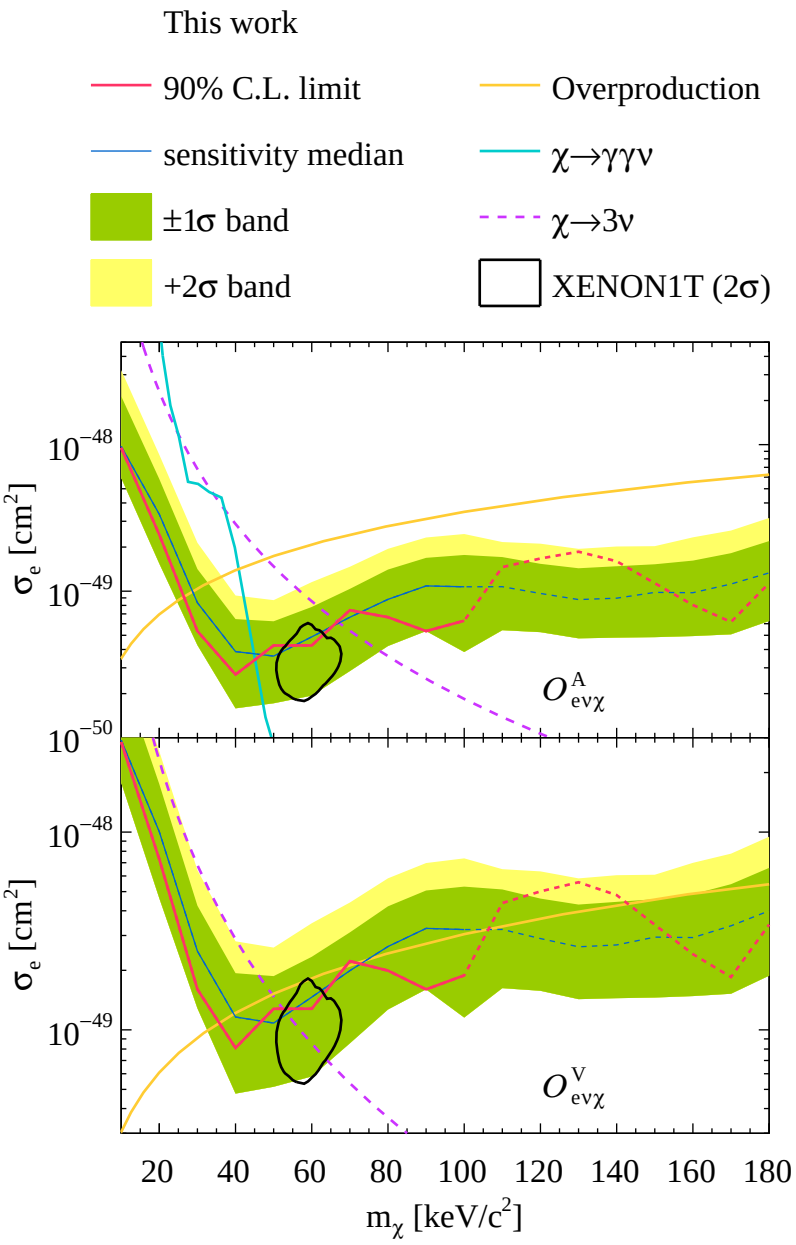

Figure 7.12: The 90% C.L. exclusion limits (red lines) and ± 1 and 2σ sensitivity (green and yellow band) on σ_e of fermionic DM absorption on electrons with the PandaX-4T commissioning data for the axial-vector (upper) and vector (lower) operators. Upper limits from the leading visible decays from X-ray satellites (blue), cosmological constraints from leading invisible decays (magenta) and DM overproduction (orange) [45] are overlaid. The 2σ contour according to the XENON1T's ER excess (black line) is overlain.

58, 227, 248].

Chapter 8: Summary and outlook

This thesis mainly presents the analysis and developments correlated to the spin-independent WIMP-nucleus scattering search in PandaX collaboration which uses the dual-phase liquid xenon time projection chamber that has presented competitive sensitivities for WIMPs from 10 to 10,000 GeV/c^2. For the nuclear recoiling signal searches in PandaX, at least one order of background attenuation would be required which is promising to be realized after integrating hardware and software efforts like radon removal with gaseous/liquid xenon circulation, reducing uncertainties in the analysis, implementing machine learning techniques with more discrimination power between a WIMP signal and backgrounds. Another important technical challenge is how to reach high electric fields in ton-scale or larger xenon detectors for a better separation between electron recoiling and nuclear recoiling bands. One promising solution is to build single-phase xenon detector but still requires extensive R&Ds to test feasiblility. As a reference, the most sensitive search on spin-independent WIMP-nucleus scattering to-date is from LZ with a lowest exclusion limit (90% C.L.) set at 6×10^{-48} cm^2 for a 30 GeV/c^2 WIMP, breaking 1×10^{-47} cm^2 line as a benchmark to explore a new parameter space [249].

If backgrounds can be lowered down to irreducible physics backgrounds from solar neutrinos and double beta decays of ^{136}Xe and we still don't find WIMPs, larger xenon detectors could be built to enlarge the exposure to close up the mass region over the neutrino floor with international

coorperation. Hopefully, with globalization, the science is moving towards with unified forces. Recently, XENON, DARWIN and LUX-ZEPLIN have formed a new collaboration XLZD for a next-generation xenon detector. PandaX-30T is also under discussion for a future plan. Holding hunting for dark matter as the same goal, we will be surprised at how borderless scientists can reach.

With no solid evidence for the dark matter signals, many other scenarios are searched extensively as well, like low-mass dark matter particles including the light fermionic dark matter discussed in this thesis, axion-like particles and primordial black holes. Another top candidate is QCD axions whose golden mass parameter space (1-50 μeV) are verified to be searchable by haloscopes integrated with quantum sensors as a matter of time for the benchmark models. But new technologies are required to extend to either a higher or lower mass parameter space.

After around one century after dark matter showing up in the history, it is still one top mystery in particle physics today, which is the most common mentioned word in the letter of interest submitted to SNOWMASS. To search for it, we do need to push every reachable technology to the extreme and also to develop some novel detector techniques in the future. It may take us another decade or century for us to reveal what dark matter is, but eventually I believe we will find the answer.

Bibliography

[1] Elizabeth A. McCutchan. Nuclear data sheets for a = 83. *Nuclear Data Sheets*, 125:201–394, 2015.

[2] Yue Meng, Zhou Wang, Yi Tao, et al. Dark matter search results from the PandaX-4T commissioning run. *Phys. Rev. Lett.*, 127:261802, Dec 2021.

[3] Vera C. Rubin and Jr. Ford, W. Kent. Rotation of the Andromeda Nebula from a Spectroscopic Survey of Emission Regions. *ApJ*, 159:379, February 1970.

[4] D. Baxter, I. M. Bloch, E. Bodnia, et al. Recommended conventions for reporting results from direct dark matter searches. *Eur. Phys. J. C*, 81(10):907, Oct 2021.

[5] Douglas Clowe, Anthony Gonzalez, and Maxim Markevitch. Weak-lensing mass reconstruction of the interacting cluster 1e 0657-558: Direct evidence for the existence of dark matter. *ApJ*, 604(2):596–603, Apr 2004.

[6] N. Aghanim, Y. Akrami, M. Ashdown, et al. Planck 2018 results - vi. cosmological parameters. *A&A*, 641:A6, 2020.

[7] R.L. Workman and others (Particle Data Group). The Review of Particle Physics. to be published in Prog. Theor. Exp. Phys., 083C01, 2022.

[8] C. Bartram, T. Braine, E. Burns, et al. Search for invisible axion dark matter in the $3.3 - 4.2$ $\mu\mathrm{eV}$ mass range. *Phys. Rev. Lett.*, 127:261803, Dec 2021.

[9] Simeon Bird, Andrea Albert, Will Dawson, et al. Snowmass2021 cosmic frontier white paper: Primordial black hole dark matter. *arXiv:2203.08967*, 2022.

[10] Julien Billard, Mark Boulay, Susana Cebrián, et al. Direct detection of dark matter—APPEC committee report. *Rep. Prog. Phys.*, 85(5):056201, apr 2022.

[11] Jingkai Xia et al. PandaX-II constraints on spin-dependent WIMP-nucleon effective interactions. *Phys. Lett. B*, 792:193–198, 2019.

[12] Lars Bergstrom, Torsten Bringmann, Ilias Cholis, et al. New Limits on Dark Matter Annihilation from AMS Cosmic Ray Positron Data. *Phys. Rev. Lett.*, 111:171101, 2013.

[13] Gaëlle Giesen, Mathieu Boudaud, Yoann Génolini, et al. AMS-02 antiprotons, at last! secondary astrophysical component and immediate implications for dark matter. *JCAP*, 2015(09):023–023, Sep 2015.

[14] R. A. Ong, T. Aramaki, R. Bird, et al. The GAPS experiment to search for dark matter using low-energy antimatter. *arXiv:1710.00452*, 2017.

[15] G. Aad et al. Search for associated production of a Z boson with an invisibly decaying Higgs boson or dark matter candidates at $\sqrt{s}$=13 TeV with the ATLAS detector. *Phys. Lett. B*, 829:137066, 2022.

[16] Kaixuan Ni. *Development of a Liquid Xenon Time Projection Chamber for the XENON Dark Matter Search*. PhD thesis, Columbia University, 2006.

[17] Laura Baudis, Hrvoje Dujmovic, Christopher Geis, Andreas James, et al. Response of liquid xenon to Compton electrons down to 1.5 keV. *Phys. Rev. D*, 87(11):115015, 2013.

[18] Qing Lin, Jialing Fei, Fei Gao, et al. Scintillation and ionization responses of liquid xenon to low energy electronic and nuclear recoils at drift fields from 236 V/cm to 3.93 kV/cm. *Phys. Rev. D*, 92(3):032005, 2015.

[19] D. S. Akerib et al. Tritium calibration of the LUX dark matter experiment. *Phys. Rev.*, D93(7):072009, 2016.

[20] L.W. Goetzke, E. Aprile, M. Anthony, et al. Measurement of light and charge yield of low-energy electronic recoils in liquid xenon. *Phys. Rev. D*, 96(10):103007, 2017.

[21] E. Aprile, C.E. Dahl, L. DeViveiros, et al. Simultaneous measurement of ionization and scintillation from nuclear recoils in liquid xenon as target for a dark matter experiment. *Phys. Rev. Lett.*, 97:081302, 2006.

[22] A. Manzur, A. Curioni, L. Kastens, D.N. McKinsey, K. Ni, and T. Wongjirad. Scintillation efficiency and ionization yield of liquid xenon for mono-energetic nuclear recoils down to 4 keV. *Phys. Rev. C*, 81:025808, 2010.

[23] Peter Sorensen. A coherent understanding of low-energy nuclear recoils in liquid xenon. *JCAP*, 09:033, 2010.

[24] E. Aprile et al. Response of the XENON100 Dark Matter Detector to Nuclear Recoils. *Phys. Rev. D*, 88:012006, 2013.

[25] D. S. Akerib et al. Low-energy (0.7-74 keV) nuclear recoil calibration of the LUX dark matter experiment using D-D neutron scattering kinematics. *arXiv:1608.05381*, 2016.

[26] E. Aprile et al. Simultaneous measurement of the light and charge response of liquid xenon to low-energy nuclear recoils at multiple electric fields. *Phys. Rev. D*, 98(11):112003, 2018.

[27] Wenbo Ma et al. Internal calibration of the PandaX-II detector with radon gaseous sources. *JINST*, 15(12):P12038–P12038, Dec 2020.

[28] Zhou Huang et al. Light yield and field dependence measurement in PandaX-II dual-phase xenon detector. *JINST*, 17(01):P01008, Jan 2022.

[29] Kaixiang Ni, Yihui Lai, et al. Searching for neutrino-less double beta decay of ^{136}Xe with PandaX-II liquid xenon detector. *CPC*, 43(11):113001, Nov 2019.

[30] J.J.L. Mulders. Yield curves and beam current dependent production rates of Rb radioisotopes produced by protons on a krypton gas target. *Int. J. Appl. Radiar. Isot.*, 35:475–480, 1984.

[31] G.F. Steyn, S.J. Mills, F.M. Nortier, and F.J. Haasbroek. Integral excitation functions for $^{\mathrm{nat}}$Kr + p up to 116 MeV and optimization of the production of ^{81}Rb for ^{81m}Kr generators. *Int. J. Appl. Radiar. Isot.*, 42:361–370, 1991.

[32] Z. Kovács, F. Tárkányi, S.M. Qaim, and G. Stocklin. Excitation functions for the formation of some radioisotopes of rubidium in proton induced nuclear reactions on $^{\mathrm{nat}}$Kr, ^{82}Kr and ^{83}Kr with special reference to the production of ^{81}Rb(^{81m}Kr) generator radionuclide. *Int. J. Appl. Radiar. Isot.*, 42:329–335, 1991.

[33] M. J. Berger, J. S. Coursey, M. A. Zucker, and J. Chang. ESTAR, PSTAR, and ASTAR: Computer programs for calculating stopping-power and range tables for electrons, protons, and helium ions (version 1.2.3). [Online] Available: http://physics.nist.gov/Star [2022, June 8]. National Institute of Standards and Technology, Gaithersburg, MD.

[34] Xiangyi Cui et al. Dark matter results from 54-ton-day exposure of PandaX-II experiment. *Phys. Rev. Lett.*, 119:181302, Oct 2017.

[35] Qibin Zheng, Yanlin Huang, Di Huang, et al. An improved design of the readout base board of the photomultiplier tube for future PandaX dark matter experiments. *JINST*, 15(12):T12006–T12006, Dec 2020.

[36] Jijun Yang, Xun Chen, Changda He, et al. Readout electronics and data acquisition system of PandaX-4T experiment. *JINST*, 17(02):T02004, Feb 2022.

[37] Li Zhao, Xiangyi Cui, Wenbo Ma, et al. The cryogenics and xenon handling system for the PandaX-4T experiment. *JINST*, 16(06):T06007, Jun 2021.

[38] Xiangyi Cui, Zhou Wang, Yonglin Ju, et al. Design and commissioning of the PandaX-4T cryogenic distillation system for krypton and radon removal. *JINST*, 16(07):P07046, Jul 2021.

[39] Peng Ji, Xun Chen, Andi Tan, et al. A low-cost slow control system for the PandaX-4T experiment. *RDTM*, 3(3):53, Jun 2019.

[40] Qiuhong Wang et al. Results of dark matter search using the full PandaX-II exposure. *CPC*, 44(12):125001, Dec 2020.

[41] Pauli Virtanen, Ralf Gommers, Travis E. Oliphant, SciPy 1.0 Contributors, et al. Scipy 1.0: fundamental algorithms for scientific computing in python. *Nat. Methods*, 17(3):261–272, Mar 2020.

[42] Esra Bulbul, Maxim Markevitch, Adam Foster, et al. Detection of an Unidentified Emission Line in the Stacked X-Ray Spectrum of Galaxy Clusters. *ApJ*, 789(1):13, July 2014.

[43] Brandon M. Roach, Kenny C. Y. Ng, Kerstin Perez, et al. NuSTAR tests of sterile-neutrino dark matter: New galactic bulge observations and combined impact. *Phys. Rev. D*, 101:103011, May 2020.

[44] Miguel D. Campos and Werner Rodejohann. Testing keV sterile neutrino dark matter in future direct detection experiments. *Phys. Rev. D*, 94:095010, Nov 2016.

[45] Shao-Feng Ge, Xiao-Gang He, Xiao-Dong Ma, and Jie Sheng. Revisiting the fermionic dark matter absorption on electron target. *JHEP*, 2022(5):191, May 2022.

[46] J. J. Aubert, U. Becker, and P. J. Biggs others. Experimental observation of a heavy particle J. *Phys. Rev. Lett.*, 33:1404–1406, Dec 1974.

[47] J. E. Augustin, A. M. Boyarski, M. Breidenbach, et al. Discovery of a narrow resonance in e^+e^- annihilation. *Phys. Rev. Lett.*, 33:1406–1408, Dec 1974.

[48] M. Banner, R.Battiston, Ph.Bloch, et al. Observation of single isolated electrons of high transverse momentum in events with missing transverse energy at the CERN pp collider. *Phys. Lett. B*, 122(5):476–485, 1983.

[49] G. Aad et al. Observation of a new particle in the search for the Standard Model Higgs boson with the ATLAS detector at the LHC. *Phys. Lett. B*, 716(1):1–29, 2012.

[50] Y. Fukuda et al. Evidence for oscillation of atmospheric neutrinos. *Phys. Rev. Lett.*, 81:1562–1567, Aug 1998.

[51] Q. R. Ahmad, R. C. Allen, T. C. Andersen, et al. Measurement of the rate of $\nu_e + d \rightarrow p + p + e^-$ interactions produced by ^8B solar neutrinos at the Sudbury Neutrino Observatory. *Phys. Rev. Lett.*, 87:071301, Jul 2001.

[52] Gerard Jungman, Marc Kamionkowski, and Kim Griest. Supersymmetric dark matter. *Phys. Rep.*, 267(5):195–373, 1996.

[53] K. J. Kang, J. P. Cheng, and Y. H. Chen others. Status and prospects of a deep underground laboratory in China. *J. Phys.: Conf. Ser*, 203:012028, Jan 2010.

[54] Li Zhao and Jianglai Liu. Experimental search for dark matter in China. *Front. Phys. (Beijing)*, 15(4):44301, 2020.

[55] D. S. Akerib et al. Results from a search for dark matter in the complete LUX exposure. *Phys. Rev. Lett.*, 118:021303, Jan 2017.

[56] E. Aprile et al. Dark matter search results from a one ton-year exposure of XENON1T. *Phys. Rev. Lett.*, 121:111302, Sep 2018.

[57] D. S. Akerib et al. Projected WIMP sensitivity of the LUX-ZEPLIN dark matter experiment. *Phys. Rev. D*, 101:052002, Mar 2020.

[58] E. Aprile et al. Projected WIMP sensitivity of the XENONnT dark matter experiment. *JCAP*, 2020(11):031–031, Nov 2020.

[59] Liron Barak et al. SENSEI: Direct-Detection Results on sub-GeV Dark Matter from a New Skipper CCD. *Phys. Rev. Lett.*, 125:171802, Oct 2020.

[60] R. Agnese et al. Projected sensitivity of the SuperCDMS snolab experiment. *Phys. Rev. D*, 95:082002, Apr 2017.

[61] Yonit Hochberg et al. Detection of sub-MeV dark matter with three-dimensional Dirac materials. *Phys. Rev. D*, 97:015004, Jan 2018.

[62] Yonit Hochberg, Yue Zhao, and Kathryn M. Zurek. Superconducting detectors for superlight dark matter. *Phys. Rev. Lett.*, 116:011301, Jan 2016.

[63] Peizhi Du, Daniel Egana-Ugrinovic, Rouven Essig, and Mukul Sholapurkar. Sources of low-energy events in low-threshold dark-matter and neutrino detectors. *Phys. Rev. X*, 12:011009, Jan 2022.

[64] R. D. Peccei and Helen R. Quinn. CP conservation in the presence of pseudoparticles. *Phys. Rev. Lett.*, 38:1440–1443, Jun 1977.

[65] D. Antypas et al. New horizons: Scalar and vector ultralight dark matter. *arXiv:2203.14915*, 2022.

[66] R. Adhikari, M. Agostini, N. Anh Ky, et al. A white paper on keV sterile neutrino dark matter. *JCAP*, 2017(01):025–025, Jan 2017.

[67] Edward W. Kolb and Andrew J. Long. Superheavy dark matter through Higgs portal operators. *Phys. Rev. D*, 96:103540, Nov 2017.

[68] F. Zwicky. Die Rotverschiebung von extragalaktischen Nebeln. *Helvetica Physica Acta*, 6:110–127, January 1933.

[69] J. H. Oort. The force exerted by the stellar system in the direction perpendicular to the galactic plane and some related problems. *BAIN*, 6:249, August 1932.

[70] Lina Necib, Mariangela Lisanti, and Vasily Belokurov. Inferred evidence for dark matter kinematic substructure with SDSS–igaia/i. *The Astrophysical Journal*, 874(1):3, Mar 2019.

[71] Robert V. Wagoner, William A. Fowler, and F. Hoyle. On the synthesis of elements at very high temperatures. *ApJ*, 148:3, April 1967.

[72] Cora Dvorkin, Tongyan Lin, and Katelin Schutz. Cosmology of sub-MeV dark matter freeze-in. *Phys. Rev. Lett.*, 127:111301, Sep 2021.

[73] Ethan M. Dolle and Shufang Su. Inert dark matter. *Phys. Rev. D*, 80:055012, Sep 2009.

[74] Géraldine Servant and Tim M.P. Tait. Is the lightest Kaluza–Klein particle a viable dark matter candidate? *Nucl. Phys. B*, 650(1):391–419, 2003.

[75] Jianglai Liu, Xun Chen, and Xiangdong Ji. Current status of direct dark matter detection experiments. *Nat. Phys.*, 13(3):212–216, Mar 2017.

[76] Jan Conrad and Olaf Reimer. Indirect dark matter searches in gamma and cosmic rays. *Nat. Phys.*, 13(3):224–231, Mar 2017.

[77] Weishuang Linda Xu, Cora Dvorkin, and Andrew Chael. Probing sub-GeV dark matter-baryon scattering with cosmological observables. *Phys. Rev. D*, 97:103530, May 2018.

[78] Keir K. Rogers, Cora Dvorkin, and Hiranya V. Peiris. Limits on the light dark matter–proton cross section from cosmic large-scale structure. *Phys. Rev. Lett.*, 128:171301, Apr 2022.

[79] William DeRocco, Peter W. Graham, Daniel Kasen, Gustavo Marques-Tavares, and Surjeet Rajendran. Supernova signals of light dark matter. *Phys. Rev. D*, 100:075018, Oct 2019.

[80] Masahiro Ibe, Wakutaka Nakano, Yutaro Shoji, and Kazumine Suzuki. Migdal effect in dark matter direct detection experiments. *JHEP*, 2018(3):194, Mar 2018.

[81] Marco Cirelli, Pasquale D Serpico, and Gabrijela Zaharijas. Bremsstrahlung gamma rays from light dark matter. *JCAP*, 2013(11):035–035, Nov 2013.

[82] Xiangyi Cui et al. Search for cosmic-ray boosted sub-GeV dark matter at the PandaX-II experiment. *Phys. Rev. Lett.*, 128:171801, Apr 2022.

[83] Jeff A. Dror, Gilly Elor, and Robert McGehee. Absorption of fermionic dark matter by nuclear targets. *JHEP*, 2020(2):134, Feb 2020.

[84] N. Castelló-Mor. DAMIC-M experiment: Thick, silicon ccds to search for light dark matter. *Nucl. Instrum.*, 958:162933, 2020. Proceedings of the Vienna Conference on Instrumentation 2019.

[85] Hao Ma et al. CDEX dark matter experiment: Status and prospects. *J. Phys. Conf. Ser.*, 1342(1):012067, Jan 2020.

[86] E. Armengaud et al. Performance of the EDELWEISS-III experiment for direct dark matter searches. *JINST*, 12(08):P08010–P08010, Aug 2017.

[87] Guillermo Fernandez Moroni et al. Skipper charge-coupled device for low-energy-threshold particle experiments above ground. *Phys. Rev. Applied*, 17:044050, Apr 2022.

[88] Alexis Aguilar-Arevalo et al. The Oscura experiment. *arXiv:2202.10518*, 2022.

[89] Laurent Canetti, Marco Drewes, Tibor Frossard, and Mikhail Shaposhnikov. Dark matter, baryogenesis and neutrino oscillations from right-handed neutrinos. *Phys. Rev. D*, 87:093006, May 2013.

[90] Laurent Canetti, Marco Drewes, and Mikhail Shaposhnikov. Sterile neutrinos as the origin of dark and baryonic matter. *Phys. Rev. Lett.*, 110:061801, Feb 2013.

[91] Takehiko Asaka, Steve Blanchet, and Mikhail Shaposhnikov. The νMSM, dark matter and neutrino masses. *Phys. Lett. B*, 631(4):151–156, 2005.

[92] A. Boyarsky, O. Ruchayskiy, D. Iakubovskyi, and J. Franse. Unidentified line in X-Ray spectra of the Andromeda galaxy and Perseus galaxy cluster. *Phys. Rev. Lett.*, 113:251301, Dec 2014.

[93] A. Boyarsky, J. Franse, D. Iakubovskyi, and O. Ruchayskiy. Checking the dark matter origin of a 3.53 keV line with the Milky Way center. *Phys. Rev. Lett.*, 115:161301, Oct 2015.

[94] Michael E. Anderson, Eugene Churazov, and Joel N. Bregman. Non-detection of X-ray emission from sterile neutrinos in stacked galaxy spectra. *Mon. Not. R. Astron. Soc.*, 452(4):3905–3923, 08 2015.

[95] Eric Carlson, Tesla Jeltema, and Stefano Profumo. Where do the 3.5 keV photons come from? a morphological study of the galactic center and of perseus. *JCAP*, 2015(02):009–009, Feb 2015.

[96] Scott Dodelson and Lawrence M. Widrow. Sterile neutrinos as dark matter. *Phys. Rev. Lett.*, 72:17–20, Jan 1994.

[97] Casey R Watson, Zhiyuan Li, and Nicholas K Polley. Constraining sterile neutrino warm dark matter with Chandra observations of the Andromeda galaxy. *JCAP*, 2012(03):018–018, Mar 2012.

[98] Shunsaku Horiuchi et al. Sterile neutrino dark matter bounds from galaxies of the local group. *Phys. Rev. D*, 89:025017, Jan 2014.

[99] Kerstin Perez et al. Almost closing the $\nu\mathrm{MSM}$ sterile neutrino dark matter window with NuSTAR. *Phys. Rev. D*, 95:123002, Jun 2017.

[100] Yonit Hochberg et al. Directional detection of dark matter with two-dimensional targets. *Phys. Lett. B*, 772:239–246, 2017.

[101] Jeff A. Dror, Gilly Elor, Robert McGehee, and Tien-Tien Yu. Absorption of sub-MeV fermionic dark matter by electron targets. *Phys. Rev. D*, 103(3):035001, 2021.

[102] Kenny C. Y. Ng et al. New constraints on sterile neutrino dark matter from NuSTAR m31 observations. *Phys. Rev. D*, 99:083005, Apr 2019.

[103] Michael Clark, Amanda Depoian, Bahaa Elshimy, et al. Direct detection limits on heavy dark matter. *Phys. Rev. D*, 102:123026, Dec 2020.

[104] Wayne Hu, Rennan Barkana, and Andrei Gruzinov. Fuzzy cold dark matter: The wave properties of ultralight particles. *Phys. Rev. Lett.*, 85:1158–1161, Aug 2000.

[105] Lam Hui et al. Ultralight scalars as cosmological dark matter. *Phys. Rev. D*, 95:043541, Feb 2017.

[106] Marc Kamionkowski and John March-Russell. Planck-scale physics and the peccei-quinn mechanism. *Phys. Lett. B*, 282(1):137–141, 1992.

[107] T. D. Lee and C. N. Yang. Question of parity conservation in weak interactions. *Phys. Rev.*, 104:254–258, Oct 1956.

[108] C. S. Wu, E. Ambler, R. W. Hayward, D. D. Hoppes, and R. P. Hudson. Experimental test of parity conservation in beta decay. *Phys. Rev.*, 105:1413–1415, Feb 1957.

[109] J. H. Christenson, J. W. Cronin, V. L. Fitch, and R. Turlay. Evidence for the 2π decay of the K_2^0 meson. *Phys. Rev. Lett.*, 13:138–140, Jul 1964.

[110] K. M. Backes et al. A quantum enhanced search for dark matter axions. *Nature*, 590(7845):238–242, Feb 2021.

[111] Mohammadtaher Safarzadeh and David N. Spergel. Ultra-light dark matter is incompatible with the Milky Way's dwarf satellites. *ApJ*, 893(1):21, Apr 2020.

[112] David J. E. Marsh and Jens C. Niemeyer. Strong constraints on fuzzy dark matter from ultrafaint dwarf galaxy Eridanus II. *Phys. Rev. Lett.*, 123:051103, Jul 2019.

[113] Vid Irsic et al. First constraints on fuzzy dark matter from Lyman-α forest data and hydrodynamical simulations. *Phys. Rev. Lett.*, 119, 2017.

[114] Jonathan L. Ouellet et al. First results from ABRACADABRA-10 cm: A search for sub-μeV axion dark matter. *Phys. Rev. Lett.*, 122:121802, Mar 2019.

[115] L. Brouwer et al. Introducing DMRadio-GUT, a search for GUT-scale QCD axions. *arXiv:2203.11246*, 2022.

[116] Timothy D. Brandt. Constraints on MACHO dark matter from compact stellar systems in ultra-faint dwarf galaxies. *ApJ*, 824(2):L31, Jun 2016.

[117] E. Aprile et al. Dark matter results from 225 live days of XENON100 data. *Phys. Rev. Lett.*, 109:181301, Nov 2012.

[118] A. H. Abdelhameed et al. First results from the CRESST-III low-mass dark matter program. *Phys. Rev. D*, 100:102002, Nov 2019.

[119] E. Aprile et al. Light dark matter search with ionization signals in XENON1T. *Phys. Rev. Lett.*, 123:251801, Dec 2019.

[120] Daniel Z. Freedman. Coherent effects of a weak neutral current. *Phys. Rev. D*, 9:1389–1392, Mar 1974.

[121] D. S. Akerib et al. Snowmass2021 cosmic frontier dark matter direct detection to the neutrino fog. *arXiv:2203.08084*, 2022.

[122] C. Amole et al. Dark matter search results from the complete exposure of the PICO-60 C_3F_8 bubble chamber. *Phys. Rev. D*, 100:022001, Jul 2019.

[123] M. Ackermann et al. Constraining dark matter models from a combined analysis of Milky Way satellites with the Fermi Large Area Telescope. *Phys. Rev. Lett.*, 107:241302, Dec 2011.

[124] Silvia Galli, Fabio Iocco, Gianfranco Bertone, and Alessandro Melchiorri. CMB constraints on dark matter models with large annihilation cross section. *Phys. Rev. D*, 80:023505, Jul 2009.

[125] M.G. Aartsen et al. Improved limits on dark matter annihilation in the sun with the 79-string IceCube detector and implications for supersymmetry. *JCAP*, 2016(04):022–022, Apr 2016.

[126] K. Choi, others, and Super-Kamiokande Collaboration. Search for neutrinos from annihilation of captured low-mass dark matter particles in the sun by Super-Kamiokande. *Phys. Rev. Lett.*, 114(14):141301, April 2015.

[127] W.J. Willis and V. Radeka. Liquid-argon ionization chambers as total-absorption detectors. *Nucl. Instrum. Meth.*, 120(2):221–236, 1974.

[128] E. Aprile and T. Doke. Liquid xenon detectors for particle physics and astrophysics. *Rev. Mod. Phys.*, 82:2053–2097, Jul 2010.

[129] K. Abe et al. A direct dark matter search in XMASS-I. *Phys. Lett. B*, 789:45–53, 2019.

[130] G. Anton et al. Search for neutrinoless double-β decay with the complete EXO-200 dataset. *Phys. Rev. Lett.*, 123:161802, Oct 2019.

[131] E. Aprile et al. Observation of two-neutrino double electron capture in ^{124}Xe with XENON1T. *Nature*, 568(7753):532–535, Apr 2019.

[132] D. S. Akerib et al. Projected sensitivity of the LUX-ZEPLIN experiment to the two-neutrino and neutrinoless double β decays of ^{134}Xe. *Phys. Rev. C*, 104:065501, Dec 2021.

[133] G Adhikari et al. nEXO: neutrinoless double beta decay search beyond 10^{28} year half-life sensitivity. *J. Phys. G: Nucl. Part. Phys.*, 49(1):015104, Dec 2021.

[134] Xiao Mengjiao. *PandaX-I Experiment for Low-mass Dark Matter Search*. PhD thesis, Shanghai Jiao Tong University, 2016.

[135] Wei Yuehuan. *Development Of A Dual Phase Xenon Time Projection Chamber For Dark Matter Search*. PhD thesis, Shanghai Jiao Tong University, 2014.

[136] Ren Xiangxiang. *Design and Realization of Electronics and Data Acquisition System for the PandaX Experiment*. PhD thesis, Shandong University, 2015.

[137] Stephenson Scott. *Probing Spin-Independent WIMP-Nucleon Interactions with the PandaX-I Detector*. PhD thesis, University of Michigan, 2015.

[138] Xiao Xiang. *Design and Performance of Time Projection Chambers for the PandaX Dark Matter Detector*. PhD thesis, Shanghai Jiao Tong University, 2015.

[139] Lin Qing. *Searching for Low Mass Dark Matter with The PandaX Liquid Xenon Detector*. PhD thesis, Shanghai Jiao Tong University, 2015.

[140] Gong Haowei. *The PandaX-I Liquid Xenon Dark Matter Direct Detection Experiment: Cryogenic Design, Construction and Experimental Data Analysis*. PhD thesis, Shanghai Jiao Tong University, 2016.

[141] Xie Pengwei. *A Search of Spin-Independent WIMP-Nucleon Interactions using the PandaX-I and PandaX-II Detectors*. PhD thesis, Shanghai Jiao Tong University, 2017.

[142] Li Shaoli. *A study of the photosensor system performance and background from radioactive gases of the PandaX-I dark matter experiment*. PhD thesis, Shanghai Jiao Tong University, 2018.

[143] Tan Andi. *PandaX-II dark matter detector and its first results*. PhD thesis, University of Maryland, College Park, 2019.

[144] Zhou Xiaopeng. *Searches of Axions and Axion-like particles with PandaX-II*. PhD thesis, Peking University, 2018.

[145] Cui Xiangyi. *PandaX-II Dark Matter Experiment and the PandaX-4T Cryogenics, Circulation and Distillation System*. PhD thesis, Shanghai Jiao Tong University, 2019.

[146] Wang Qiuhong. *PandaX-II Experiment for Dark Matter Search*. PhD thesis, University of Chinese Academy of Sciences, 2020.

[147] Yan Binbin. *A search of spin-dependent WIMP-nucleon interactions using the PandaX-II detector*. PhD thesis, Shandong, University, 2019.

[148] Wang Zhou. *Development and Experimental Study and Optimization of An Ultra High Purity Xenon/Krypton Cryogenic Distillation System*. PhD thesis, Shanghai Jiao Tong University, 2015.

[149] X. Cui et al. Design and commissioning of the PandaX-4T cryogenic distillation system for krypton and radon removal. *JINST*, 16(07):P07046, Jul 2021.

[150] Wang Xuming. *Radioactive Background Control for PandaX Experiment and Corresponding Analysis*. PhD thesis, Shanghai Jiao Tong University, 2017.

[151] Lin Zhao et al. Measurement of muon-induced neutron production at China Jinping Underground Laboratory. *arXiv:2108.04010*, 2021.

[152] N. J. T. Smith. The SNOLAB deep underground facility. *The European Physical Journal Plus*, 127(9):108, Sep 2012.

[153] Andi Tan et al. Dark matter search results from the commissioning run of PandaX-II. *Phys. Rev. D*, 93:122009, Jun 2016.

[154] Xiaopeng Zhou et al. A search for solar axions and anomalous neutrino magnetic moment with the complete PandaX-II data. *Chin. Phys. Lett.*, 38(1):011301, 2021.

[155] QiuHong Wang et al. An improved evaluation of the neutron background in the PandaX-II experiment. *Sci. China: Phys. Mech. Astron.*, 63(3):231011, Nov 2019.

[156] Abdusalam Abdukerim et al. Study of background from accidental coincidence signals in the pandax-ii experiment. *CPC*, Jul 2022.

[157] Dan Zhang et al. $^{83}\mathrm{Rb}/^{83m}\mathrm{Kr}$ production and cross-section measurement with 3.4 MeV and 20 MeV proton beams. *Phys. Rev. C*, 105:014604, Jan 2022.

[158] Laura I. Bodine. Molecular effects in tritium beta-decay neutrino-mass measurement. *Doctoral dissertation, University of Washington*, 2015.

[159] E. H. Miller et al. Constraining radon backgrounds in LZ. 1921:050003, Jan 2018.

[160] MengJiao Xiao et al. First dark matter search results from the PandaX-I experiment. *Sci. China: Phys. Mech. Astron.*, 57(11):2024–2030, Nov 2014.

[161] Andi Tan et al. Dark matter results from first 98.7 days of data from the PandaX-II experiment. *Phys. Rev. Lett.*, 117(12):121303, 2016.

[162] M. Zbořil et al. Ultra-stable implanted ^{83}Rb/^{83m}Kr electron sources for the energy scale monitoring in the KATRIN experiment. *JINST*, 8:P03009, 2006.

[163] A. Chan et al. Performance of the HPC calorimeter in DELPHI. *IEEE Trans. Nucl. Sci.*, 42:491–498, 1995.

[164] J. Stiller. Gain calibration of the ALICE TRD using the decay of ^{83m}Kr by internal conversion. *Nucl. Instrum. Meth. A*, 706:20–22, 2013.

[165] L.W. Kastens et al. Calibration of liquid xenon detector with $^{83m}\mathrm{Kr}$. *Phys. Rev. C*, 80:045809, 2009.

[166] W. H. Lippincott et al. Calibration of liquid argon and neon detectors with $^{83m}\mathrm{Kr}$. *Phys. Rev. C*, 81:045803, Apr 2010.

[167] A Manalaysay et al. Spatially uniform calibration of a liquid xenon detector at low energies using (83m)kr. *Rev. Sci. Instrum.*, 81(7):073303, July 2010.

[168] L. D. Landau and E. M. Lifshitz. *Quantum Mechanics Non-Relativistic Theory, Third Edition: Volume 3*. Pergamon Press, Headington Hill Hall, Oxford OX3 0BW, England, 1977.

[169] Xuming Wang, Xun Chen, Changbo Fu, et al. Material screening with HPGe counting station for PandaX experiment. *JINST*, 11(12):T12002–T12002, Dec 2016.

[170] Meng Wang, George Audi, Filip G Kondev, et al. The AME2016 atomic mass evaluation (II). tables, graphs and references. *CPC*, 41(3):030003, 2017.

[171] National Electrostatics Corp. Complete pelletron systems for ion beam analysis.

[172] V. Hannen et al. Limits on the release of Rb isotopes from a zeolite based ^{83m}Kr calibration source for the XENON project. *JINST*, 6:P10013, 2011.

[173] Saes getters. http://www.saespuregas.com/Library/specifications-brochures/s110-233_a_521.pdf.

[174] A L Read. Presentation of search results: the CL_s technique. *J. Phys. G: Nucl. Part. Phys.*, 28(10):2693–2704, Sep 2002.

[175] C. S. Amarasinghe et al. Feasibility study to use neutron capture for an ultra-low energy nuclear-recoil calibration in liquid xenon. *arXiv:2204.03109*, 4 2022.

[176] Robert M. Gray and Albert Macovski. Maximum a posteriori estimation of position in scintillation cameras. *IEEE Trans. Nucl. Sci.*, 23(1):849–852, 1976.

[177] V. N. Solovov et al. Position reconstruction in a dual phase xenon scintillation detector. 59(6):3286–3293, 2012.

[178] D.S. Akerib et al. Position reconstruction in LUX. *JINST*, 13(02):P02001–P02001, Feb 2018.

[179] A. Lindote et al. Preliminary results on position reconstruction for ZEPLIN-III. *Nucl. Instrum. Methods Phys. Res. A*, 573(1):200–203, 2007. Proceedings of the 7th International Conference on Position-Sensitive Detectors.

[180] B.J. Philip. *Reconstruction in DarkSide-50*. PhD thesis, Princeton University, 2015.

[181] E. Aprile et al. XENON1T dark matter data analysis: Signal reconstruction, calibration, and event selection. *Phys. Rev. D*, 100:052014, Sep 2019.

[182] D. Zhang, A. Tan, et al. Horizontal position reconstruction in PandaX-II. *JINST*, 16(11):P11040, Nov 2021.

[183] T Ling, T H Burnett, T K Lewellen, and R S Miyaoka. Parametric positioning of a continuous crystal PET detector with depth of interaction decoding. *Phys. Med. Biol.*, 53(7):1843–1863, April 2008.

[184] D. Zhang. Estimating the surface backgrounds in PandaX-II WIMP search data. *JINST*, 14(10):C10039–C10039, Oct 2019.

[185] Xun Chen, Chen Cheng, Mengting Fu, et al. BambooMC — a GEANT4-based simulation program for the PandaX experiments. *JINST*, 16(09):T09004, Sep 2021.

[186] Erik Dietz-Laursonn. Peculiarities in the simulation of optical physics with geant4. *arXiv:1612.05162*, 2016.

[187] A. Howard. Optical photons. 2019. https://indico.cern.ch/event/866056/contributions/3648975/attachments/1949282/3552948/AH_OpticalPhotons_G4advanced.pdf.

[188] Eilam Gross and Ofer Vitells. Trial factors for the look elsewhere effect in high energy physics. *Eur. Phys. J. C*, 70(1):525–530, Nov 2010.

[189] Module implementing kernel-based estimation of density of probability. https://pythonhosted.org/PyQt-Fit/mod_kde.html.

[190] Zhicheng Qian, Lin Si, et al. Low radioactive material screening and background control for the pandax-4t experiment. *JHEP*, 2022(6):147, Jun 2022.

[191] X. Yan, X. Chen, Y. Chen, et al. Slow control system for PandaX-III experiment. *JINST*, 16(05):T05004, May 2021.

[192] S. Agostinelli et al. GEANT4: A simulation toolkit. *Nucl. Instrum. Meth.*, A506:250–303, 2003.

[193] Matthew Szydagis et al. Noble element simulation technique v2.0, 2018.

[194] Matthew Szydagis et al. A review of basic energy reconstruction techniques in liquid xenon and argon detectors for dark matter and neutrino physics using nest. *Instruments*, 5(1), 2021.

[195] CAEN V1725. http://npg.dl.ac.uk/MIDAS/MIDASWebServices/VME/docs/UM2792_V1730_V1725_rev2.pdf.

[196] E Aprile et al. The neutron background of the XENON100 dark matter search experiment. *J. Phys. G: Nucl. Part. Phys.*, 40(11):115201, Sep 2013.

[197] Richard H. Helm. Inelastic and elastic scattering of 187-MeV electrons from selected even-even nuclei. *Phys. Rev.*, 104:1466–1475, Dec 1956.

[198] Jingke Xu, Sergey Pereverzev, Brian Lenardo, et al. Electron extraction efficiency study for dual-phase xenon dark matter experiments. *Phys. Rev. D*, 99:103024, May 2019.

[199] Gary J. Feldman and Robert D. Cousins. Unified approach to the classical statistical analysis of small signals. *Phys. Rev. D*, 57:3873–3889, Apr 1998.

[200] Don van Ravenzwaaij, Pete Cassey, and Scott D. Brown. A simple introduction to Markov Chain Monte Carlo sampling. *Psychonomic Bulletin & Review*, 25(1):143–154, Feb 2018.

[201] M. Baak et al. Interpolation between multi-dimensional histograms using a new non-linear moment morphing method. *Nucl. Instrum. Methods Phys. Res. A*, 771:39–48, 2015.

[202] Alan M. Ferrenberg and Robert H. Swendsen. New Monte Carlo technique for studying phase transitions. *Phys. Rev. Lett.*, 61:2635–2638, Dec 1988.

[203] James S. Gainer et al. Exploring Theory Space with Monte Carlo Reweighting. *JHEP*, 10:078, 2014.

[204] Olivier Mattelaer. On the maximal use of Monte Carlo samples: re-weighting events at nlo accuracy. *Eur. Phys. J. C*, 76(12):674, Dec 2016.

[205] Ron S. Dembo and Trond Steihaug. Truncated-newtono algorithms for large-scale unconstrained optimization. *Math. Program.*, 26(2):190–212, Jun 1983.

[206] M. J. D. Powell. An efficient method for finding the minimum of a function of several variables without calculating derivatives. *Comput. J.*, 7(2):155–162, 01 1964.

[207] F. James and M. Roos. Minuit - a system for function minimization and analysis of the parameter errors and correlations. *Comput. Phys. Commun.*, 10(6):343–367, 1975.

[208] T. Doke. Fundamental properties of liquid argon, krypton and xenon as radiation detector media. *Portugal. Phys.*, 12:9–48, 1981.

[209] J. Lindhard. *Range Concepts and Heavy Ion Ranges: (Notes on Atomic Collisions, II)*. Matematisk-fysiske Meddelelser udgivet af det Kong. Danske Videnskabernes Selskab. Munksgaard, 1963.

[210] Binbin Yan et al. Determination of responses of liquid xenon to low energy electron and nuclear recoils using a PandaX-II detector. *CPC*, 45(7):075001, Jul 2021.

[211] J. Aalbers et al. Finding dark matter faster with explicit profile likelihoods. *Phys. Rev. D*, 102:072010, Oct 2020.

[212] Minuit2 vs other optimisers. https://iminuit.readthedocs.io/en/stable/benchmark.html.

[213] Gianfranco Bertone, Dan Hooper, and Joseph Silk. Particle dark matter: evidence, candidates and constraints. *Phys. Rep.*, 405(5):279–390, 2005.

[214] R. D. Peccei and Helen R. Quinn. CP conservation in the presence of pseudoparticles. *Phys. Rev. Lett.*, 38:1440–1443, Jun 1977.

[215] Jihn E. Kim. Weak-interaction singlet and strong CP invariance. *Phys. Rev. Lett.*, 43:103–107, Jul 1979.

[216] M.A. Shifman, A.I. Vainshtein, and V.I. Zakharov. Can confinement ensure natural CP invariance of strong interactions? *Nucl. Phys. B.*, 166(3):493–506, 1980.

[217] Steven Weinberg. A new light boson? *Phys. Rev. Lett.*, 40:223–226, Jan 1978.

[218] F. Wilczek. Problem of strong p and t invariance in the presence of instantons. *Phys. Rev. Lett.*, 40:279–282, Jan 1978.

[219] Julio F. Navarro, Carlos S. Frenk, and Simon D. M. White. The structure of cold dark matter halos. *ApJ*, 462:563, May 1996.

[220] Ben Moore. Evidence against dissipation-less dark matter from observations of galaxy haloes. *Nature*, 370(6491):629–631, Aug 1994.

[221] Anatoly Klypin, Andrey V. Kravtsov, Octavio Valenzuela, and Francisco Prada. Where are the missing galactic satellites? *Astrophys. J.*, 522(1):82–92, Sep 1999.

[222] Ben Moore, Sebastiano Ghigna, Fabio Governato, et al. Dark matter substructure within galactic halos. *Astrophys. J.*, 524(1):L19–L22, Oct 1999.

[223] Michael Boylan-Kolchin, James S. Bullock, and Manoj Kaplinghat. Too big to fail? The puzzling darkness of massive Milky Way subhaloes. *Mon. Not. R. Astron. Soc.: Lett.*, 415(1):L40–L44, 07 2011.

[224] Marc Kamionkowski and John March-Russell. Planck-scale physics and the Peccei-Quinn mechanism. *Phys. Lett. B*, 282(1):137–141, 1992.

[225] S. M. Barr and D. Seckel. Planck-scale corrections to axion models. *Phys. Rev. D*, 46:539–549, Jul 1992.

[226] P. Agnes et al. DarkSide-50 532-day dark matter search with low-radioactivity argon. *Phys. Rev. D*, 98:102006, Nov 2018.

[227] C. E. Aalseth et al. DarkSide-20k: A 20 tonne two-phase LAr TPC for direct dark matter detection at LNGS. *Eur. Phys. J. Plus*, 133(3):131, Mar 2018.

[228] E. Behnke et al. Final results of the PICASSO dark matter search experiment. *Astropart. Phys.*, 90:85–92, 2017.

[229] Ohjoon Kwon et al. First results from an axion haloscope at CAPP around 10.7 μeV. *Phys. Rev. Lett.*, 126:191802, May 2021.

[230] Matteo Viel et al. Constraining warm dark matter candidates including sterile neutrinos and light gravitinos with WMAP and the Lyman-α forest. *Phys. Rev. D*, 71:063534, Mar 2005.

[231] Keith A. Olive and Michael S. Turner. Cosmological bounds on the masses of stable, right-handed neutrinos. *Phys. Rev. D*, 25:213–216, Jan 1982.

[232] Christophe Yèche et al. Constraints on neutrino masses from Lyman-α forest power spectrum with BOSS and XQ-100. *JCAP*, 2017(06):047–047, Jun 2017.

[233] Xiangdong Shi and George M. Fuller. New dark matter candidate: Nonthermal sterile neutrinos. *Phys. Rev. Lett.*, 82:2832–2835, Apr 1999.

[234] Takehiko Asaka, Mikhail Shaposhnikov, and Alexander Kusenko. Opening a new window for warm dark matter. *Phys. Lett. B*, 638(5):401–406, 2006.

[235] F. Bezrukov, H. Hettmansperger, and M. Lindner. keV sterile neutrino dark matter in gauge extensions of the standard model. *Phys. Rev. D*, 81:085032, Apr 2010.

[236] Jeff A. Dror, Gilly Elor, and Robert Mcgehee. Directly Detecting Signals from Absorption of Fermionic Dark Matter. *Phys. Rev. Lett.*, 124(18):18, 2020.

[237] Dan Zhang et al. A search for light fermionic dark matter absorption on electrons in pandax-4t. *arXiv:2206.02339*, 2022.

[238] J.D. Lewin and P.F. Smith. Review of mathematics, numerical factors, and corrections for dark matter experiments based on elastic nuclear recoil. *Astropart. Phys.*, 6(1):87–112, 1996.

[239] Shao-Feng Ge, Pedro Pasquini, and Jie Sheng. Solar neutrino scattering with electron into massive sterile neutrino. *Phys. Lett. B*, 810:135787, 2020.

[240] Riccardo Catena, Timon Emken, Nicola A. Spaldin, and Walter Tarantino. Atomic responses to general dark matter-electron interactions. *Phys. Rev. Research*, 2:033195, Aug 2020.

[241] W. Ma et al. Internal calibration of the PandaX-II detector with radon gaseous sources. *JINST*, 15(12):P12038–P12038, Dec 2020.

[242] Alan M. Ferrenberg and Robert H. Swendsen. Optimized Monte Carlo data analysis. *Phys. Rev. Lett.*, 63:1195–1198, Sep 1989.

[243] Jin-Yuan Liao et al. Background model for the low-energy telescope of Insight-HXMT. *J. High Energy Phys.*, 27:24–32, 2020.

[244] Laurent Bouchet et al. Diffuse emission measurement with INTEGRAL/SPI as indirect probe of cosmic-ray electrons and positrons. *Astrophys. J.*, 739(1):29, Sep 2011.

[245] Yan Gong and Xuelei Chen. Cosmological constraints on invisible decay of dark matter. *Phys. Rev. D*, 77:103511, May 2008.

[246] Glen Cowan, Kyle Cranmer, Eilam Gross, and Ofer Vitells. Power-constrained limits. 2011.

[247] Mukesh K. Pandey et al. Constraints from a many-body method on spin-independent dark matter scattering off electrons using data from germanium and xenon detectors. *Phys. Rev. D*, 102:123025, Dec 2020.

[248] Hongguang Zhang et al. Dark matter direct search sensitivity of the PandaX-4T experiment. *Sci. China Phys. Mech. Astron.*, 62(3):31011, 2019.

[249] J. Aalbers et al. First dark matter search results from the LUX-ZEPLIN (LZ) experiment. *arXiv:2207.03764*, 2022.